STARS

2012

State (hydrodynamics) Identification In The Lower St. Johns River Using The Ensemble Kalman Filter

Hitoshi Tamura
University of Central Florida

Showcase of Text, Archives, Research & Scholarship

STATE (HYDRODYNAMICS) IDENTIFICATION
IN THE LOWER ST. JOHNS RIVER
USING THE ENSEMBLE KALMAN FILTER

by

HITOSHI TAMURA
B.S. Chuo University, Tokyo, Japan, 2007

A thesis submitted in partial fulfillment of the requirements
for the degree of Master of Science
in the Department of Civil, Environmental, and Construction Engineering
in the College of Engineering and Computer Science
at the University of Central Florida
Orlando, Florida

Spring Term
2012

Major Professors: Scott C. Hagen and Dingbao Wang

ABSTRACT

This thesis presents a method, Ensemble Kalman Filter (EnKF), applied to a high-resolution, shallow water equations model (DG ADCIRC-2DDI) of the Lower St. Johns River with observation data at four gauging stations. EnKF, a sequential data assimilation method for non-linear problems, is developed for tidal flow simulation for estimation of state variables, i.e., water levels and depth-integrated currents for overland unstructured finite element meshes. The shallow water equations model is combined with observation data, which provides the basis of the EnKF applications. In this thesis, EnKF is incorporated into DG ADCIRC-2DDI code to estimate the state variables.

Upon its development, DG ADCIRC-2DDI with EnKF is first validated by implementing to a low-resolution, shallow water equations model of a quarter annular harbor with synthetic observation data at six gauging stations. Second, DG ADCIRC-2DDI with EnKF is implemented to a high-resolution, shallow water equations model of the Lower St. Johns River with real observation data at four gauging stations. Third, four different experiments are performed by applying DG ADCIRC-2DDI with EnKF to the Lower St. Johns River.

ACKNOWLEDGMENTS

Finally, I would like to thank my family in Japan. They always encouraged me by phone calls, e-mail, and letters. I do not think I could finalize my research with their support. Also, they always said 'Believe yourself. You can do it!' when I was depressed. Again, I am deeply grateful to my family for their guidance, understanding, and encouragement.

TABLE OF CONTENTS

LIST OF FIGURES

LIST OF TABLES

LIST OF ACRONYMS/ABBREVIATIONS

2D	Two-Dimensional
ADCIRC-2DDI	Advanced Circulation Model for Oceanic, Coastal, and Estuarine Waters, Two-Dimensional Depth-Integrated
DG	Discontinuous Galerkin method
EnKF	Ensemble Kalman filter
KF	Kalman filter
NAVD88	North American Vertical Datum of 1988
NOAA	National Oceanic and Atmospheric Administration
RMSE	Root mean square errors
UU	Depth-integrated velocity for Easting direction
VV	Depth-integrated velocity for Northing direction

CHAPTER 1: INTRODUCTION

In the following research, an Ensemble Kalman Filter (EnKF) is coupled with an

ADvanced CIRCulation (ADCIRC) numerical code to simulate water surface elevations and

depth-integrated velocities in the St. Johns River for a 30-day time period spanning September

21 – October 21, 1999. The St. John River is located in north Florida (Figure 1). The watershed

of the St. Johns River is over 22,000 km^2 in area and the overall length of the St. Johns River is

over 500 km (Sucsy and Morris, 2002). Tides extend 160 km upstream to Lake George

(Giardino, 2009). River flow is slow and lazy because of an average river bed slope of only 2.2

cm of drop per km of length (Toth, 1993). In the Lower St. Johns River, four observation

stations are available (Bourgerie, 1999): 1) Mayport; 2) Fulton; 3) Dames Point; and 4)

Jacksonville. The locations of the stations are shown in Table 1. Boundary conditions are

applied on the open ocean boundary as a water surface elevation that is composed of seven

astronomical tidal constituents (K_1, O_1, M_2, S_2, N_2, K_2, and Q_1). Previous research (Bacopoulos,

2009) applied a spatial distribution of Manning's n values based on two classes, 'open water' (n

$= 0.025$); and 'emergent herbaceous wetland' ($n = 0.050$).

The major goal of this research is that EnKF, a sequential data assimilation method, will

be used to improve model prediction through the incorporation of observation data into a

hydrodynamic model. This research will develop and couple EnKF with a high-resolution

hydrodynamic model of the Lower St. Johns River (Bacopoulos 2009) for estimating of water

levels and depth-integrated currents. In this research, EnKF is incorporated into the

hydrodynamic model included a shallow water equations model DG ADCIRC-2DDI (Ethan, et al., 2006).

There are three objectives in this research. The first objective is to validate the development of DG ADICRC-2DDI with EnKF using a low resolution, shallow water equations model of a quarter annular harbor (http://www.adcirc.org/) with synthetic observation data at six gauging stations for estimations of the water surface elevations and depth-integrated velocities. The second objective is to apply DG ADCIRC-2DDI with EnKF to a high-resolution, shallow equations model of the Lower St. Johns River for estimations of water levels and depth-integrated currents with real observation data at three stations for data assimilations and one station, not used for data assimilation, for comparisons. The station, used for the comparisons, is called a target station. The third objective is to perform four different experiments by applying DG ADICRC-2DDI with EnKF to the Lower St. Johns River.

Table 1   **Locations of four gauging stations.**

Gauging Station	Latitude (N)	Longitude (W)
Mayport	30.38	81.46
Fulton	30.39	81.51
Dames Point	30.39	81.56
Jacksonville	30.38	81.63
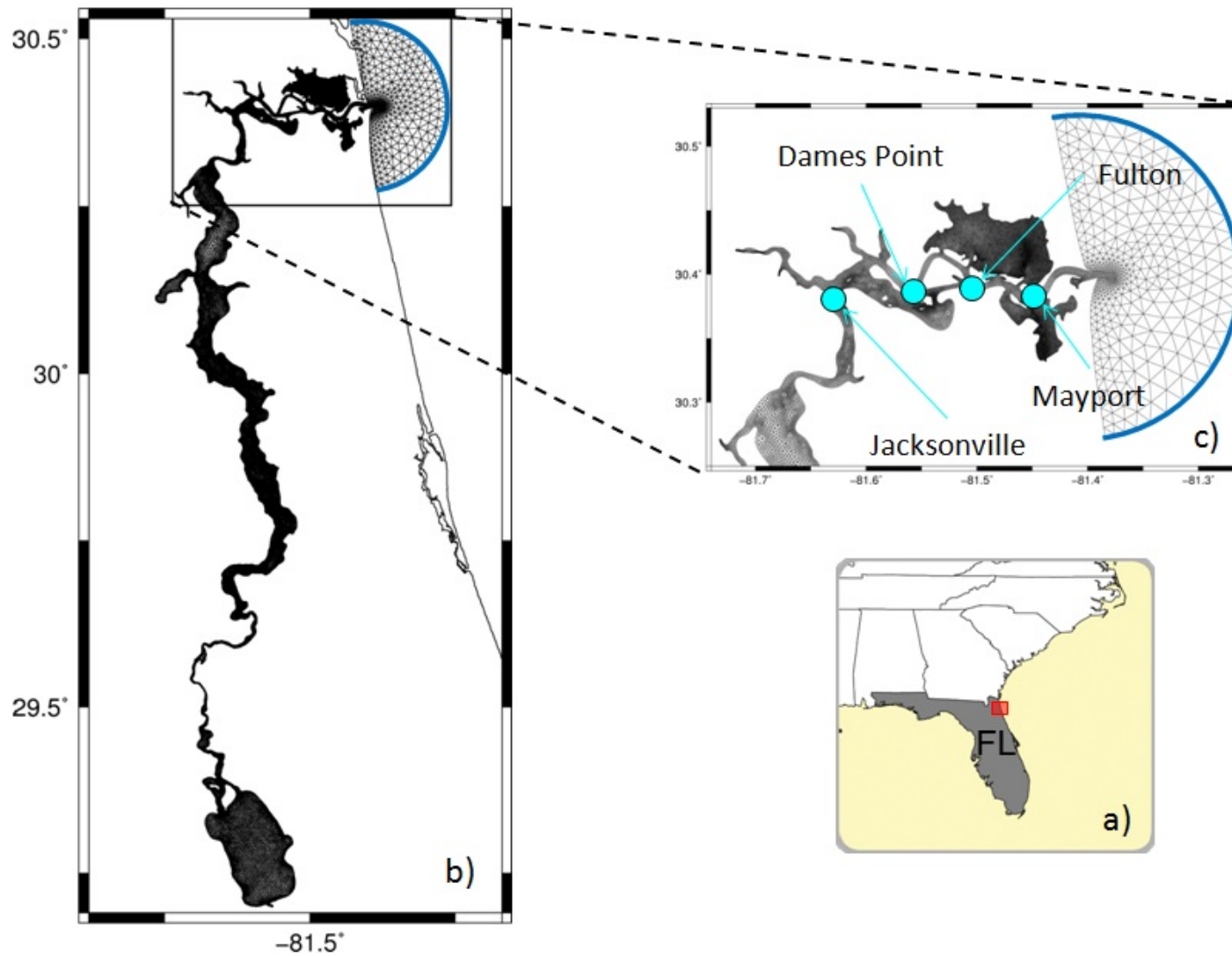
Figure 1   Locator Map; a) shown in red is St. Johns River location, b) shown in black box is the Lower St. Johns River, and c) the Lower St. Johns River with four gauging stations.

CHAPTER 2: LITERATURE REVIEW

This chapter presents a literature review of the following three topics related data

assimilation techniques: 1) a general concept of data assimilation and its applications, 2) a basic

concept of KF and its applications, and 3) EnKF and its applications.

2.1. Data Assimilation

Wei et al. (2009) states that (p. 3)

"Data assimilation methods synthesize numerical solutions with the available

observations to obtain an optimal estimation which can be used as the new initial

condition for model forecasting…Since numerical models contain errors due to the

incomplete physics and numerical implementation, insufficient resolution, and errors in

forcing functions and observations, it is necessary to correct simulation results. This

process can be done in data assimilation. In general, the analysis procedure minimizes

the mean square error between the model states and the observations."

Figure 2 illustrates the procedures of data assimilation (Miyoshi, 2005). Shown in black dashed

arrows is a true state variable which is usually unknown. Thus, a state variable is predicted using

a numerical calculation model. At the time when an observed state variable is available, the

predicted state variable is updated using the observed state variable. The updated state variable

is calculated using the optimal weights of the predicted and observed state variables.
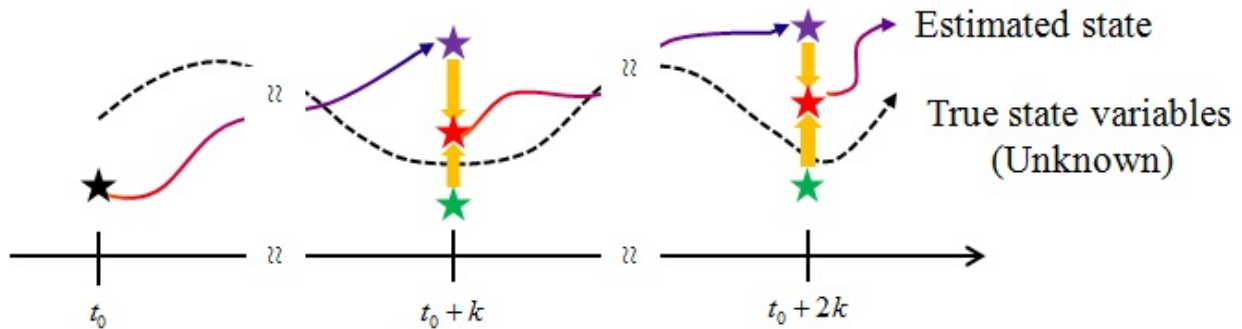
Figure 2   **Data assimilation scheme taken from Miyoshi (2005). t_0 is the initial time, k is the time interval of observation data, shown in black star is initial state variable, in green star is observed state variable, in purple star is predicted state variable, and in red star is updated state variable.**

Data assimilation utilizes observation data, numerical models, and updated system

(Robinson and Lermusiaux, 2000). Data assimilation considers modeling error and observation

error. All hydrodynamic models are not perfect because of discretization of continuous system

and parameter settings. Some sources of error associated with observation include: 1) error of

measurement noise; 2) error of measurement interpretation. Thus, data assimilation combines

uncertainties of numerical models and observation data in the updated system.

Data assimilation is used in many fields of geosciences, most importantly in weather

forecasting and hydrology (Fisher, et. al., 2009). Some of the data assimilation methods are

nudging methods (Auroux and Blum, 2008), optimal interpolation methods (Tombette, et. al.,

2009), inverse methods (Evensen, 1994), and Kalman filtering methods. In this study, Kalman

filtering based methods are used.

2.2. Kalman Filter

Kalman Filter (KF), a method of data assimilation, is a mathematical method for a linear

system. KF estimates state variables using the observation values and predicted values from

numerical model. The estimations consider the uncertainty of the predicted value and

observation value, and compute a weighted average of the predicted value and the observed

value (Welch and Bishop, 2006). KF has been used since the 1960's in scientific fields for

communication and navigation systems. More recently, KF is used in variety fields for

numerical model estimation.

Kalman (1960) emphasizes the concept of *state* and *state transition* which is a dynamic

system. KF uses the dynamic system's model, e.g., laws of physics, known control inputs to the

dynamic system, and observations within the environment, to calculate an estimation of the

variables in the dynamic system. KF is an attractive method for practical problems of prediction

since it considers the uncertainties of the dynamic system and the observations.

There are three sources of uncertainty associated with the modeling of a dynamic system.

First, one error source is 'formulation' error of the physical system within the natural world. A

discrete representation of the continuous system is used for the modeling. For example,

geographical features, such as the bottom of the sea, coastline, and riverline cannot be fully

represented in the model as continuous features. The second error source is 'numerical' error.

The numerical errors are mainly from the truncation of the infinite series involved in the

numerical approximation but also from round-off of calculated values (machine precision). The

third error source is 'data' error. Observed data contain error. This is because the observation of

a physical process in the natural world involves uncertainty, e.g., with the sensors used for

measurement, environmental conditions during the time of measurement, and interpretation and

processing of the measurements.

The following equations are the basis of KF as presented by Ojima (2009). KF is based

on a system equation that predicts the state estimate:

$$x_{k+1} = \mathbf{F}_k x_k + \mathbf{G}_k w_k \dots \dots \dots (2.1)$$

and the observation equation that relates the observed data and the state estimate:

$$y_k = \mathbf{H}_k x_k + v_k \dots \dots \dots (2.2)$$

where x_k is a vector of the state estimate at time k, $\mathbf{F}_k$ is the state transition matrix which

represents the prediction model, $\mathbf{G}_k$ is the driving matrix, w_k is the system noise, y_k is a vector

of the observations at time k, $\mathbf{H}_k$ is the coefficient matrix, expressed as the correspondence

between the observation and state estimate, and v_k is the observation noise. The mean errors of

7

the system noise is assumed to be equal to zero $E\{w_k\} = 0$, which generates the following

covariance matrix:

$$\text{cov}\{w_k, w_j\} = E\{w_k, w_j^{\text{T}}\} = \mathbf{Q}_{w_k}\delta_{kj} \quad\ldots\ldots\ldots\ldots\ldots\ldots\ldots\ldots\ldots\ldots\ldots (2.3)$$

and making the same assumption for the observation noise $E\{v_k\} = 0$ generates the following

covariance matrix:

$$\text{cov}\{v_k, v_j\} = E\{v_k, v_j^{\text{T}}\} = \mathbf{R}_{v_k}\delta_{kj} \quad\ldots\ldots\ldots\ldots\ldots\ldots\ldots\ldots\ldots\ldots\ldots (2.4)$$

with $E\{w_k, v_j\} = 0$ and where δ_{kj} is Kroncker's delta (Zwillinger, 2003):

$$\delta_{kj} = \begin{cases} 1, & k = j \\ 0, & \text{otherwise} \end{cases} \quad\ldots\ldots\ldots\ldots\ldots\ldots\ldots\ldots\ldots\ldots\ldots\ldots\ldots\ldots\ldots (2.5)$$

in which E is the mean value operator, $\mathbf{Q}$ is the system error covariance, and $\mathbf{R}$ is the

observation error covariance matrix.

External forcing can be applied using boundary conditions, which modifies the system

equation (Eq. [2.1]) accordingly:

$$x_{k+1} = \mathbf{F}_k x_k + \mathbf{D}_k u_k + \mathbf{G}_k w_k \quad\ldots\ldots\ldots\ldots\ldots\ldots\ldots\ldots\ldots\ldots\ldots\ldots (2.6)$$

where u_k represents the boundary input and $\mathbf{D}_k$ takes the form of the state transition matrix which represents the treatment of boundary conditions by the prediction model.

The optimal estimate $\hat{x}_k$ is defined as the average of the predictions x_k given the observed data at the current time step y_k: $\hat{x}_k = E\{x_k, y_k\}$. The estimated error covariance is written as:

$$\mathbf{P}_k = \mathrm{cov}\{x_k, y_k\} = E\left\{\left(x_k - \hat{x}_k\right)\left(x_k - \hat{x}_k\right)^{\mathrm{T}}\right\} \quad\dots\dots\dots\dots\dots\dots\dots\dots\dots (2.7)$$

and the estimate x_k^* is defined as the average of the predictions x_k given the observed data at the previous time step y_{k-1}: $x_k^* = E\{x_k, y_{k-1}\}$. The predicted error covariance is written as:

$$\mathbf{\Gamma}_k = \mathrm{cov}\{x_k, y_{k-1}\} = E\left\{\left(x_k - x_k^*\right)\left(x_k - x_k^*\right)^{\mathrm{T}}\right\} \quad\dots\dots\dots\dots\dots\dots\dots\dots (2.8)$$

Bayes' theorem (Zwillinger, 2003) is written in terms of the predictions x_k and observations y_k:

$$P\left(x_k|y_k\right) = \frac{P\left(y_k|x_k\right)P\left(x_k|y_{k-1}\right)}{P\left(y_k|y_{k-1}\right)} \quad\dots\dots\dots\dots\dots\dots\dots\dots\dots\dots\dots (2.9)$$

from which are derived the optimal estimate $\hat{x}_k$:

$$\hat{x}_k = x_k^* + \mathbf{K}_k\left(y_k - \mathbf{H}_k x_k^*\right) \quad\dots\dots\dots\dots\dots\dots\dots\dots\dots\dots\dots (2.10a)$$

where the Kalman-gain $\mathbf{K}_k$ is computed as:

$$\mathbf{K}_k = \mathbf{\Gamma}_k \mathbf{H}_k^{\mathrm{T}} \left(\mathbf{R}_{v_k} + \mathbf{H}_k \mathbf{\Gamma}_k \mathbf{H}_k^{\mathrm{T}} \right)^{-1} \dots\dots\dots\dots\dots\dots\dots\dots\dots\dots\dots\dots\dots \quad (2.10\text{b})$$

where the estimated error covariance $\mathbf{P}_k$ is computed as:

$$\mathbf{P}_k = \left(\mathbf{I} - \mathbf{K}_k \mathbf{H}_k \right) \mathbf{\Gamma}_k \dots\dots\dots\dots\dots\dots\dots\dots\dots\dots\dots\dots\dots\dots\dots\dots\dots \quad (2.10\text{c})$$

and the predicted error covariance $\mathbf{\Gamma}_{k+1}$ is computed as:

$$\mathbf{\Gamma}_{k+1} = \mathbf{F}_k \mathbf{P}_k \mathbf{F}_k^{\mathrm{T}} + \mathbf{G}_k \mathbf{Q}_{w_k} \mathbf{G}_k^{\mathrm{T}} \dots\dots\dots\dots\dots\dots\dots\dots\dots\dots\dots\dots\dots \quad (2.10\text{d})$$

where $\mathbf{I}$ is the identify matrix, $\mathbf{Q}$ is the system error covariance, and $\mathbf{R}$ is the observation error covariance.

The algorithm of KF is written as (Ojima and Kawahara, 2009):

$$\mathbf{\Gamma}_0 = \left\{ \hat{x}_{\text{init}} \right\} = \left\{ \hat{x}_0 \right\} \dots\dots\dots\dots\dots\dots\dots\dots\dots\dots\dots\dots\dots\dots \quad (2.11\text{a})$$

$$\mathbf{K}_k = \mathbf{\Gamma}_k \mathbf{H}^{\mathrm{T}} \left(\mathbf{R}_v + \mathbf{H}\mathbf{\Gamma}_k \mathbf{H}^{\mathrm{T}} \right)^{-1} \dots\dots\dots\dots\dots\dots\dots\dots\dots\dots\dots\dots \quad (2.11\text{b})$$

$$\mathbf{P}_k = (\mathbf{I} - \mathbf{K}_k \mathbf{H})\boldsymbol{\Gamma}_k \quad \cdots\cdots\cdots\cdots\cdots\cdots\cdots\cdots\cdots\cdots\cdots\cdots\cdots\cdots\cdots \quad (2.11c)$$

$$\boldsymbol{\Gamma}_{k+1} = \mathbf{F}_k \mathbf{P}_k \mathbf{F}_k^{\mathrm{T}} + \mathbf{G}_k \mathbf{Q}_w \mathbf{G}_k^{\mathrm{T}} \quad \cdots\cdots\cdots\cdots\cdots\cdots\cdots\cdots\cdots\cdots\cdots \quad (2.11d)$$

$$\{x_k^*\} = \mathbf{F}_k \{\hat{x}_k\} + \mathbf{D}_k u_k \quad \cdots\cdots\cdots\cdots\cdots\cdots\cdots\cdots\cdots\cdots\cdots\cdots \quad (2.11e)$$

$$\{\hat{x}_k\} = \{x_k^*\} + \mathbf{K}_k \left(\{y_k\} - \mathbf{H}\{x_k^*\}\right) \quad \cdots\cdots\cdots\cdots\cdots\cdots\cdots\cdots\cdots \quad (2.11f)$$

where $\{\hat{x}_k\}$ is a vector of the state estimate at time k and $\boldsymbol{\Gamma}$, $\mathbf{K}$, and $\mathbf{P}$ are the predicted error covariance, Kalman-gain, and estimated error covariance, respectively. Eqs. (2.11a) to (2.11d) are called offline calculation because they do not rely on the observation data. Conversely, Eqs. (2.11e) and (2.11f) are called online calculation because they use the observation data.

As mentioned earlier, KF is a data assimilation method for linear systems. However, most ocean and coastal processes are non-linear. As an extension of KF, EnKF is developed for non-linear problems.

2.3. Ensemble Kalman Filter

EnKF is a sequential data assimilation method for non-linear problems. Burgers et al. (1998) states that (p. 1)

"EnKF is first introduced by Evensen (1994) as an alternative to the traditional extended

Kalman filter, which has been shown to be based on a statistical linearization or closure

approximation that is too severe to be useful for some cases with strongly non-linear

dynamics... EnKF is attractive since it avoids many of the problems associated with the

traditional extended Kalman filter; for example there is no closure problem as is

introduced in the extended Kalman filter by neglecting contributions from higher-order

statistical moments in the error covariance evolution equation… It can also be computed

at a much lower numerical cost, since usually a rather limited number of model states are

sufficient for reasonable statistical convergence. For sufficient ensemble sizes, the errors

will be dominated by statistical noise, not by closure problems or unbounded error

variance growth."

Then, it has been studied by a lot of researchers (Evensen, 2003; Houtekamer and Mitchell,

1998; Tippett et al., 2003; Zang and Malanotte-Rizzoli, 2003; Chen et al., 2008).

EnKF is composed of data assimilation and ensemble prediction (Miyoshi, 2005).

Ensemble prediction is mainly used for weather forecasting (Manousos, 2006). Ensemble

prediction calculates an ensemble of the state variables in the dynamic system for a future time

using different ensemble state variables that are generated from the state variable at the current

time (Figure 3). Ensemble state variables at time t are generated by adding small error and

translating them to the future time step. Then, an average of ensemble can be calculated using

the ensemble state variables at the future time step. The averaged state variable is a better

prediction because error is canceled out by ensemble state variables at the future time step.
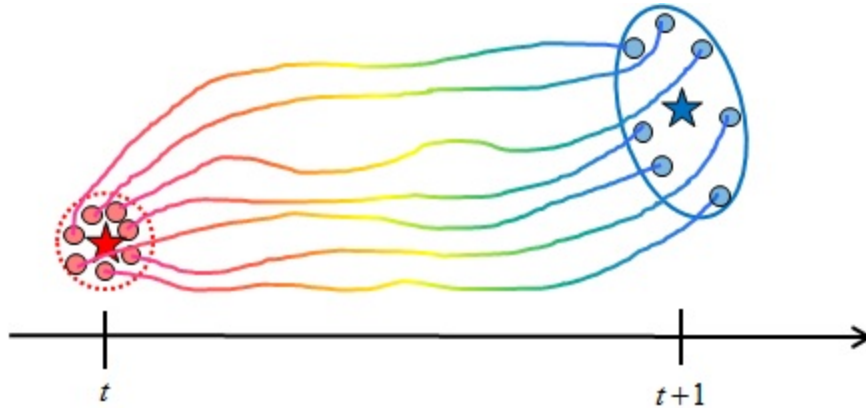
Figure 3   **Ensemble prediction scheme taken form Miyoshi (2005). Shown in red star is the state variable at time *t*, in red circle is ensemble state variables at time *t*, in red dash circle is ensemble spread at time *t*, in blue circle is ensemble state variables at time *t*+1, in blue star is the average of state variables at time *t*+1, and in blue ellipsoidal circle is ensemble state spread at time *t*+1.**

EnKF is based on ensemble integrations. An ensemble of model states is integrated forward in time, and the mean and error covariance matrices are calculated at analysis times. According to Evensen (2004), the error covariance matrices for the forecasted and the analyzed estimate, $\mathbf{P}^f$ and $\mathbf{P}^a$, are defined in the KF in terms of the true state as

$$\mathbf{P}^f = \overline{\left(\psi^f - \psi^t\right)\left(\psi^f - \psi^t\right)^T} \quad\dots\dots\dots\dots\dots\dots\dots\dots\dots\dots\dots\dots\dots (2.12)$$

$$\mathbf{P}^a = \overline{\left(\psi^a - \psi^t\right)\left(\psi^a - \psi^t\right)^T} \quad\dots\dots\dots\dots\dots\dots\dots\dots\dots\dots\dots\dots (2.13)$$

where the overbar denotes an expected value, ψ is the model state vector at a particular time, and the superscripts f, a, and t represent forecast, analyzed, and true state, respectively.

However, since the true state is not known, it is more convenient to consider ensemble covariance matrices around the ensemble mean $\overline{\psi}$:

$$\mathbf{P}^f \simeq \mathbf{P}_e^f = \overline{\left(\psi^f - \overline{\psi^f}\right)\left(\psi^f - \overline{\psi^f}\right)^T} \quad\ldots\ldots\ldots\ldots\ldots\ldots\ldots\ldots\ldots\ldots\ldots\ldots (2.14)$$

$$\mathbf{P}^a \simeq \mathbf{P}_e^a = \overline{\left(\psi^a - \overline{\psi^a}\right)\left(\psi^a - \overline{\psi^a}\right)^T} \quad\ldots\ldots\ldots\ldots\ldots\ldots\ldots\ldots\ldots\ldots\ldots\ldots (2.15)$$

where the overbar denotes an average over the ensemble. The ensemble covariance is considered the best estimation of the error covariance since the ensemble mean cancels out the errors by ensemble members.

The following equations include the base equations and the algorithm for EnKF as presented by Wang et al., 2009. For a general stochastic dynamic model the system equation is:

$$x_{k+1} = f\left(x_k, \theta\right) + w_k, w_k \sim N\left(0, U_k\right) \quad\ldots\ldots\ldots\ldots\ldots\ldots\ldots\ldots\ldots\ldots\ldots\ldots (2.16)$$

where x_k is the state vector at time k (size n by 1), θ is the system parameter vector (size l by 1) and assumed to be known, f represents the model structure, and w_k (size n by 1) is the model error term, which takes the form of a Gaussian distribution with zero mean and covariance matrix U_k (size n by n) which is diagonal. The observation equation is:

$$y_{k+1} = h\left(x_{k+1}, \theta\right) + v_{k+1}, v_{k+1} \sim N\left(0, R_{k+1}\right) \quad\ldots\ldots\ldots\ldots\ldots\ldots\ldots\ldots\ldots\ldots\ldots\ldots (2.17)$$

where y_{k+1} is the observation vector at time $k + 1$ (size m by 1), h is a measurement function that describes the relationship between observation and the state variables, and v_{k+1} (size m by 1) is the measurement error which has a Gaussian distribution with zero mean and covariance matrix R_{k+1} (size m by m) which is diagonal. The model and observation errors are assumed to be uncorrelated, i.e., $E\left[w_k v_{k+1}^T \right] = 0$, where the superscript T denotes the matrix transpose. The EnKF translates an ensemble of states in parallel based on Eq. (2.16):

$$x_{k+1|k}^i = f\left(x_{k|k}^i, \theta \right) + w_k^i \quad \cdots\cdots\cdots\cdots\cdots\cdots\cdots\cdots\cdots\cdots\cdots\cdots\cdots\cdots \quad (2.18)$$

where $x_{k+1|k}^i$ is the ith ensemble member forecast at time $k + 1$, $x_{k|k}^i$ is the ith updated ensemble member at time k and w_k^i is the generated system noise for the ith ensemble member. The error covariance matrix is calculated based on the forecasted ensemble members:

$$\sum\nolimits_{k+1|k}^{xx} = \frac{1}{N-1} X_{k+1|k} X_{k+1|k}^T, \; X_{k+1|k} = \left[x_{k+1|k}^1 - \overline{x}_{k+1|k}, \cdots, x_{k+1|k}^N - \overline{x}_{k+1|k} \right] \quad \cdots\cdots\cdots\cdots\cdots\cdots \quad (2.19)$$

where $\overline{x}_{k+1|k}$ is the ensemble mean of the forecasted members and N is the ensemble size. The updated state is calculated by a linear correction, and the analysis step is:

$$x_{k+1|k+1}^i = x_{k+1|k}^i + K_{k+1} \left[y_{k+1}^i - h\left(x_{k+1|k}^i, \theta \right) \right] \cdots\cdots\cdots\cdots\cdots\cdots\cdots\cdots\cdots\cdots\cdots \quad (2.19)$$

where y_{k+1}^i is the ith observation sample generated by adding the observation error v_{k+1}^i to the actual observation:

$$y_{k+1}^i = y_{k+1} + v_{k+1}^i \quad \cdots\cdots\cdots\cdots\cdots\cdots\cdots\cdots\cdots\cdots\cdots\cdots\cdots\cdots\cdots\cdots (2.20)$$

The same KF approach is used, however, for each of the ensemble members. The important fact is that the addition of random perturbations to the observations preserves the variance of the analyzed ensemble.

The Kalman gain matrix K_{k+1} can be calculated by:

$$K_{k+1} = \sum\nolimits_{k+1|k}^{xy} \left[\sum\nolimits_{k+1|k}^{yy} + R_{k+1} \right]^{-1} \cdots\cdots\cdots\cdots\cdots\cdots\cdots\cdots\cdots\cdots\cdots (2.21)$$

where $\sum\nolimits_{k+1|k}^{xy}$ is the cross covariance of the forecasted states $x_{k+1|k}^i$ and the forecasted output $h\left(x_{k+1|k}^i, \theta\right)$, and it is approximated as:

$$\sum\nolimits_{k+1|k}^{xy} = \frac{1}{N-1} X_{k+1|k} Y_{k+1|k}^T, \; Y_{k+1|k} = \left[y_{k+1|k}^1 - \overline{y}_{k+1|k}, \cdots, y_{k+1|k}^N - \overline{y}_{k+1|k} \right] \cdots\cdots\cdots\cdots (2.22)$$

where $y_{k+1|k}^i$ is the forecasted output $h\left(x_{k+1|k}^i, \theta\right)$, and $\overline{y}_{k+1|k}$ is the forecasted ensemble mean.

$\sum\nolimits_{k+1|k}^{yy}$ is the error covariance matrix of the forecasted output:

$$\sum{}_{k+1|k}^{yy} = \frac{1}{N-1} Y_{k+1|k} Y_{k+1|k}^{T} \quad \cdots\cdots\cdots\cdots\cdots\cdots\cdots\cdots\cdots\cdots\cdots\cdots\cdots (2.23)$$

The updated state error covariance matrix is calculated by the updated states similarly as Eq.

(2.19). In the ensemble Kalman filter, the translation of the state error covariance matrix is not

needed, and the covariance matrices ($\sum{}_{k+1|k}^{xy}$, $\sum{}_{k+1|k}^{yy}$, and $\sum{}_{k+1|k}^{xx}$) are computed through the

ensemble of members avoiding the computation of observation matrix H.

Figure 4 depicts the ensemble Kalman filter as the propagation of the state ensemble for a

simulation where ensemble observations are used in the model estimation method.

Observation

y_{t-k} y_t y_{t+k}

Ensemble Observations

$y^i_{k-t} = y_{k-t} + v^i_{k-t}$ $y^i_t = y_t + v^i_t$ $y^i_{t+k} = y_{t+k} + v^i_{t+k}$

Ensemble State variables

$x^i_{t-k|t-k-1}$ $x^i_{t-k|t-k}$ $x^i_{t|t-1}$ $x^i_{t|t}$ $x^i_{t+k|t+k-1}$ $x^i_{t+k|t+k}$

$t-k$ t $t+k$
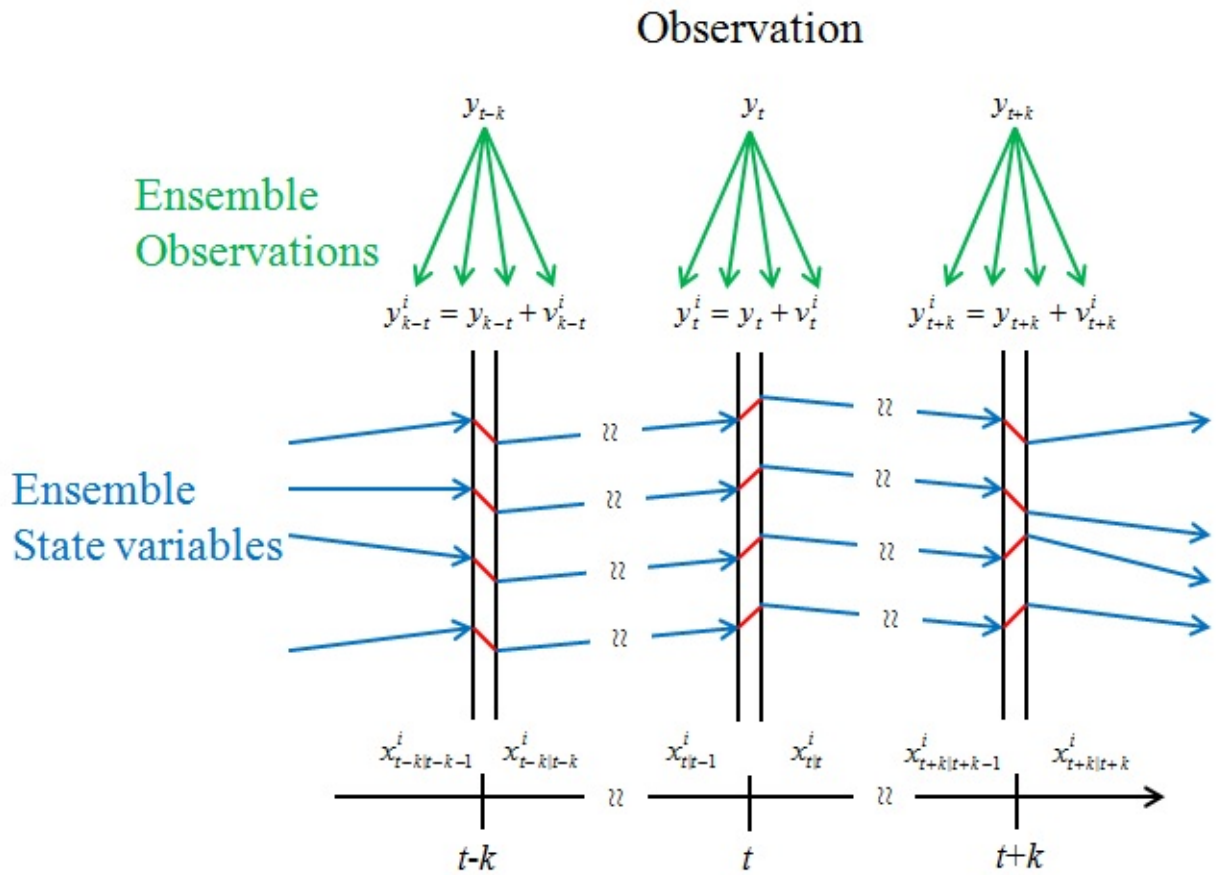
Figure 4   **Schematic of the ensemble Kalman filter take from Moradkhani et al. (2005). *t* is the time, and *k* is the time interval of the observation.**

Ensemble Kalman filters have been applied in coastal area modeling (Madsen and Canizares, 1999), the ensemble Kalman filter in the Selat Pauh of Singapore (Wei and Malanotte-Rizzoli, 2009), and dual state-parameter estimation of hydrological models using ensemble Kalman filter (Moradkhani et al., 2005; Wang et al., 2009).

CHAPTER 3: MANNING'S N VALUES

3.1. Overview

In hydrodynamic modeling, friction coefficients are commonly used to parameterize drag (Hsu et al., 1999). Drag refers to the hydraulic resistance occurring over the wetted perimeter of the flow. In the estuarine setting, hydraulic resistance generally accounts for roughness due to soil grain, bedform variations, and vegetation.

Manning's roughness, frequently used in the calculation of open channel flows (Chow, 1959), will be employed herein for the parameterization of bottom stress:

$$Q = \frac{A}{n} R^{2/3} S_0^{1/2} \quad \text{(metric units)} \quad \dots\dots\dots\dots\dots\dots\dots\dots\dots\dots\dots\dots\dots \text{(3.1)}$$

where Q = flow; A = cross-sectional area of flow; n = Manning's roughness coefficient; $R = A/P$ = hydraulic radius of flow, where P = wetted perimeter; and S_0 = bed slope. Manning's roughness coefficients have been tabulated by Chow (1959) for different material types and channel geometries. Barnes (1967) catalogued Manning's n values for typical rivers and creeks, which range from 0.024 to 0.075.

Arcement and Schneider (1989) tabulated Manning's roughness coefficients for natural channels and floodplains as being the composite effect of (Cowen, 1956):

19

$$n = (n_0 + n_1 + n_2 + n_3 + n_4)m \cdots\cdots\cdots\cdots\cdots\cdots\cdots\cdots\cdots\cdots\cdots\cdots\cdots\cdots (3.2)$$

where n_0 = base value for bare soil; n_1 = correction factor for irregularities; n_2 = correction factor for cross-sectional variations; n_3 = correction factor for obstructions; n_4 = correction factor for vegetation; m = correction factor for sinuosity. With respect to the marshes of the Lower St. Johns River, $n = n_0 + n_4$, since vegetation is prevalent in the domain.

Vegetation can dominate drag in shallow water flow (Fathi-Moghadam and Kouwen, 1997). Arcement and Schneider (1989) suggested adjustment for n_4 values as small as 0.001 – 0.010 for little vegetation to as large as 0.100 – 0.200 for extreme vegetation. Chow (1959) suggested Manning's n values as small as 0.025 – 0.050 for pasture with no brush to as large as 0.110 – 0.160 for areas with trees.

3.2. Spatially Distributed Bottom Roughness

Base knowledge of spatially distributed Manning's n values for the Lower St. Johns River is obtained from Bacopoulos (2009). In the work of Bacopoulos (2009), two classes of landcover (Table 2) were used over the entire domain in the Lower St. Johns River: 'open water ($n = 0.025$)'; and 'emergent herbaceous wetlands ($n = 0.050$)'.

The bottom roughness is another source of uncertainty. Thus, the ensemble Manning's n values are generated;

$$n^i = n_{base} + \theta * N(0,1) \dots \dots \dots \dots \dots \dots \dots \dots \dots \dots \dots \dots \dots \dots \dots (3.3)$$

where n^i is i^{th} ensemble Manning's n, n_{base} is the base value of Manning's n for each landcover (Table 2), θ is the parameter error coefficient, and $N(0,1)$ is the standard normal distribution with zero mean and variance 1. Constraints will be integrated into the EnKF in order to keep the ensemble Manning's n^i values within physically reasonable limits. The spatial distribution of Manning's n values used herein will be bounded as shown in Table 2. Bacopoulos (2009) used 0.025 for 'open water,' while Mattocks et al. (2006) and Loder et al. (2009) used 0.020. Herein, the lower limit for 'open water' is set equal to 0.010 to be representative of well-compacted mud. The upper limit is set equal to 0.035 to be representative of a sandy, undulating bottom. Bacopoulos (2009) used 0.050 for 'emergent herbaceous wetlands,' while Mattocks et al. (2006) used 0.045.

Table 2   **Physically based ranges of Manning's n values.**

Landcover/vegetation	Base value[a]	Lower limit	Upper limit
'Open water'	0.025 / 0.020	0.010	0.035
'Emergent herbaceous wetlands'	0.035 / 0.045 / 0.050	0.025	0.075

[a] Base values are from either Mattocks et al. (2006), Bacopoulos (2009), or Loder et al. (2009).

CHAPTER 4: SHALLOW WATER EQUATIONS MODEL

4.1. Governing Equations and Discretization

ADCIRC - 2DDI is the depth-integrated version of the hydrodynamic code ADCIRC and is governed by shallow water equations (Luettich and Westerink 2006b; Kolar et al. 1994a; Westerink et al. 2008). In their barotropic form, the shallow water equations are expressed in a spherical coordinate system as (Kolar et al., 1994a; Westerink et al., 2008):

$$\frac{\partial \zeta}{\partial t} + \frac{1}{R\cos\phi}\left[\frac{\partial UH}{\partial \lambda} + \frac{\partial(VH\cos\phi)}{\partial \phi}\right] = 0 \quad \dots\dots\dots\dots\dots\dots\dots\dots\dots\dots (4.1)$$

$$\underbrace{\frac{\partial U}{\partial t}}_{\text{Local acceleration}} + \underbrace{\frac{1}{R\cos\phi}U\frac{\partial U}{\partial \lambda}}_{\text{Advection}} + \underbrace{\frac{1}{R}V\frac{\partial U}{\partial \phi}}_{\text{Advection}} - \underbrace{\left(\frac{\tan\phi}{R}U + f\right)V}_{\text{Coriolis effects}} =$$

$$-\frac{1}{R\cos\phi}\frac{\partial}{\partial \lambda}\left[\underbrace{\frac{p_S}{\rho_0}}_{\text{Atmospheric pressure}} + g\left(\underbrace{\zeta}_{\text{Water-level pressure}} - \underbrace{\alpha\eta}_{\text{Local tide}}\right)\right] + \underbrace{\frac{1}{H}M_\lambda}_{\text{Diffusion}} + \underbrace{\frac{\tau_{S\lambda}}{\rho_0 H}}_{\text{Surface stress}} - \underbrace{\tau_* U}_{\text{Bottom stress}} \quad \dots\dots (4.2)$$

$$\underbrace{\frac{\partial V}{\partial t}}_{\text{Local acceleration}} + \underbrace{\frac{1}{R\cos\phi}U\frac{\partial V}{\partial \lambda}}_{\text{Advection}} + \underbrace{\frac{1}{R}V\frac{\partial V}{\partial \phi}}_{\text{Advection}} + \underbrace{\left(\frac{\tan\phi}{R}U + f\right)U}_{\text{Coriolis effects}} =$$

$$-\frac{1}{R}\frac{\partial}{\partial \phi}\left[\underbrace{\frac{p_S}{\rho_0}}_{\text{Atmospheric pressure}} + g\left(\underbrace{\zeta}_{\text{Water-level pressure}} - \underbrace{\alpha\eta}_{\text{Local tide}}\right)\right] + \underbrace{\frac{1}{H}M_\phi}_{\text{Diffusion}} + \underbrace{\frac{\tau_{S\phi}}{\rho_0 H}}_{\text{Surface stress}} - \underbrace{\tau_* V}_{\text{Bottom stress}} \quad \dots\dots\dots\dots (4.3)$$

22

where depth-integrated momentum dispersion $M_{\lambda,\phi}$ in the longitudinal and latitudinal directions, respectively, is given by (Blumberg and Mellor, 1987; Kolar and Gray, 1990):

$$M_{\lambda,\phi} = \frac{E_{h_2}}{R^2}\left[\frac{1}{\cos^2\phi}\frac{\partial^2(U,V)H}{\partial\lambda^2} + \frac{\partial^2(U,V)H}{\partial\phi^2}\right] \dots\dots\dots\dots\dots\dots\dots\dots\dots (4.4)$$

and t = time; λ, ϕ = degrees longitude (east of Greenwich positive) and latitude (north of equator positive), respectively; U, V = depth-integrated velocity in the longitudinal (traversing meridians of longitude/east-west movement) and latitudinal (traversing parallels of latitude/north-south movement) directions, respectively; H = total height of the water column, $h + \zeta$; h = bathymetric depth, relative to NAVD88; ζ = free surface elevation, relative to NAVD88; R = radius of the Earth; $f = 2\Omega\sin\phi$ Coriolis parameter; Ω = angular speed of the Earth; p_s = atmospheric pressure at the free surface; ρ_0 = reference density of water; g = acceleration due to gravity; α = Earth elasticity factor; E_{h_2} = horizontal eddy viscosity; $\tau_{s\lambda}$, $\tau_{s\phi}$ = applied free surface stress in the longitudinal and latitudinal directions, respectively; τ_* = bottom stress; and η = Newtonian tide potential (Reid, 1990).

ADCIRC solves the shallow water equations in the form of the Generalized Wave Continuity Equation (GWCE) to provide highly accurate, noise free, finite element-based solutions (Lynch and Gray 1979; Kinnmark 1985; Kolar et al. 1994b). A standard Galerkin finite element method is applied on linear, triangular finite elements in space, and a three-level implicit scheme in time.

ADCIRC utilizes a quadratic slip formulation for the bottom stress term (Luettich and Westerink 2006a), which herein is expressed in terms of Manning's roughness:

$$\frac{\tau_{u,v}}{\rho_0} = C_f \frac{\sqrt{U^2 + V^2}}{H}(U,V) \quad \text{where} \quad C_f = \frac{g}{H^{1/3}} n^2 \ldots\ldots\ldots\ldots\ldots\ldots\ldots\ldots\ldots\ldots\ldots\ldots (4.5)$$

and $\tau_{u,v}$ = bottom stress components in the longitudinal and latitudinal directions; ρ_0 = reference density of water; U, V = depth-integrated velocity in the longitudinal and latitudinal directions; H = water column depth; C_f = (dimensionless) bottom friction coefficient; g is acceleration due to gravity; and n is the Manning's roughness coefficient.

4.2. DG ADCIRC with EnKF

EnKF is incorporated into DG ADCIRC (Ethan, et. al., 2006a, 2006b, 2007a, 2007b, 2008, 2009a, and 2009b). The original DG ADCIRC codes (DG_ADCIRC_hydro_trans_v20.2) are provided from Dr. Ethan Kubatko at The Ohio State University. In this research, the following three program files are primarily developed: 1) ADCIRC.F, 2) READ_INPUT.F, and 3) DG_TIMESTEP.F. Shown in red are newly developed in DG ADCIRC codes for EnKF. More detail of the developments is shown in Appendix A.

Table 3   Original DG ADCIRC code vs. DG ADCIRC with EnKF code.

	DG ADCIRC	DG ADCIRC with EnKF

1)	Call READ_INPUT.F
	
	Call CSTART.F or HSTART.F
	
	Set Flags and coefficients used in time stepping
	
	Call PREP_DG.F
	
	DO ITIME_A = ITHS+1,NT
	
	   Call DG_TIMESTEP.F
	
	END DO
		Call READ_INPUT.F
		
		Call CSTART.F or HSTART.F
		
		Set Flags and coefficients used in time stepping
		
		Call PREP_DG.F
		
		Generate initial ensemble states
		
		Generate ensemble parameters
		
		DO ITIME_A = ITHS+1,NT
		
		   Call DG_TIMESTEP.F
		
		END DO

2)	Read fort.14 file Read fort.15 file Read fort.13 file Read fort.dg file	Read fort.14 file Read fort.15 file Read fort.13 file Read fort.dg file Read INPUT.TEXT Read ZE_OBS.TEXT Read UU_OBS.TEXT Read VV_OBS.TEXT
3)	Call DG_HYDRO_TIMESTEP.F Call DG_SED_TIMESTEP.F Call WRITE_RESUTLS.F	Call DG_HYDRO_TIMESTEP.F Call DG_SED_TIMESTEP.F Call MPI_ALLREDUCE Calculate Cross Covariance Calculate Output Error Covariance Calculate Kalman Gain Update states variables and/or parameters Call WRITE_RESUTLS.F

CHAPTER 5: IDEALIZED MODEL ESTIMATION

EnKF is validated for preliminary model estimation using the quarter annular harbor

mesh (http://www.adcirc.org/) (Figure 5) as the test case. The mesh contains 64 nodes and 96

elements. As mentioned earlier, since observation data are required to implement DG ADCIRC-

2DDI with EnKF, six nodes shown in red circle in Figure 5 are set as observation gauging

stations (from gauges a to f). To show the validation of the development, two types of

Manning's *n* are used for the simulations. One is set to $n = 0.025$ called 'True' Manning's *n*.

The other is set to $n = 0.035$ called 'Applied' Manning's *n*.

5.1. Model Setup

Three simulations are performed for the mesh: 1) running original DG ADCIRC-2DDI

using 'True' Manning's *n* ($= 0.025$) called a true simulation; 2) running original DG ADCIRC-

2DDI using 'Applied' Manning's *n* ($= 0.035$) called an original simulation; and 3) running

developed DG ADCIRC-2DDI with EnKF using 'Applied' Manning's *n* ($= 0.035$) called an

EnKF simulation. As mentioned in Chapter 3.2., the ensemble Manning's n^i are need to be

calculated for the EnKF simulation. The base value (n_{base}), the lower limit (n_{Lower}), and upper

limit (n_{Upper}) of the ensemble Manning's n^i are set to 0.035, 0.025, and 0.045, respectively.

Finite amplitude and advective terms enabled. The total simulation length is 30 days with

boundary conditions ramped up the first 3 days. M2 tidal forcing (amplitude = 0.309 m) is

applied on open ocean boundary shown in blue line (Figure 5). Tidal potential forcings and

harmonic analysis are not included. Wetting and drying capability is disabled with the minimum

water depth set to 1.0 m. Time step is set to 180-second because of the very simple grid. The

GWCE weighting parameter is set equal to -0.01 (Kolar *et al.*, 1994a).

EnKF is applied during the last 10 days of simulation. To implement DG ADCIRC-

2DDI with EnKF, the ensemble sizes are set to 20, the observation error coefficients are set to

30% for WSE, UU, and VV at all gauging stations, and the model error coefficients are set to

10% for WSE, UU, and VV. RMSE are calculated for each state variable. $RMSE_{Original}$ for the

original simulation results can be calculated as:

$$Error_{True-Original}^{Time\_i} = States_{True}^{Time\_i} - States_{Original}^{Time\_i} \quad \dots\dots\dots\dots\dots\dots\dots\dots\dots\dots\dots\dots\dots (5.1)$$

$$\widehat{Error}_{True-Original} = \frac{\displaystyle\sum_{Time\_i=IFirst}^{NTotal} Error_{True-Original}^{Time\_i}}{NTotal} \quad \dots\dots\dots\dots\dots\dots\dots\dots\dots\dots\dots (5.2)$$

$$RMSE_{Original} = \sqrt{\frac{\displaystyle\sum_{Time\_i=IFirst}^{NTotal} \left(\widehat{Error}_{True-Original} - Error_{True-Original}^{Time\_i} \right)}{NTotal}} \quad \dots\dots\dots\dots\dots\dots\dots (5.3)$$

where $States_{True}^{Time\_i}$ is state variable at iteration *i* from the true simulation ($n = 0.025$), $States_{Original}^{Time\_i}$

is state variable at iteration *i* from the original simulation ($n = 0.035$), *IFirst* is the first iteration

that EnKF is applied (= day 20th), *Time_i* is the iteration step (day $20 \leq Time\_i \leq$ day 30 every 6

min.), and *NTotal* is the *Time_i* during the last 10 days (2401). Similarly, $RMSE_{EnKF}$ for the

EnKF simulation results can be calculated as:

$$Error_{True-EnKF}^{Time\_i} = States_{True}^{Time\_i} - States_{EnKF}^{Time\_i} \dots \dots \dots \dots \dots \dots \dots \dots \dots \dots \dots \dots (5.4)$$

$$\widehat{Error}_{True-EnKF} = \frac{\sum_{Time\_i=IFirst}^{NTotal} Error_{True-EnKF}^{Time\_i}}{NTotal} \quad \dots \dots \dots \dots \dots \dots \dots \dots \dots \dots \dots (5.5)$$

$$RMSE_{EnKF} = \sqrt{\frac{\sum_{Time\_i=IFirst}^{NTotal} \left(\widehat{Error}_{True-EnKF} - Error_{True-EnKF}^{Time\_i} \right)}{NTotal}} \quad \dots \dots \dots \dots \dots \dots \dots \dots (5.6)$$

where $States_{EnKF}^{Time\_i}$ is state variable at iteration *i* from the EnKF simulation ($n = 0.035$).
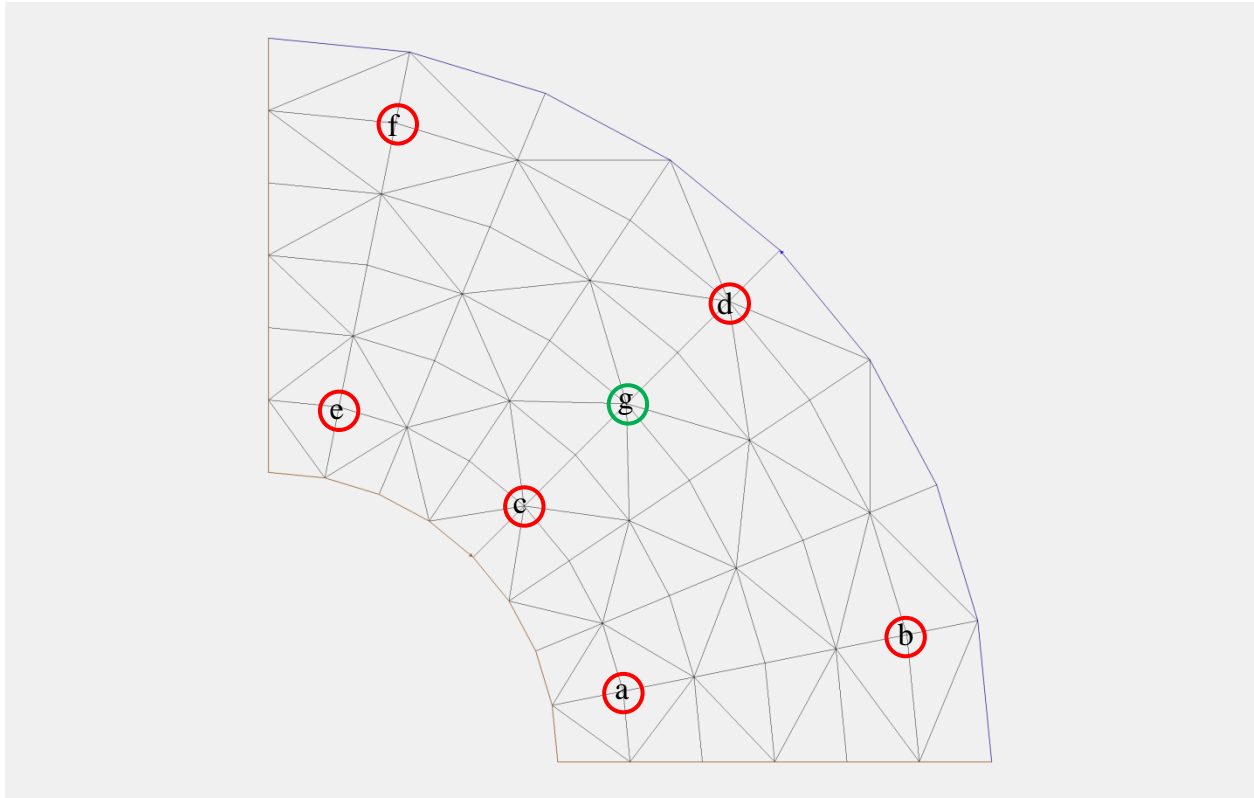
Figure 5 **Quarter Annular Harbor mesh taken from ADCIRC (http://www.adcirc.org/). Synthetic observation data is available on the gauging stations shown in red. Shown in green circle is non-gauging station node.**

<u>5.2. Synthetic Observation Data</u>

The synthetic observation data are generated from the true simulation ($n = 0.025$) for all variables (WSE, UU, and VV) at each gauging station (gauges a to f) every 30 minutes over the last 10 days. Figures 6 to 8 shows observation data at gauges a and f for WSE, UU and VV. The observation data at the other gauging stations are shown in Appendix B.
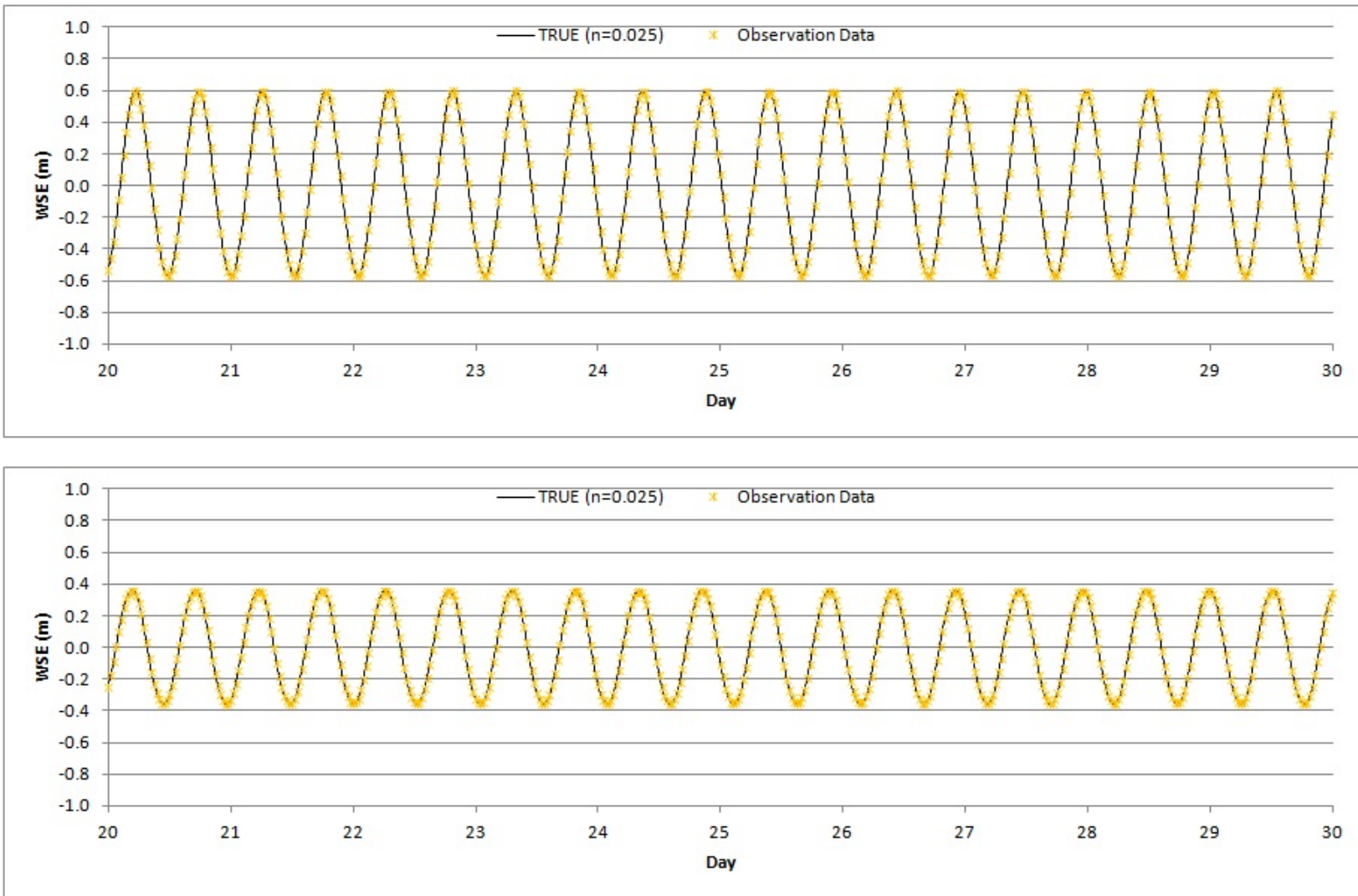
Figure 6   **Observation data for WSE at gauge a (upper) and gauge f (bottom).**
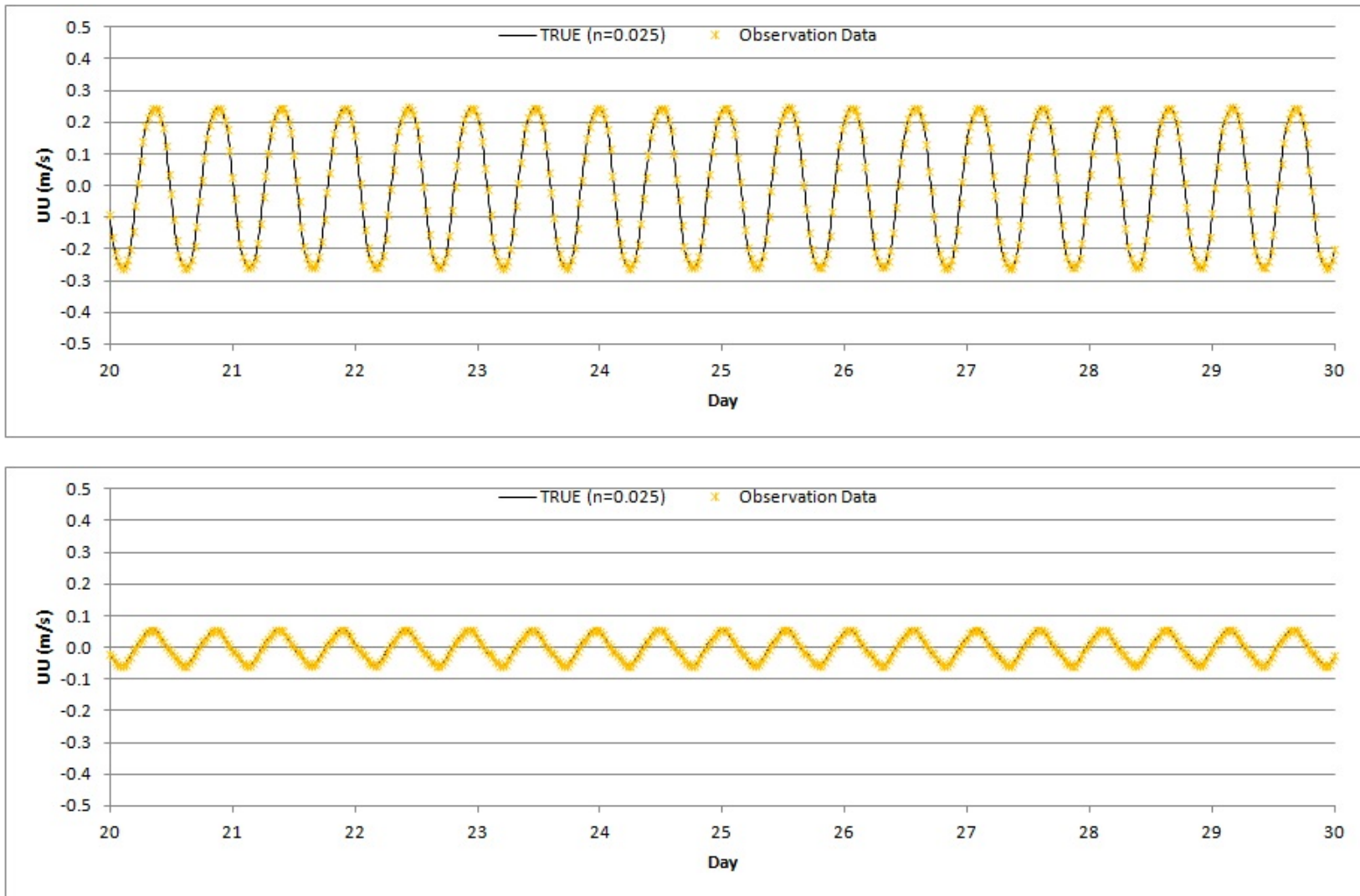
Figure 7   **Observation data for UU at gauge a (upper) and gauge f (bottom).**
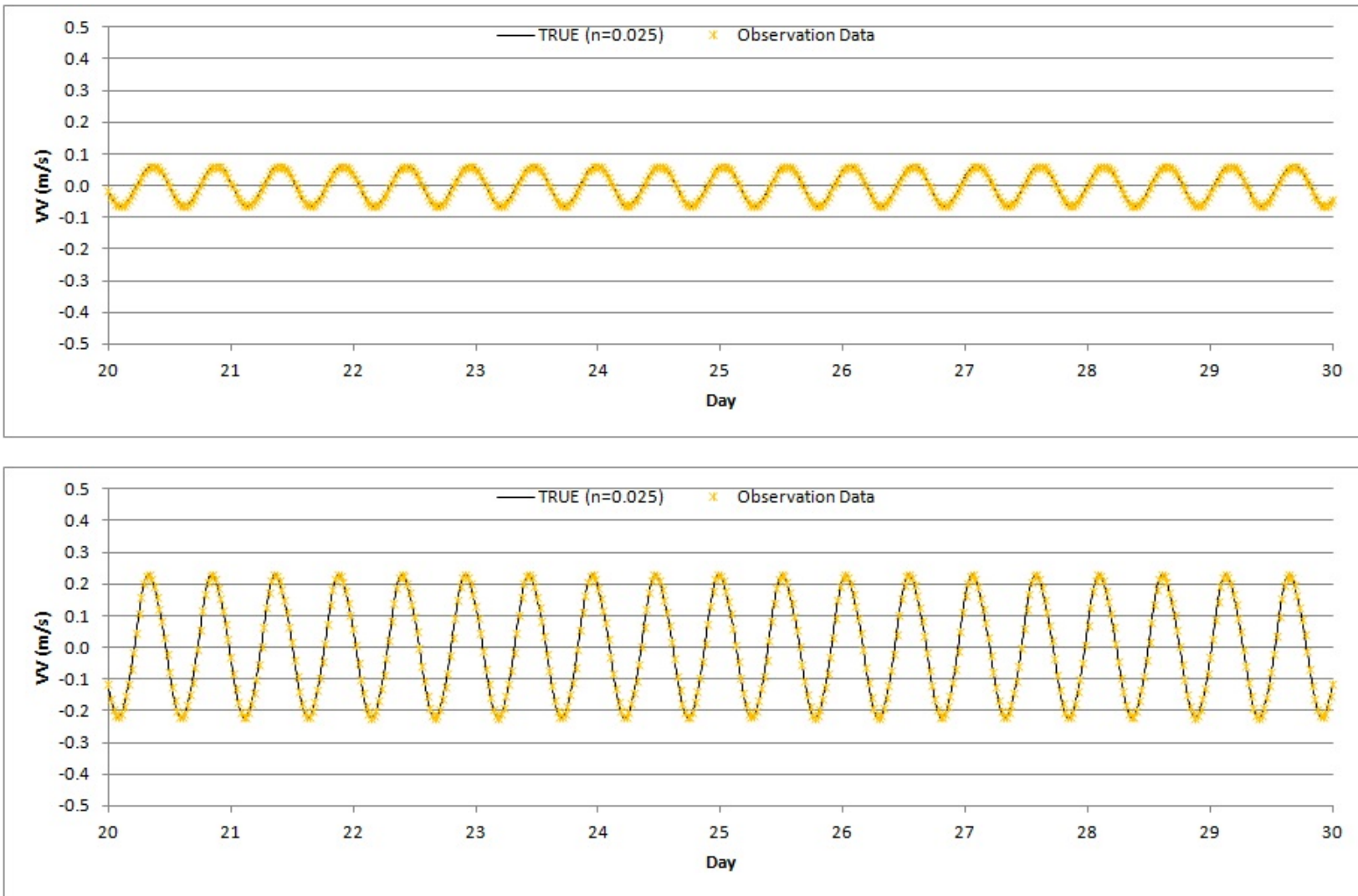
Figure 8   Observation data for VV at gauge a (upper) and gauge f (bottom).

32

5.3. Results at gauging station nodes

In this section, simulation results on two observation gauging stations (gauges a and f) will be discussed during the last 10 days. Also, the simulation results on the gauging stations are shown at the first day (day 19.5^{th} to 20.5^{th}), the middle day (day 24.5^{th} to 25.5^{th}), and the last day (day 29th to 30th). The simulation results on the other gauging stations are shown in Appendix B.

5.3.1. Water surface elevation

Time series of WSE during the last 10 days on the gauging stations are shown in Figure 9. Shown in black line is the WSE from the true simulations using 'True' Manning's n (0.025), shown in green line is the WSE from the original simulations using 'Applied' Manning's n (0.035), and shown in red line is the averaged ensemble WSE from EnKF simulations using 'Applied' Manning's n (0.035). Time series of WSE at the first day, middle day, and last day on the gauging stations are shown in Figures 10 to 12. Shown in yellow star is the average of generated ensemble observed WSE which is taken from the EnKF simulation, in blue circle is the average of ensemble predicted WSE which is taken from the EnKF simulation, and in red diamond is the average of ensemble updated WSE which is taken from the EnKF simulation.

33
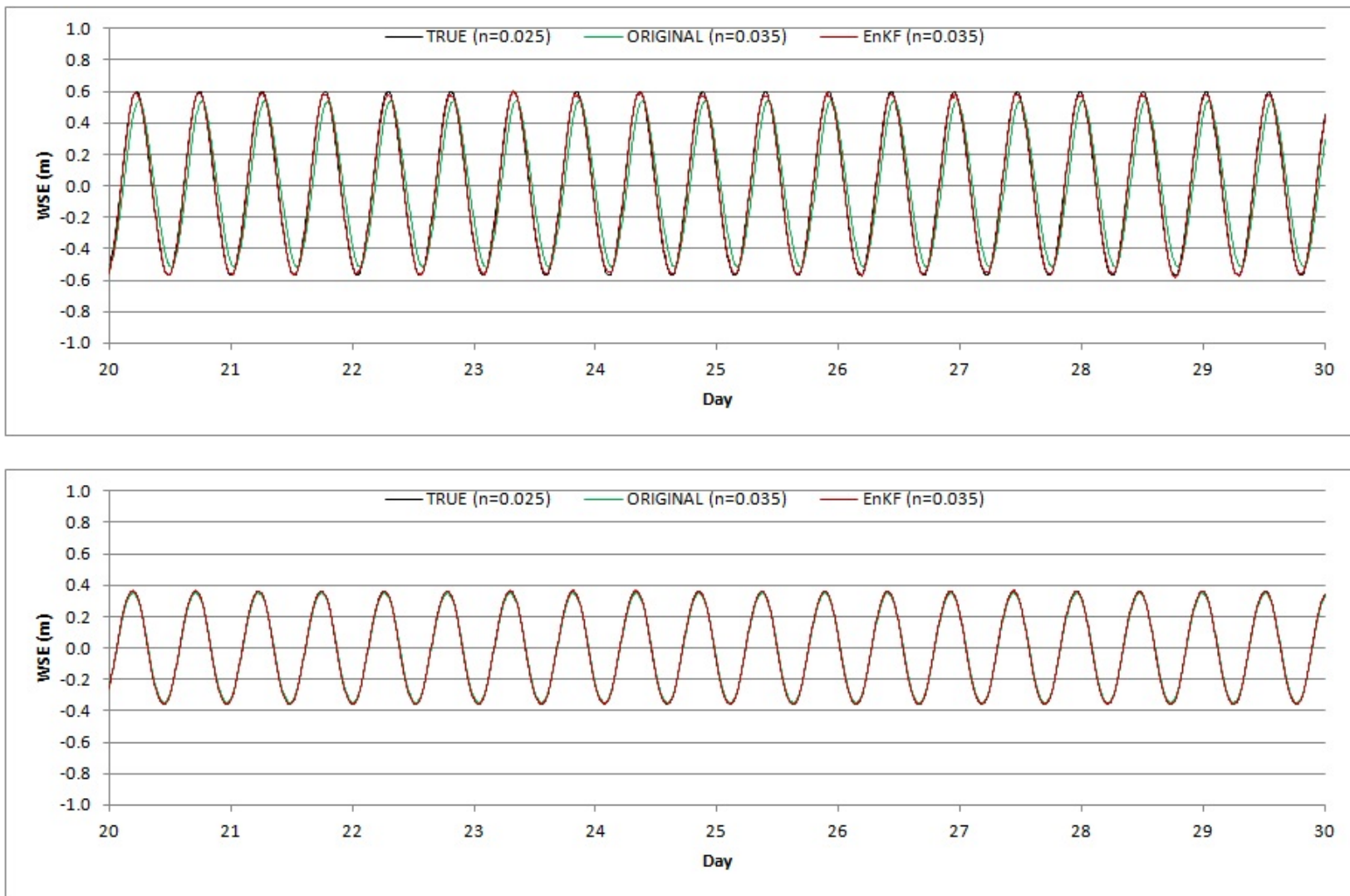
Figure 9　　　**Time series of WSE at gauge a (upper) and gauge f (bottom) during last 10 days.**
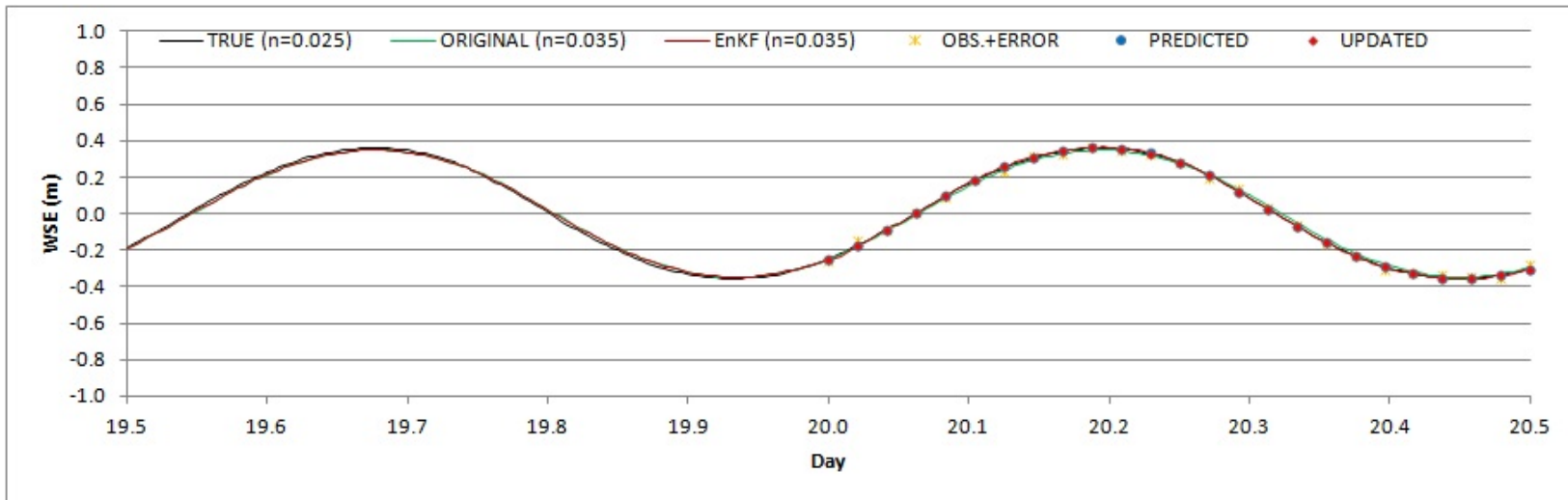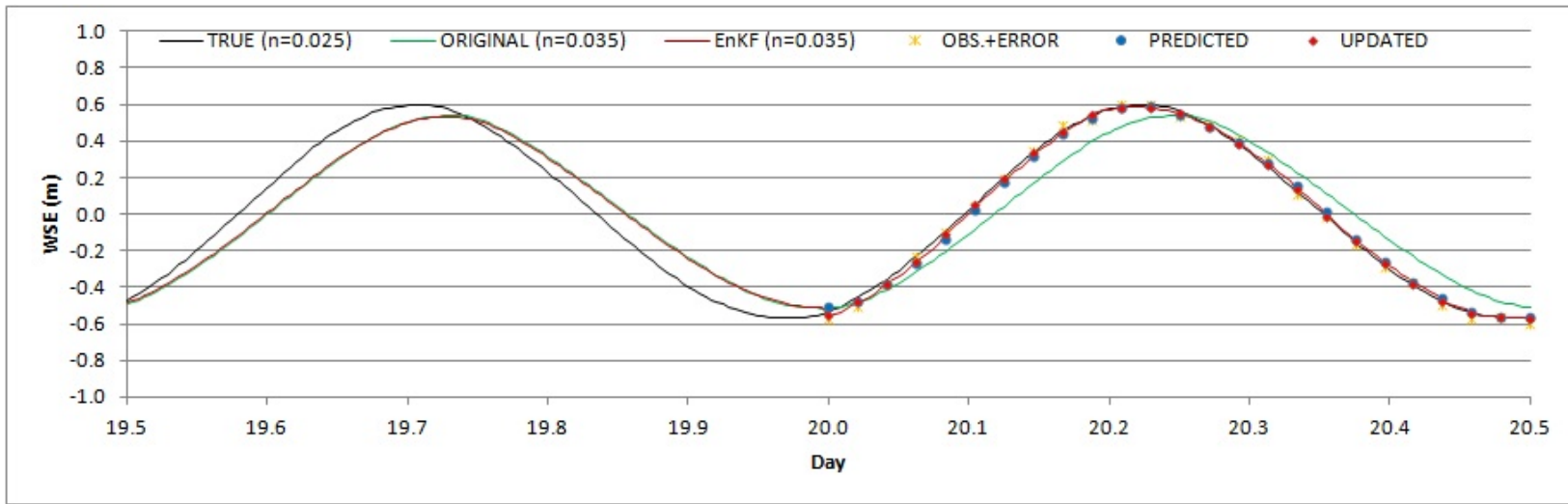
Figure 10   Time series of WSE at gauge a (upper) and gauge f (bottom) at the first day.

35

Figure 11 Time series of WSE at gauge a (upper) and gauge f (bottom) at the middle day.

Figure 12   Time series of WSE at gauge a (upper) and gauge f (bottom) at the last day.

As shown in the figures above, the original simulation using 'Applied' Manning's n (= 0.035) results in smaller amplitudes and delayed phases compared to the true simulation (n = 0.025) results at the gauge a. On the gauge f, differences of amplitudes and phases are not as obvious, which is because of gauge f so closely located to the open ocean boundary. Simulation results from EnKF match the amplitudes and phases to the true simulation results on the gauge a.

RMSE of WSE on the two gauging stations for the original simulation and the EnKF simulation are listed below (Table 4).

Table 4   **RMSE of WSE for the simulations on two gauging stations.**

Gauge No.	RMSE of WSE		
	Original (m)	EnKF (m)	$\dfrac{RMSE_{Original} - RMSE_{EnKF}}{RMSE_{Original}}(\%)$
Gauge a	1.126E-01	0.154E-01	86.3
Gauge f	1.118E-02	0.343E-02	69.4

RMSEs on the other gauging stations are listed in Appendix B. As shown in the table above, the errors are improved with EnKF by 86% on gauge a and by 70% on gauge f. DG ADCIRC-2DDI with EnKF works effectively on gauging stations for WSE.

5.3.2. Depth-integrated velocities in the Easting direction

Time series of UU during the last 10 days on the gauging stations are shown in Figure 13. Shown in black line is the UU from the true simulations using 'True' Manning's n (0.025), in green line is the UU from the original simulations using 'Applied' Manning's n (0.035), and in red line is the averaged ensemble UU from EnKF simulations using 'Applied' Manning's n (0.035). Time series of UU at the first day, middle day, and last day on the gauging stations are shown in Figures 14 to 16. Shown in yellow star is the average of the generated ensemble observed UU which is taken from the EnKF simulation, in blue circle is the average of ensemble predicted UU which is taken from the EnKF simulation, and in red diamond is the average of ensemble updated UU which is taken from the EnKF simulation.
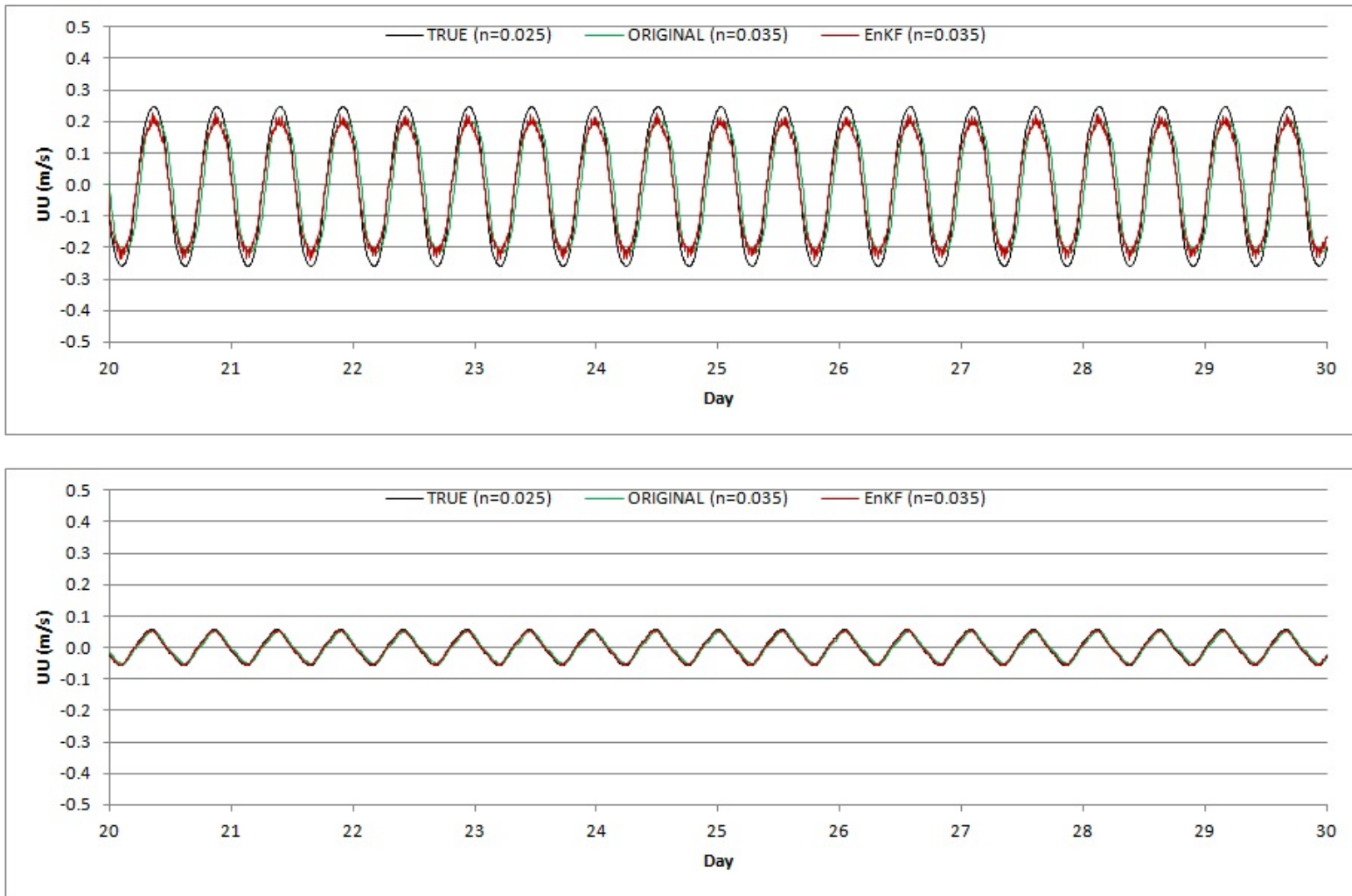
Figure 13   **Time series of UU at gauge a (upper) and gauge f (bottom) during last 10 days.**

40

Figure 14   Time series of UU at gauge a (upper) and gauge f (bottom) at the first day.

Figure 15 Time series of UU at gauge a (upper) and gauge f (bottom) at the middle day.

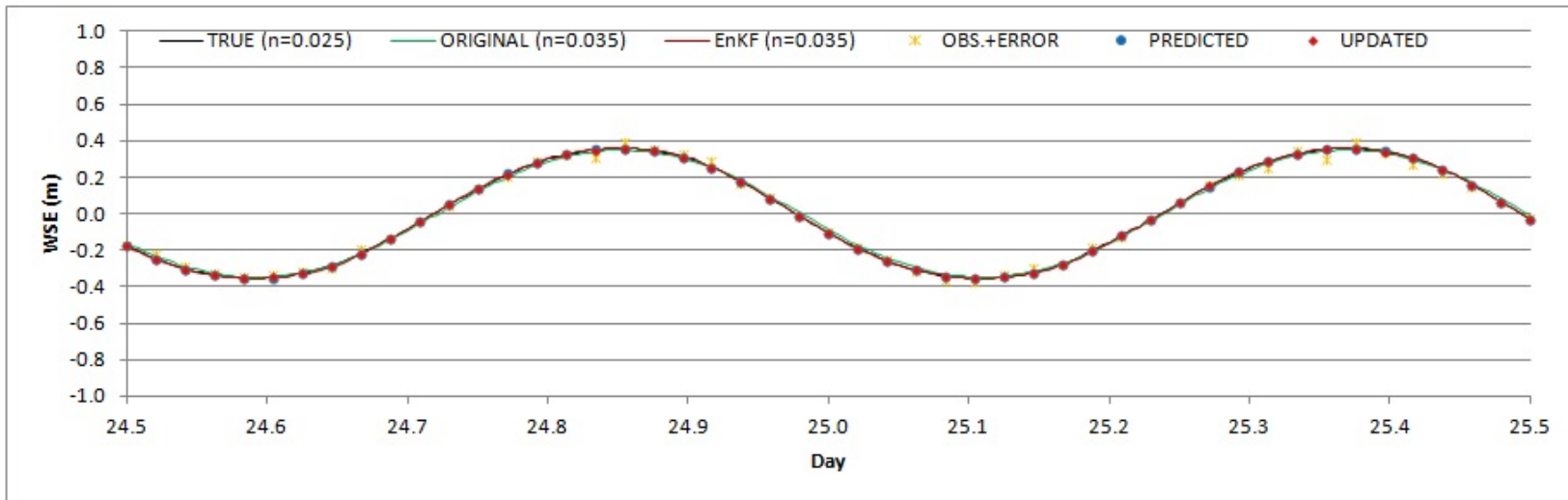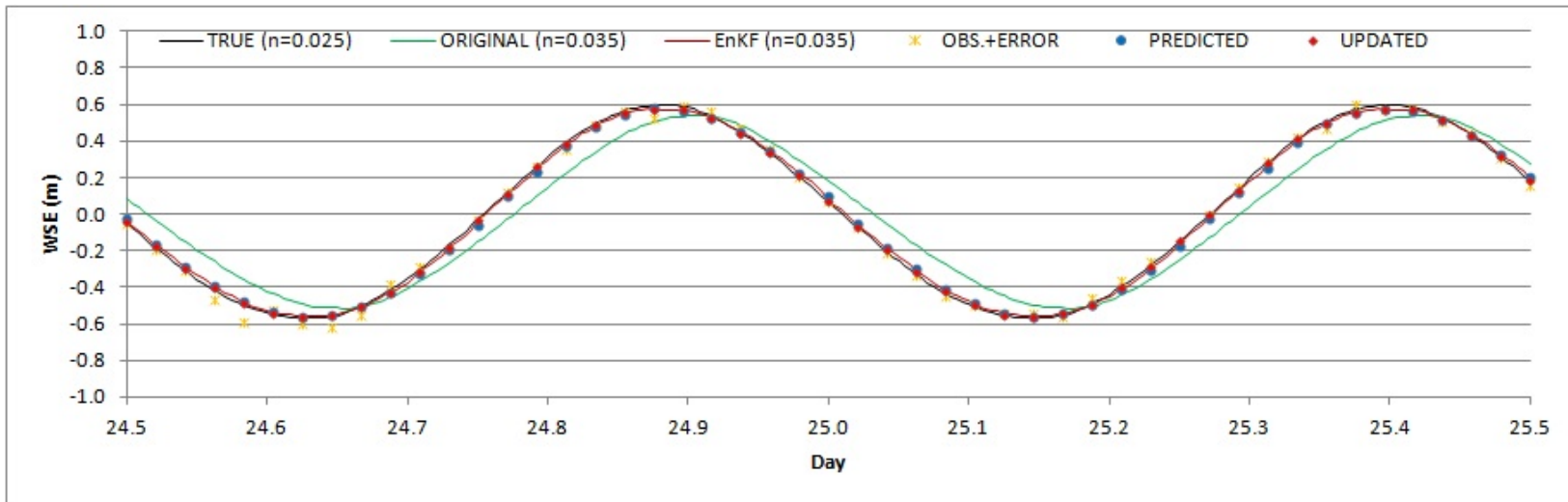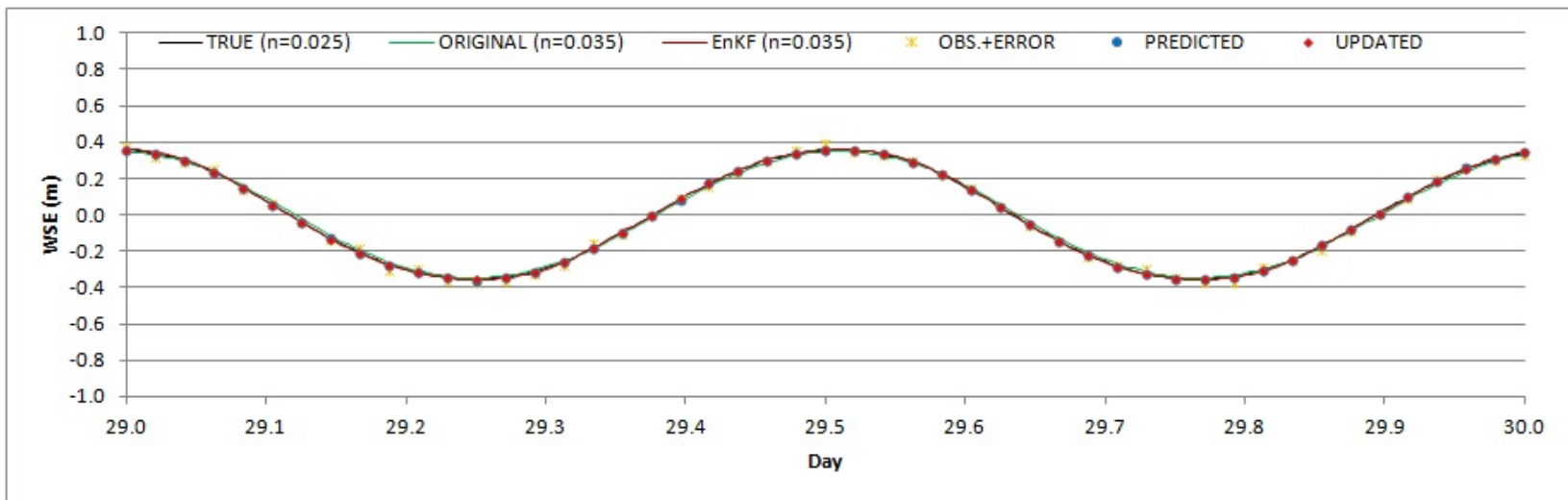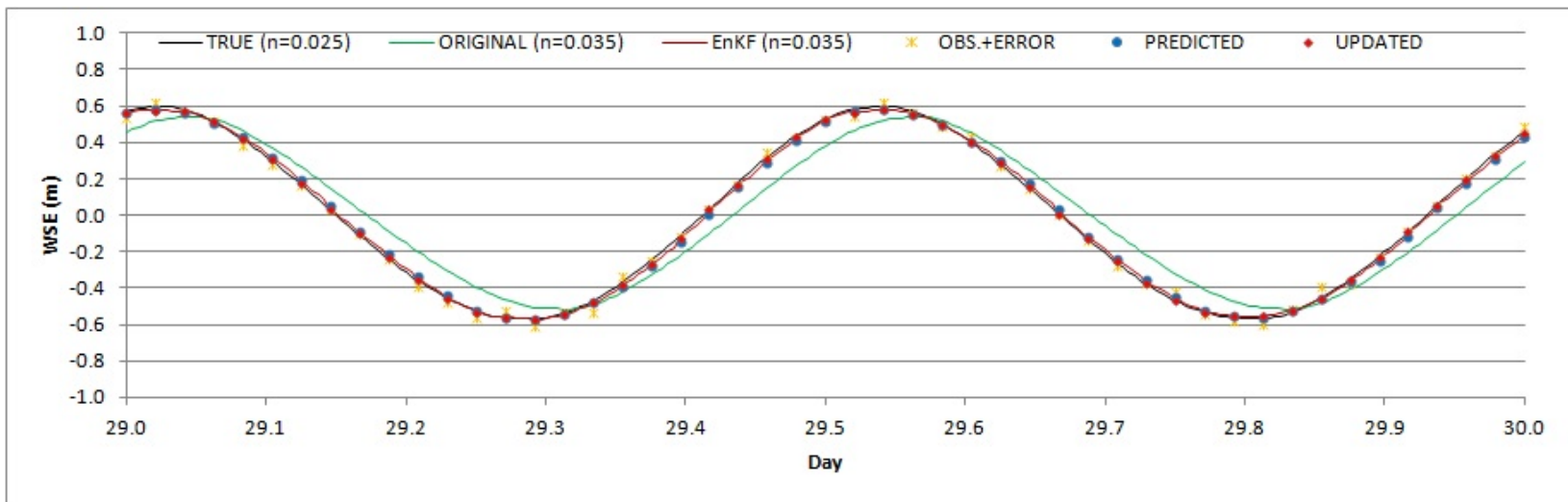**Figure 16** Time series of UU at gauge a (upper) and gauge f (bottom) at the last day.

As shown in the figures above, the original simulation using 'Applied' Manning's n (= 0.035) results in smaller amplitudes and delayed phases compared to the true simulation (n = 0.025) results at gauge a. On gauge f, differences of amplitudes and phases are not as obvious, which is because of gauge f so closely located to the open ocean boundary. The phases of EnKF simulation results match well with the phases of the true simulation results. The amplitudes of the EnKF simulation results are updated, i.e., fixed, to the amplitudes of the true simulation results. After EnKF is applied, predicted UU converges to the amplitudes of original simulation results, which is because the amplitudes of the velocity are more sensitive to Manning's n.

RMSE of UU on the two gauging stations for the original simulation and the EnKF simulation are listed below (Table 5).

**Table 5**   **RMSE of UU for the simulations on two gauging stations.**

Gauge No.	RMSE of UU		
	Original (m/s)	EnKF (m/s)	$\dfrac{RMSE_{Original} - RMSE_{EnKF}}{RMSE_{Original}}$ (%)
Gauge a	5.785E-02	3.714E-02	35.8
Gauge f	7.675E-03	3.189E-03	58.4

RMSEs on the other gauging stations are listed in Appendix B. As shown in the table above, the errors are improved with EnKF by 36% on gauge a and by 58% on gauge f. DG ADCIRC-2DDI with EnKF works effectively on gauging stations for UU.

5.3.3. Depth-integrated velocities in the Northing direction

Time series of VV during the last 10 days on the gauging stations are shown in Figure 17. Shown in black line is the VV from the true simulations using 'True' Manning's n (0.025), in green line is the VV from the original simulations using 'Applied' Manning's n (0.035), and in red line is the averaged ensemble VV from EnKF simulations using 'Applied' Manning's n (0.035). Time series of VV at the first day, middle day, and last day on the gauging stations are shown in Figures 18 to 20. Shown in yellow star is the average of generated ensemble observed VV which is taken from the EnKF simulation, in blue circle is the average of ensemble predicted VV which is taken from the EnKF simulation, and in red diamond is the average of ensemble updated VV which is taken from the EnKF simulation.
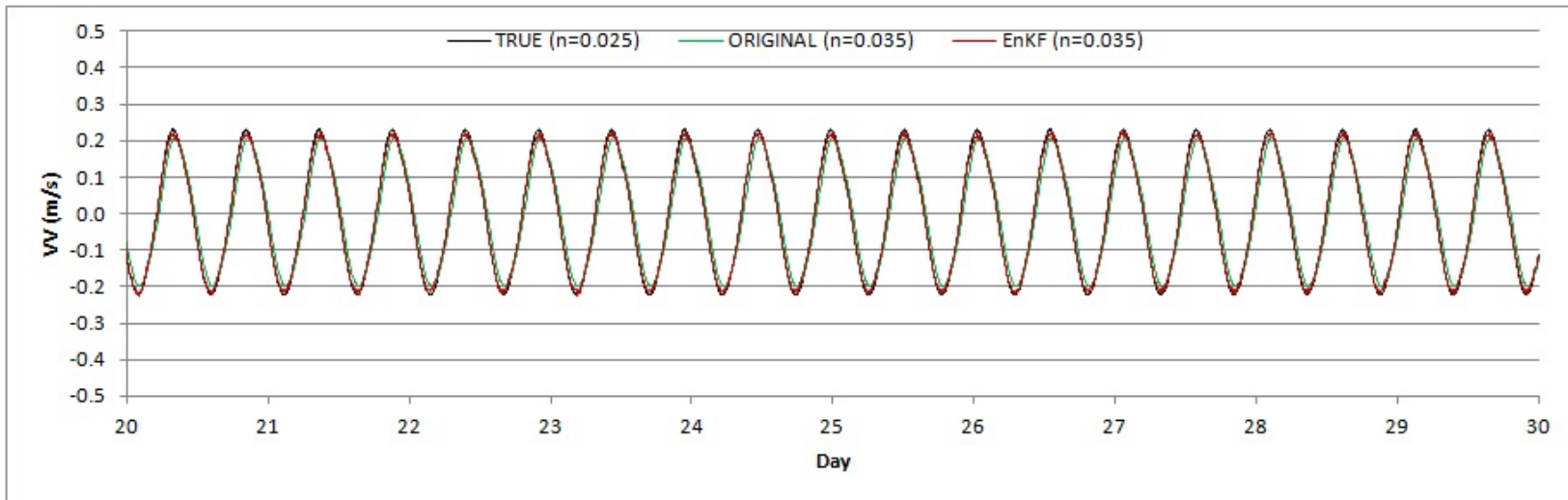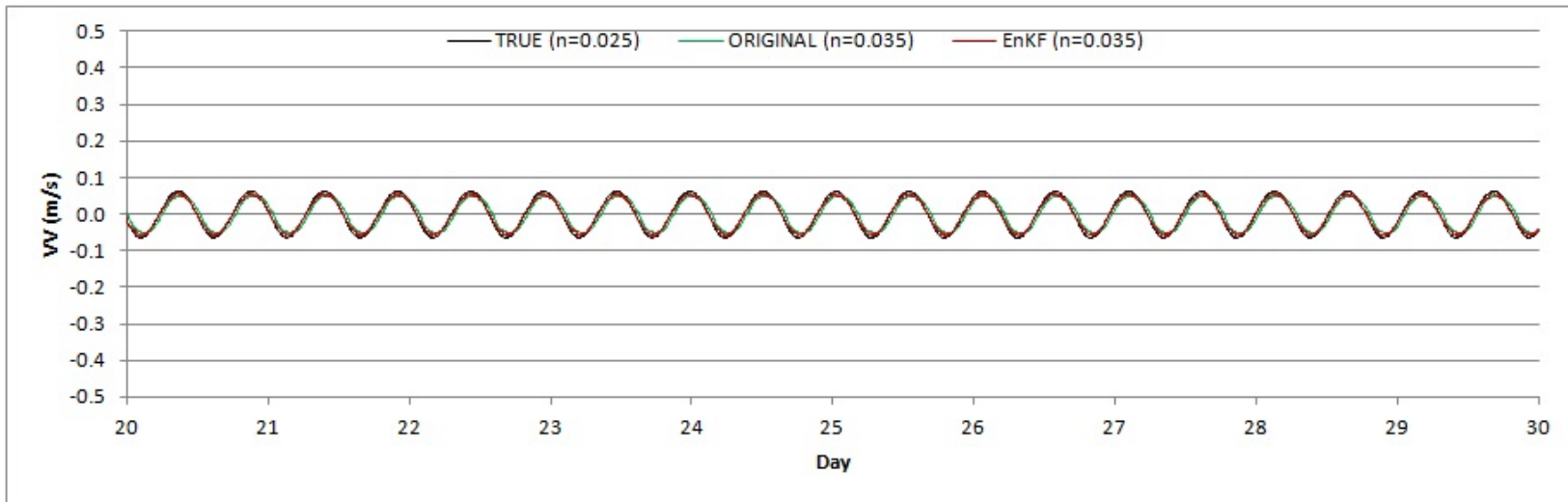
Figure 17   **Time series of VV at gauge a (upper) and gauge f (bottom) during last 10 days.**
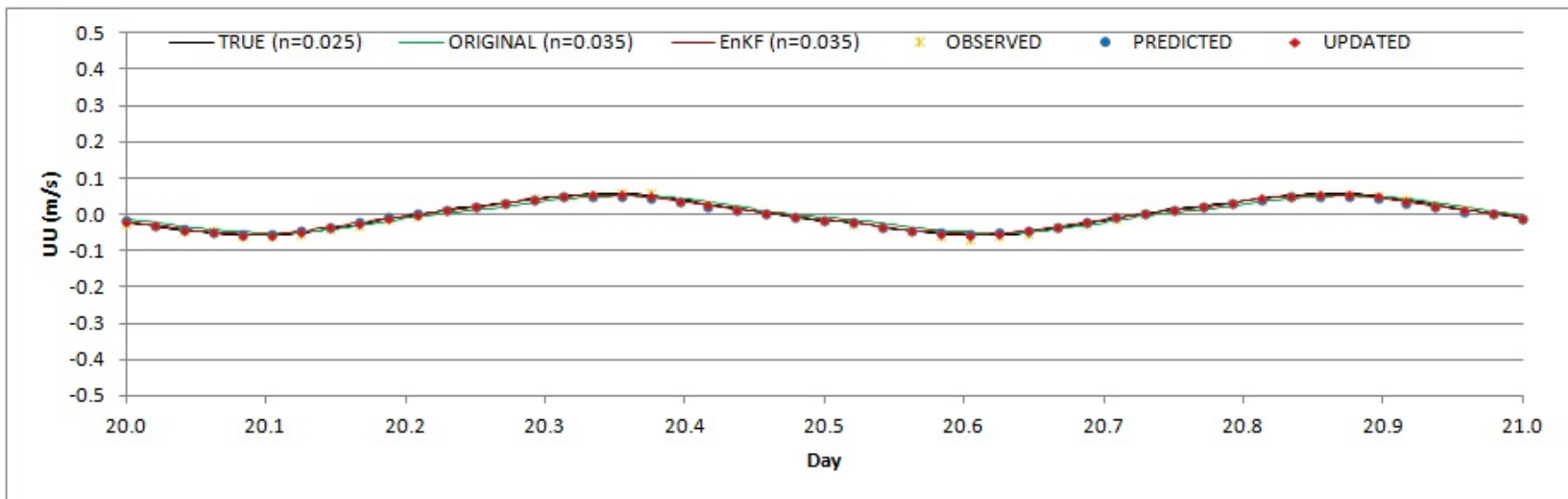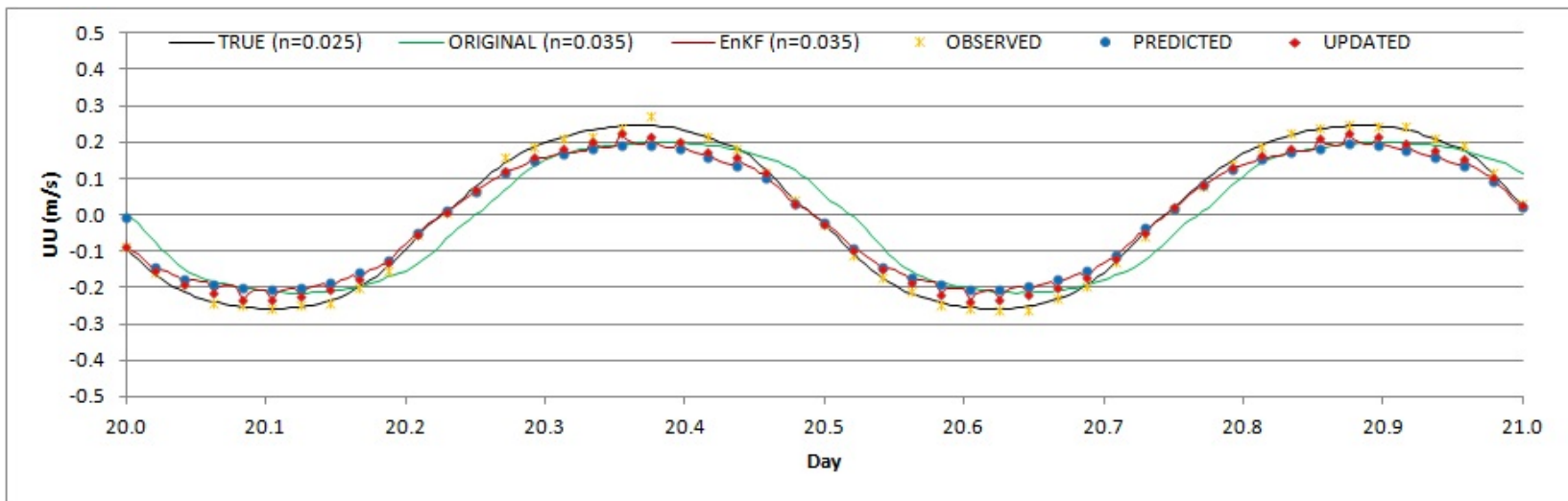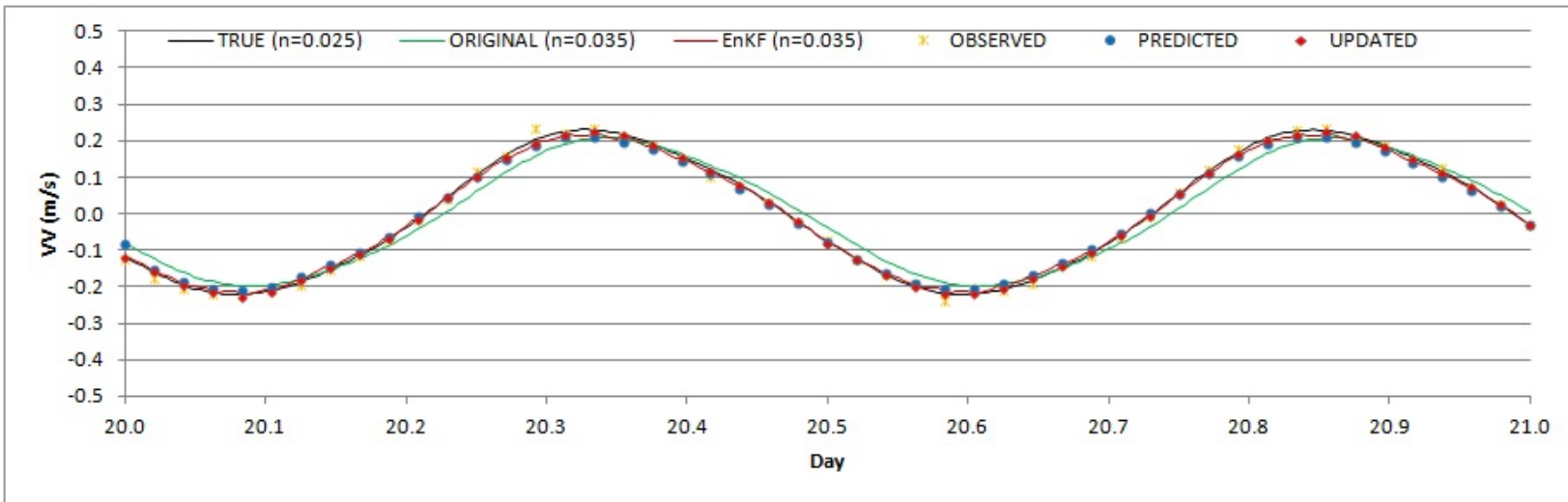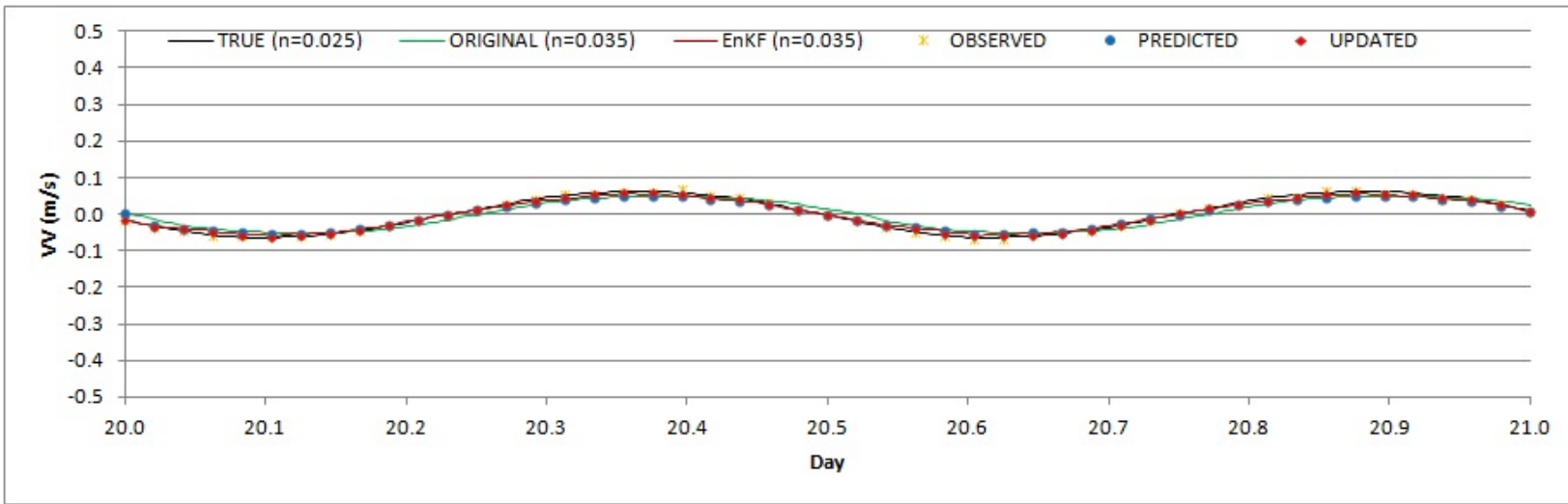
Figure 18 Time series of VV at gauge a (upper) and gauge f (bottom) at the first day.
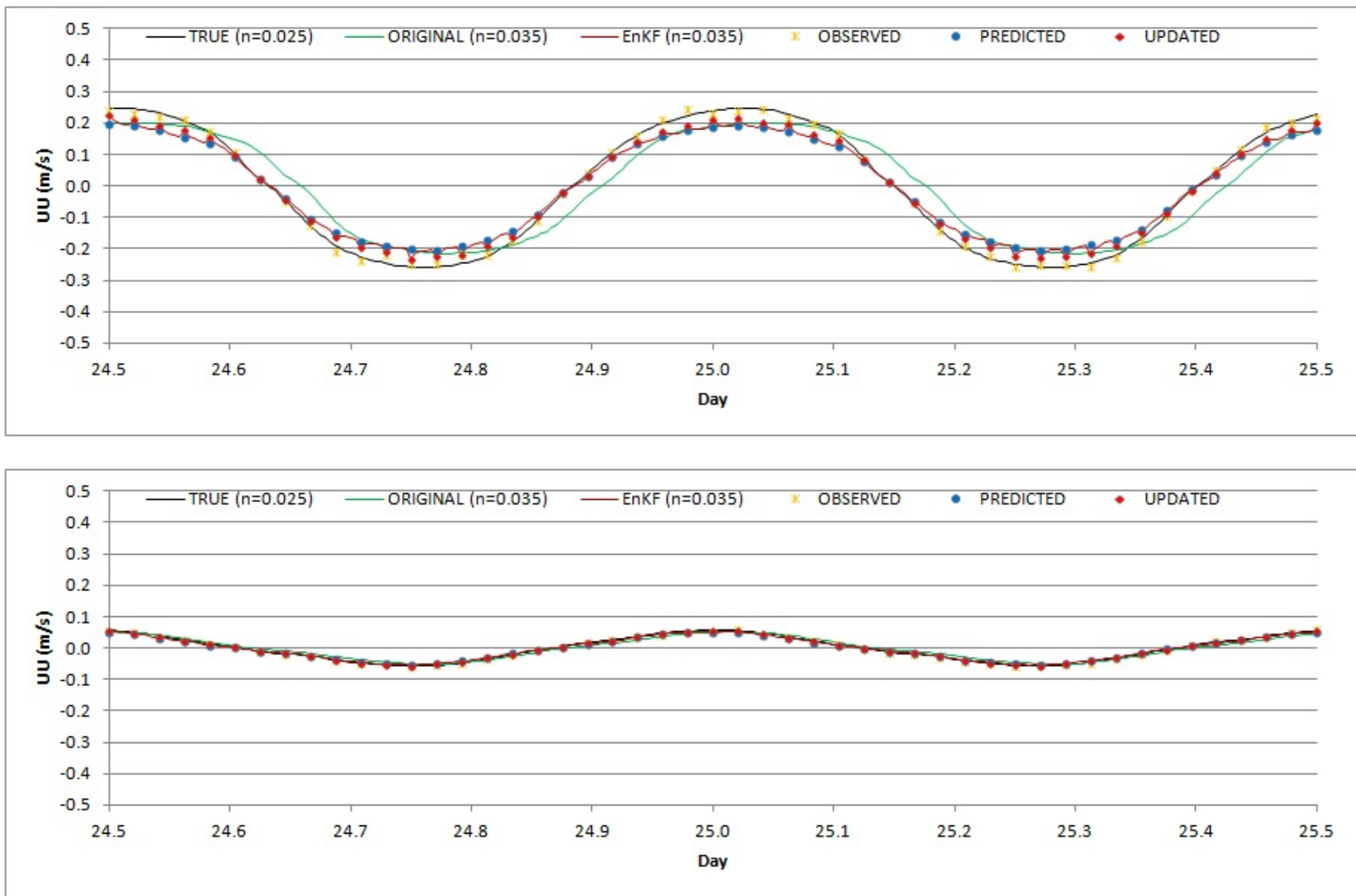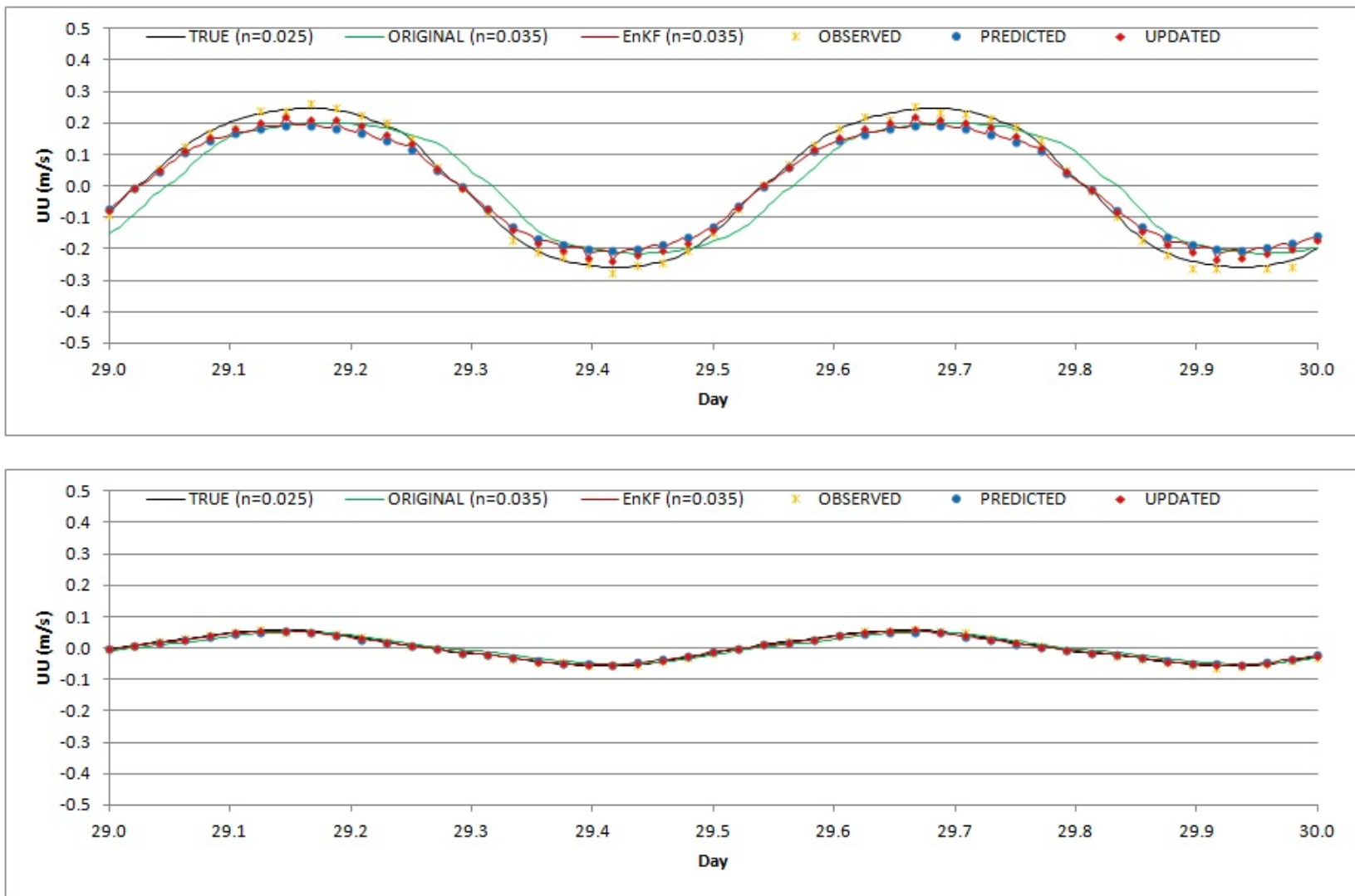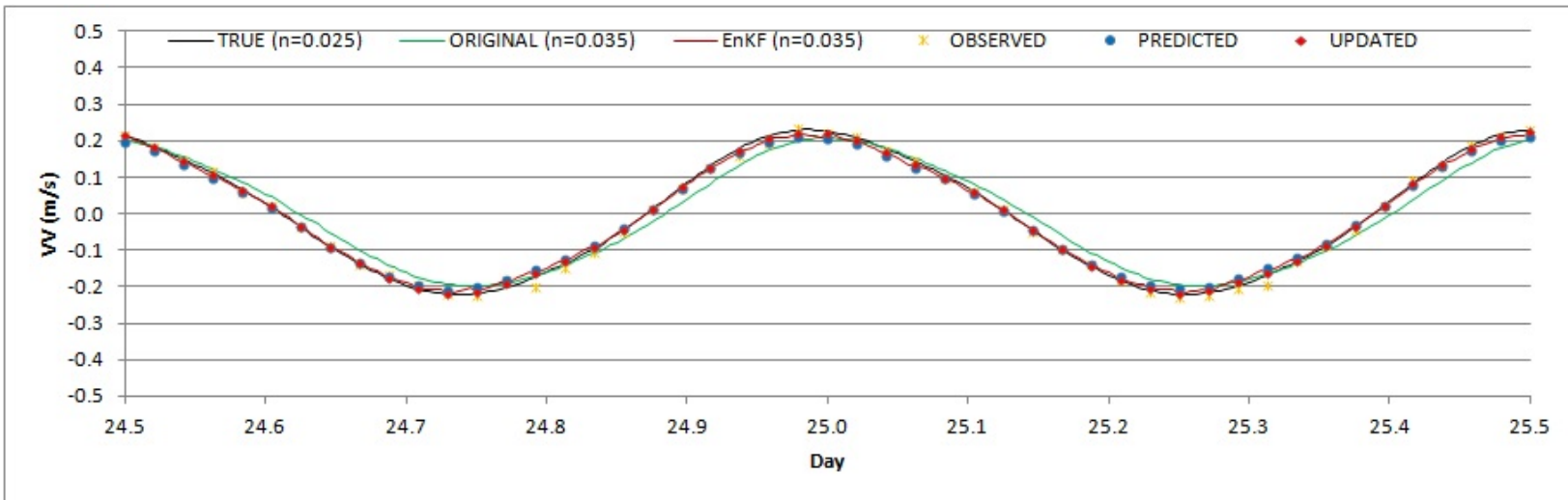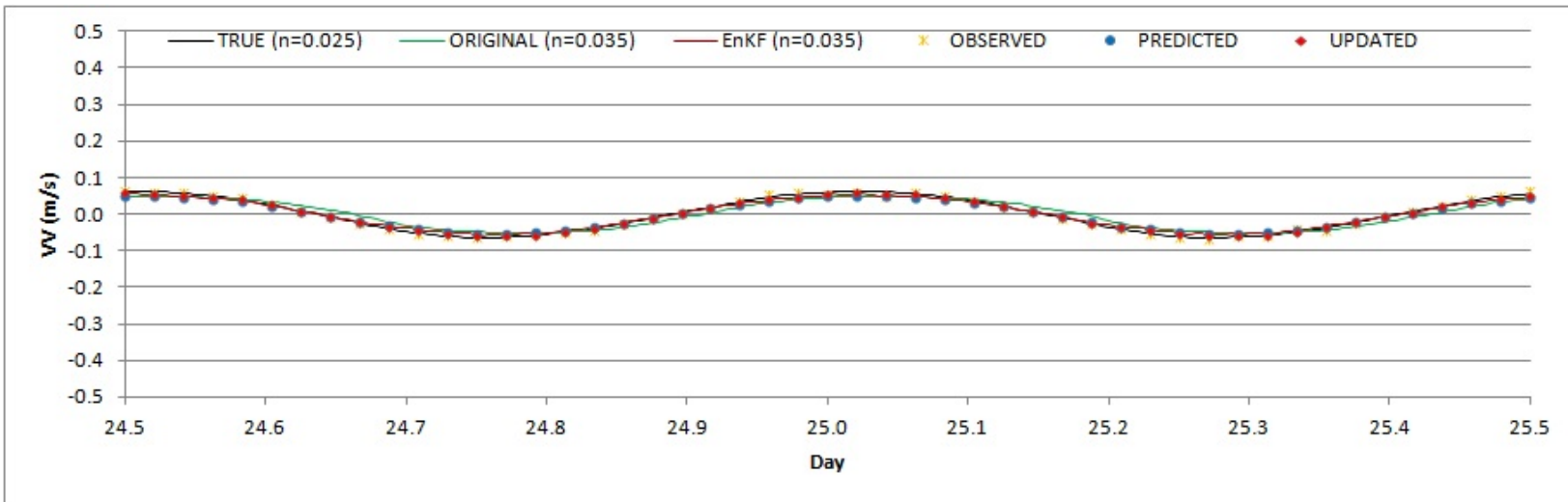
Figure 19   Time series of VV at gauge a (upper) and gauge f (bottom) at the middle day.
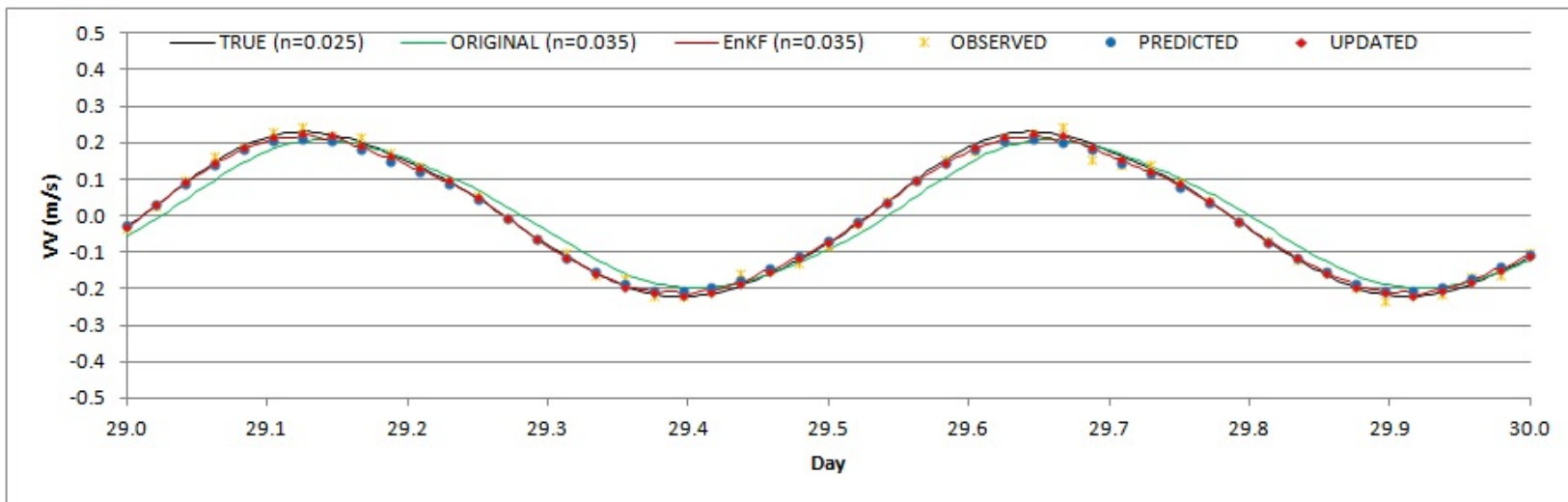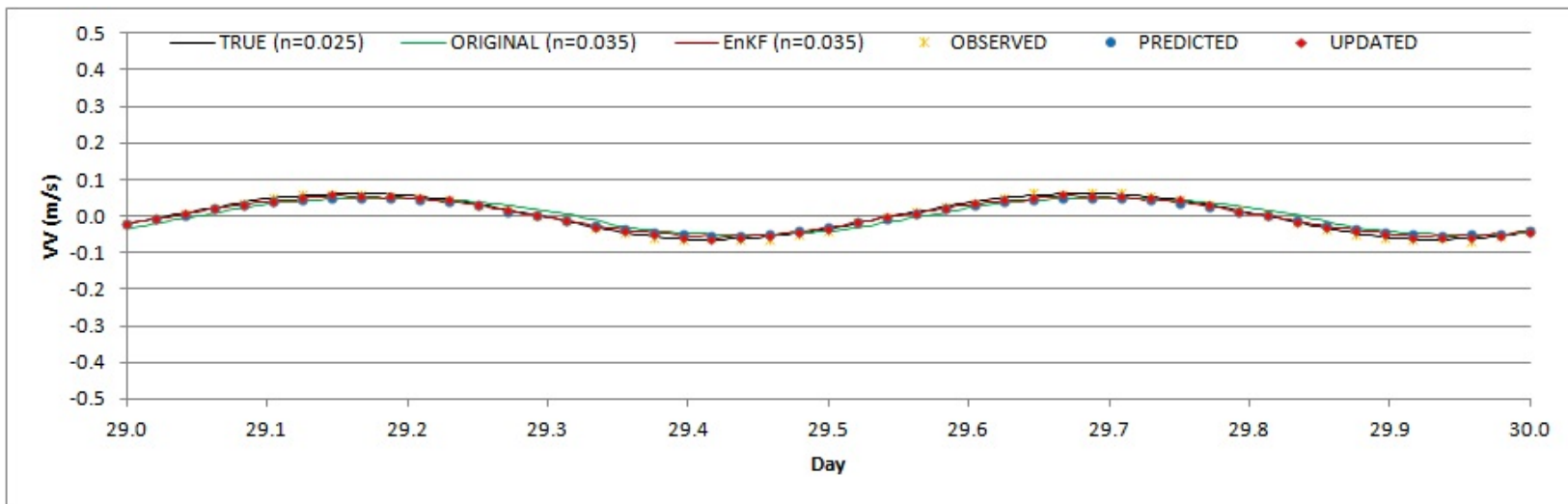
Figure 20   **Time series of VV at gauge a (upper) and gauge f (bottom) at the last day.**

49

As shown in Figure 17 above, the differences between the true simulation results and original simulation results are not as obvious on both gauges a and f. However, the amplitudes and phases of the original simulation results are smaller and delayed compared to the true simulation results shown in the Figures 18 to 20. On the other hand, the amplitudes and phases of EnKF simulation results match well with the true simulation results. After EnKF is applied, predicted VV converges to the amplitudes of original simulation results, which is because amplitudes of the velocity are more sensitive to Manning's n.

RMSE of VV on the two gauging stations for the original simulation and the EnKF simulation are listed below (Table 6).

Table 6   **RMSE of VV for the simulations on two gauging stations.**

Gauge No.	RMSE of VV		
	Original (m/s)	EnKF (m/s)	$\dfrac{RMSE_{Original} - RMSE_{EnKF}}{RMSE_{Original}}(\%)$
Gauge a	1.340E-02	0.603E-02	55.0
Gauge f	2.851E-02	0.793E-02	72.2

RMSEs on the other gauging stations are listed in Appendix B. As shown in the table above, errors are improved using EnKF by 55% on gauge a and by 72% on gauge f. DG ADCIRC-2DDI with EnKF works effectively on gauging stations for VV. Thus, DG ADCIRC-2DDI with EnKF works effectively on gauging stations for all state variables.

In this section, simulation results for the last 10 days at a non-gauging station (gauge g)

shown in Figure 5 will be discussed. At the non-gauging station, there are no synthetic

observation data, but state variables can be updated using EnKF. The non-gauging station is

called as a target station. The simulation results on the target station are shown at the first day

(day 19.5^{th} to 20.5^{th}), and the middle day (19.5^{th} to 20.5^{th}), and the last day (day 29.0^{th} to 30.0^{th}).

5.4.1. Water surface elevation

Time series of WSE during the last 10 days on the target station are shown in the top of

Figure 21. Shown in black line is the WSE from the true simulations, in green line is the WSE

from original simulation, and in red line is the averaged ensemble WSE from EnKF simulations.

Time series of WSE for the first day are shown in the bottom of Figure 21, for the middle day are

shown in the top of Figure 22, and for the last day are shown in the bottom of Figure 22. Shown

in blue circle is the average of ensemble predicted WSE which is taken from the EnKF

simulation and in red diamond is the average of ensemble updated WSE which is taken from the

EnKF simulation.
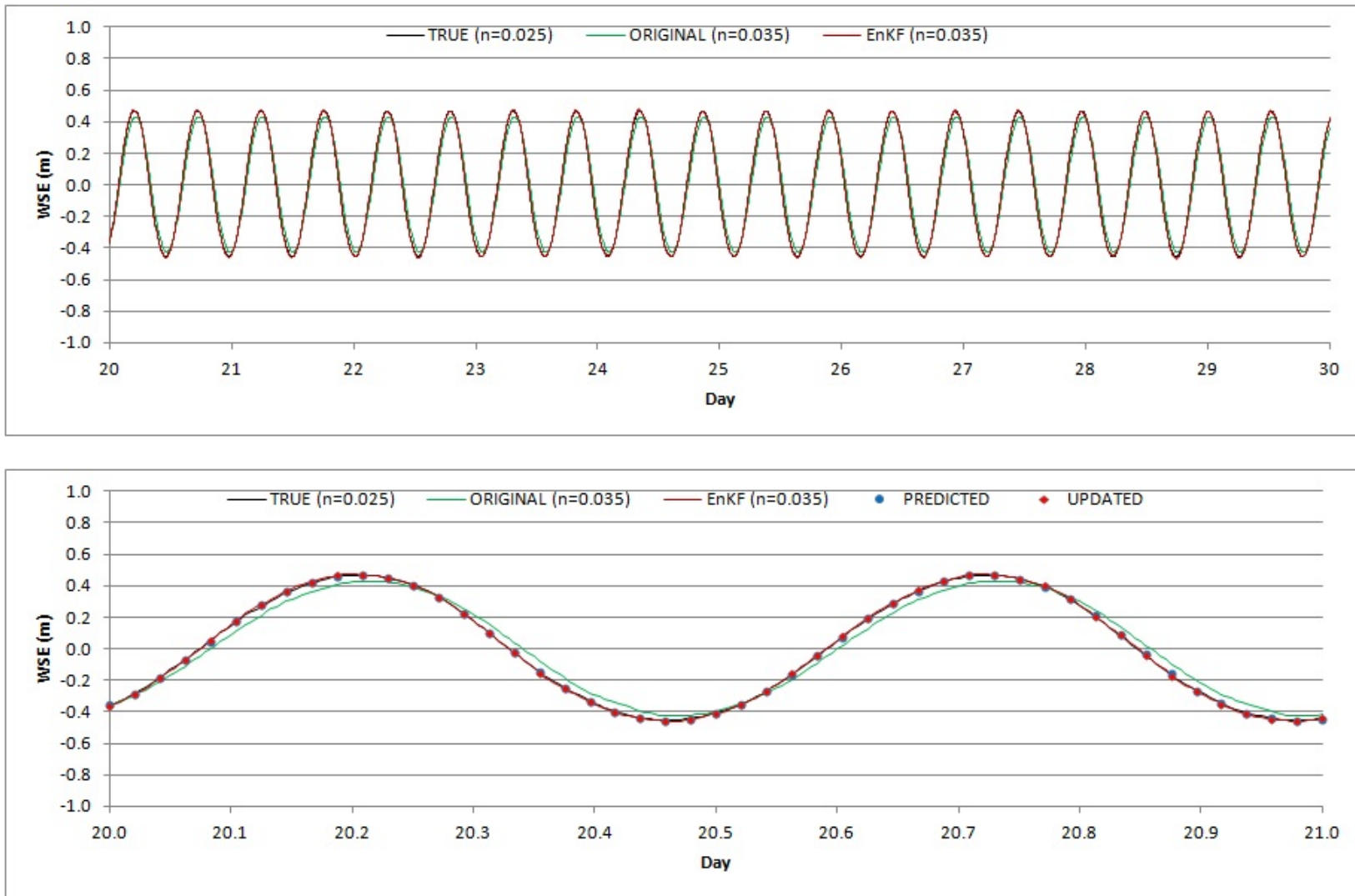
Figure 21 Time series of WSE at the target station g during last 10 days (upper) and at the first day (bottom).
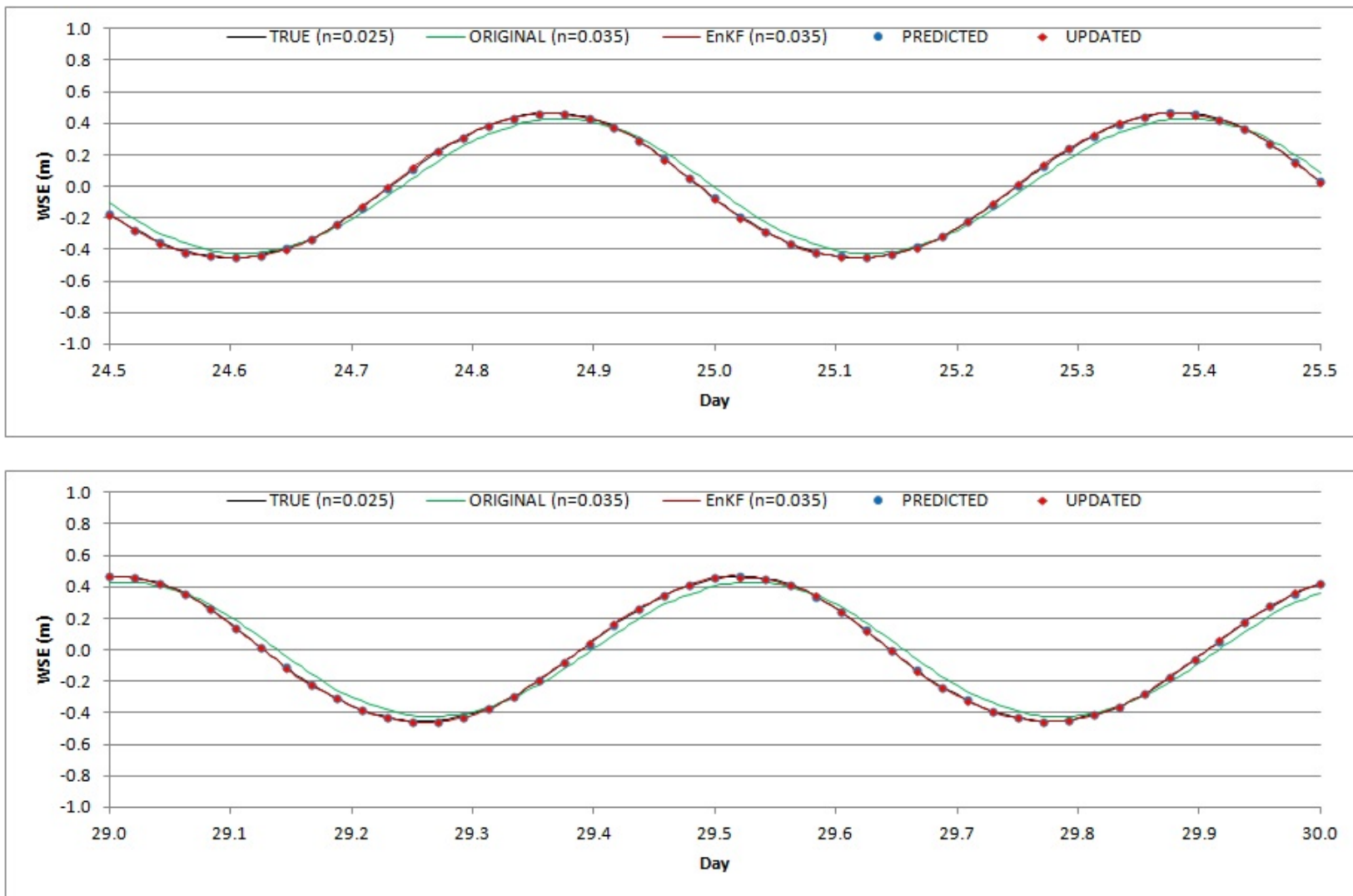
Figure 22   Time series of WSE at the target station g at the middle day (upper) and at the last day (bottom).

As shown in the figures above, the amplitudes and phases of the original simulation results are smaller and delayed compared to the true simulation at the target station. Both the amplitudes and phases of the EnKF simulation results match well with to the true simulation results.

RMSE of WSE at the target station and two gauging stations for the original simulation and the EnKF simulation are listed below (Table 7).

Table 7   **RMSE of WSE at the target station and gauging stations.**

Gauge No.	RMSE of WSE		
	Original (m)	EnKF (m)	$\dfrac{RMSE_{Original} - RMSE_{EnKF}}{RMSE_{Original}}(\%)$
Gauge g	4.447E-02	0.576E-02	87.1
Gauge a	1.126E-01	0.154E-01	86.3
Gauge f	1.118E-02	0.343E-02	69.4

As shown in the table above, the errors are improved using EnKF by 87% at the target station using EnKF. DG ADCIRC-2DDI with EnKF works effectively on the target station as well as on the gauging stations for WSE.

5.4.2. Depth-integrated velocities in the Easting direction

Time series of UU during the last 10 days on the target station are shown in the top of Figure 23. Shown in black line is the UU from the true simulations, in green line is the UU from original simulation, and in red line is the averaged ensemble UU from EnKF simulations. Time series of UU for the first day are shown in the bottom of Figure 23, for the middle day are shown in the top of Figure 24, and for the last day are shown in the bottom of Figure 24. Shown in blue circle is the average of ensemble predicted UU which is taken from the EnKF simulation and in red diamond is the average of ensemble updated UU which is taken from the EnKF simulation.
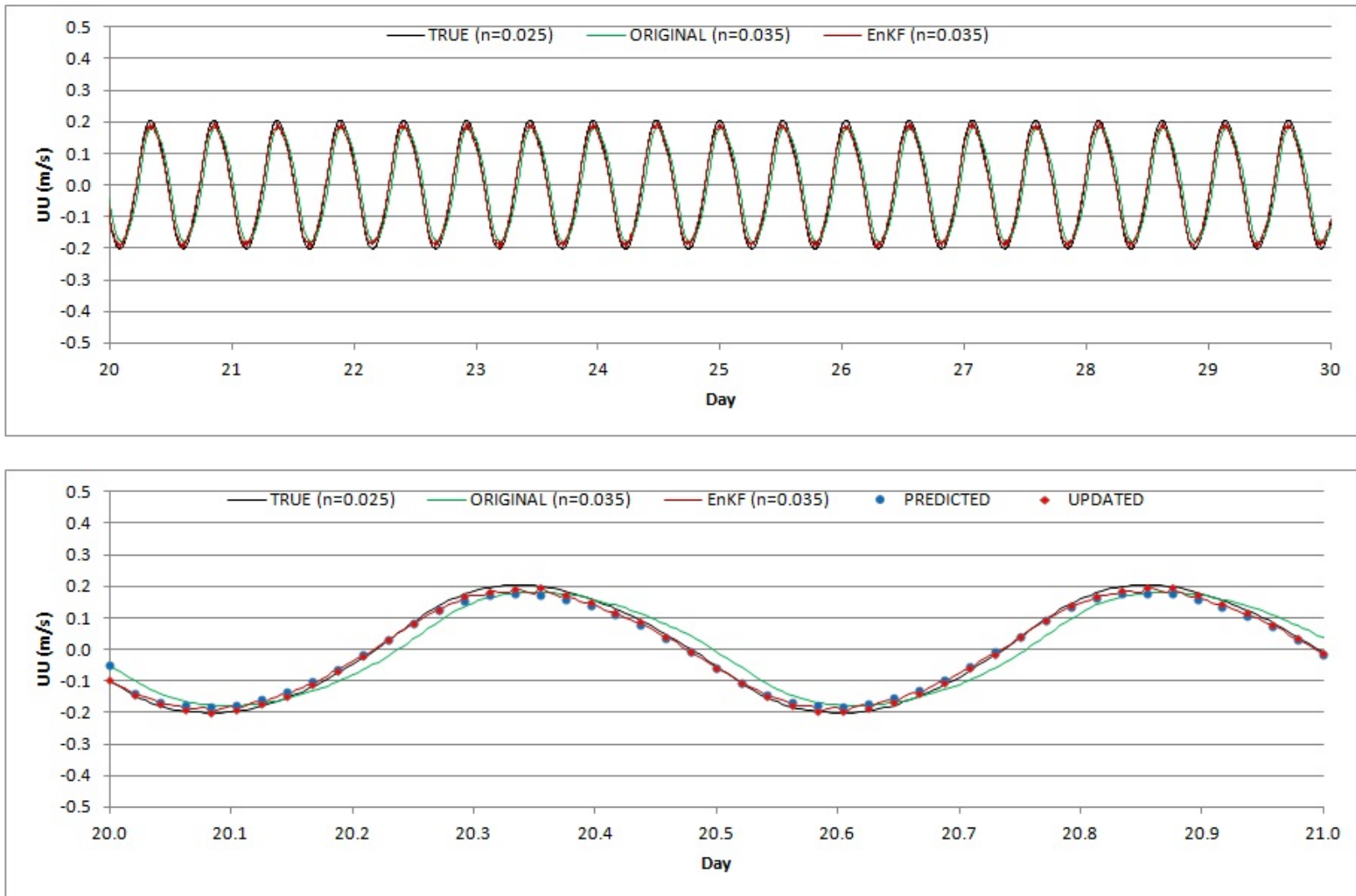
Figure 23   **Time series of UU at the target station g during last 10 days (upper) and at the first day (bottom).**
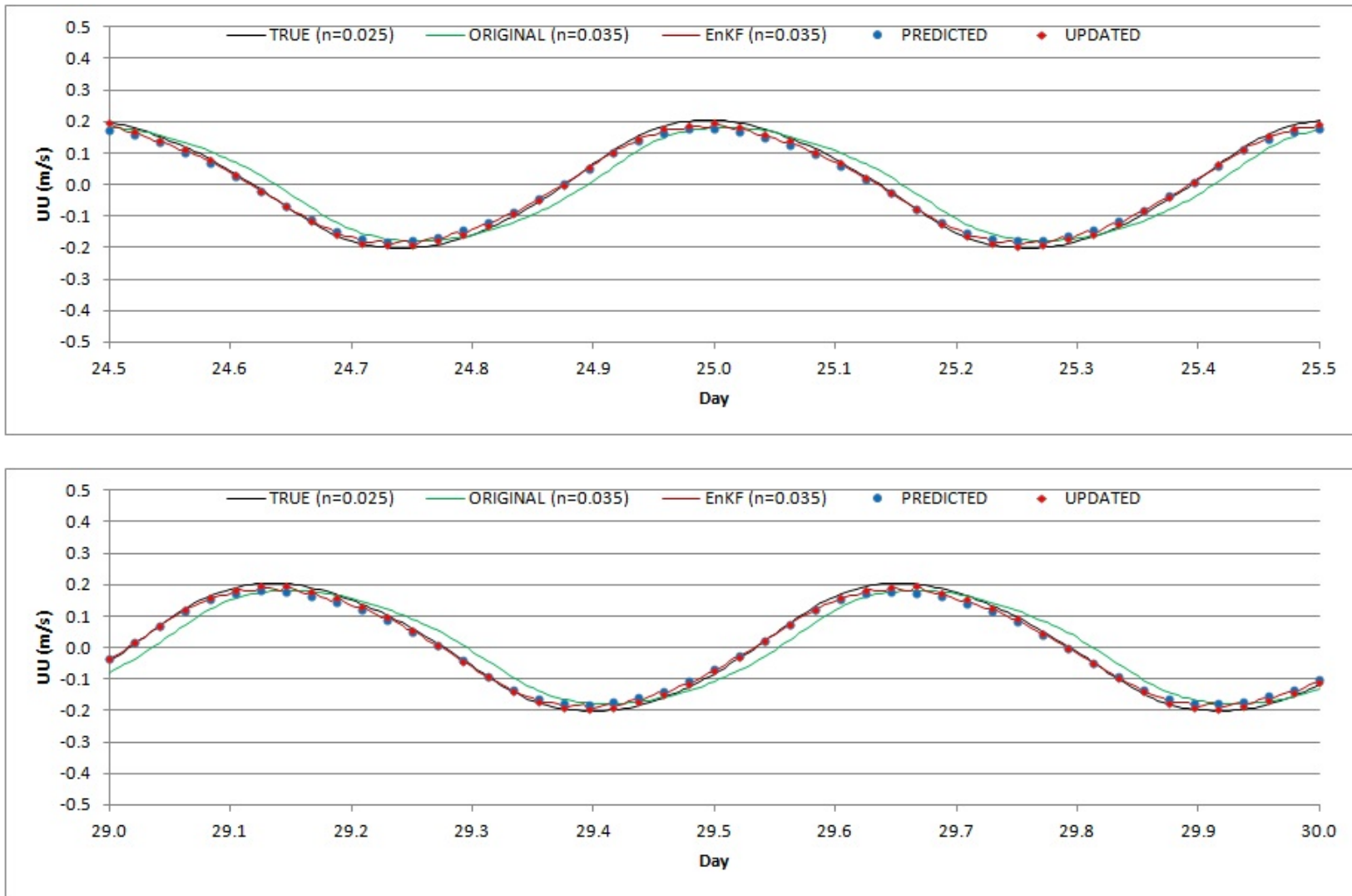
Figure 24   Time series of UU at the target station g at the middle day (upper) and at the last day (bottom).

As shown in the figures above, the amplitudes and phases of the original simulation results are smaller and delayed compared to the true simulation results at the target station. On the other hand, both amplitudes and phases of the EnKF results match well with the true simulation results. After EnKF is applied, predicted UU converges to the amplitudes of the original simulation results, which is because amplitudes of the velocity are more sensitive to Manning's *n*.

RMSE of UU at the target station and two gauging stations for the original simulation and the EnKF simulation are listed below (Table 8).

**Table 8**   **RMSE of UU at the target station and gauging stations.**

Gauge No.	RMSE of UU		
	Original (m/s)	EnKF (m/s)	$\dfrac{RMSE_{Original} - RMSE_{EnKF}}{RMSE_{Original}}(\%)$
Gauge g	3.317E-02	1.276E-02	61.5
Gauge a	5.785E-02	3.714E-02	35.8
Gauge f	7.675E-03	3.189E-03	58.4

As shown in the table above, the errors are improved by 62% at the target station using EnKF. DG ADCIRC-2DDI with EnKF works effectively at the target station as well as on gauging station.

5.4.3. Depth-integrated velocities in the Northing direction

Time series of VV during the last 10 days on the target station are shown in the top of Figure 25. Shown in black line is the VV from the true simulations, in green line is the VV from original simulation, and in red line is the averaged ensemble VV from EnKF simulations. Time series of VV for the first day are shown in the bottom of Figure 25, for the middle day are shown in the top of Figure 26, and for the last day are shown in the bottom of Figure 26. Shown in blue circle is the average of ensemble predicted VV which is taken from the EnKF simulation, and shown in red diamond is the average of ensemble updated VV which is taken from the EnKF simulation.
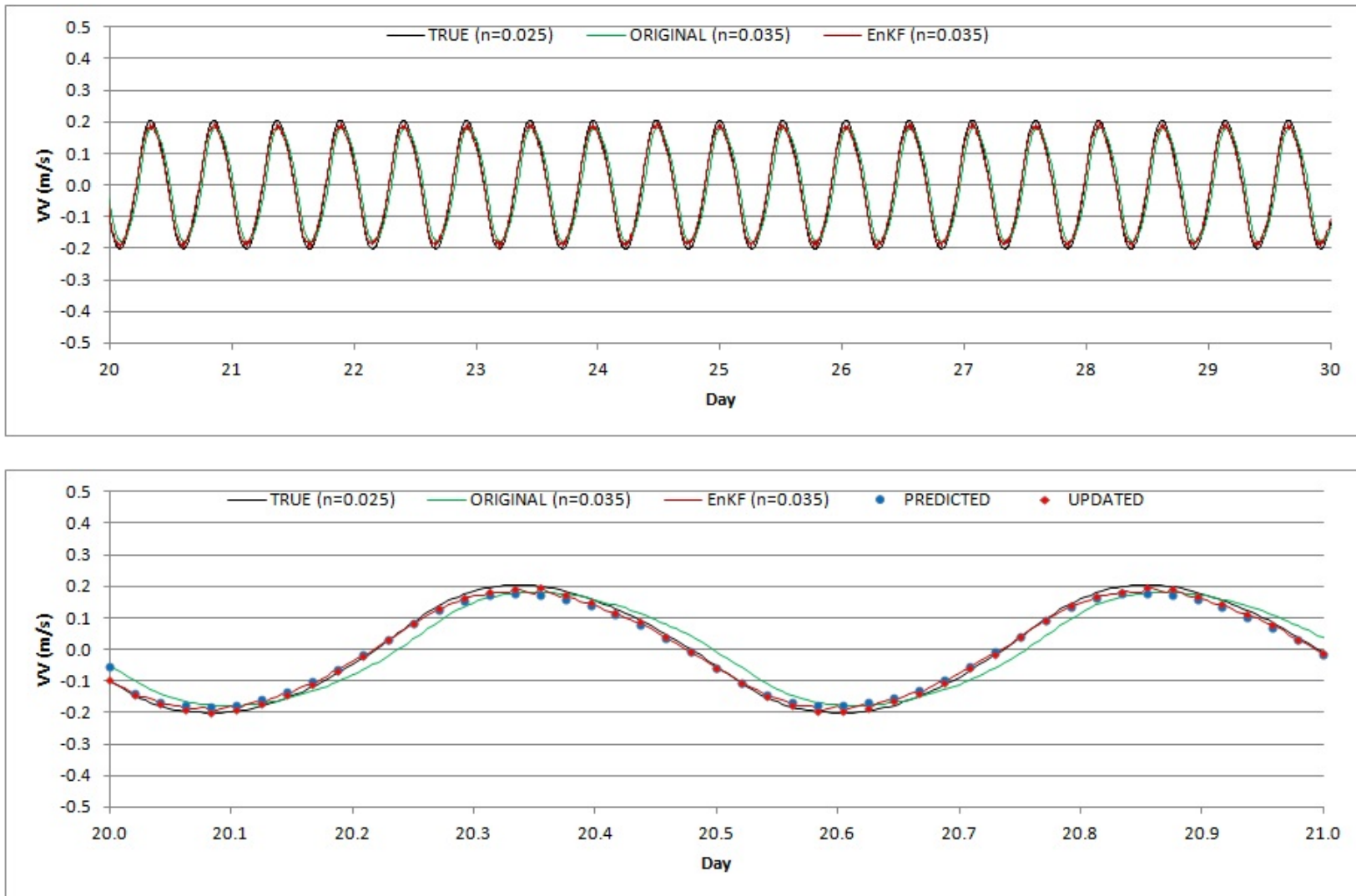
Figure 25   Time series of VV at the target station g during last 10 days (upper) and at the first day (bottom).

60
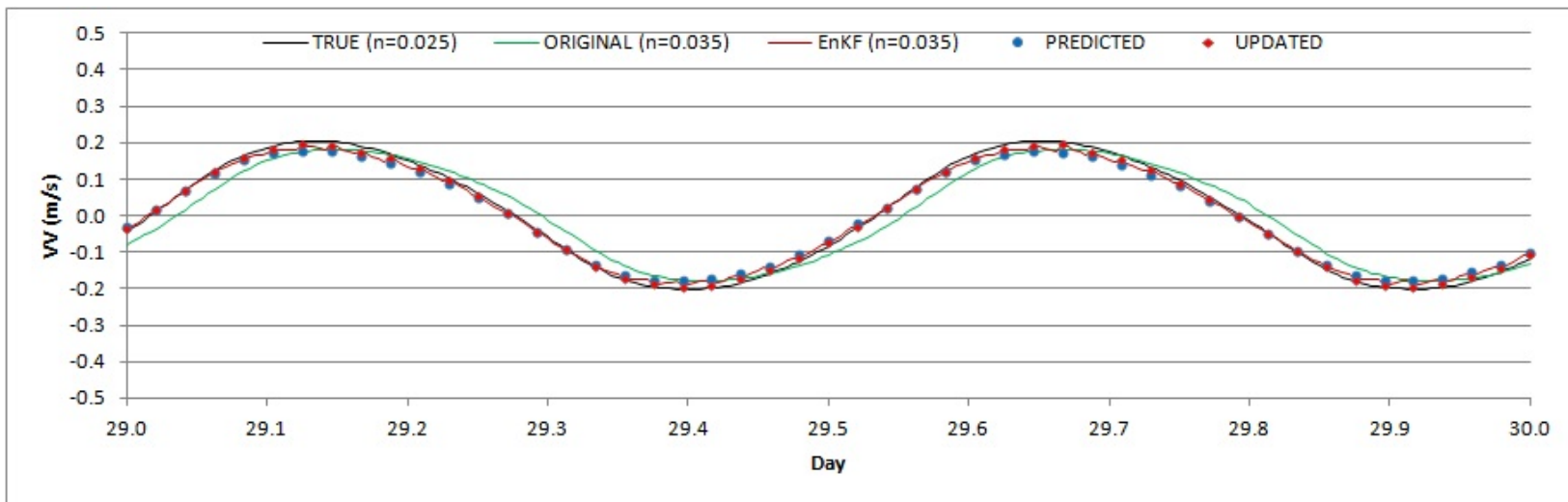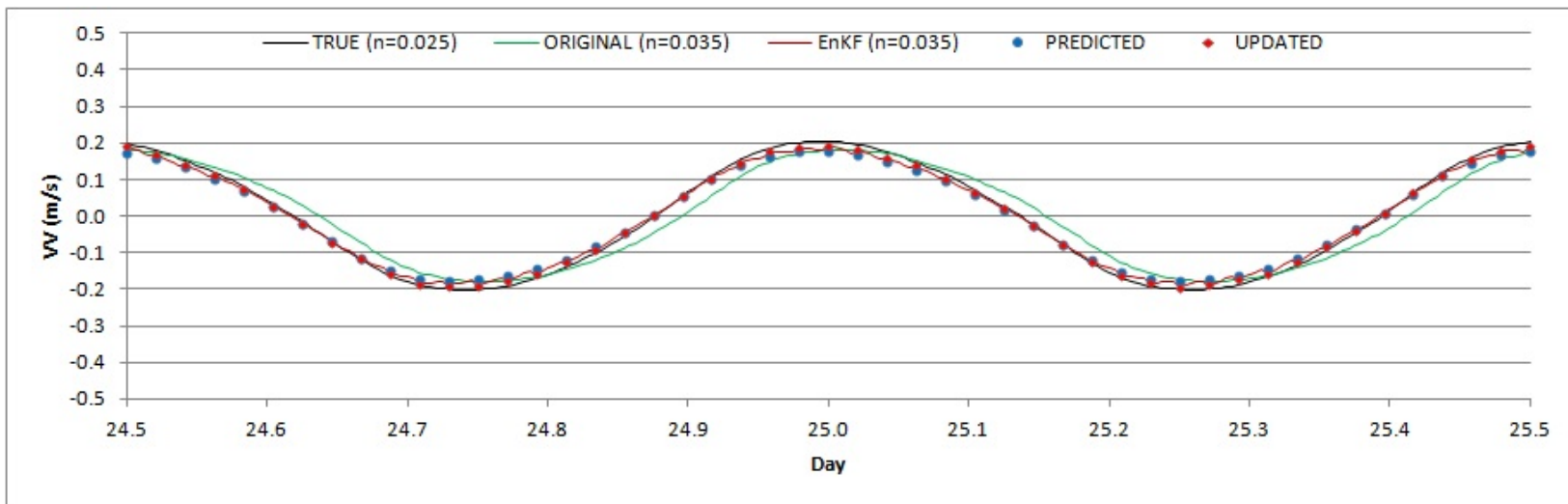
Figure 26   Time series of VV at the target station g at the middle day (upper) and at the last day (bottom).

61

As shown in the figures above, the amplitudes and phases of the original simulation results are smaller and delayed compared to the true simulation results at the target station. On the other hand, both amplitudes and phases of the EnKF results match well with the true simulation results. After EnKF is applied, predicted VV converges to the amplitudes of original simulation results, which is because amplitudes of the velocity are more sensitive to Manning's *n*.

RMSE of VV at the target station and two gauging stations for the original simulation and the EnKF simulation are listed below (Table 9).

Table 9 **RMSE of VV at the target station and gauging stations**

| Gauge No.	RMSE of VV		
	Original (m/s)	EnKF (m/s)	$\dfrac{RMSE_{Original} - RMSE_{EnKF}}{RMSE_{Original}}(\%)$
Gauge g	3.317E-02	1.309E-02	60.5
Gauge a	1.340E-02	0.603E-02	55.0
Gauge f	2.851E-02	0.793E-02	72.2

As shown in the table above, the errors are improved by 61% at the target station using EnKF. DG ADCIRC-2DDI with EnKF works effectively on the target station as well as on the gauging stations for VV. Thus, DG ADCIRC-2DDI with EnKF works effectively on not only the gauging station but also the target station for all state variables.

CHAPTER 6: APPLICATION TO LOWER ST. JOHNS RIVER

Four numerical experiments for a real test case are presented in this chapter. DG ADCIRC-2DDI with EnKF is applied to the St. Johns River (Figure 27-a). The total number of nodes and elements in the finite element mesh (Bacopoulos et al. 2012) are 30472 and 56262, respectively. Four NOAA gauging stations are located in the Lower St. Johns River (Figure 27-b). In each experiment, three gauging stations (of the four totals) are used in EnKF estimation and remaining gauging station is used for comparison, called the target station. Thus, there are four combinations of gauging-target stations for the four experiments: 1) Mayport is the target station, 2) Fulton is the target station, 3) Dames Point is the target station, and 4) Jacksonville is the target station.
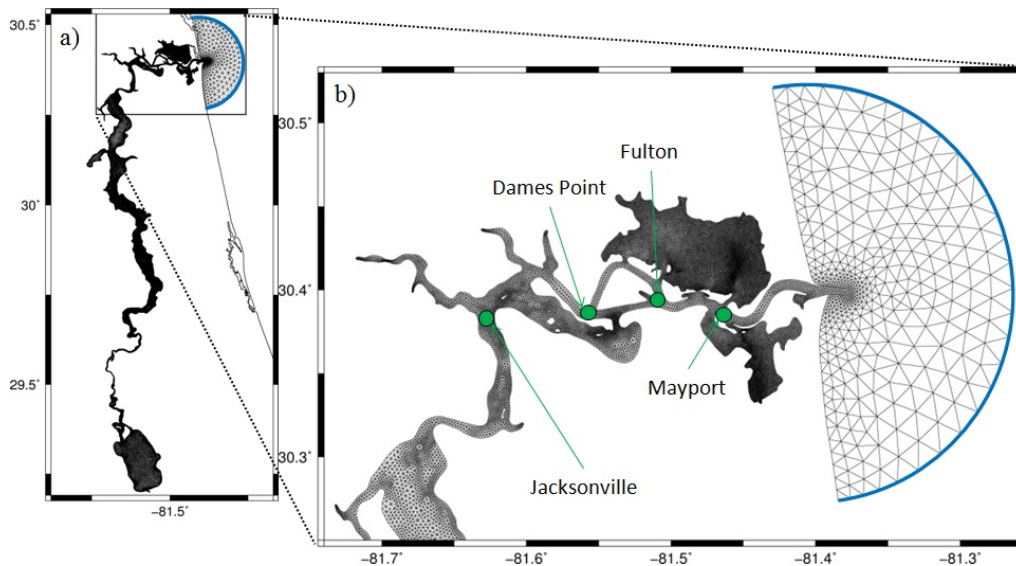
Figure 27   a) St. Johns River and b) Lower St. Johns River with four NOAA gauging stations.

6.1. Model Setup

The model simulates 30 days of tides from September 21st to October 21st, 1999, the boundary conditions are ramped up over the first 5.0 days, and the time step is 1.5 sec. Boundary conditions include a tidal elevation forcing on the open boundary and no-normal flow constraints (with free tangential slip) along all coastlines. The tidal elevation forcing is composed of seven principal tidal constituents (K1, O1, M2, S2, N2, K2, and Q1; see Table 10) interpolated from the South Atlantic Bight mesh of Bacopoulos et al. (2011). Tidal potential forcings are not indluded. Wetting and drying is disabled with the minimum bathymetric depth set to 1.0 m. The advective terms are enabled. Horizontal eddy viscosity is set equal to 0.0 m^2/s. The GWCE weighting parameter is set equal to –0.01 (Kolar et al. 1994a). Ensemble Manning's *n* for 'open water' and 'emergent herbaceous wetlands' are calculated using Equation 3.3. The base values, lower limits, and upper limits of the two landcover classes are shown in Table 2.

EnKF is applied during last 10 days. To implement DG ADCIRC-2DDI with EnKF, the ensemble sizes are set to 30, and model error coefficients are set to 10% for WSE, UU and VV.

Table 10 **The 7 tidal constituents employed by ADCIRC are sorted in ascending order by frequency.**

Constituent	Speed (°/hr)	Period (hr)
Q1	13.40	26.87
O1	13.94	25.82
K1	15.04	23.93
N2	28.44	12.66
M2	28.98	12.42
S2	30.00	12.00
K2	30.08	11.97

<div align="center">6.2. Observation data</div>

Observation data are generated by tidal resynthesis using five constituents (M_2, S_2, N_2, K_1, and O_1) that are derived from raw data at NOAA tide gauging stations (Zang et al., 2006 and Bourgerie, 1999). Time series of observed tidal water levels and along-channel velocities are shown in Figures 28 to 31 at each target station. The observed along-channel velocities cannot be directly used in DG ADCIRC-2DDI with EnKF because state variables of DG ADCIRC-2DDI with EnKF are WSE, UU and VV. Thus, the along-channel velocities have to be decomposed into UU and VV:

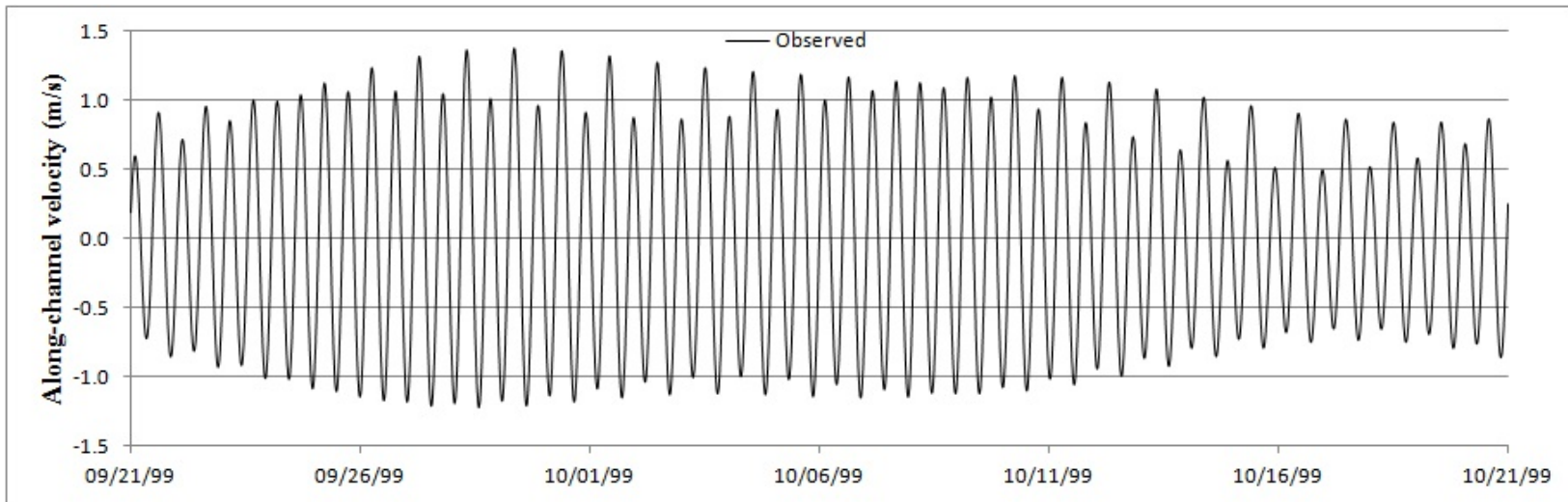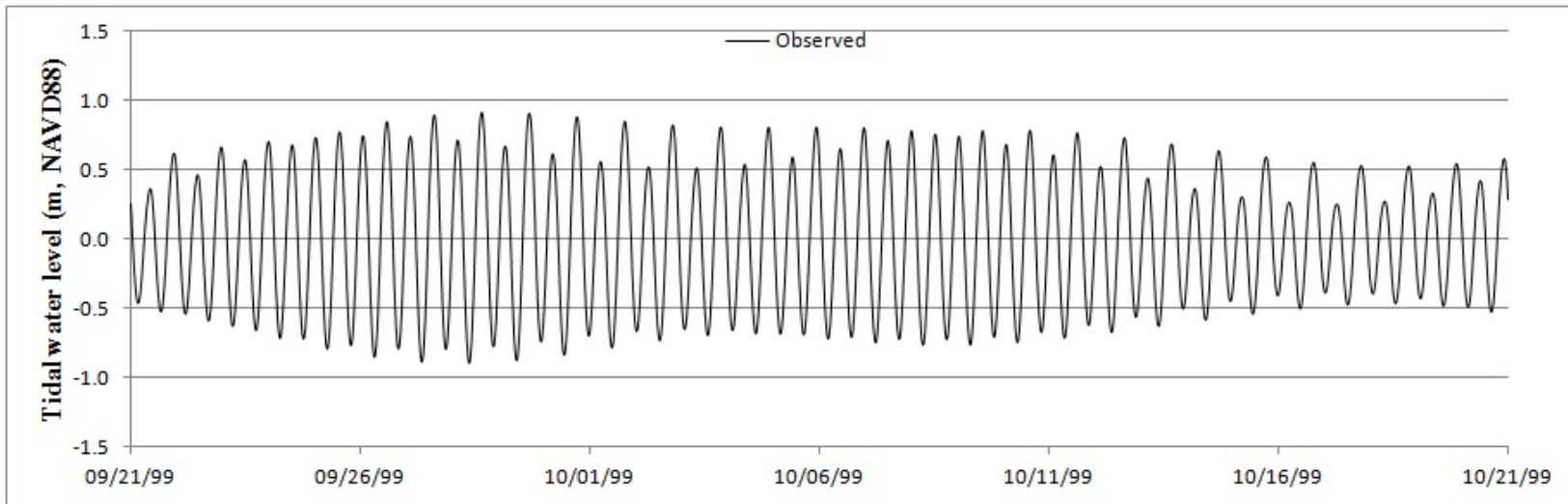$$UU = \text{Along-channel velocity} * COS(Angles) \dots\dots\dots\dots\dots\dots\dots\dots\dots (6.1)$$

$$VV = \text{Along-channel velocity*SIN}\left(Angles\right)\dots\dots\dots\dots\dots\dots\dots\dots\dots\dots\dots(6.2)$$

Each angle is shown in the table below (Bourgerie, 1999).

Table 11   **Conversion angles at each gauging station (Bourgerie, 1999).**

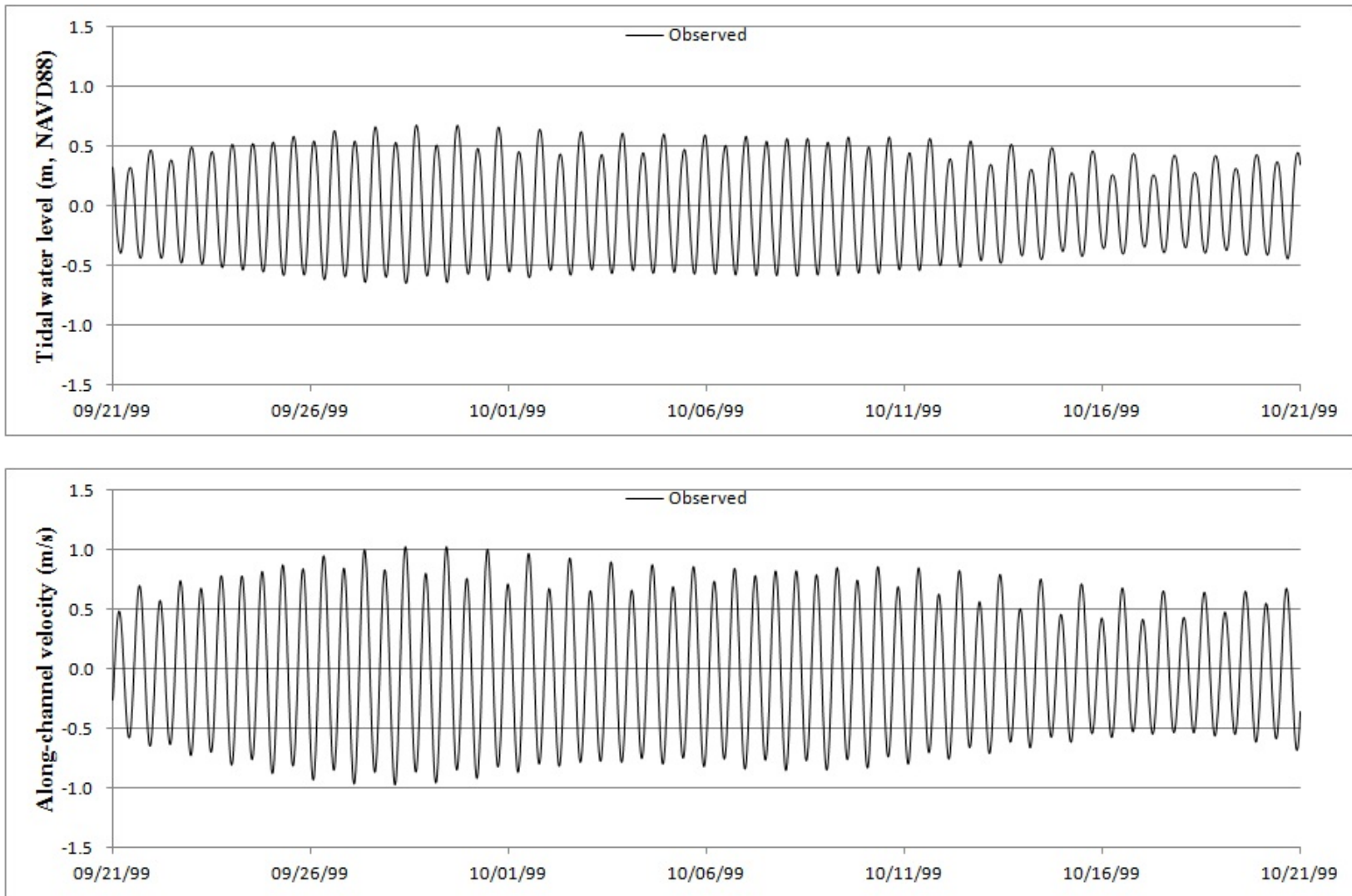| Gauge	Mayport	Fulton	Dames Point	Jacksonville
Angle	152.46	153.00	175.23	259.90

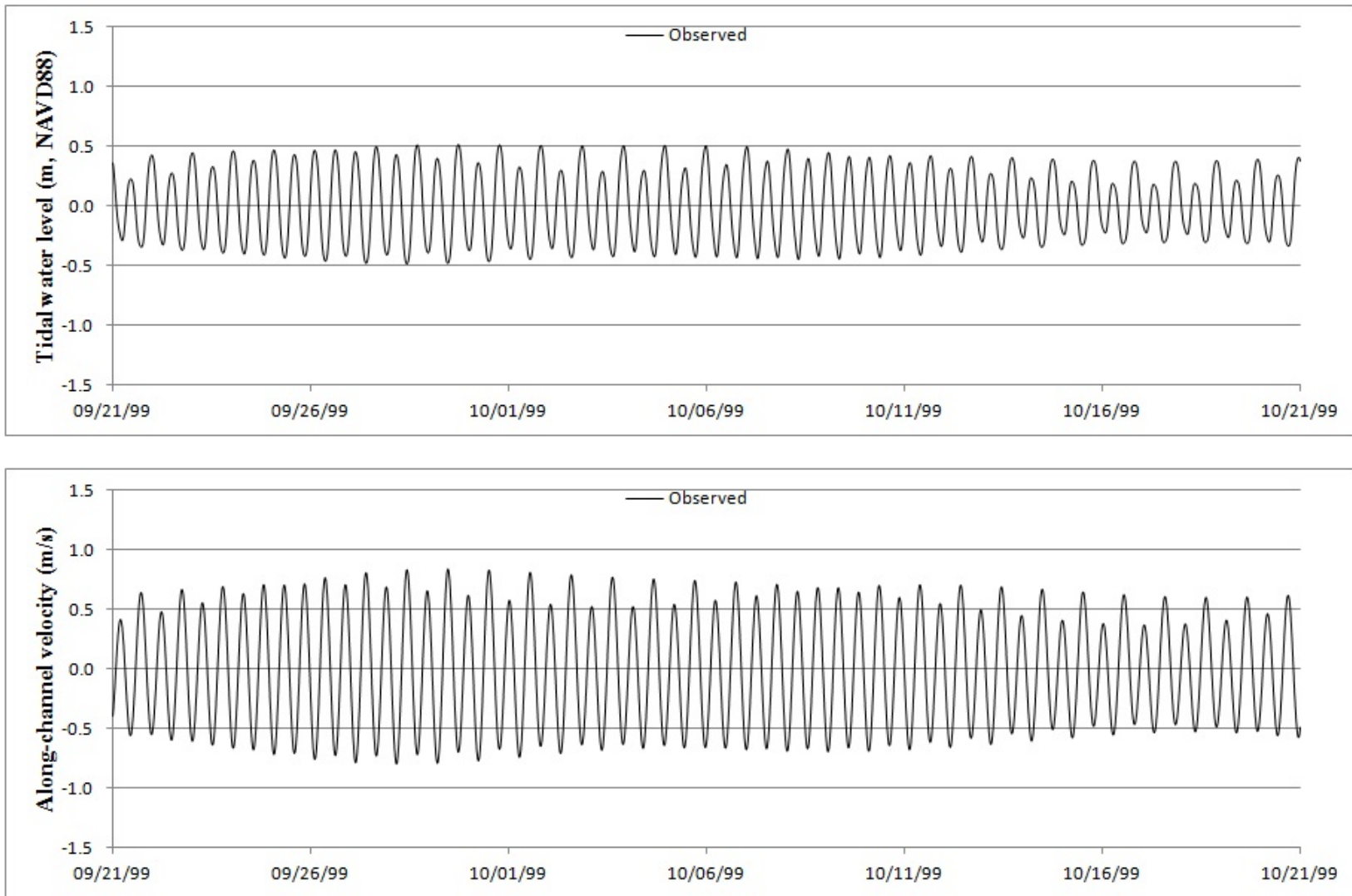Time series of observed UU and VV are shown in Figures 32 to 35 at each target station.

Figure 28 Times series of observed tidal water level and along-channel velocity at Mayport.
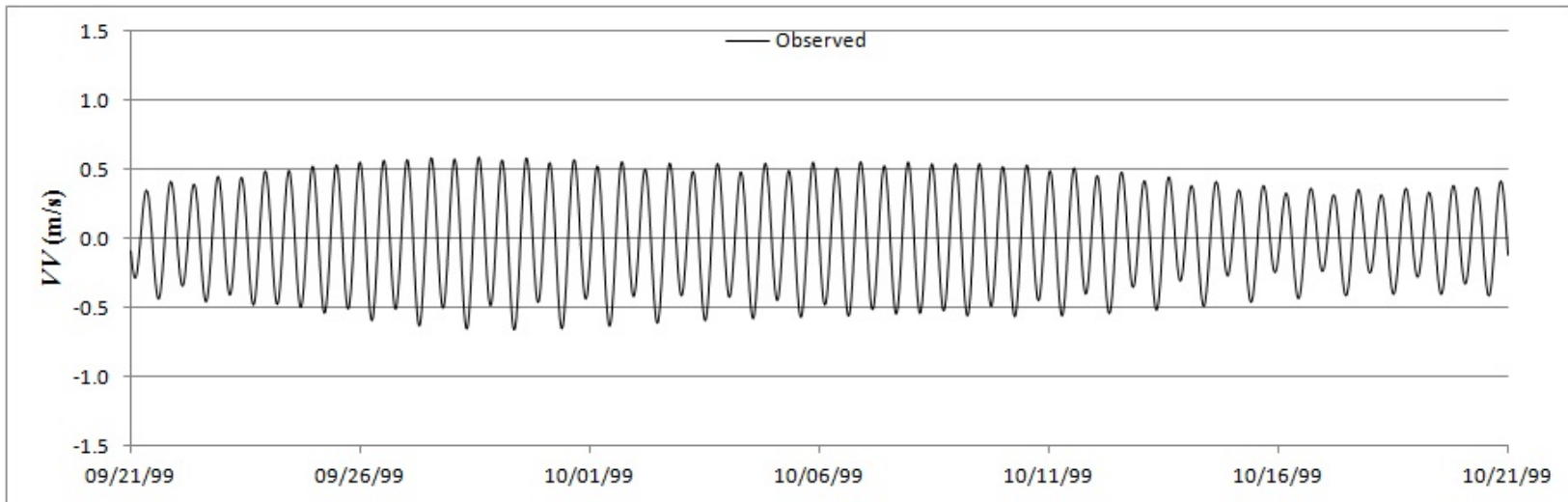
67
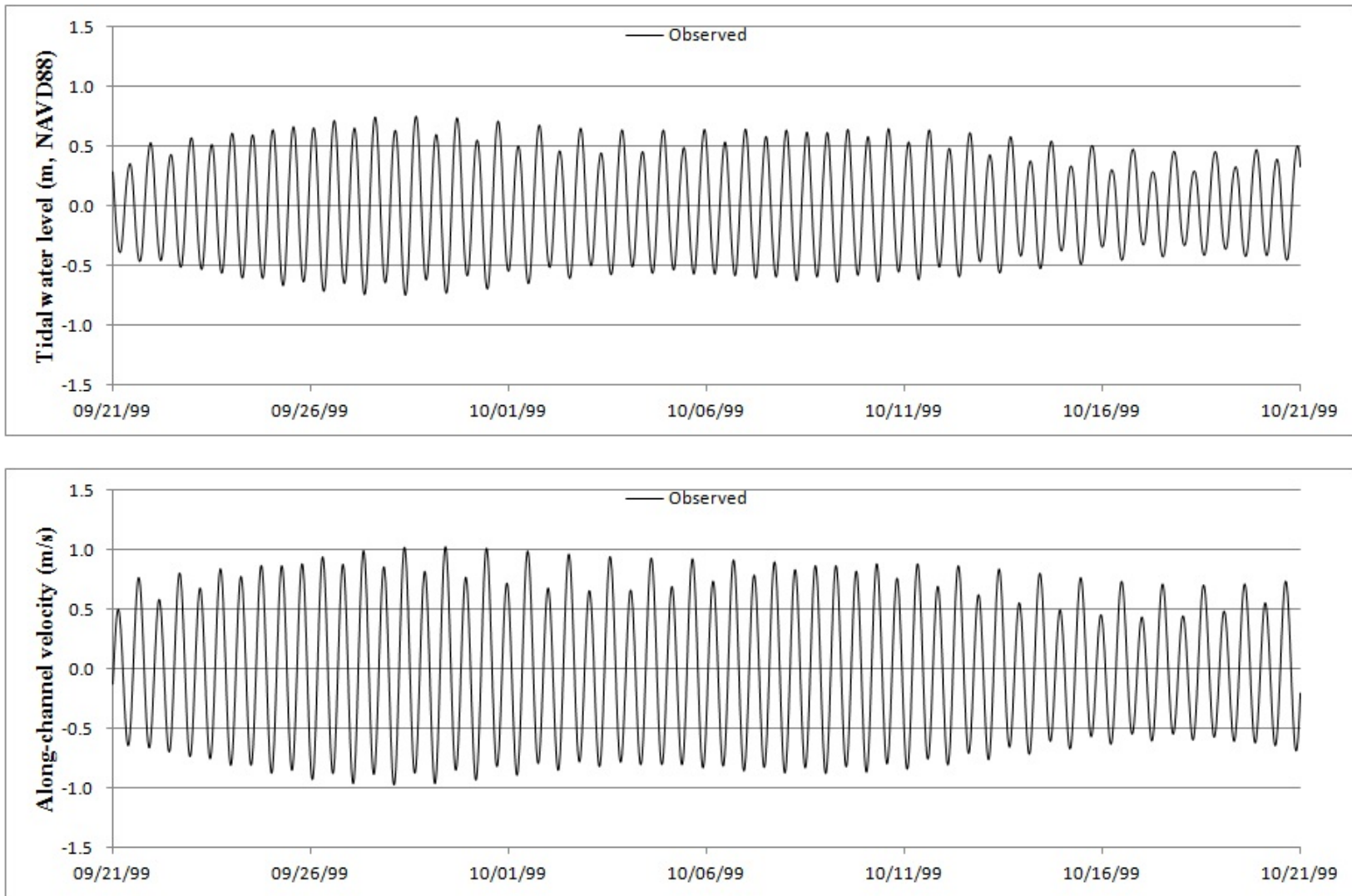
Figure 29 Time series of observed tidal water level and along-channel velocity at Fulton.
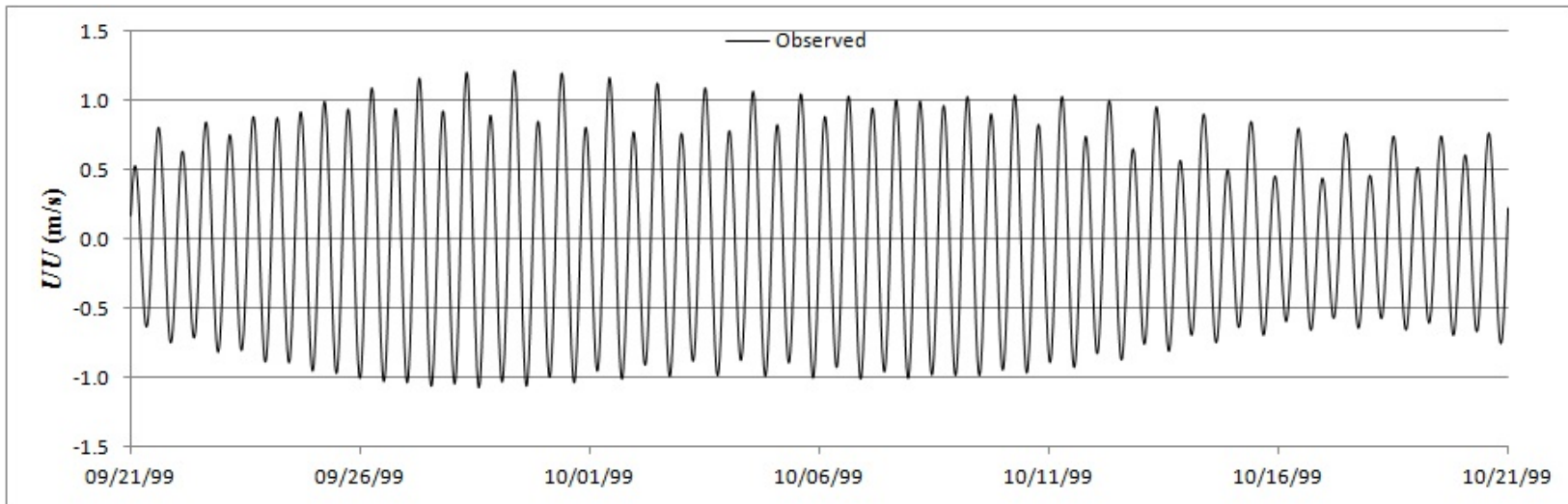
Figure 30   Times series of observed tidal water level and along-channel velocity at Dames Point.

69
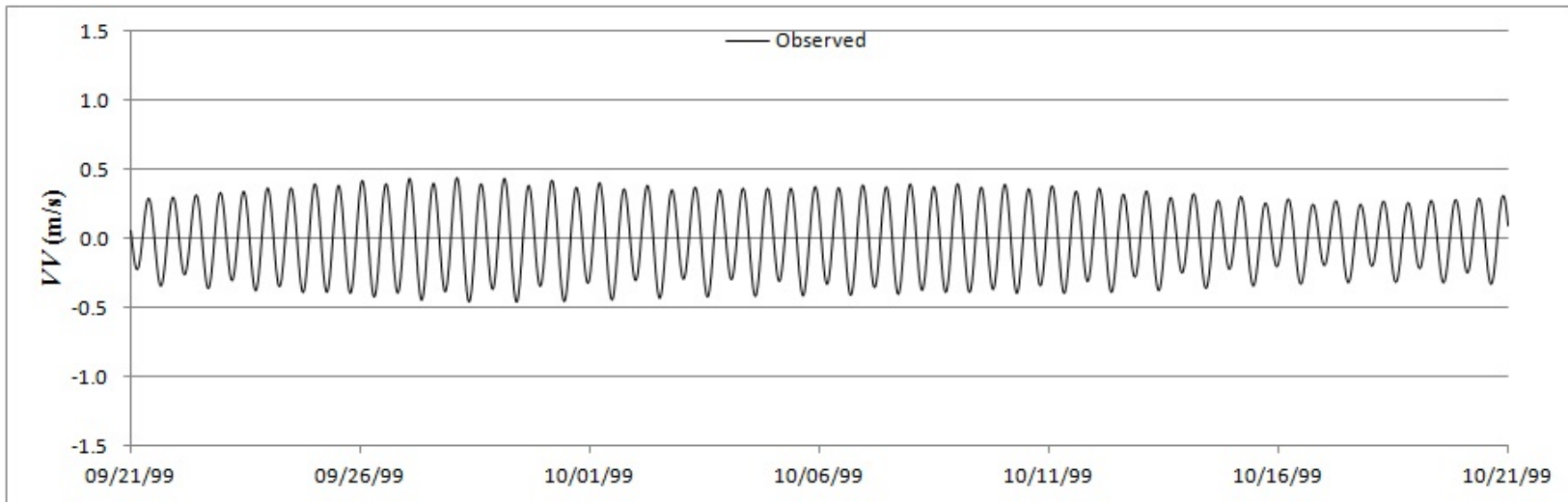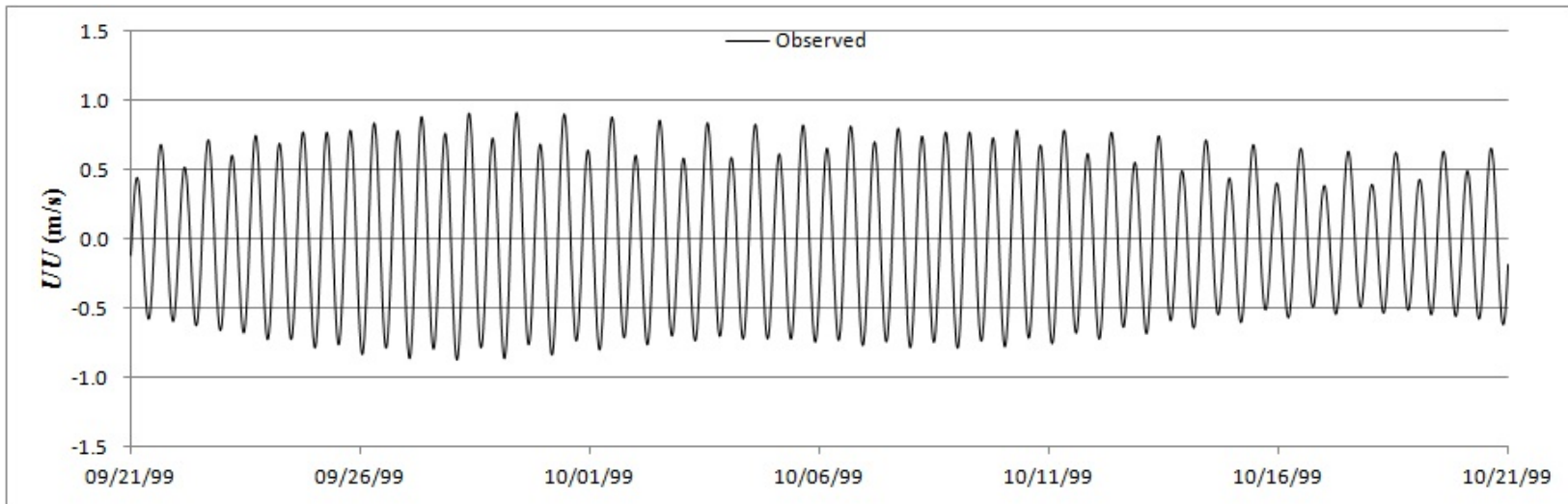
Figure 31 Time series of observed tidal water level and along-channel velocity at Jacksonville.
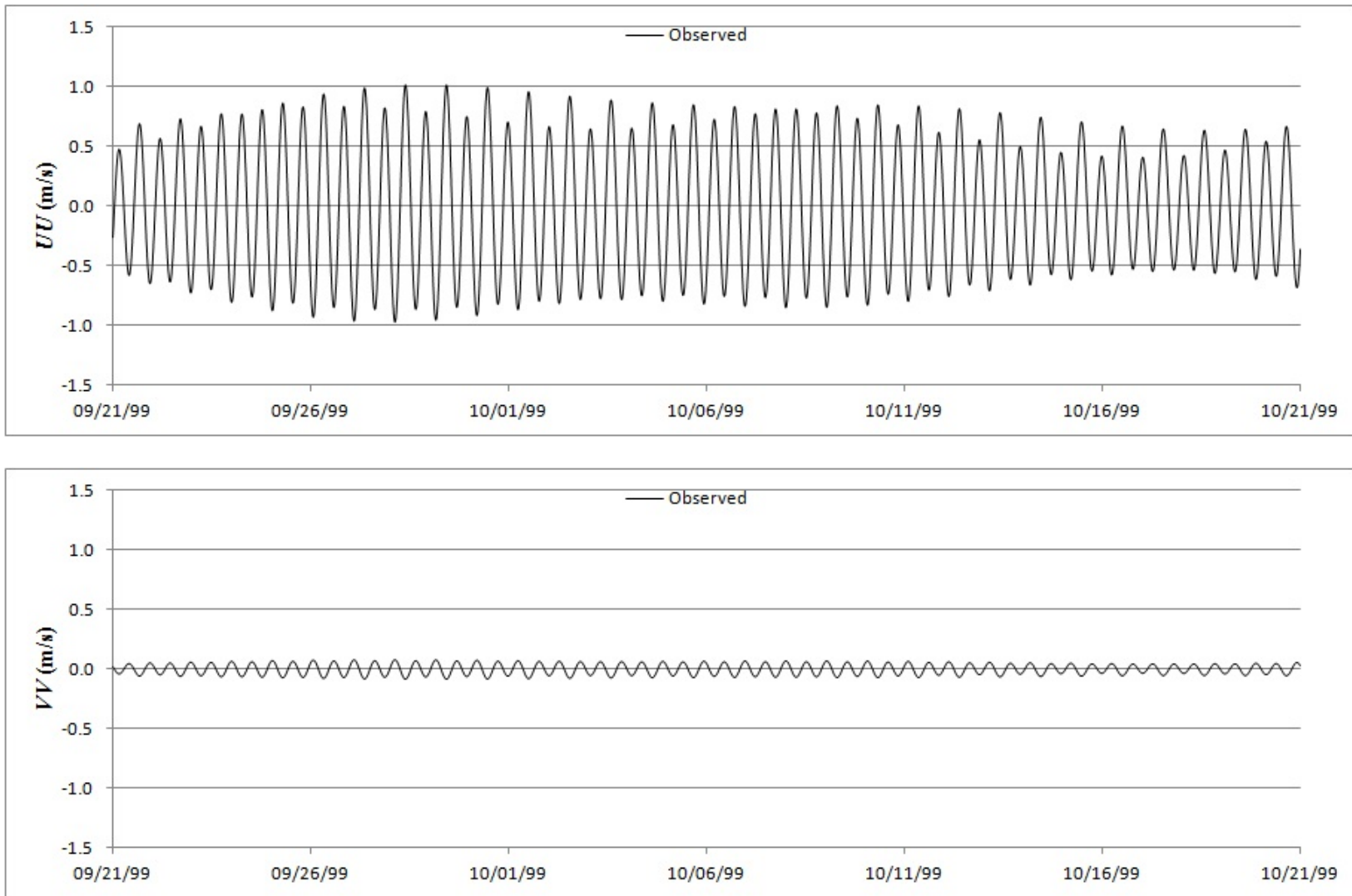
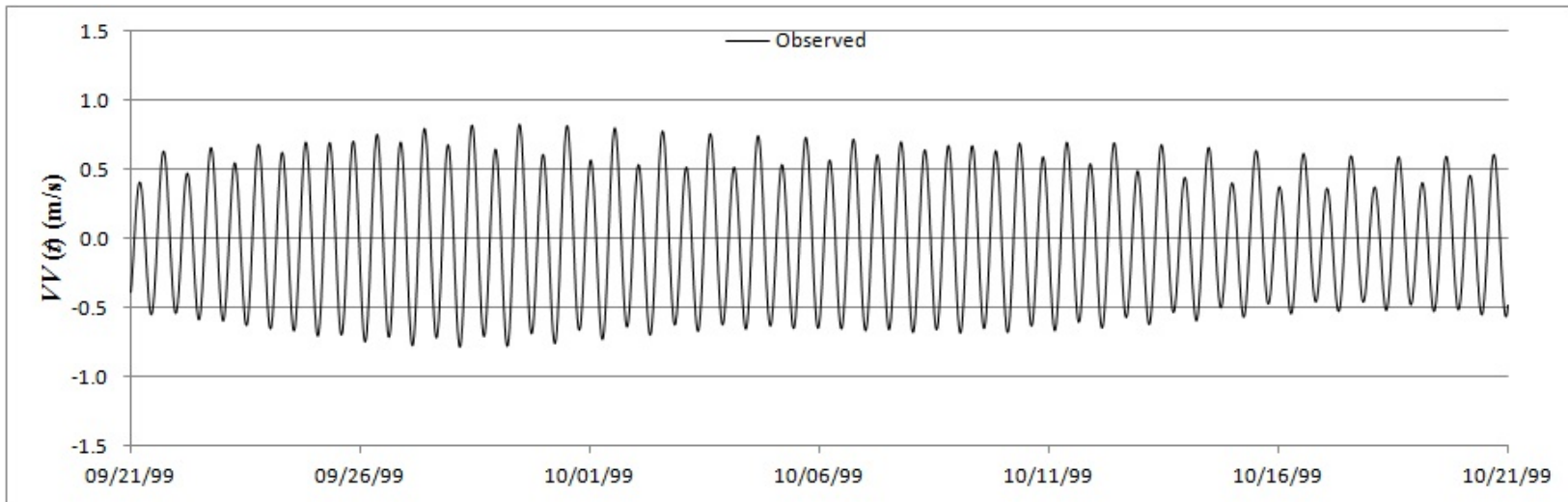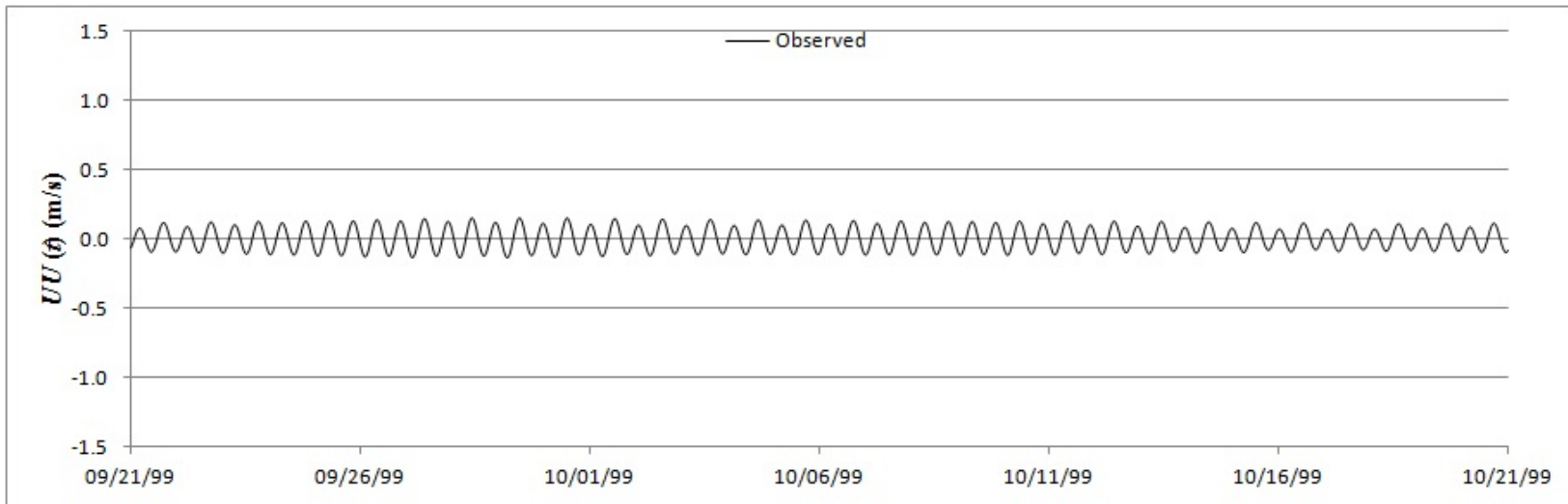**Figure 32**   Times series of observed UU and VV at Mayport.

71

Figure 33   Time series of observed UU and VV at Fulton.

Figure 34 Time series of observed UU and VV at Dames Point.

Figure 35   Time series of observed UU and VV at Jacksonville.

6.2.1. Potential error for observed tidal water level

As mentioned above, observed tidal water levels are generated using five constituents that derived from raw data at NOAA tide gauging stations. However, observed data includes uncertainty (error). Three potential errors include error of pressure transducer of the tide gauge (up to 2cm; IOC 2006), error of geodetic benchmarking of the tide gauge (up to 1cm; Hicks et al. 1987), and error of harmonic analysis of tide measurements (up to 2cm; Zhang et al. 2006). The percentages of the total potential error for the tidal water levels are listed below (Table 12) at each gauging station.

Table 12   **Total potential errors for tidal water levels at each gauging station.**

	Mayport	Fulton	Dames Point	Jacksonville
Maximum tide (m)	0.90	0.75	0.70	0.50
Minimum tide (m)	-0.90	-0.75	-0.70	-0.50
Total potential error (%)	5.6	6.7	7.1	10.0

6.2.2. Potential error for observed along-channel velocity

Similarly, two potential errors include error of harmonic analysis of observed tidal current constituents (up to 13cm; Bourgerie 1999) and error of conversion from along-channel velocities to UU & VV (up to ± 3 degree; Bougerie 1999). The percentages of the total potential error for the along-channel velocities for each gauging station are listed below (Table 13).

Table 13   **Total potential errors for tidal water levels at each gauging station.**

|	Mayport	Fulton	Dames Point	Jacksonville
Peak ebb velocity (m/s)	1.40	1.00	1.00	0.85
Peak flood velocity (m/s)	1.20	1.00	1.00	0.70
Total potential error (%)	12.3	16.0	16.0	20.6

6.3. Simulation 1: Comparison at Mayport

In this section, simulation results during the last 10 days (October 11th to 21st, 1999) at the target station Mayport will be discussed. In addition, simulation results are shown for the first day (October 10th at 18:00PM to 11th at 6:00AM, 1999), middle day (October 17th at 0:00AM to at 12:00AM, 1999), and last day (October 20th at 12AM to 21st at 0:00AM, 1999). Simulation results at the gauging stations are shown in Appendix C.

6.3.1. Tidal water level

Time series of the tidal water level during the last 10 days at the target station Mayport are shown in the top of Figure 36. Shown in black line is the observed tidal water level, in green line is the tidal water level from the original DG ADCIRC simulation, and in red line is the average of ensemble tidal water levels from DG ADCIRC with EnKF simulation. Time series of the tidal water level for the first day are shown in the bottom of Figure 36, for the middle day are shown in the top of Figure 37, and for the last day are shown in the bottom of Figure 37. Shown in blue circle is the average of ensemble predicted tidal water levels which is taken from EnKF simulation and red diamond is the average of ensemble updated tidal water levels which is taken from EnKF simulation.
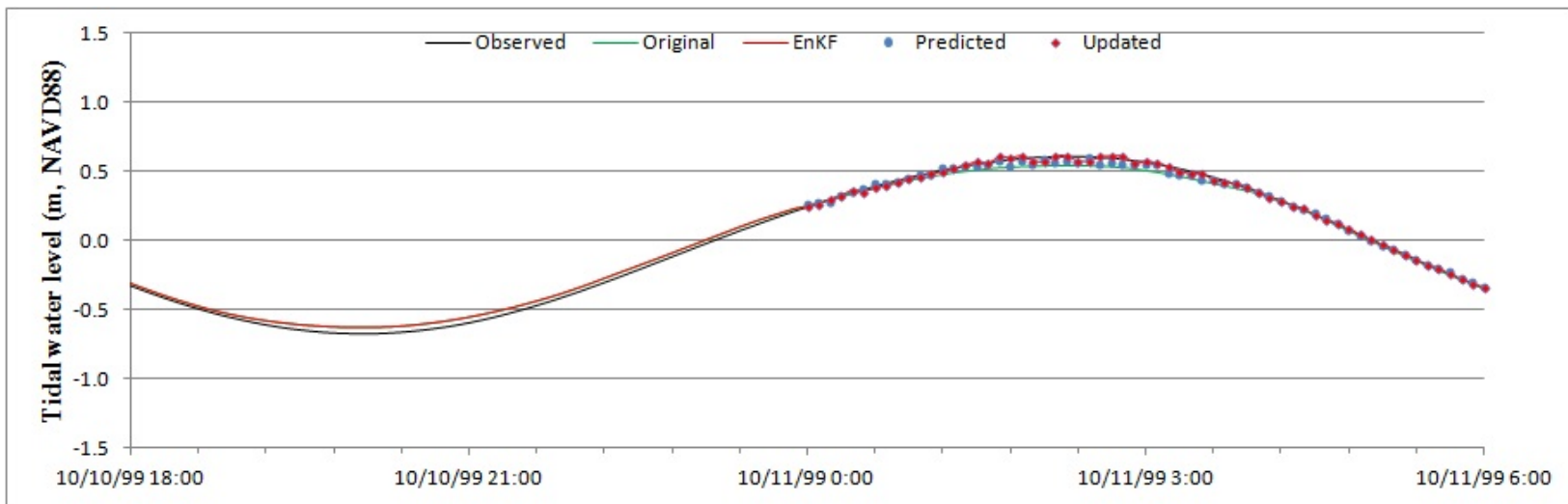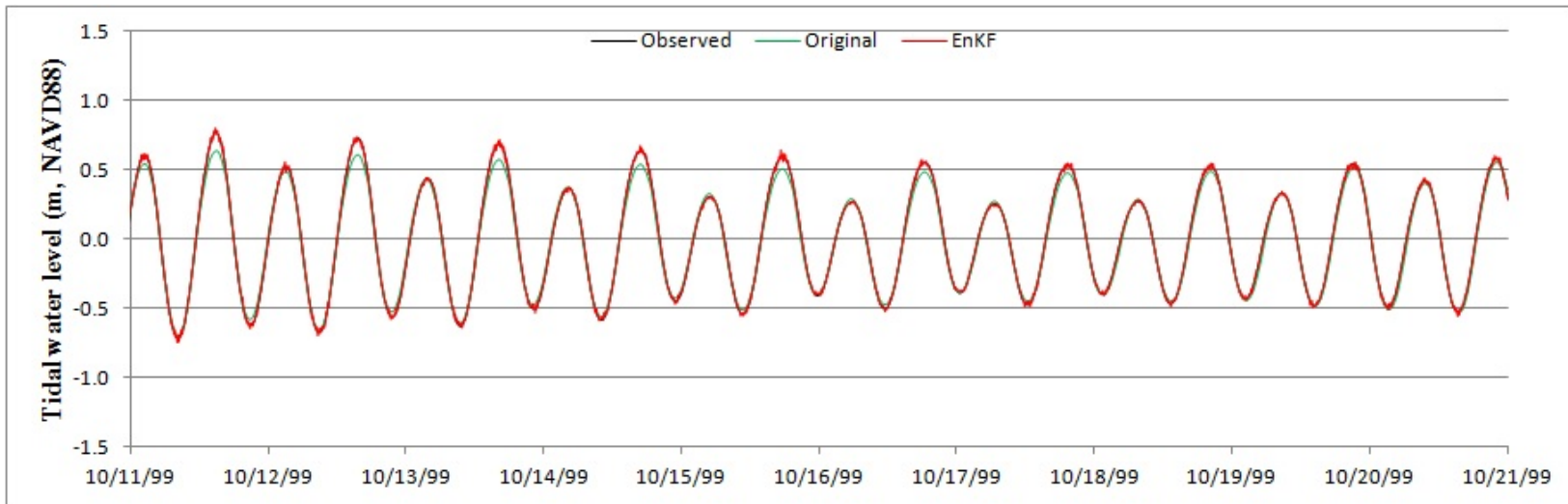
Figure 36 Time series of the tidal water level during the last 10 days (upper) and at the first day (bottom) at the target station (Mayport).
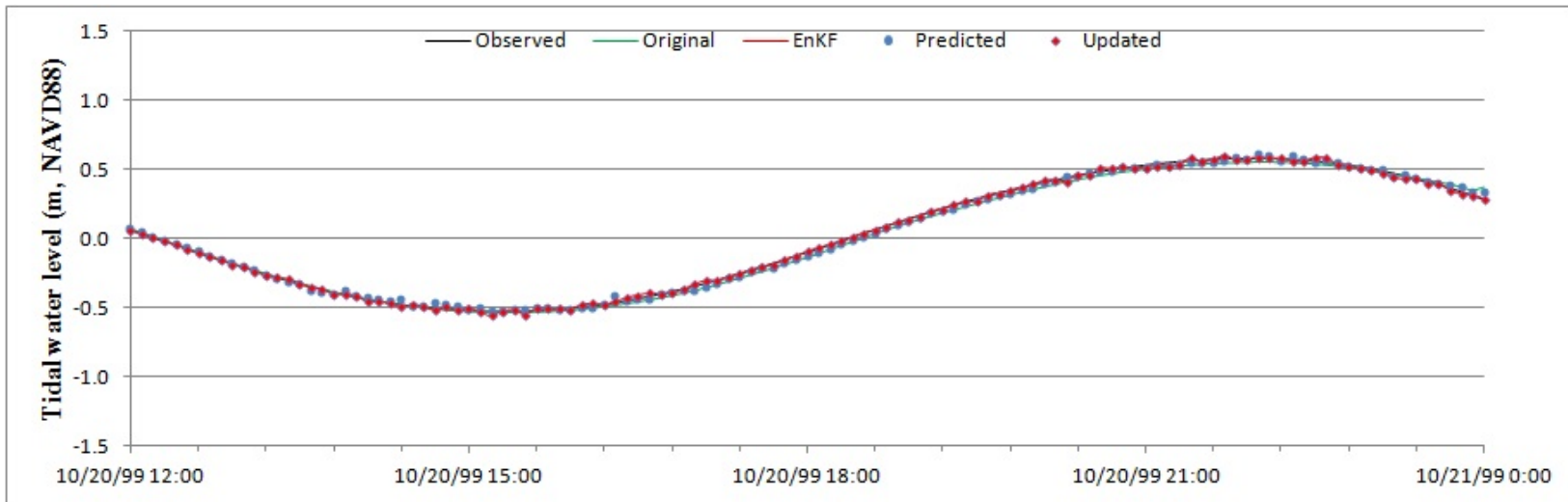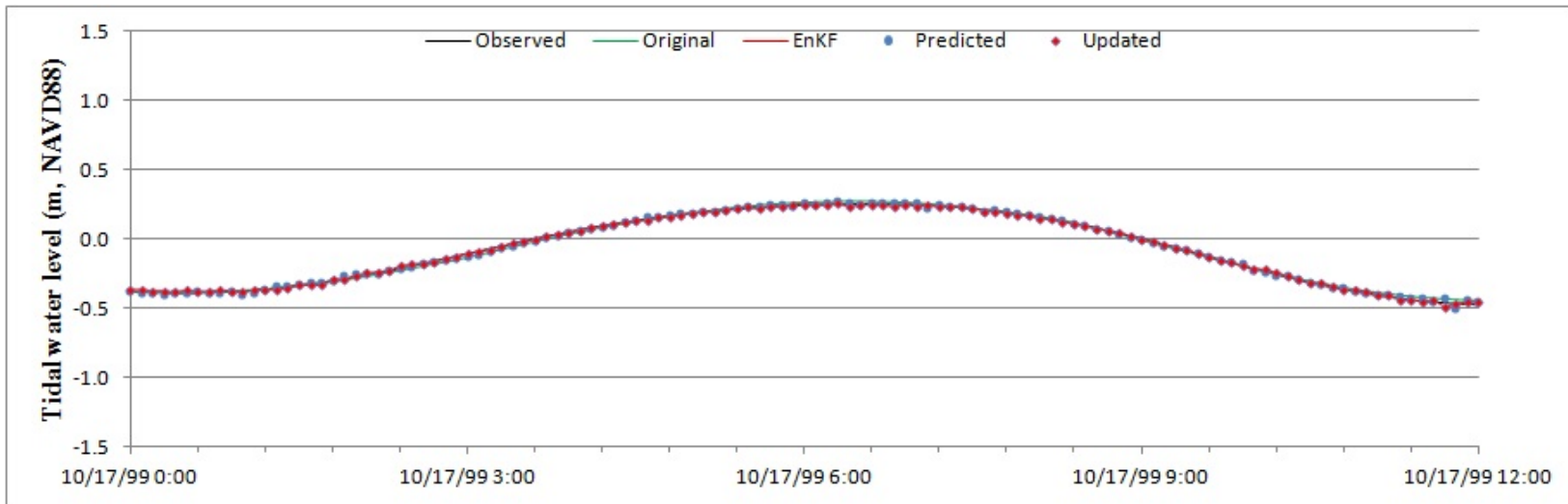
Figure 37 Time series of the tidal water level at the middle day (upper) and at the last day (bottom) at the target station (Mayport).

As shown in the figures above, the amplitudes of the original simulation results do not compare well with the observed tidal water level. However, the amplitudes of the EnKF simulation results compare well with the amplitudes of the observed tidal water level.

RMSE of the tidal water level at the target station for the original simulation and the EnKF simulation are listed below (Table 14).

Table 14   **RMSE of the tidal water level at the target station Mayport.**

| Gauge Name.	RMSE of the tidal water level		
	Original (m)	EnKF (m)	$\dfrac{RMSE_{Original} - RMSE_{EnKF}}{RMSE_{Original}}(\%)$
Mayport	3.262E-02	2.147E-02	34.2

As shown in the table above, the errors are improved by 34% at the target station using EnKF. RMSEs of the tidal water level at the gauging stations are listed in Appendix C.
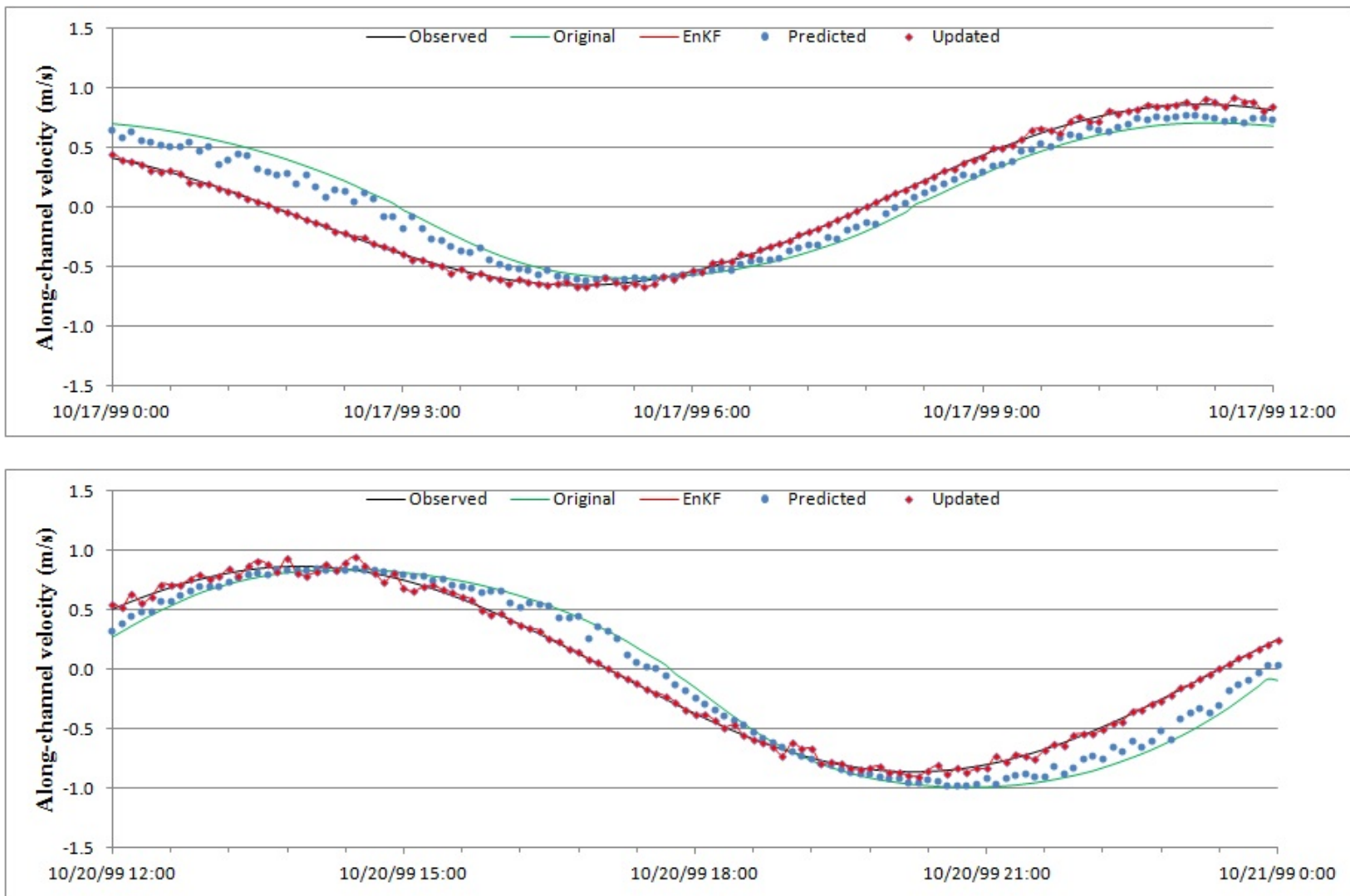
6.3.2. Along-channel velocity

Time series of the along-channel velocity during the last 10 days at the target station are shown in the top of Figure 38. Shown in black line is the observed along-channel velocity, in green line is the along-channel velocity from the original DG ADCIRC simulation, and in red line is the average of ensemble along-channel velocities from the DG ADCIRC with EnKF simulation. Time series of the along-channel velocity for the first day are shown in the bottom of Figure 38, for the middle day are shown in the top of Figure 39, and for the last day are shown in the bottom of Figure 39. Shown in blue circle is the average of ensemble predicted along-channel velocities which is taken from EnKF simulation and in red diamond is the average of ensemble updated along-channel velocities which is taken from EnKF simulation.
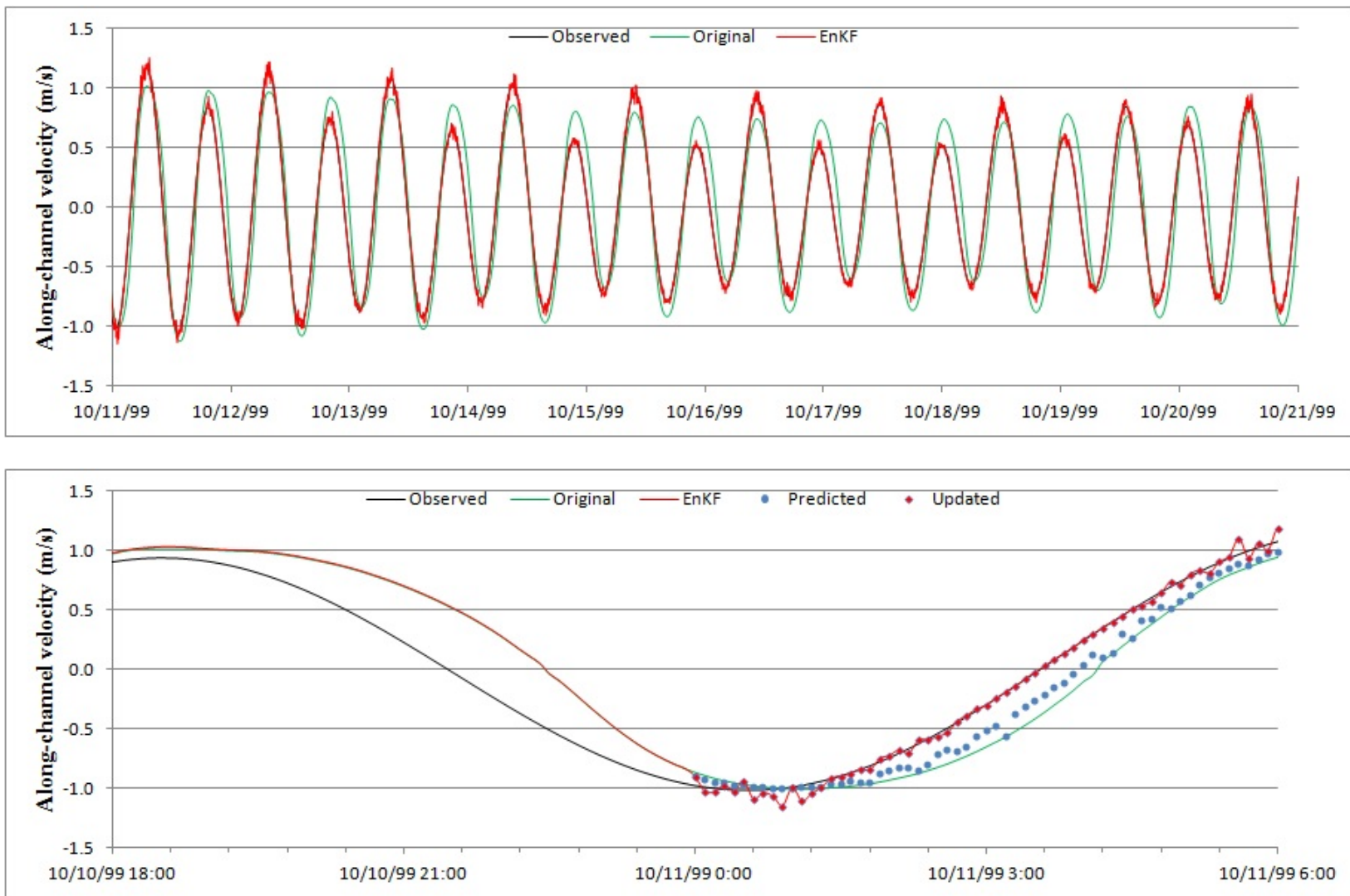
Figure 38   Time series of the along-channel velocity during the last 10 days (upper) and at the first day (bottom) at the target station (Mayport).

Figure 39 Time series of the along-channel velocity at the middle day (upper) and at the last day (bottom) at the target station (Mayport).

83

As shown in the figures above, the amplitudes and phases of the original simulation results do not compare well with the observed along-channel velocity. The amplitude and phases of the predicted along-channel velocity shown in blue circle of EnKF simulation results converge to the original simulation results. However, both amplitudes and phases of the EnKF simulation results compare well with the observed data.

RMSE of the along-channel velocity at the target station for the original simulation and the EnKF simulation are listed below (Table 15).

Table 15　　　　　　　**RMSE of the along-channel velocity at the target station Mayport.**

| Gauge Name.	RMSE of the along-channel velocity		
	Original (m/s)	EnKF (m/s)	$\dfrac{RMSE_{Original} - RMSE_{EnKF}}{RMSE_{Original}}(\%)$
Mayport	2.354E-01	4.041E-02	82.8

As shown in the table above, the errors are improved using EnKF by 83% at the target station. RMSEs of the along-channel velocity at the gauging stations are listed in Appendix C.

6.4. Simulation 2: Comparison at Fulton

In this section, simulation results during the last 10 days (October 11th to 21st, 1999) at the target station Fulton will be discussed. In addition, simulation results are shown at the first day (October 10th at 18:00PM to 11th at 6:00AM, 1999), middle day (October 17th at 0:00AM to at 12:00AM, 1999), and last day (October 20th at 12AM to 21st at 0:00AM, 1999). Simulation results at the gauging stations are shown in Appendix C.

6.4.1. Tidal water level

Time series of the tidal water level during the last 10 days at the target station are shown in the top of Figure 40. Shown in black line is the observed tidal water level, in green line is the tidal water level from the original DG ADCIRC simulation, and in red line is the average of ensemble tidal water levels from the DG ADCIRC with EnKF simulation. Time series of the tidal water level for the first day are shown in the bottom of Figure 40, for the middle day are shown in the top of Figure 41, and for the last day are shown in the bottom of Figure 41. Shown in blue circle is the average of ensemble predicted tidal water levels which is taken from the EnKF simulation and in red diamond is the average of ensemble updated tidal water levels which is taken from the EnKF simulation.
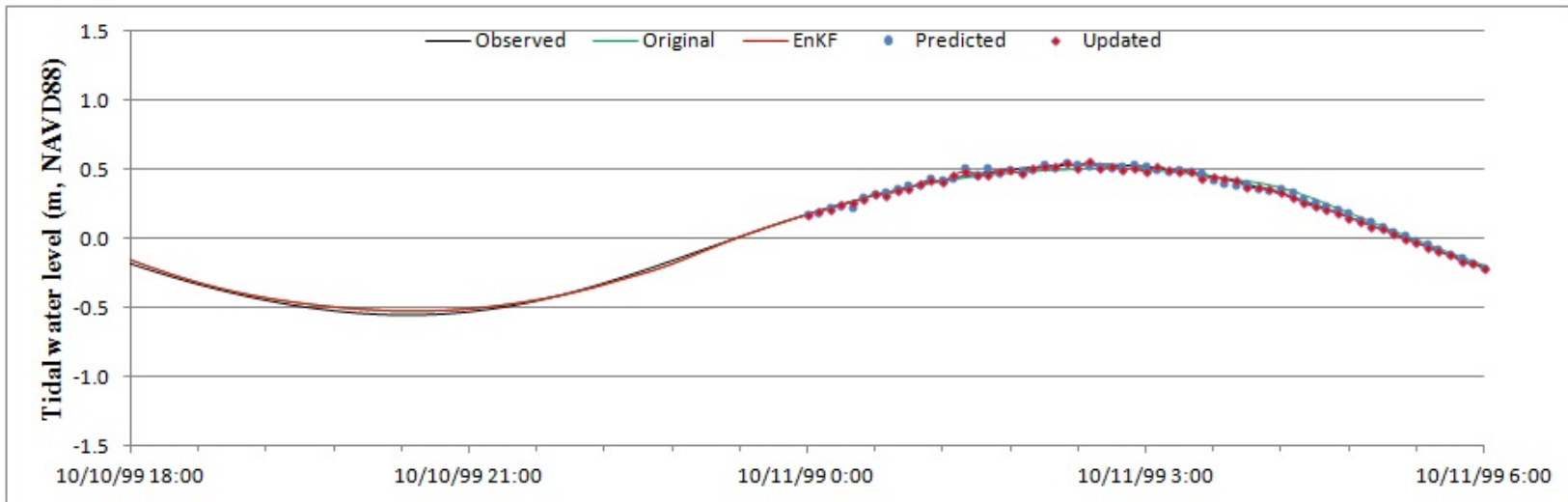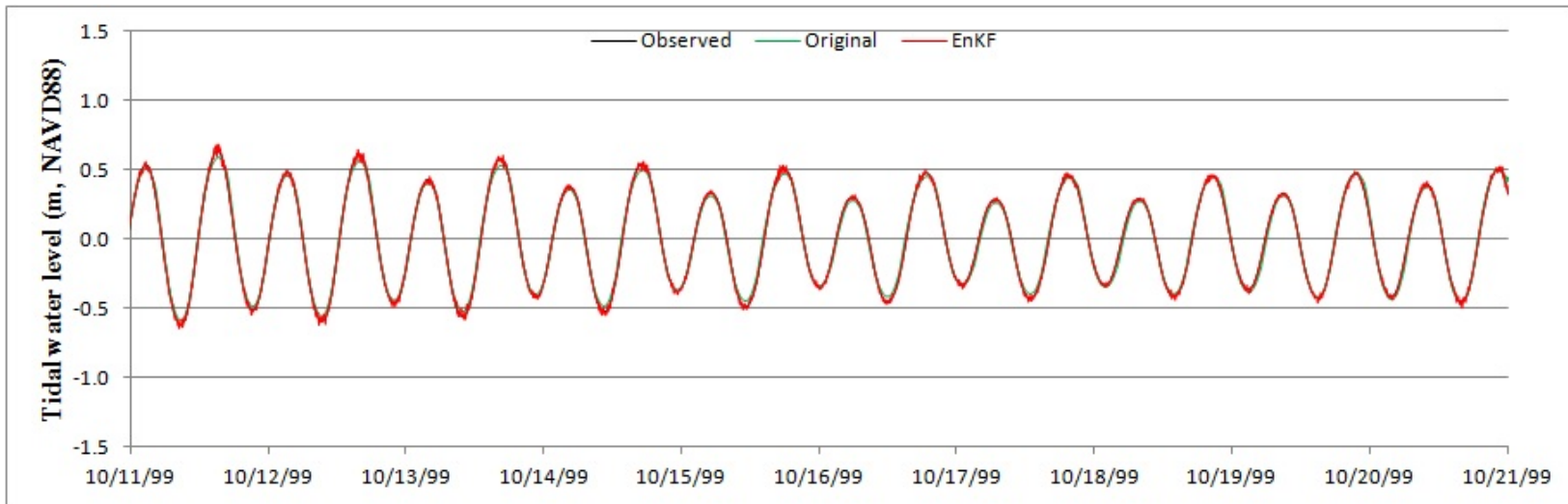
Figure 40   Time series of the tidal water level during the last 10 days (upper) and at the first day (bottom) at the target station (Fulton).
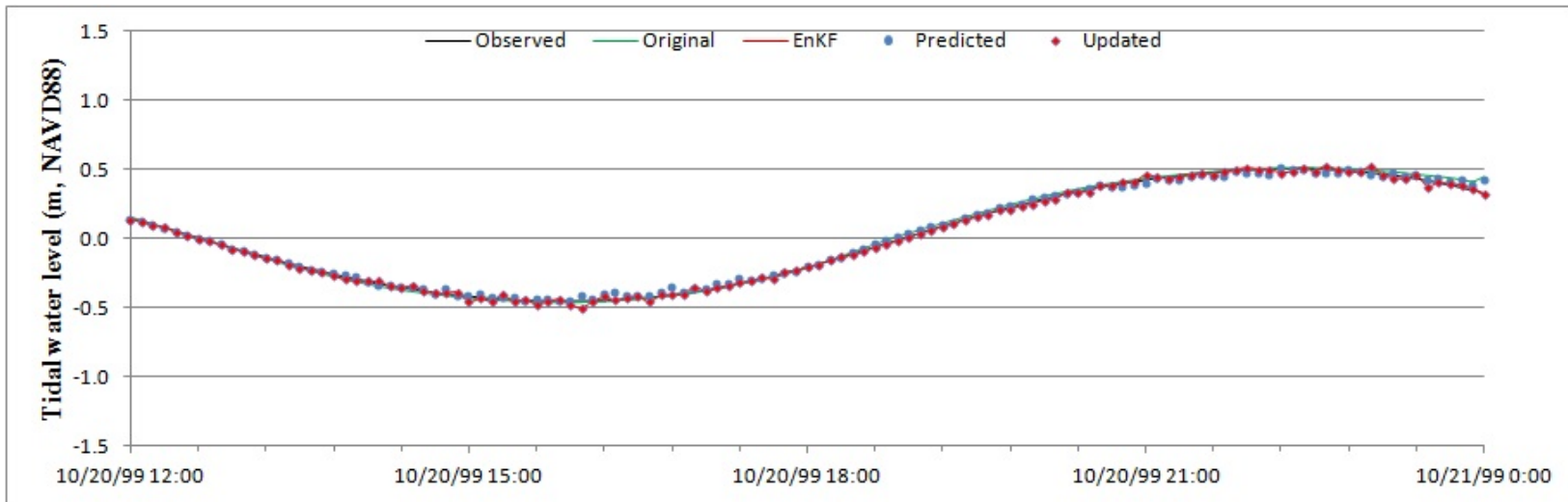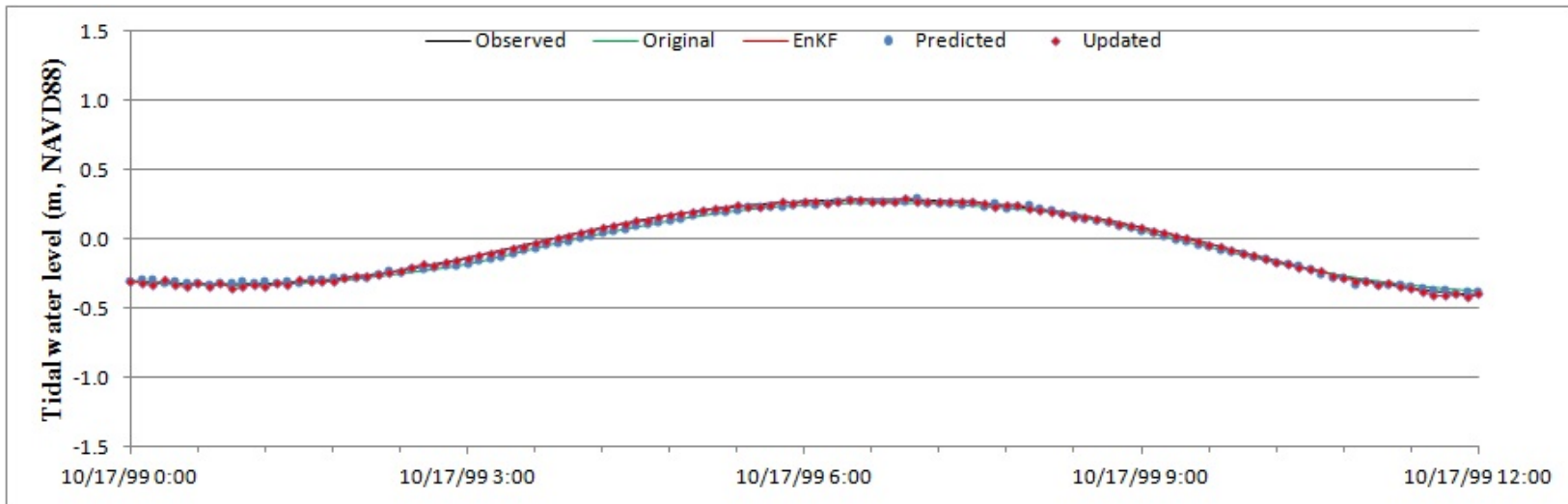
Figure 41 Time series of the tidal water level at the middle day (upper) and at the last day (bottom) at the target station (Fulton).

As shown in the figures above, the amplitudes of the original simulation results compare fairly

well with the observed tidal water level. However, the amplitudes of the original simulation

results are 0.05m smaller than the amplitudes of the observed tidal water level around high or

low tides. On the other hand, the amplitudes of the EnKF simulation results match well with the

amplitudes of the observed tidal water levels.

RMSE of the tidal water level at the target station for the original simulation and the

EnKF simulation are listed below (Table 16).

Table 16   **RMSE of the tidal water level at the target station Fulton.**

Gauge Name.	RMSE of the tidal water level		
	Original (m)	EnKF (m)	$\dfrac{RMSE_{Original} - RMSE_{EnKF}}{RMSE_{Original}}(\%)$
Fulton	2.481E-02	2.058E-02	17.06

As shown in the table above, the errors are improved by 17% at the target station using EnKF.

RMSEs of the tidal water level at the gauging stations are listed in Appendix C.
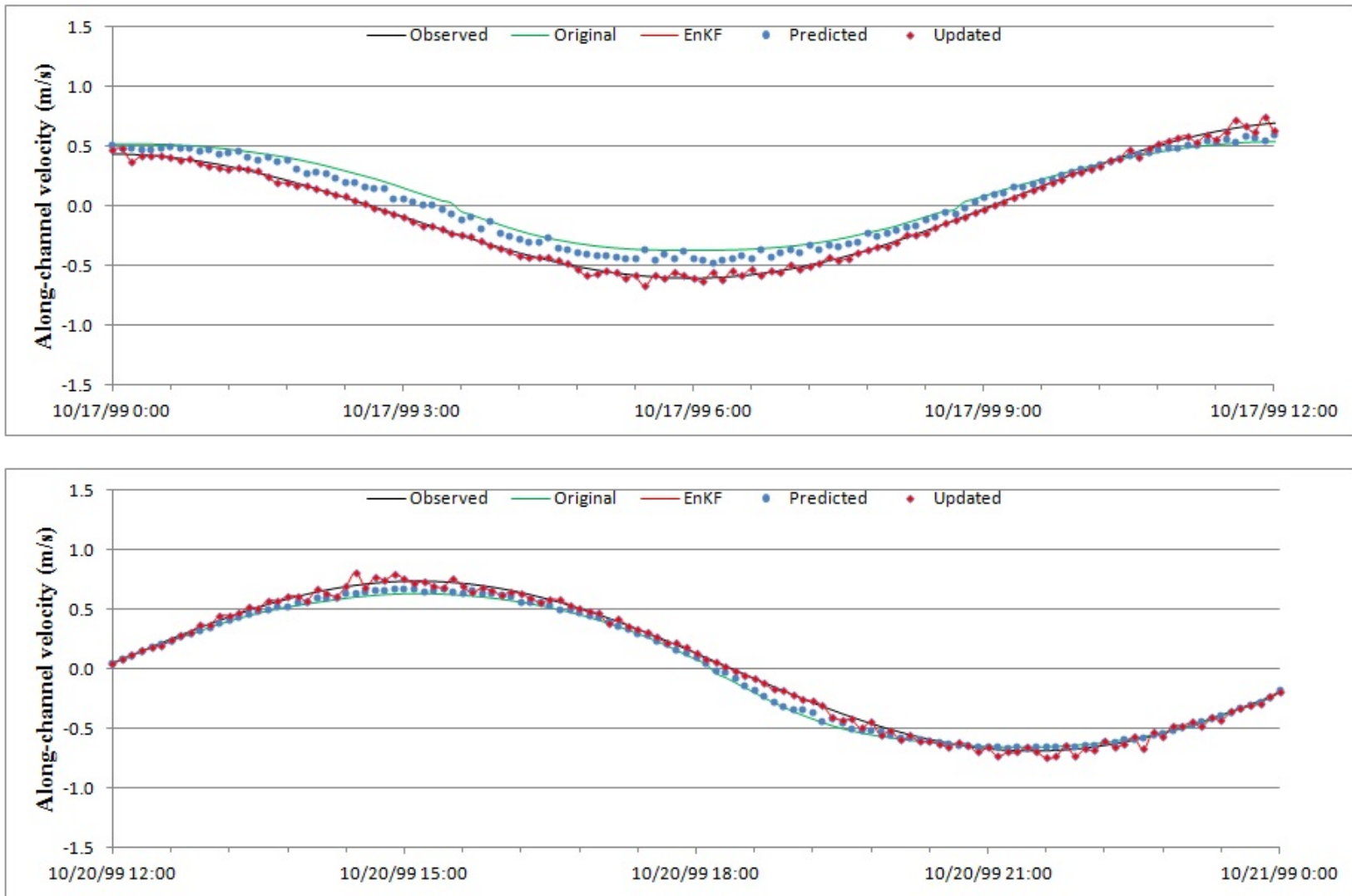
6.4.2. Along-channel velocity

    Time series of the along-channel velocity during the last 10 days at the target station are

shown in the top of Figure 42. Shown in black line is the observed along-channel velocity, in

green line is the along-channel velocity from the original DG ADCIRC simulation, and in red

line is the average of ensemble along-channel velocities from the DG ADCIRC with EnKF

simulation. Time series of the along-channel velocity for the first day are shown in the bottom of

Figure 42, for the middle day are shown in the top of Figure 43, and for the last day are shown in

the bottom of Figure 43. Shown in blue circle is the average of ensemble predicted along-

channel velocities which is taken from the EnKF simulation and in red diamond is the average of

ensemble updated along-channel velocities which is taken from the EnKF simulation.

Figure 42   Time series of the along-channel velocity during the last 10 days (upper) and at the first day (bottom) at the target station (Fulton).

90

Figure 43   Time series of the along-channel velocity at the middle day (upper) and at the last day (bottom) at the target station (Fulton).

91

As shown in the figures above, the amplitudes and phases of the original simulation results do not compare well with the observed along-channel velocity. The amplitudes and phases of the predicted along-channel velocity shown in blue circle are closer to the original simulation results. On the other hand, both amplitudes and phases of the EnKF simulation results compare well with the observed data.

RMSE of the along-channel velocity at the target station for the original simulation and the EnKF simulation are listed below (Table 17).

Table 17   **RMSE of the along-channel velocity at the target station Fulton.**

Gauge Name.	RMSE of the along-channel velocity		
	Original (m)	EnKF (m)	$\dfrac{RMSE_{Original} - RMSE_{EnKF}}{RMSE_{Original}}(\%)$
Fulton	1.346E-01	3.652E-02	72.9

As shown in the table above, the errors are improved using EnKF by 73% at the target station. RMSEs of the along-channel velocity on gauging stations are listed in Appendix C.

6.5. Simulation 3: Comparison at Dames Point

In this section, simulation results during the last 10 days (October 11th to 21st, 1999) at the target station Dames Point will be discussed. In addition, the simulation results are shown at the first day (October 10th at 18:00PM to 11th at 6:00AM, 1999), middle day (October 17th at 0:00AM to at 12:00AM, 1999), and last day (October 20th at 12AM to 21st at 0:00AM, 1999). Simulation results at the gauging stations are shown in Appendix C.

6.5.1. Tidal water level

Time series of the tidal water level during the last 10 days at the target station are shown in the top of Figure 44. Shown in black line is the observed tidal water level, in green line is the tidal water level from the original DG ADCIRC simulation, and in red line is the average of ensemble tidal water levels from the DG ADCIRC with EnKF simulation. Time series of the tidal water level for the first day are shown in the bottom of Figure 44, for the middle day are shown in the top of Figure 45, and for the last day are shown in the bottom of Figure 45. Shown in blue circle is the average of ensemble predicted tidal water levels which is taken from the EnKF simulation and in red diamond is the average of ensemble updated tidal water levels which is taken from the EnKF simulation.
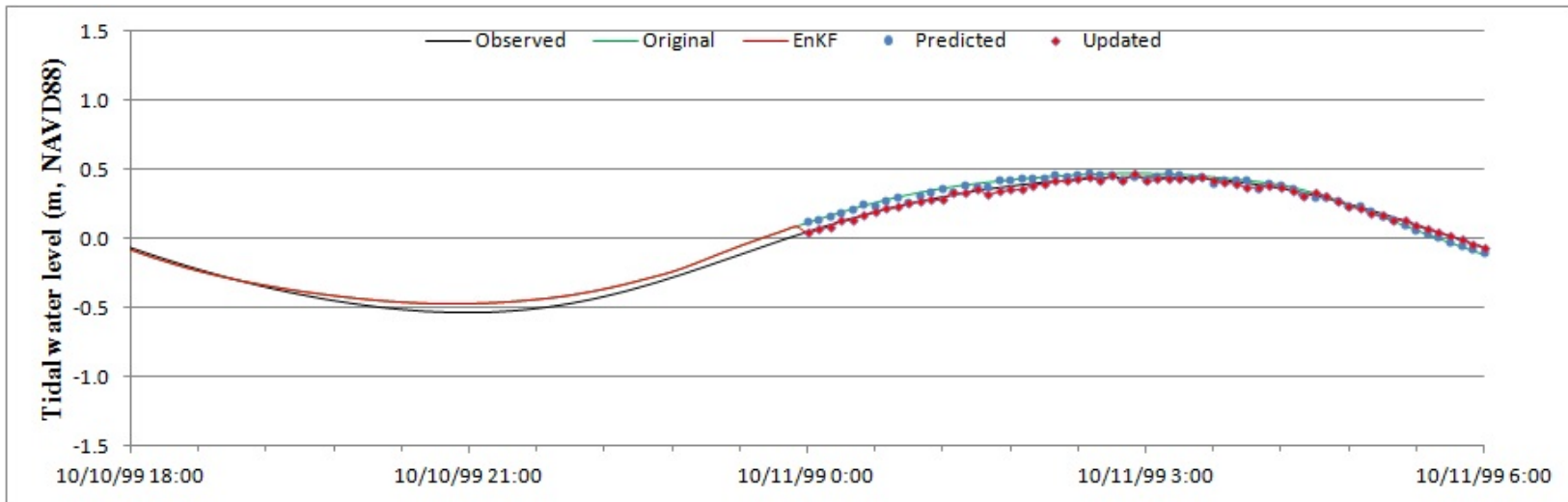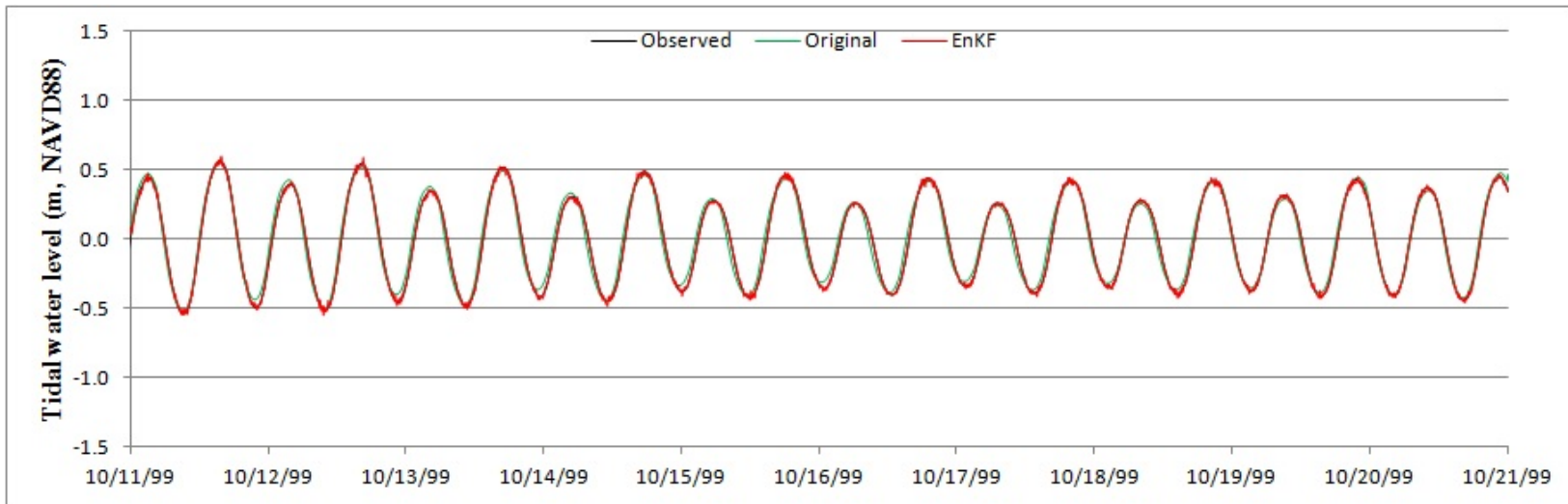
Figure 44 Time series of the tidal water level during the last 10 days (upper) and at the first day (bottom) at the target station (Dames Point).
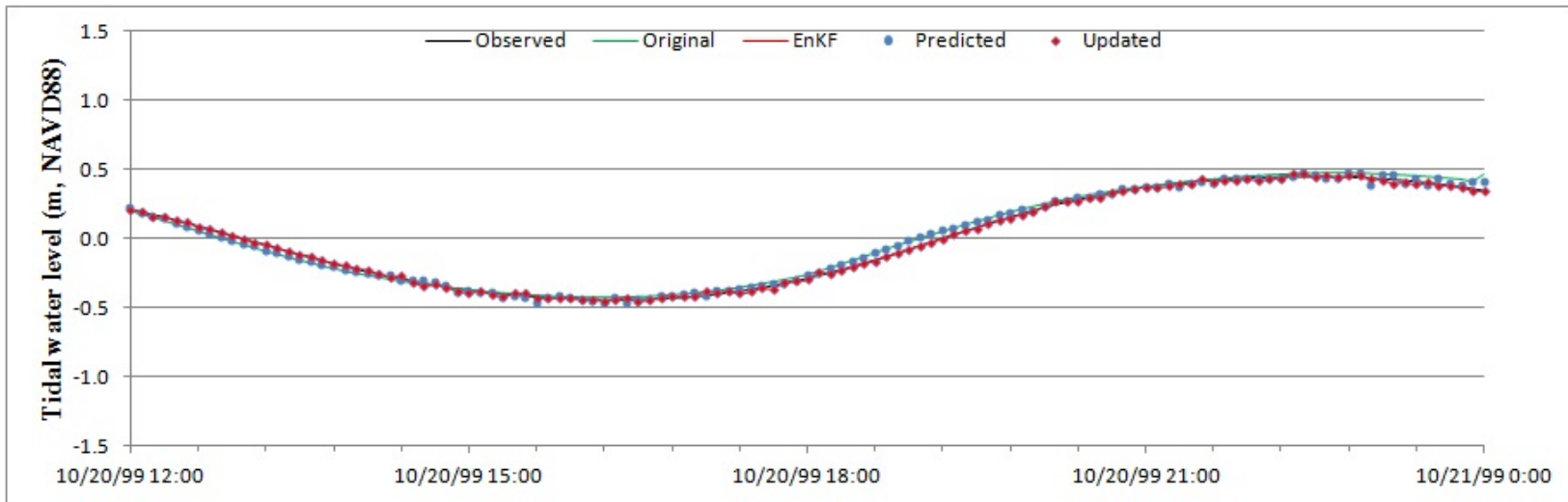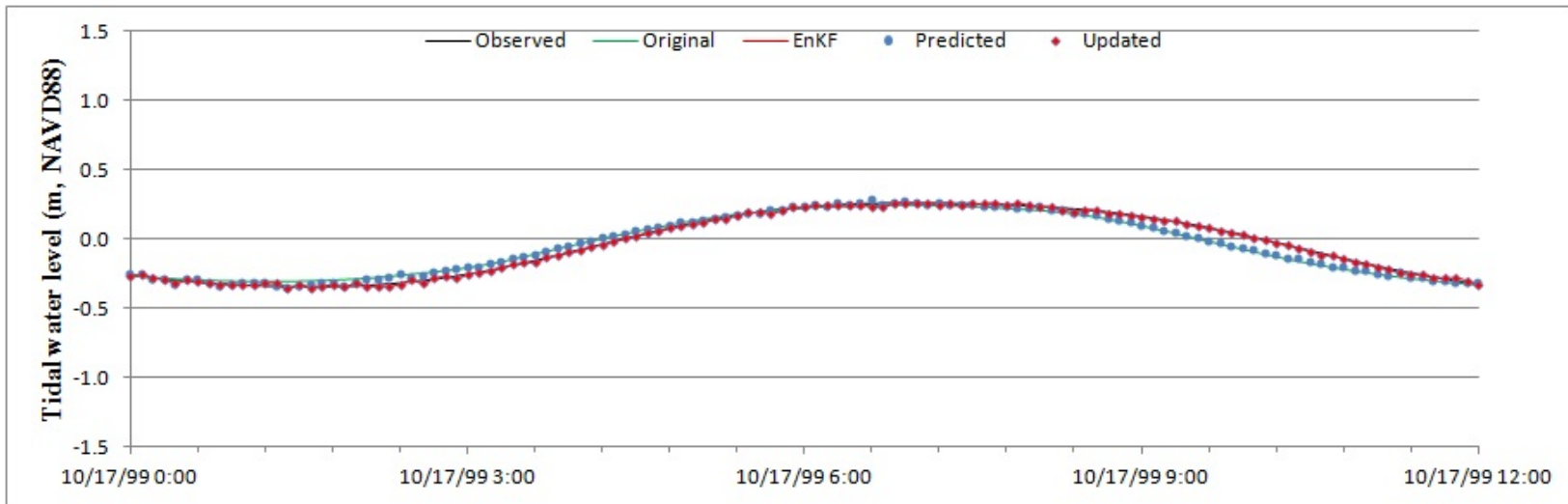
Figure 45   Time series of the tidal water level at the middle day (upper) and at the last day (bottom) at the target station (Dames Point).

95

As shown in the figures above, the amplitudes and phases of the original simulation results are different from the observed tidal water level. However, the amplitudes and phases of the EnKF simulation results match well with the observed tidal water level.

RMSE of the tidal water level at the target station for the original simulation and the EnKF simulation are listed below (Table 18).

Table 18   **RMSE of the tidal water level at the target station Dames Point.**

Gauge Name.	RMSE of the tidal water level		
	Original (m)	EnKF (m)	$\dfrac{RMSE_{Original} - RMSE_{EnKF}}{RMSE_{Original}}(\%)$
Dames Point	4.617E-02	1.933E-02	57.1

As shown in the table above, the errors are improved by 57% at the target station using EnKF. RMSEs of the tidal water level on gauging station are listed in Appendix C.

6.5.2. Along-channel velocity

Time series of the along-channel velocity during the last 10 days at the target station are shown in the top of Figure 46. Shown in black line is the observed along-channel velocity, in green line is the along-channel velocity from the original DG ADCIRC simulation, and in red line is the average of ensemble along-channel velocities from the DG ADCIRC with EnKF simulation. Time series of the along channel velocity for the first day are shown in the bottom of Figure 46, for the middle day are shown in the top of Figure 47, and for the last day are shown in the bottom of Figure 47. Shown in blue circle is the average of ensemble predicted along-channel velocities which is taken from the EnKF simulation and in red diamond is the average of ensemble updated along-channel velocities which is taken from the EnKF simulation.
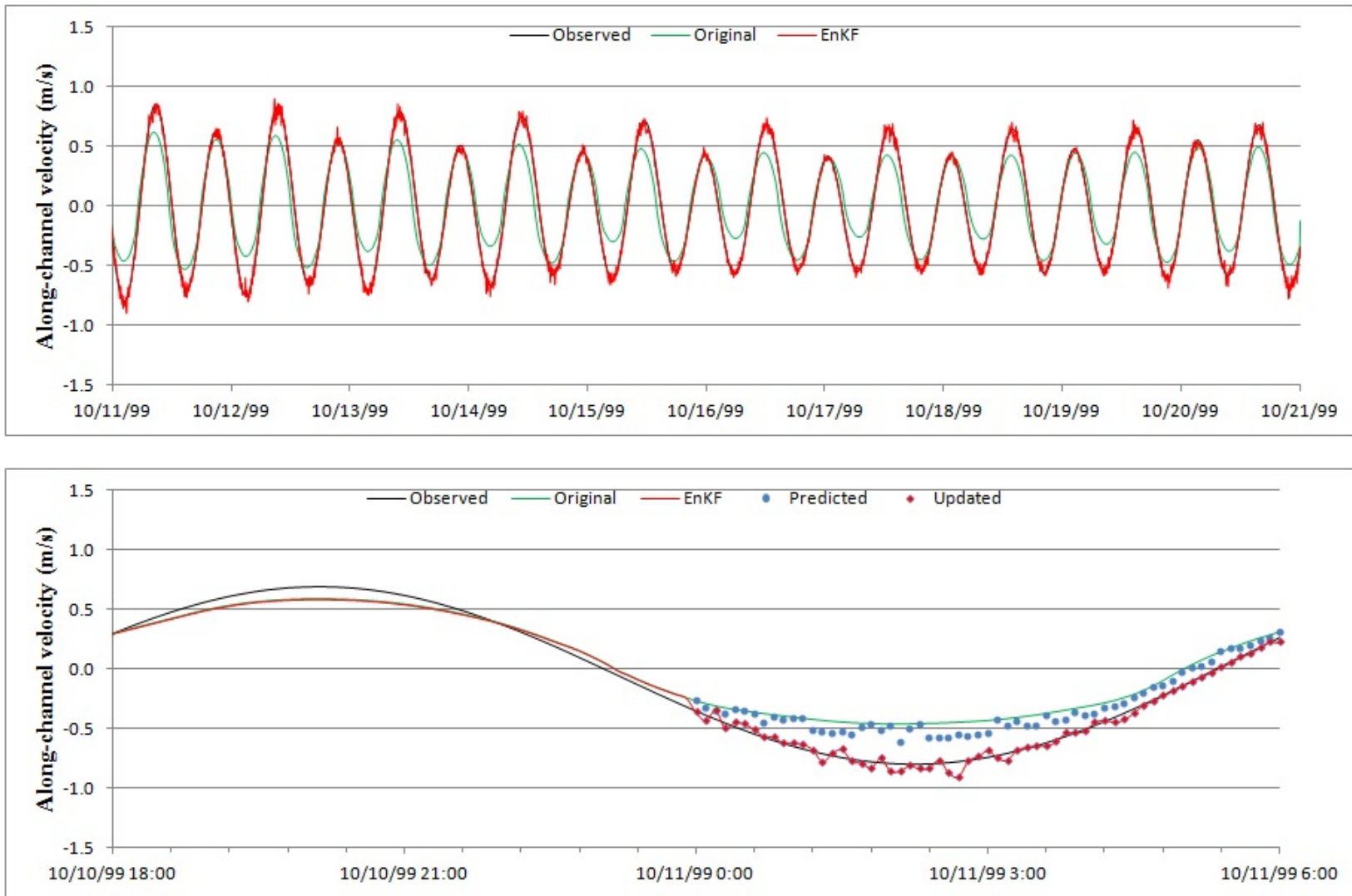
Figure 46 Time series of the along-channel velocity during the last 10 days (upper) and at the first day (bottom) at the target station (Dames Point).
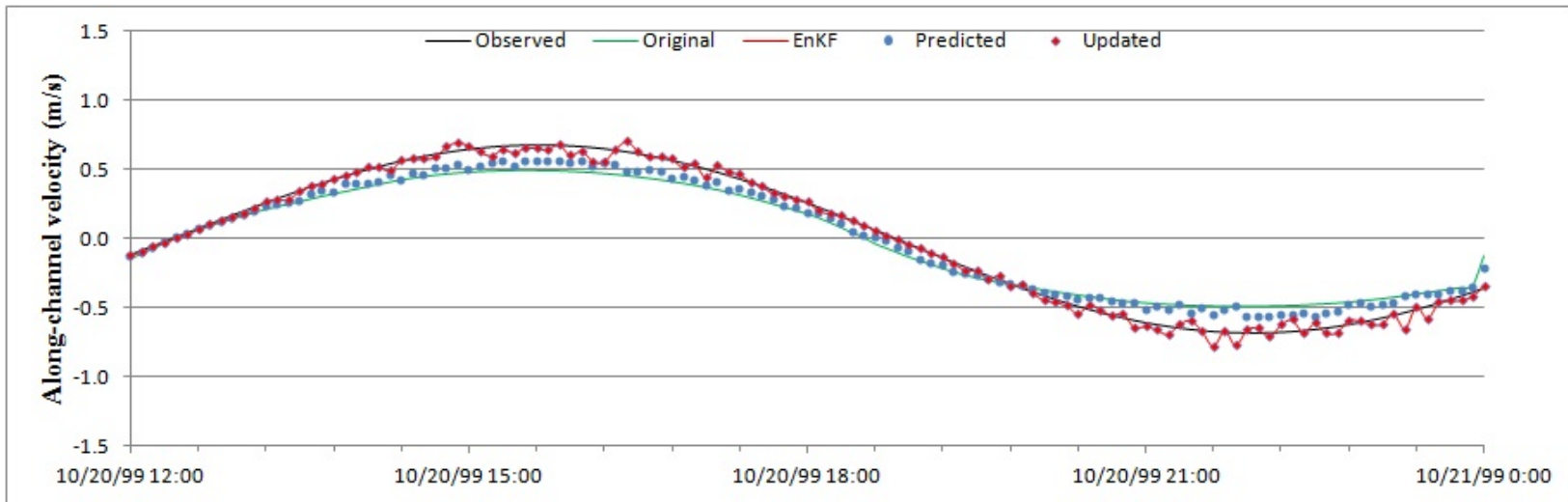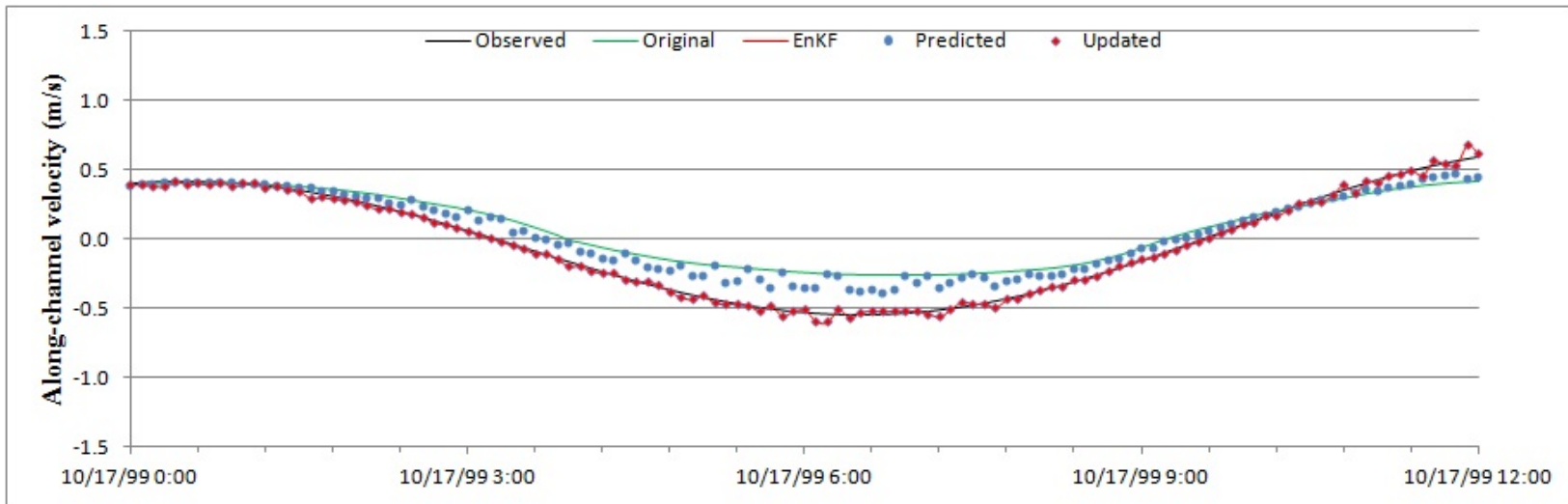
Figure 47 Time series of the along-channel velocity at the middle day (upper) and at the last day (bottom) at the target station (Dames Point).

As shown in the figures above, the amplitudes and phases of the original simulation results are different from the observed along-channel velocity. The amplitudes and phases of the predicted along-channel velocity shown in blue circle do not match well with the observed along-channel velocity. However, the amplitudes and phases of the updated along-channel velocity shown in red diamond match well with the observed along-channel velocity.

RMSE of the along-channel velocity at the target station for the original simulation and the EnKF simulation are listed below (Table 19).

Table 19   **RMSE of along-channel velocity at the target station Dames Point.**

Gauge Name.	RMSE of along-channel velocity		
	Original (m)	EnKF (m)	$\dfrac{RMSE_{Original} - RMSE_{EnKF}}{RMSE_{Original}}(\%)$
Dames Point	1.544E-01	3.519E-02	77.2

As shown in the table above, the errors are improved using EnKF by 77% at the target station. RMSEs of the along-channel velocity at the gauging stations are listed in Appendix C.

6.6. Simulation 4: Comparison at Jacksonville

In this section, simulation results during the last 10 days (October 11th to 21st, 1999) at the target station Jacksonville will be discussed. In addition, the simulation results are shown at the first day (October 10th at 18:00PM to 11th at 6:00AM, 1999), middle day (October 17th at 0:00AM to at 12:00AM, 1999), and last day (October 20th at 12AM to 21st at 0:00AM, 1999). Simulation results at the gauging stations are shown in Appendix C.

6.6.1. Tidal water level

Time series of the tidal water level during the last 10 days at the target station are shown in the top of Figure 48. Shown in black line is the observed tidal water level, in green line is the tidal water level from the original DG ADCIRC simulation, and in red line is the average of ensemble tidal water level from the DG ADCIRC with EnKF simulation. Time series of the tidal water level for the first day are shown in the bottom of Figure 48, for the middle day are shown in the top of Figure 59, and for the last day are shown in the bottom of Figure 59. Shown in blue circle is the average of ensemble predicted tidal water levels which is taken from the EnKF simulation and in red diamond is the average of ensemble updated tidal water levels which is taken from the EnKF simulation.
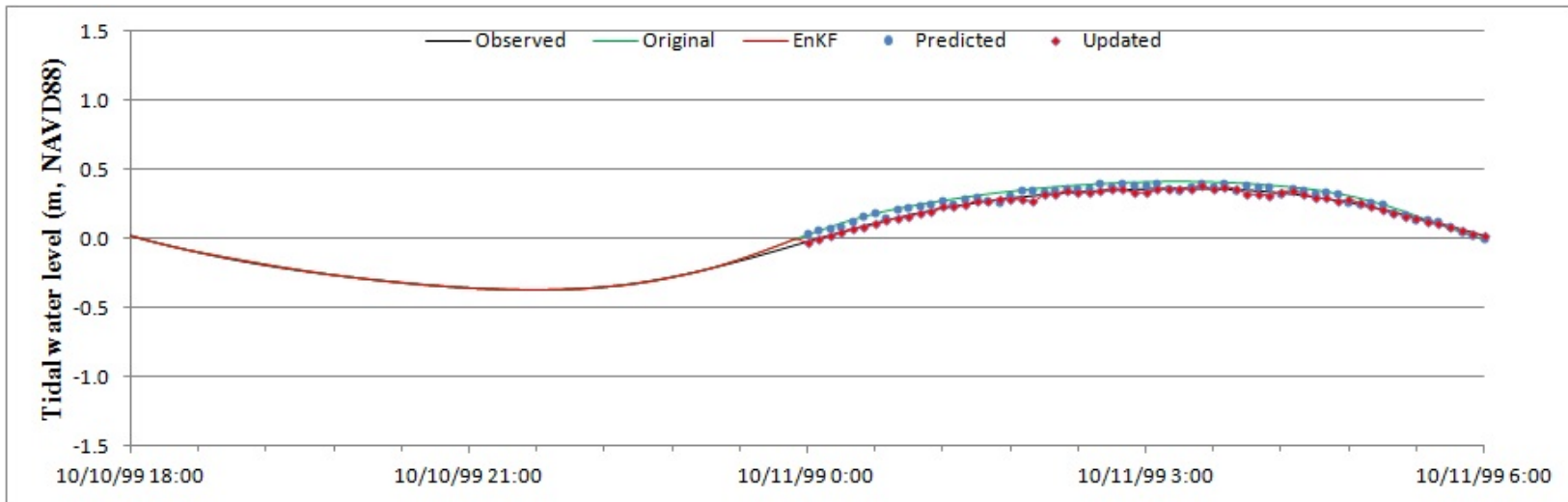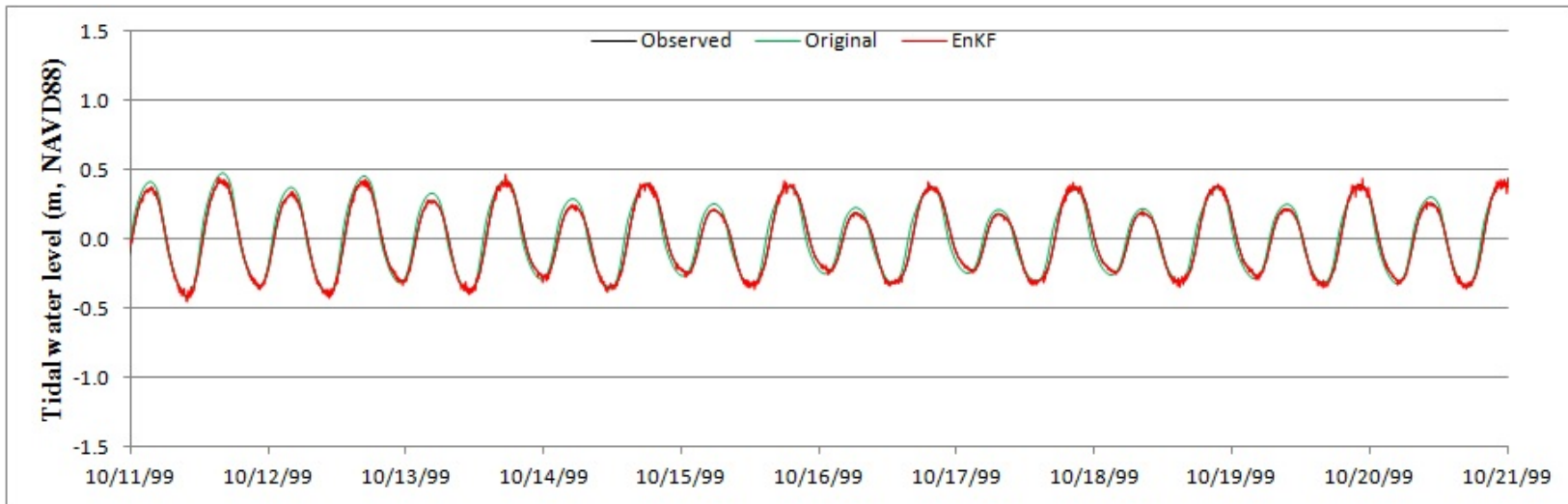
Figure 48   Time series of the tidal water level during the last 10 days (upper) and at the first day (bottom) at the target station (Jacksonville).
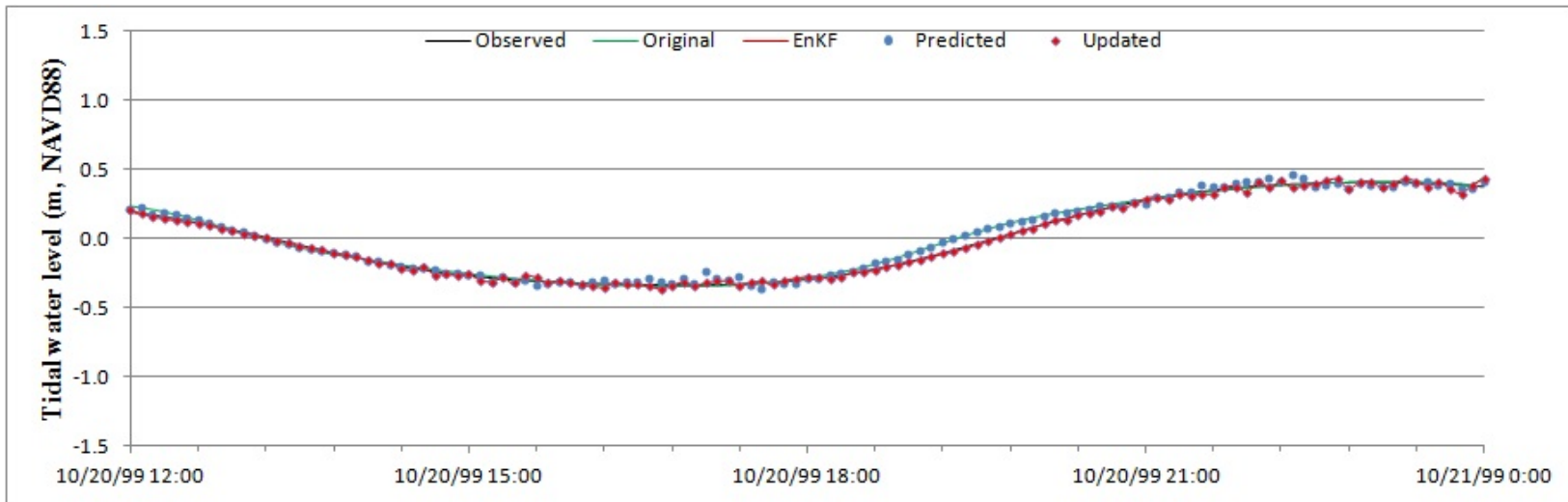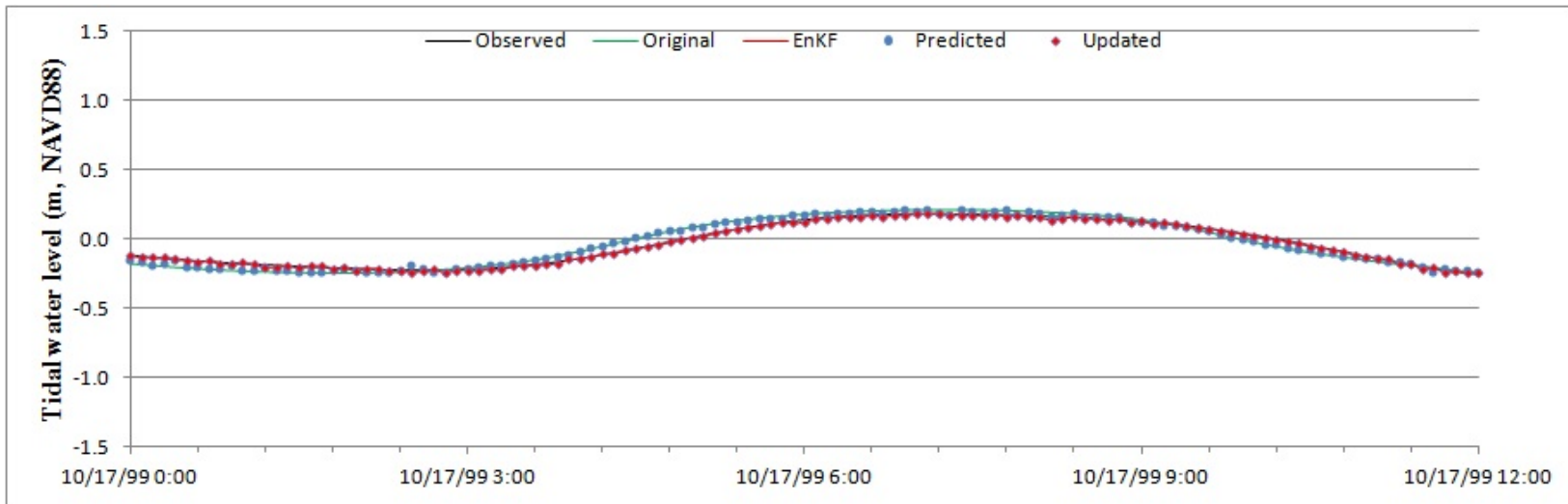
Figure 49 Time series of the tidal water level at the middle day (upper) and at the last day (bottom) at the target station (Jacksonville).

As shown in the figures above, the amplitudes and phases of the original simulation results do not match well with the observed tidal water level. On the other hand, the amplitudes and phases of the EnKF simulation results match well with the observed tidal water level.

RMSE of the tidal water level at the target station for the original simulation and the EnKF simulation are listed below (Table 20).

Table 20   **RMSE of the tidal water level at the target station Jacksonville.**

Gauge Name.	RMSE of the tidal water level		
	Original (m)	EnKF (m)	$\dfrac{RMSE_{Original} - RMSE_{EnKF}}{RMSE_{Original}}(\%)$
Jacksonville	4.695E-02	1.806E-02	61.5

As shown in the table above, the errors are improved by 62% at the target station using EnKF. RMSEs of the tidal water level at the gauging stations are listed in Appendix C.

6.6.2. Along-channel velocity

Time series of the along-channel velocity during the last 10 days at the target station are shown in the top of Figure 50. Shown in black line is the observed along-channel velocity, in green line is the along-channel velocity from the original DG ADCIRC simulation, and in red line is the average of ensemble along-channel velocities from the DG ADCIRC with EnKF simulation. Time series of the along-channel velocity for the first day are shown in the bottom of Figure 50, for the middle day are shown in the top of Figure 51, and for the last day are shown in the bottom of Figure 51. Shown in blue circle is the average of ensemble predicted along-channel velocities which is taken from EnKF simulation and in red diamond is the average of ensemble updated along-channel velocities which is taken from EnKF simulation.
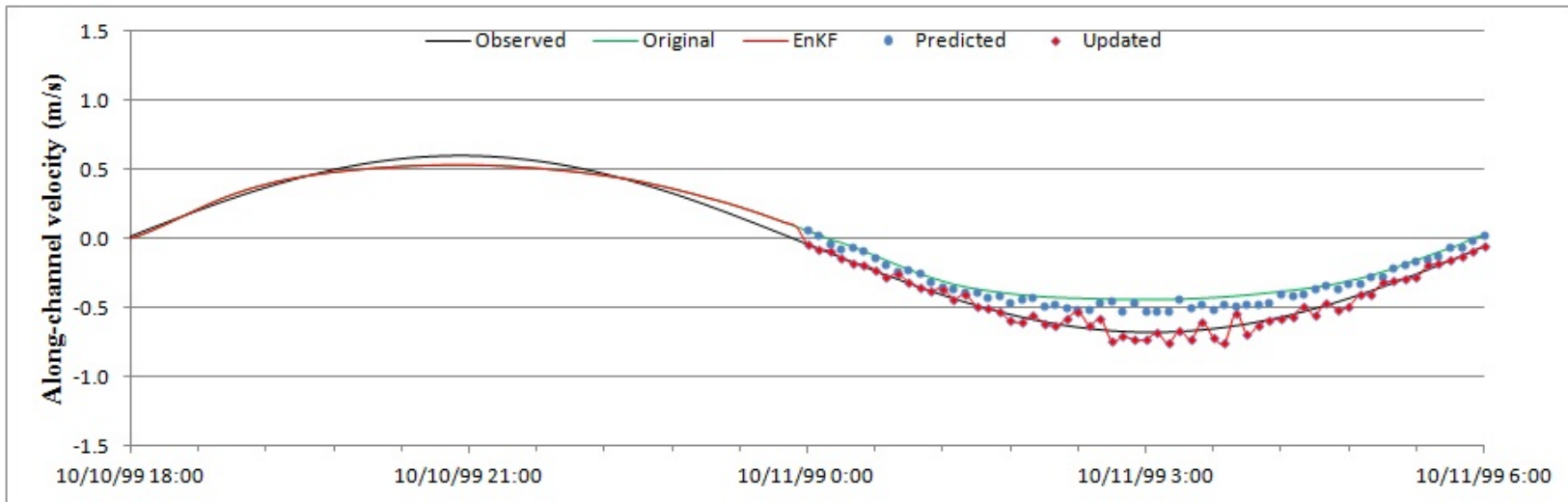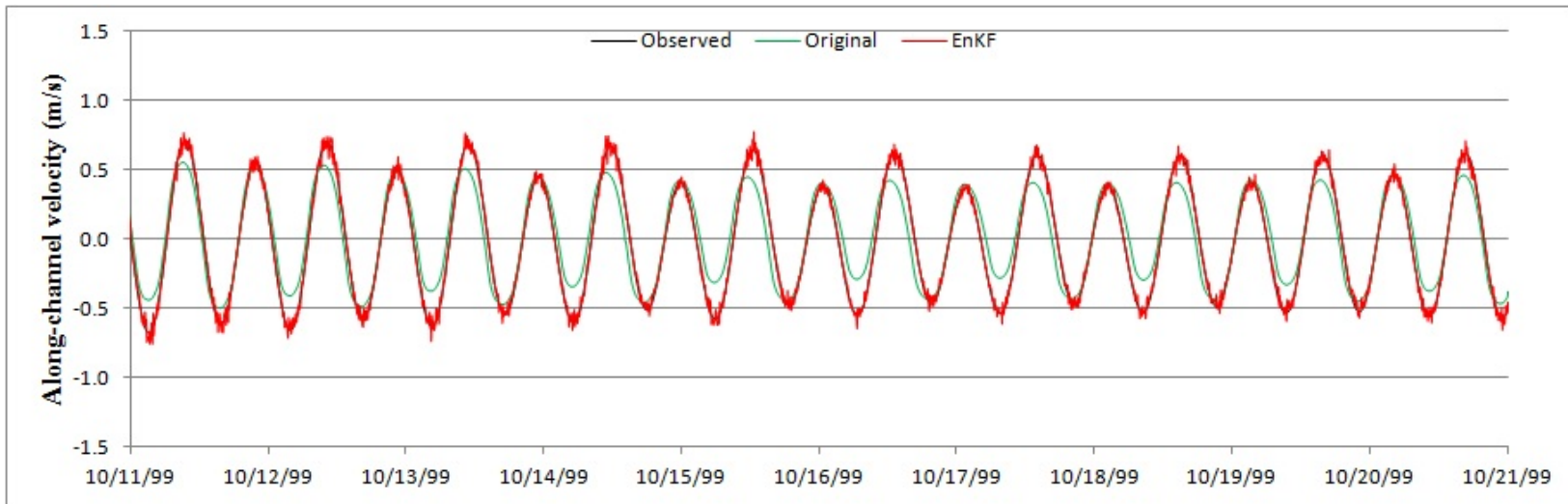
Figure 50   Time series of the along-channel velocity during the last 10 days (upper) and at the first day (bottom) at the target station (Jacksonville).
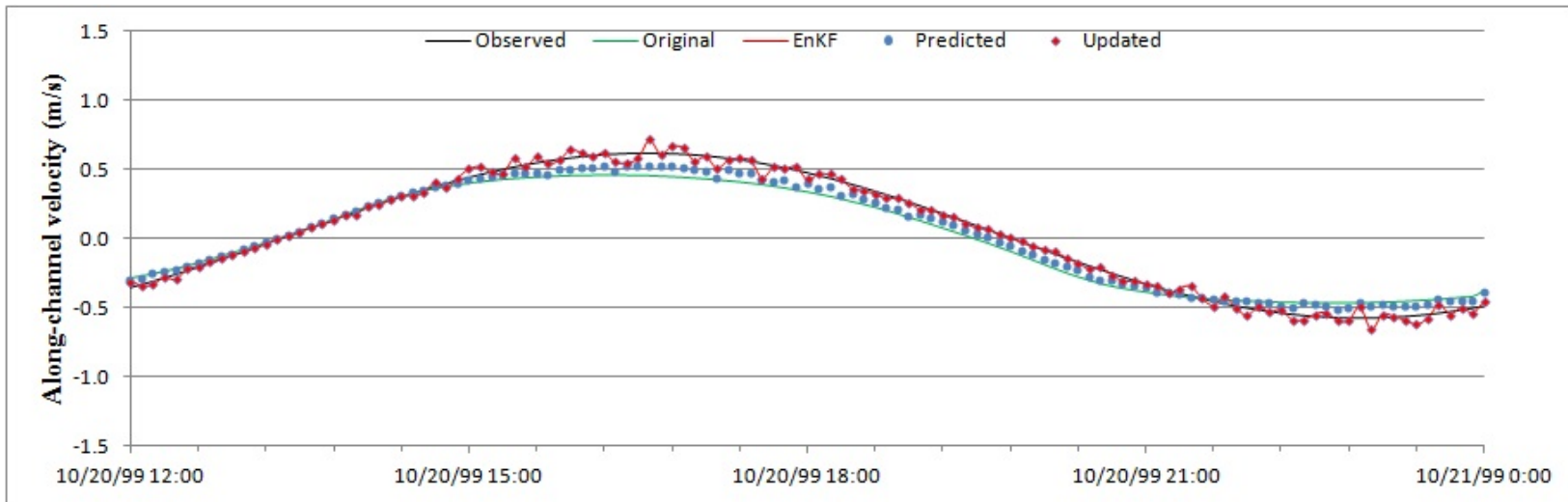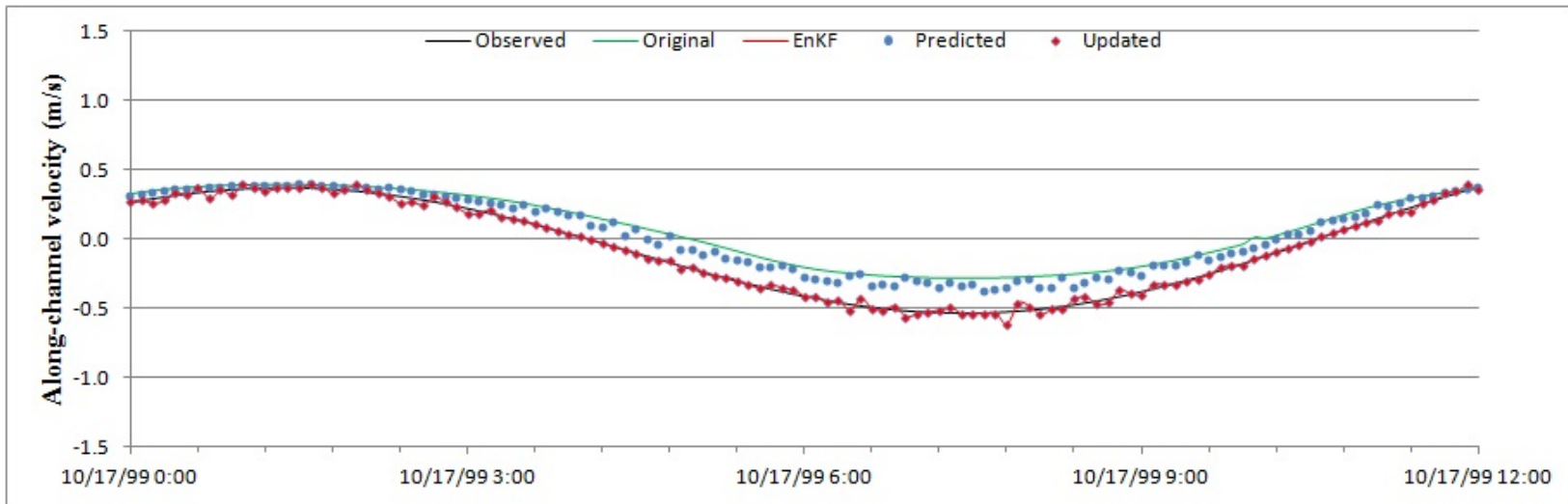
Figure 51 Time series of the along-channel velocity at the middle day (upper) and at the last day (bottom) at the target station (Jacksonville).

107

As shown in the figures above, the amplitudes and phases of the original simulation results do not compare well with the observed along-channel velocity. The amplitudes of phases of the predicted along-channel velocity shown in blue circle are closer to the original simulation results. However, both amplitudes and phases of the updated along-channel velocity compare well with the observed along-channel velocity.

RMSE of the along-channel velocity at the target station for the original simulation and the EnKF simulation are listed below (Table 21).

Table 21   **RMSE of along-channel velocity at the target station Jacksonville.**

Gauge Name.	RMSE of the along-channel velocity		
	Original (m)	EnKF (m)	$\dfrac{RMSE_{Original} - RMSE_{EnKF}}{RMSE_{Original}}(\%)$
Jacksonville	1.343E-01	3.677E-02	72.6

As shown in the table above, the errors are improved using EnKF by 73% at the target station. RMSEs of the along-channel velocity at the gauging stations are listed in Appendix C.

CHAPTER 7: CONCLUSION

This thesis presents Ensemble Kalman Filter (EnKF), a sequential data assimilation method for non-linear problems, coupled with an ADvanced CIRCulation (ADCIRC) model for estimation of state variables (water surface elevations and depth-integrated velocities) in the Lower St. Johns River. EnKF is used to improve state estimation through the incorporation of observation data into ADCIRC. EnKF is incorporated into DG ADCIRC-2DDI for estimating state variables. For the development, the numerical codes of DG ADCIRC-2DDI are modified.

First, the development was validated by applying DG ADCIRC-2DDI with EnKF to an idealized model with synthetic observation data at six gauging stations. The quarter annular harbor mesh was used as the idealized model. The simulation run 30-day time period, and EnKF was applied during last 10 days. The errors were improved by 76% for WSE at all gauging stations using EnKF. Similarly, the errors were improved by 55% for UU and 57% for VV at all gauging stations using EnKF. Also, the errors were improved by 87% for WSE, 62% for UU, and 61% for VV at a non-gauging station using EnKF.

The developed model was further applied to the St. Johns River as a real case. Observation data of tides and tidal currents were assembled from four NOAA gauging stations located in the Lower St. Johns River. In the real model estimations, observation data at three stations, called gauging stations, were used for EnKF, and observation data at the one station, called a target station, was compared to simulation results. Thus, four different experiments using DG ADCIRC-2DDI with EnKF were performed. In each experiment, the errors were

improved by 43% for the tidal water levels at the target stations using EnKF. Also, the errors were improved by 76% for the along-channel velocities at the target stations using EnKF.

Thus, DG ADCIRC-2DDI with EnKF worked effectively for estimations of state variables on the gauging stations as well as non-gauging stations. DG ADCIRC-2DDI with EnKF adds to the modeling community a practical tool to use for nowcasting and forecasting of hydrodynamics in real systems as well as a scientific tool to learn more about the hydrodynamics process, both the modeling and observation of, in real systems. Future work of the thesis is to show model sensitivities for the estimation model for the Lower St. Johns River. One is to perform the performance vs. computational cost, i.e. changing ensemble size and increasing model error. The model estimation might be improved with large ensemble size, but the computational time is excessive. Additional sensitivity is the design of observation networks, i.e. the total number of observation stations for EnKF and the frequency of observation data. Model sensitivity will also be examined with respect to how Manning's n is parameterized over the domain.

APPENDIX A: DG ADCIRC WITH EnKF

ADCIRC.F

ADCIRC.F is a main program in DG ADCIRC codes. The main tasks for the program
are to setup model parameter and initial variables, read input files, and call timestep iteration. In
the EnKF program, generate initial ensemble variables and ensemble parameters.

READ_INPUT.F

READ_INPUT.F, called in ADCIRC.F, is a subroutine in DG ADCIRC codes. The main
tasks for the subroutine are to read input files (e.g. fort.13, fort.14, fort.15, and fort.dg etc.). In
the EnKF program, new input files are read. The EnKF general information is read from
INPUT.TEXT (e.g. ensemble size, first iteration that EnKF is applied, observation nodes, and
observation error coefficients etc.). Also, observation data are read at gauging stations from
ZE_OBS.TEXT, UU_OBS.TEXT, and VV_OBS.TEXT.

DG_TIMESTEP.F

DG_TIMESTEP.F, called in ADCIRC.F, is a subroutine in DG ADCIRC codes. The
main tasks for the subroutine are to call simulation subroutines (DG_HYDRO_TIMESTEP.F and
DG_SED_TIMESTEP.F). In the EnKF program, main EnKF calculations are performed in the
subroutine. EnKF is applied when observation data are available. In the other iteration step,
original DG ADCIRC is run. For the EnKF iteration step, original DG ADCIRC is run as a
prediction step. Then, a global communication is used to collect results of the prediction step at
gauging station for each processer. After the global communication, the cross covariance, the

112

output error covariance, and the Kalman gain are calculated. Then, all variables are updated

using the Kalman gain, the observation data, and the predicted states.

APPENDIX B: IDEALIZED MODELS
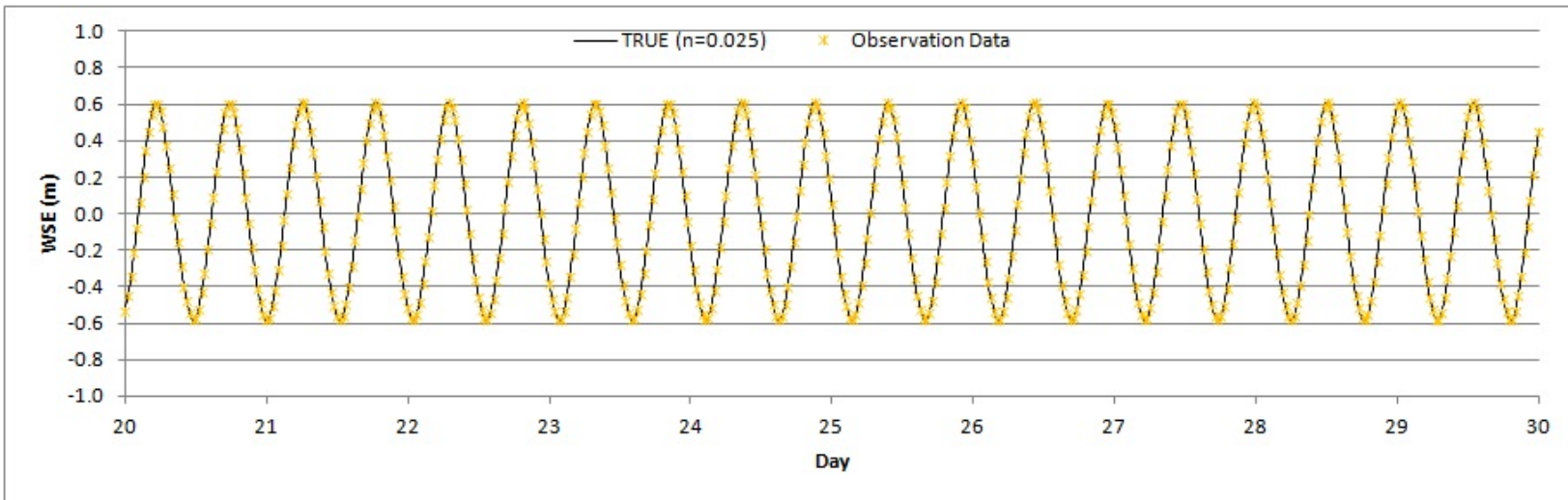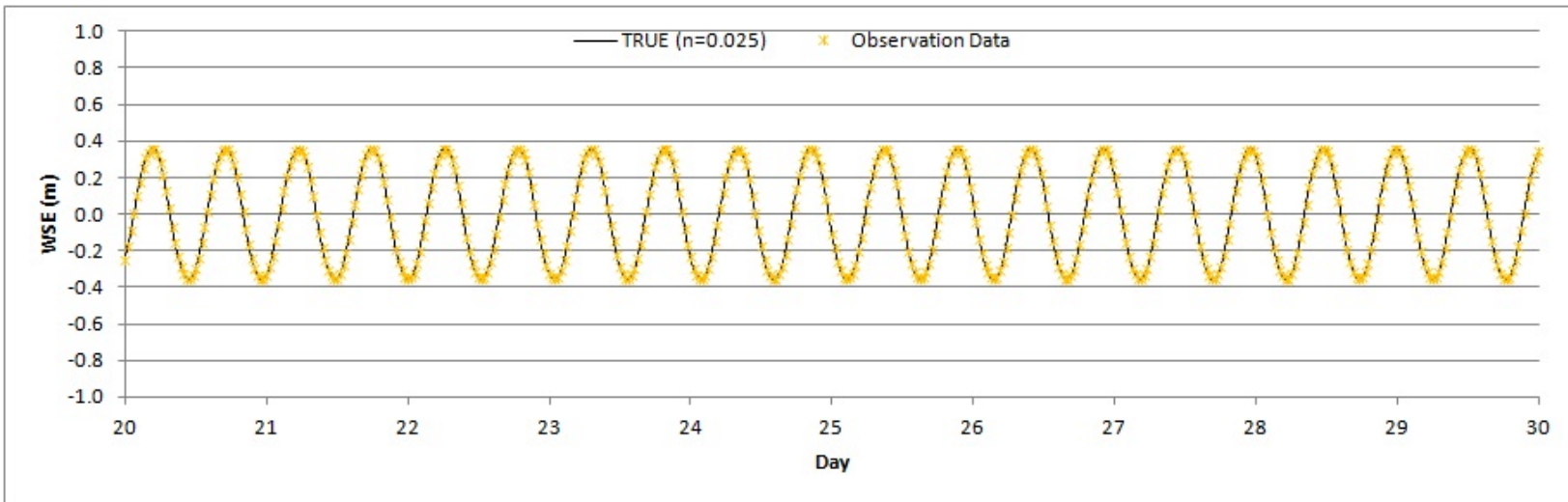
Figure 52   **Observation data for WSE at gauge b (upper) and gauge c (bottom).**
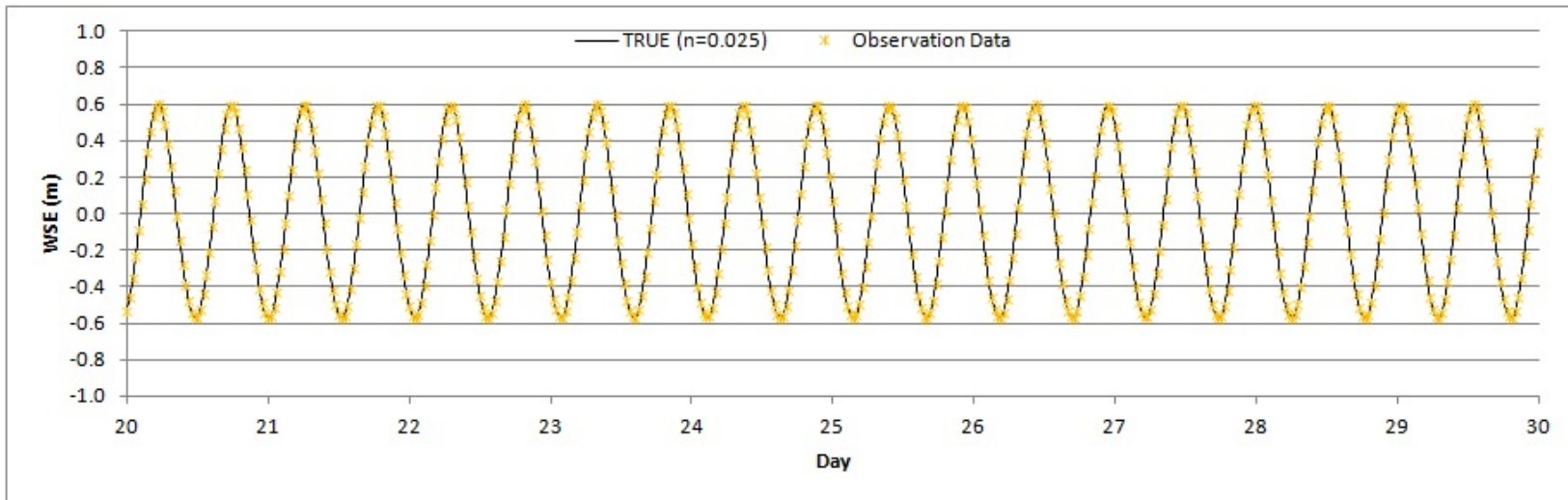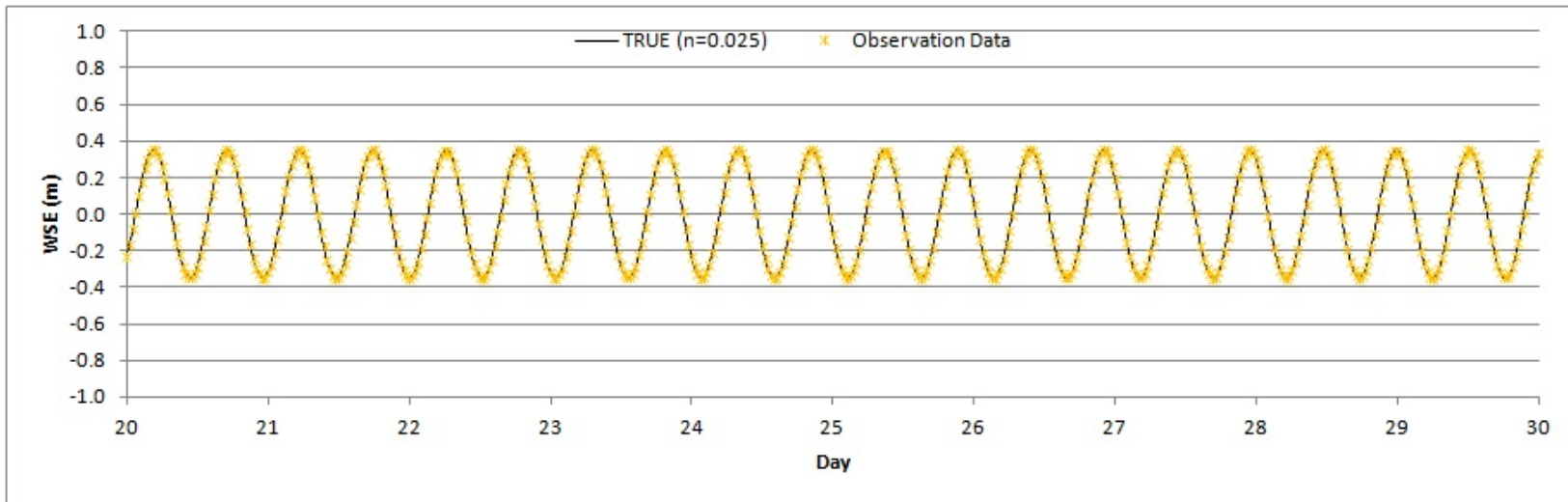
Figure 53   Observation data for WSE at gauge d (upper) and gauge e (bottom).

116
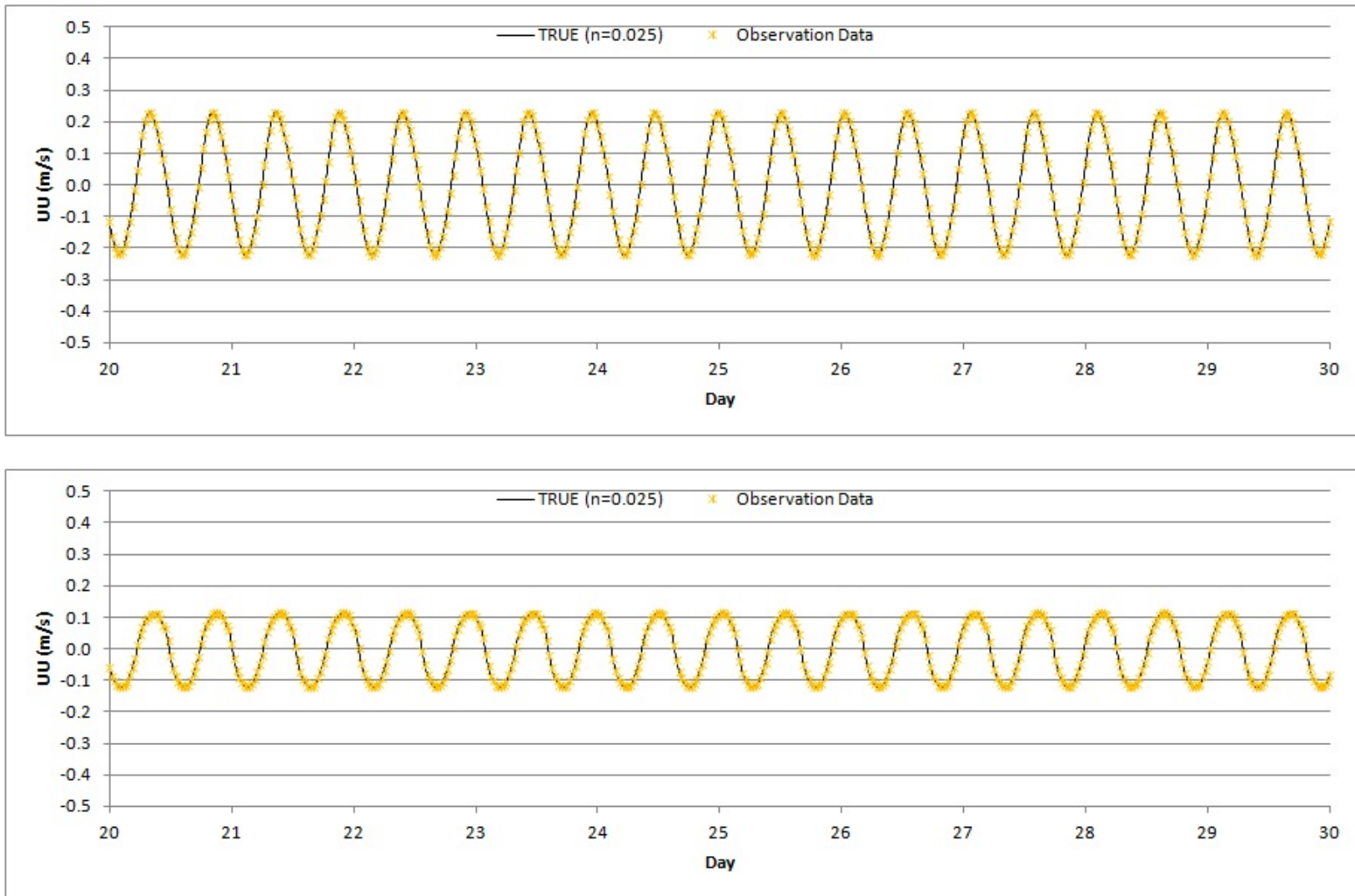
Figure 54   Observation data for UU at gauge b (upper) and gauge c (bottom).

117
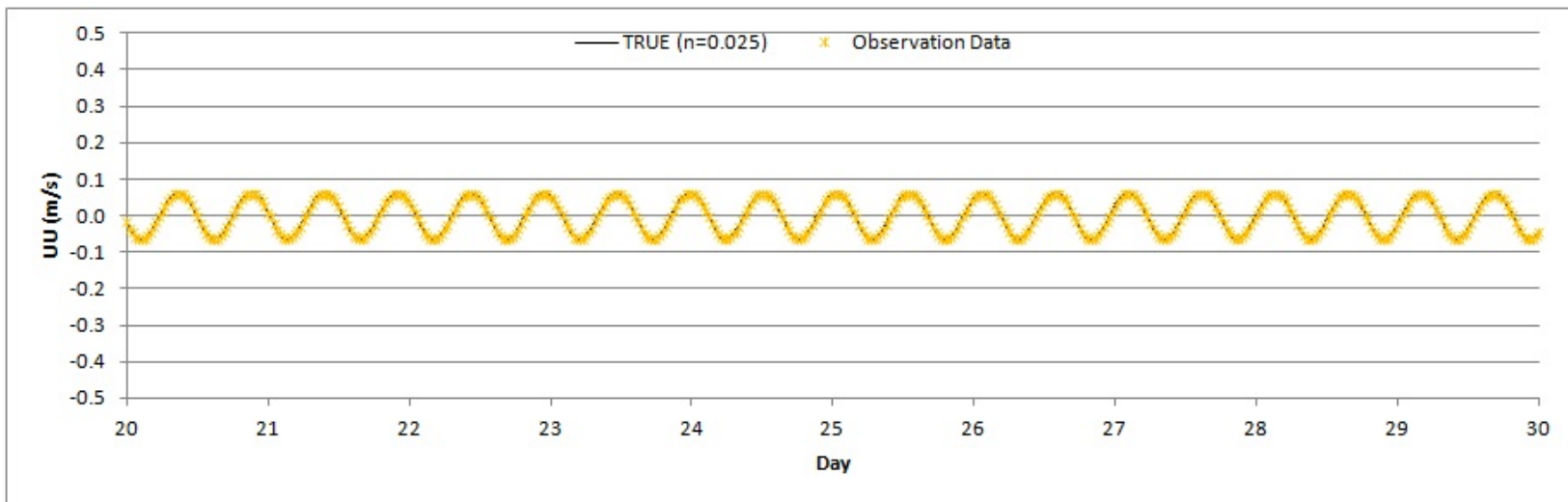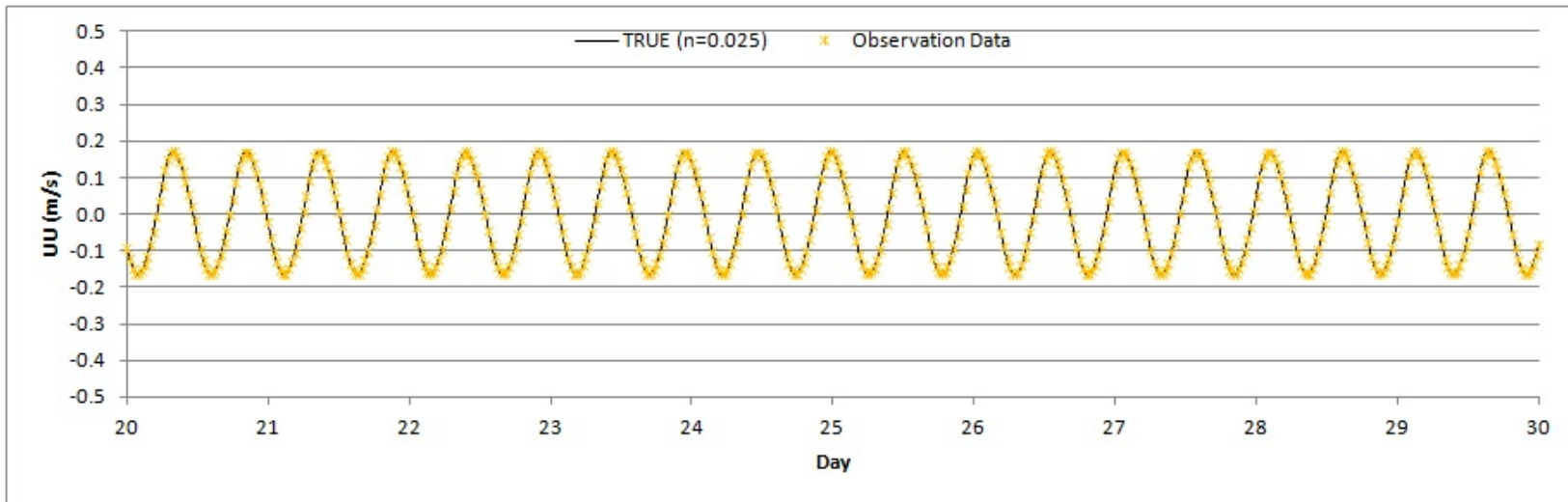
Figure 55   Observation data for UU at gauge d (upper) and gauge e (bottom).

118
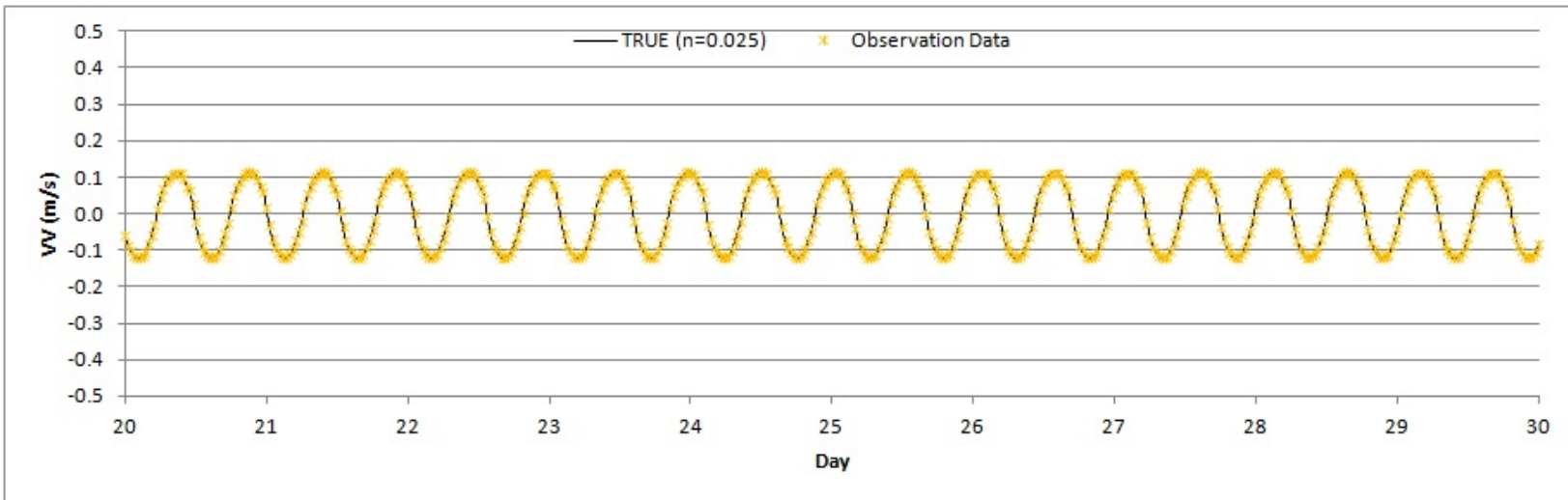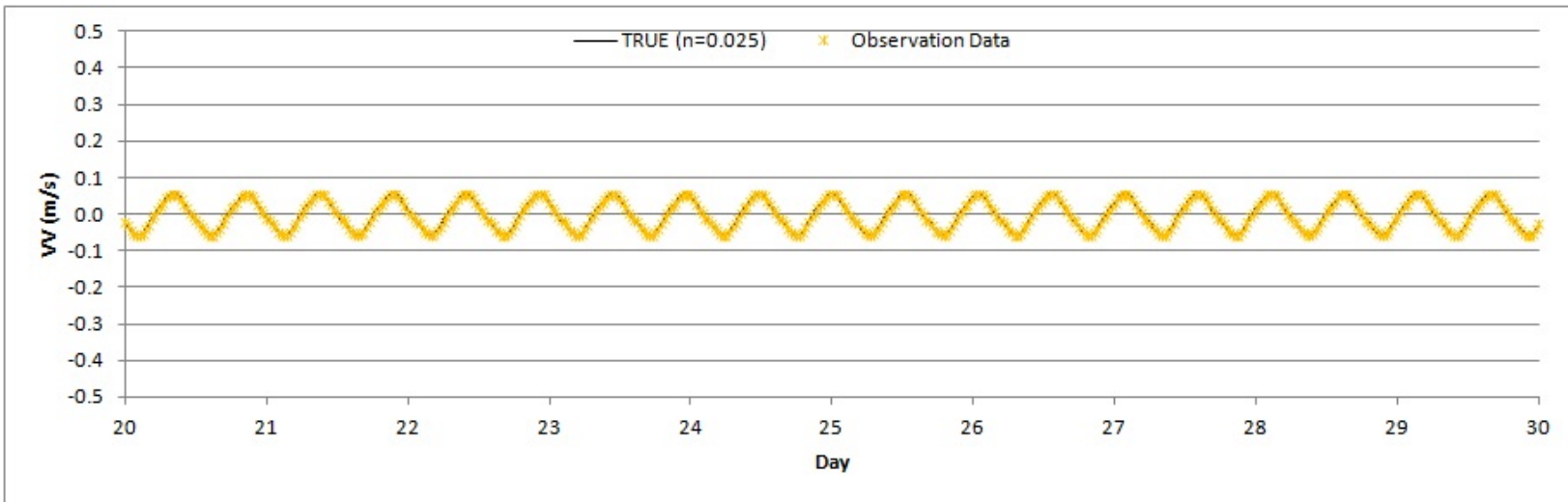
Figure 56 **Observation data for VV at gauge b (upper) and gauge c (bottom).**

119
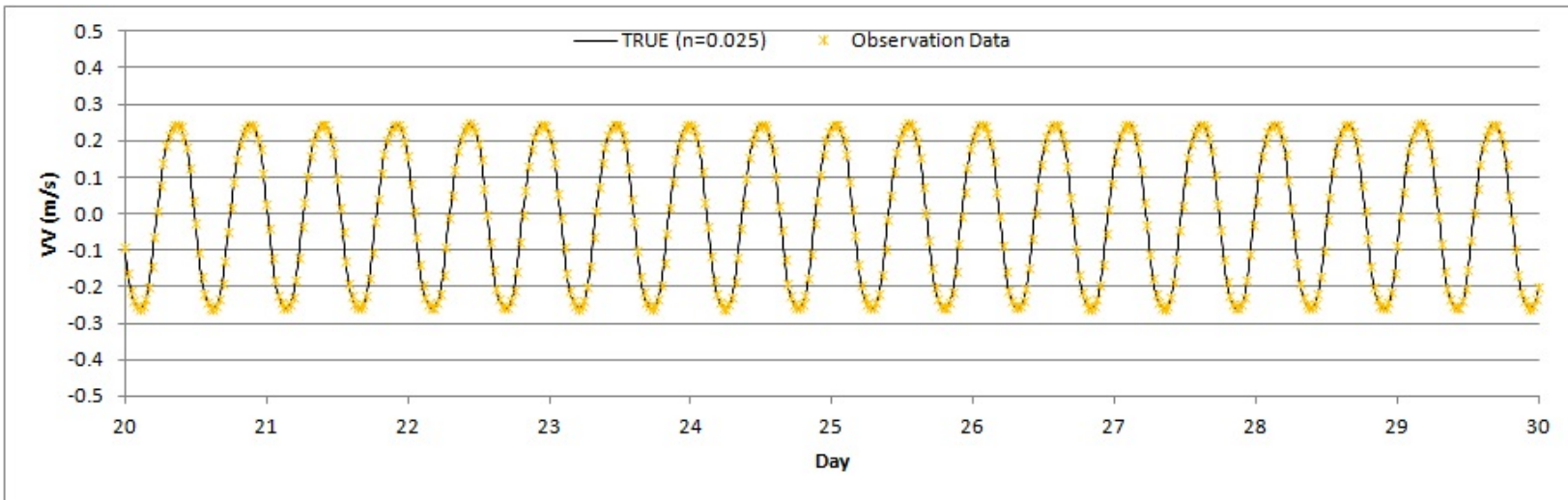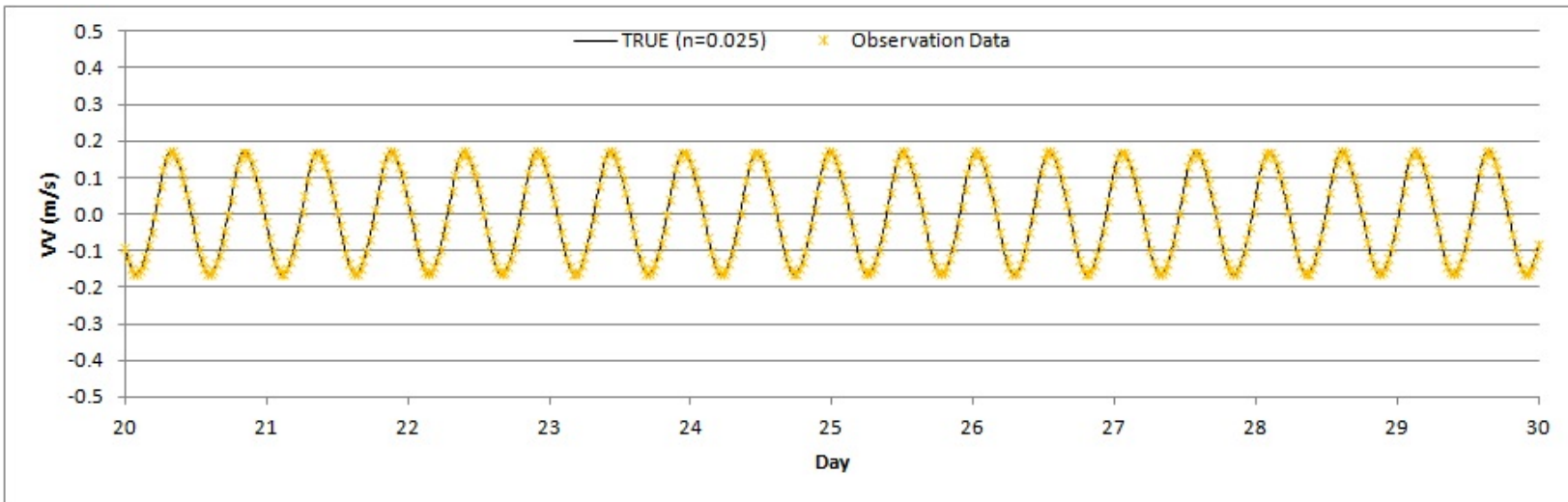
Figure 57   Observation data for VV at gauge d (upper) and gauge e (bottom).

120
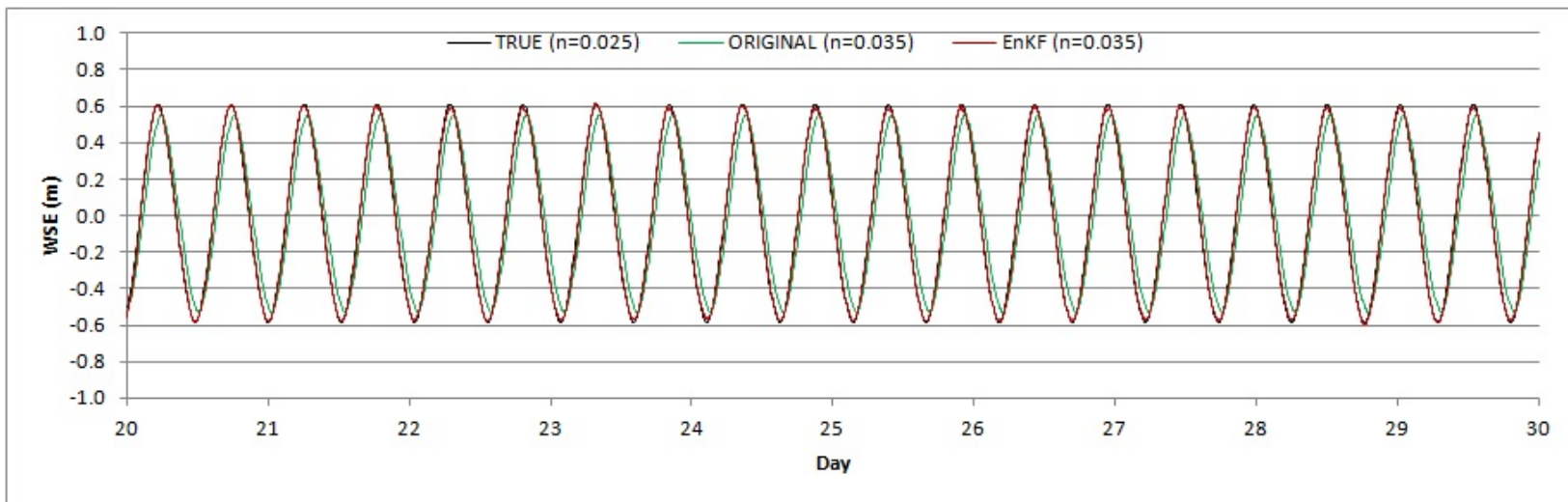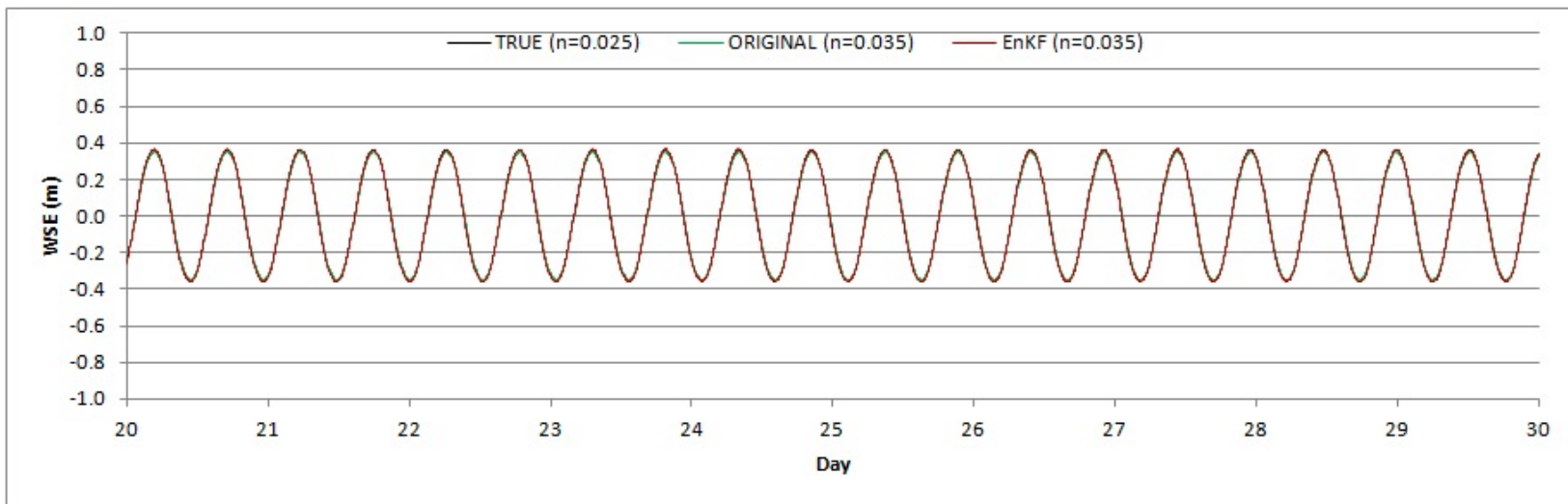
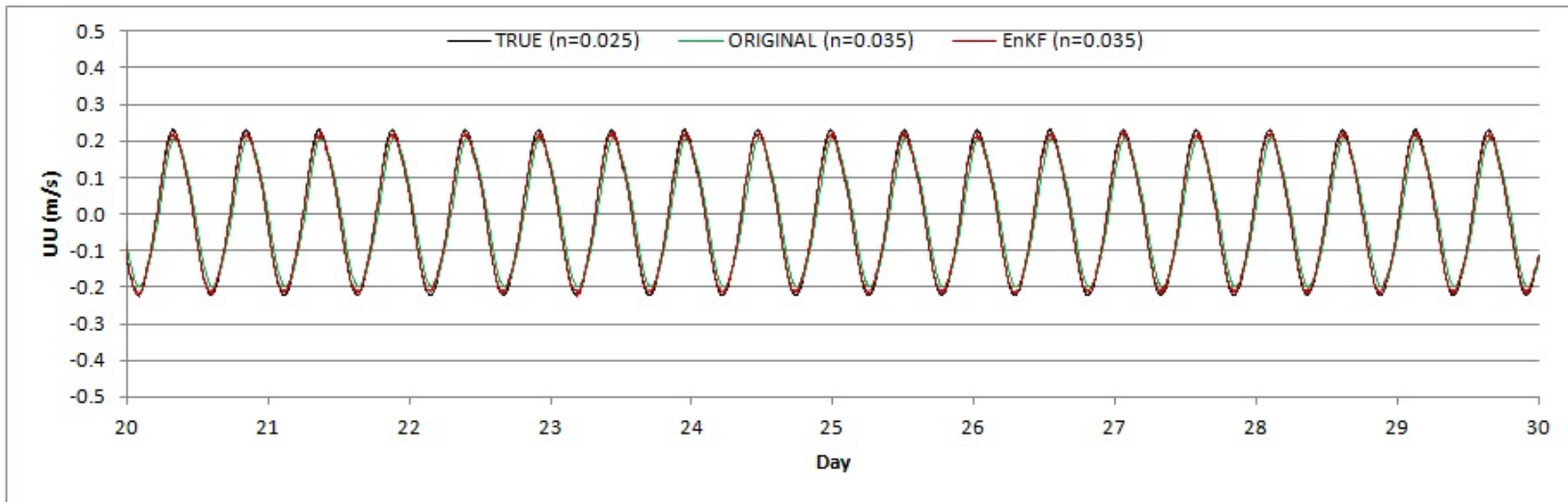**Figure 58** **Time series of WSE at gauge b (upper) and gauge c (bottom) during last 10 days.**
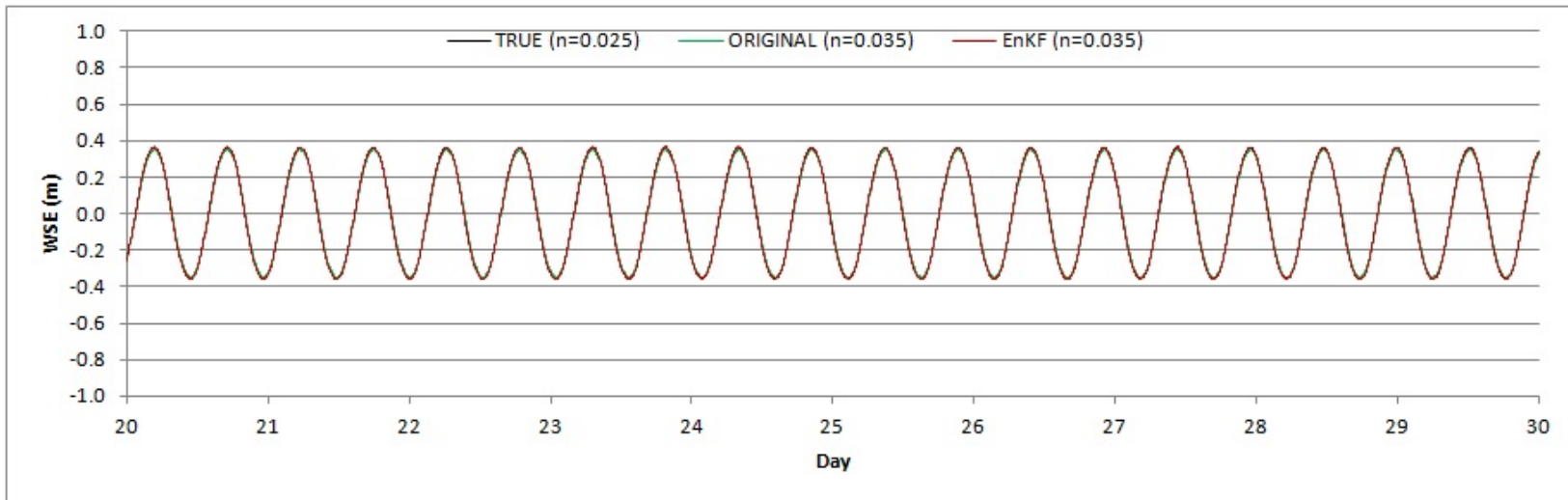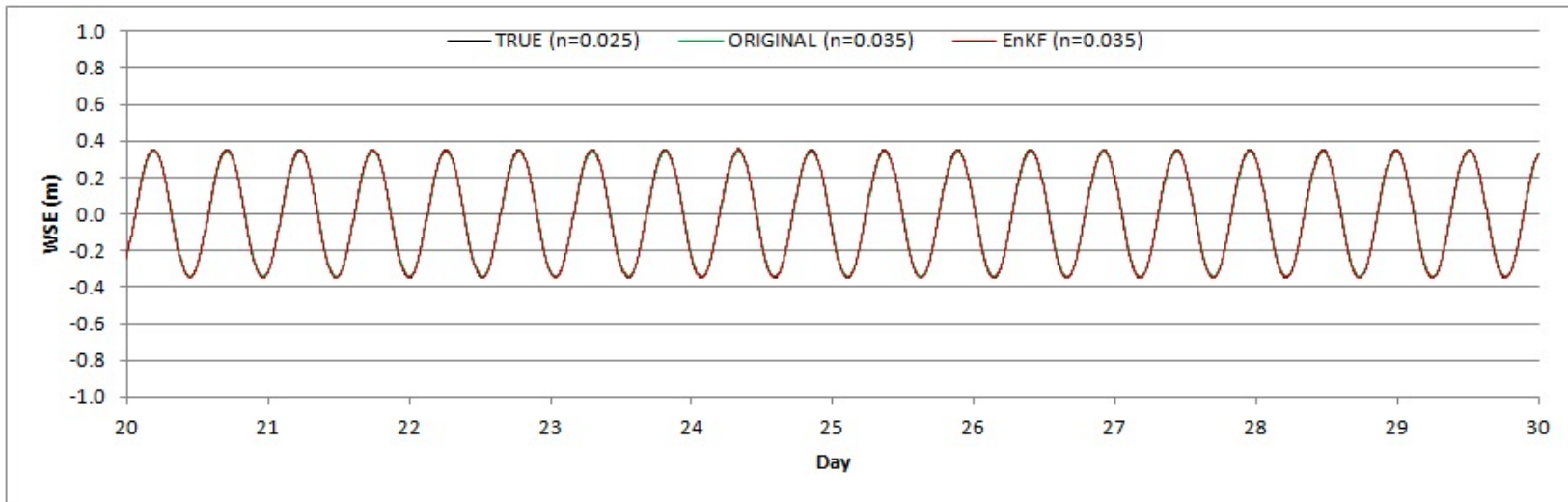
Figure 59   **Time series of WSE at gauge d (upper) and gauge e (bottom) during last 10 days.**

122
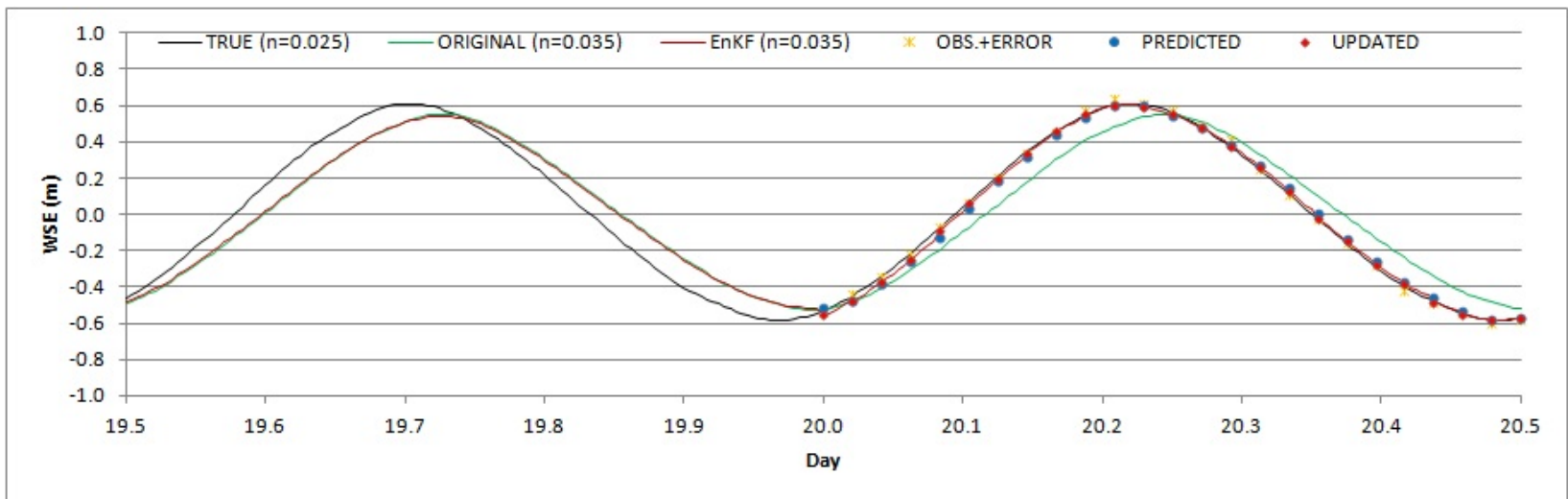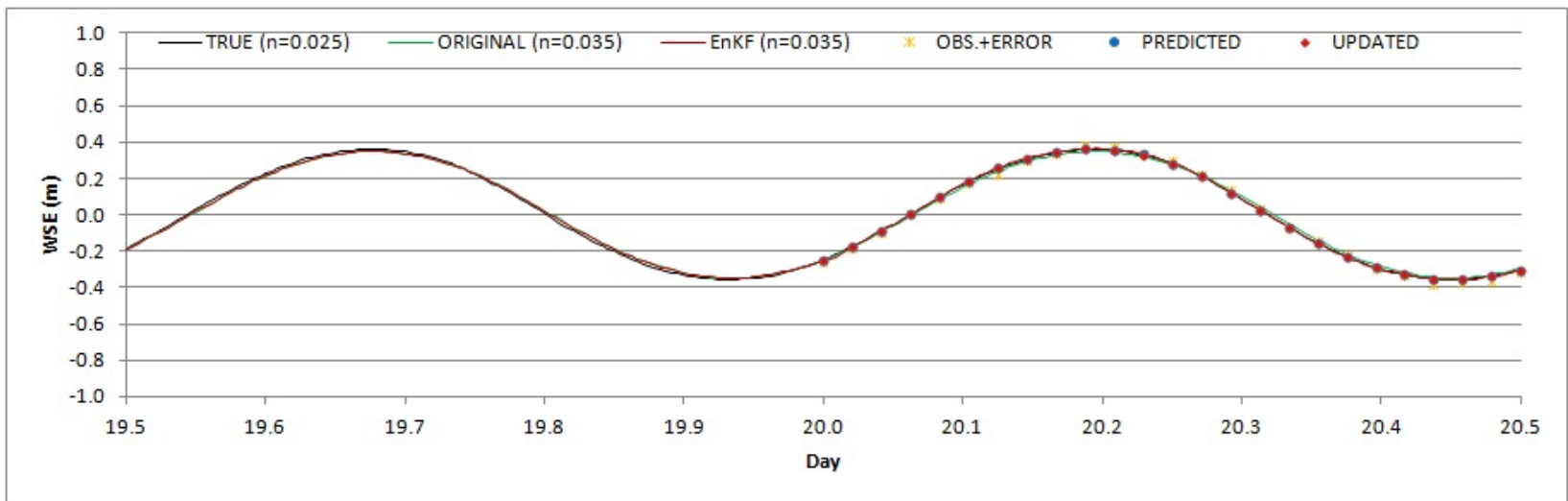
Figure 60   Time series of WSE at gauge b (upper) and gauge c (bottom) at the first day.

123
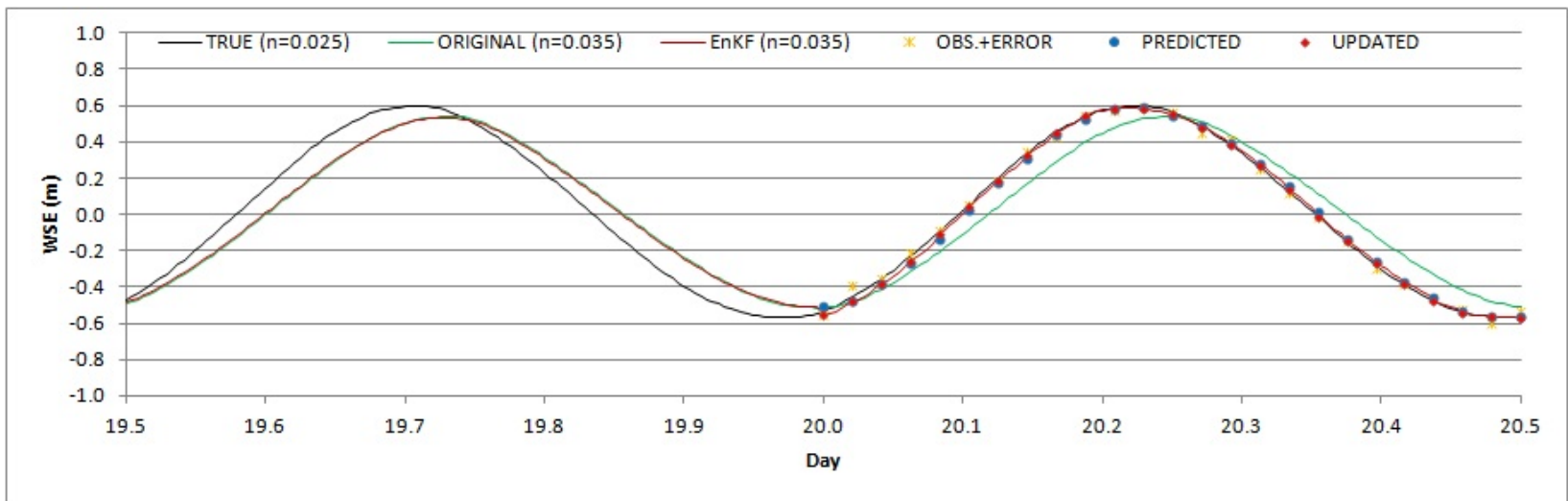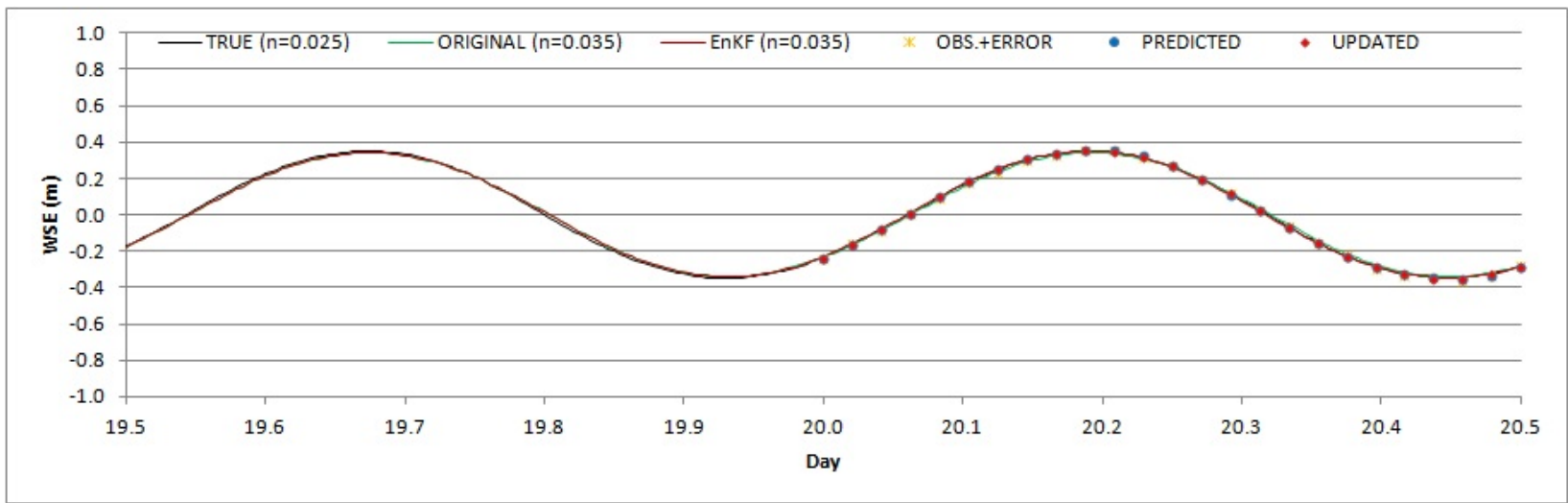
Figure 61   Time series of WSE at gauge d (upper) and gauge e (bottom) at the first day.
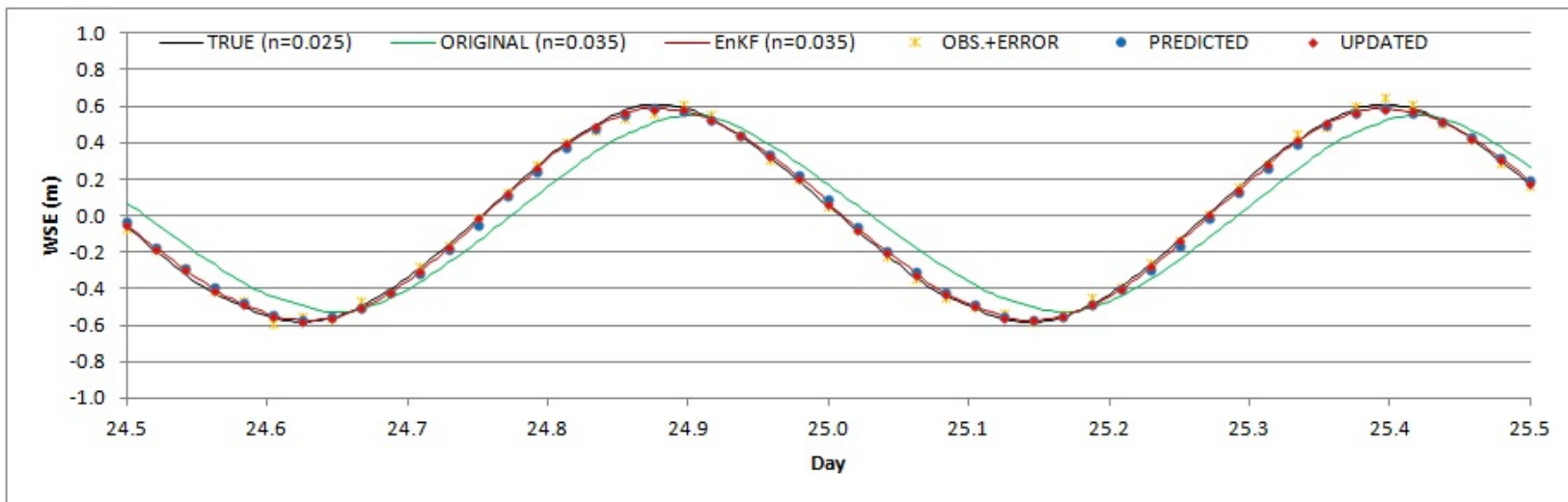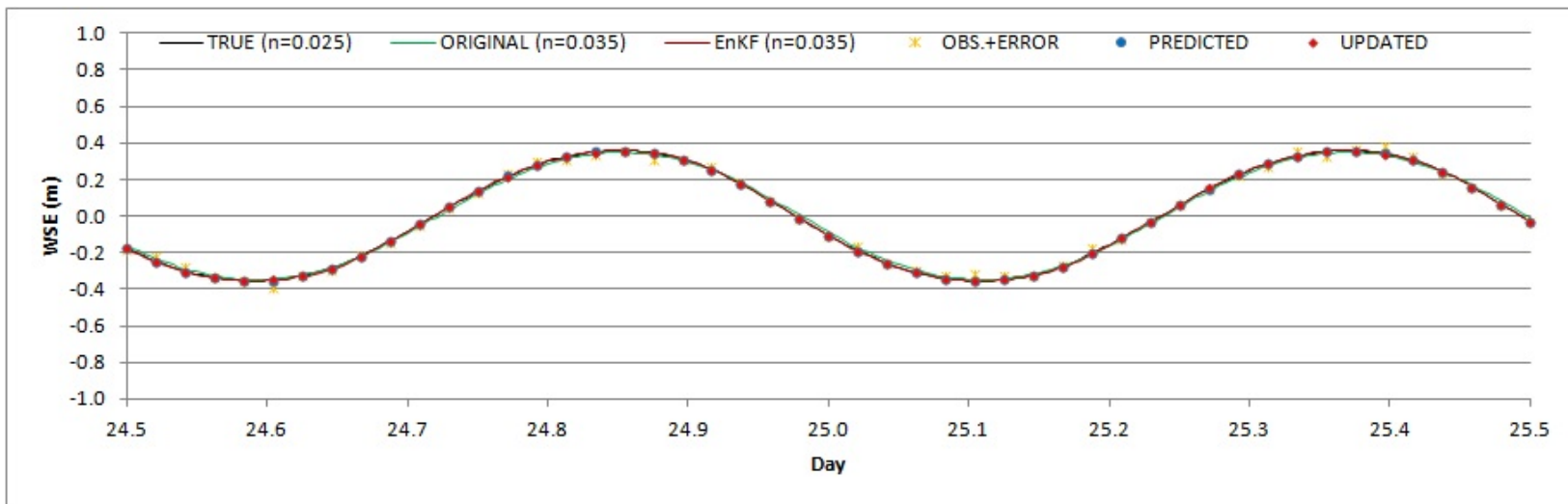
Figure 62   Time series of WSE at gauge b (upper) and gauge c (bottom) at the middle day.
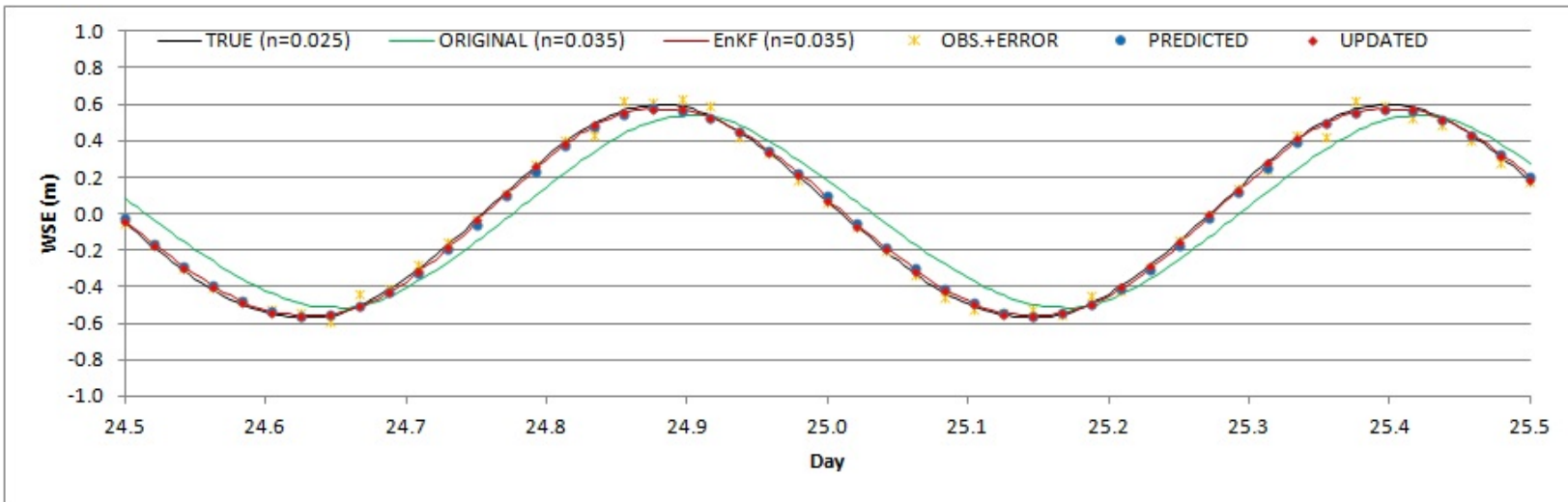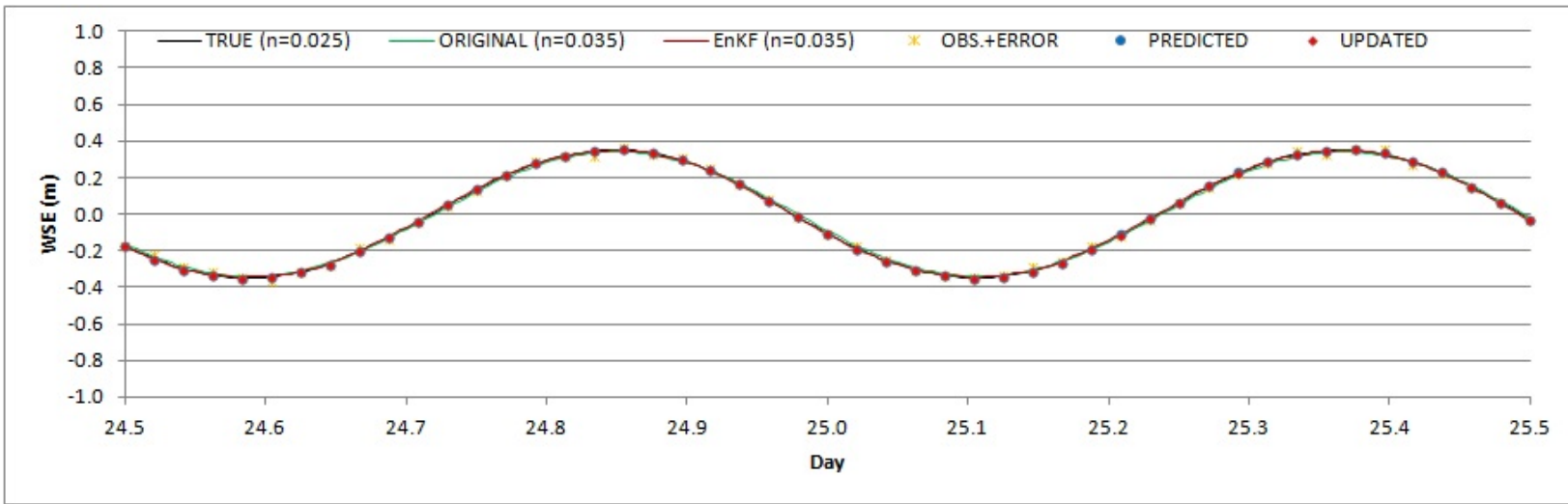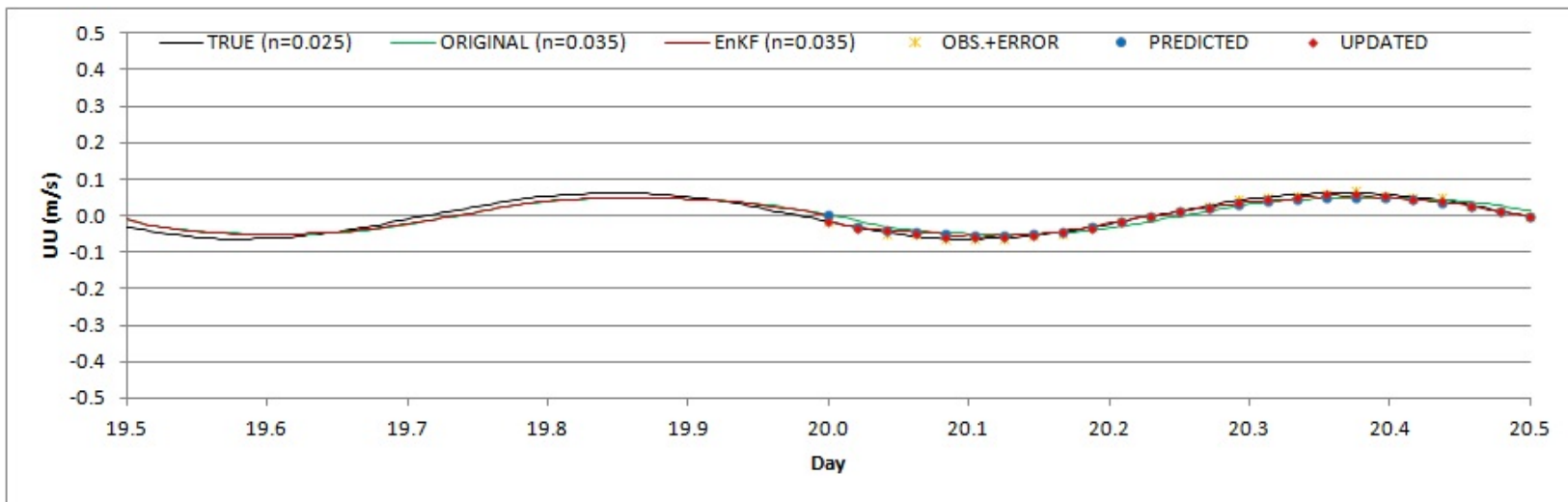
Figure 63 Time series of WSE at gauge d (upper) and gauge e (bottom) at the middle day.
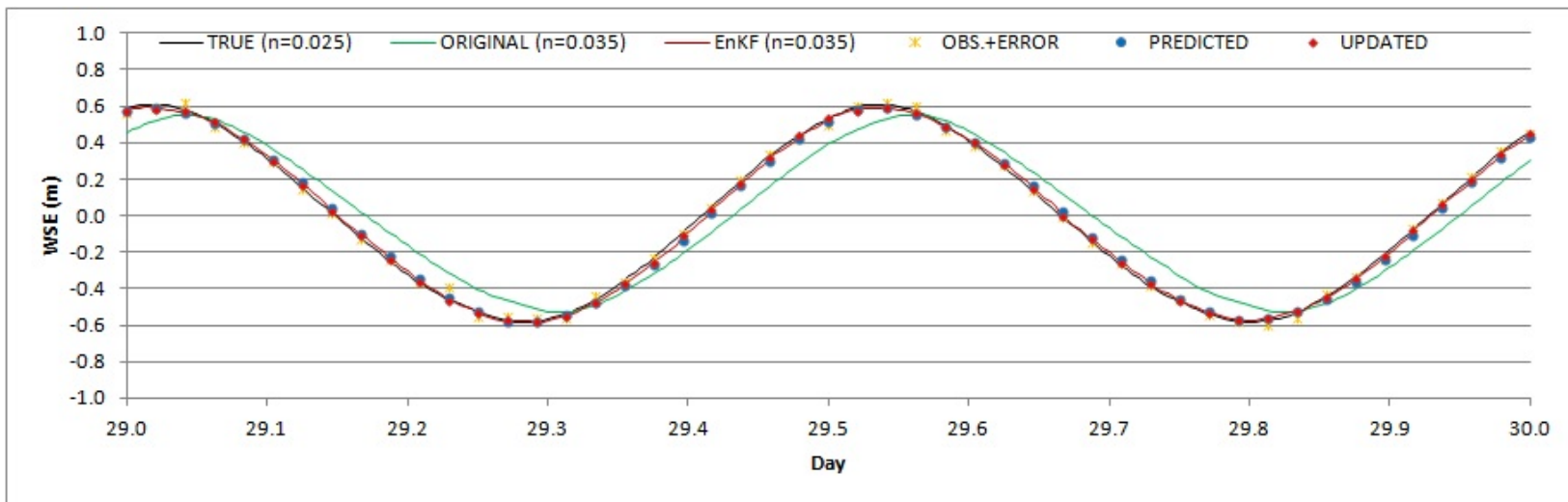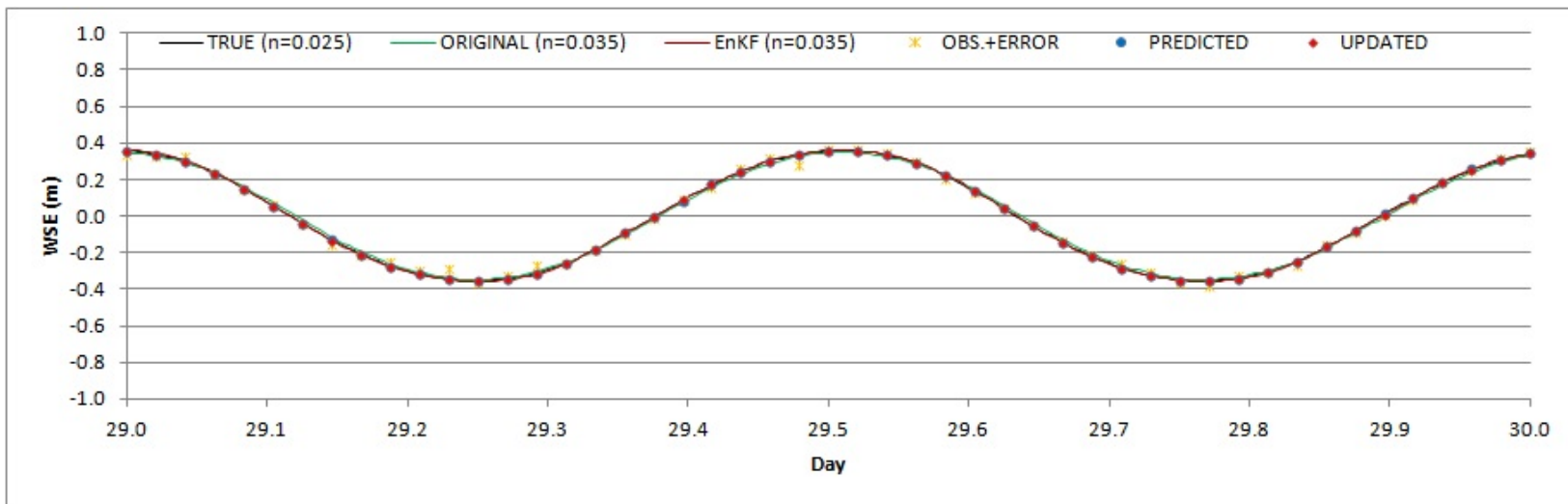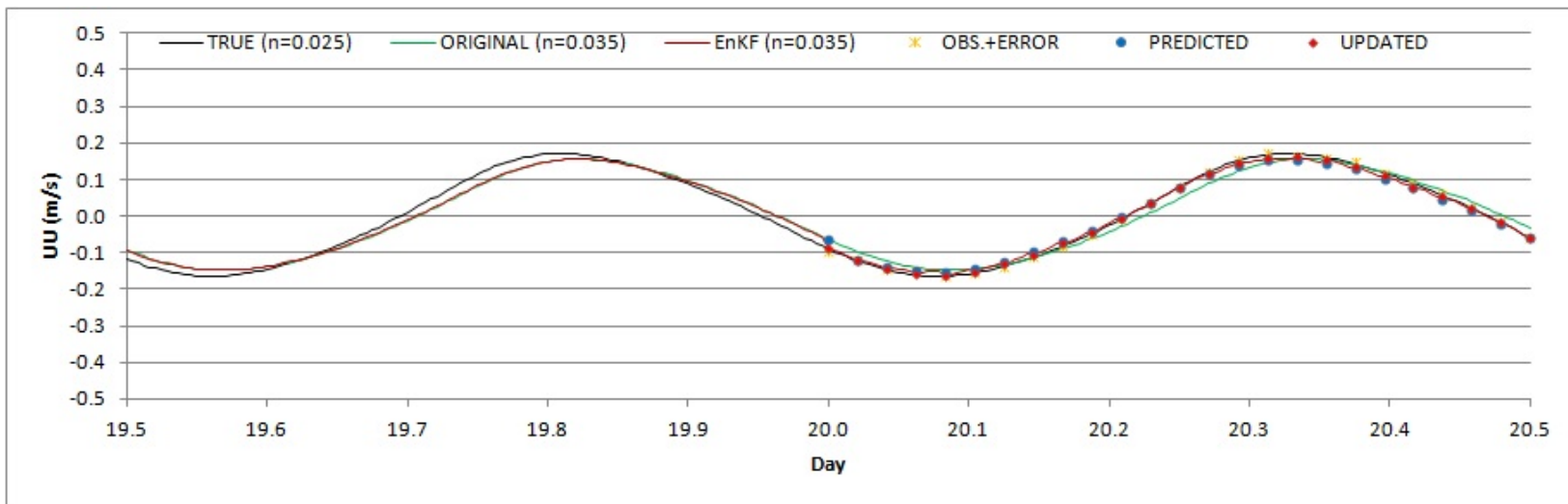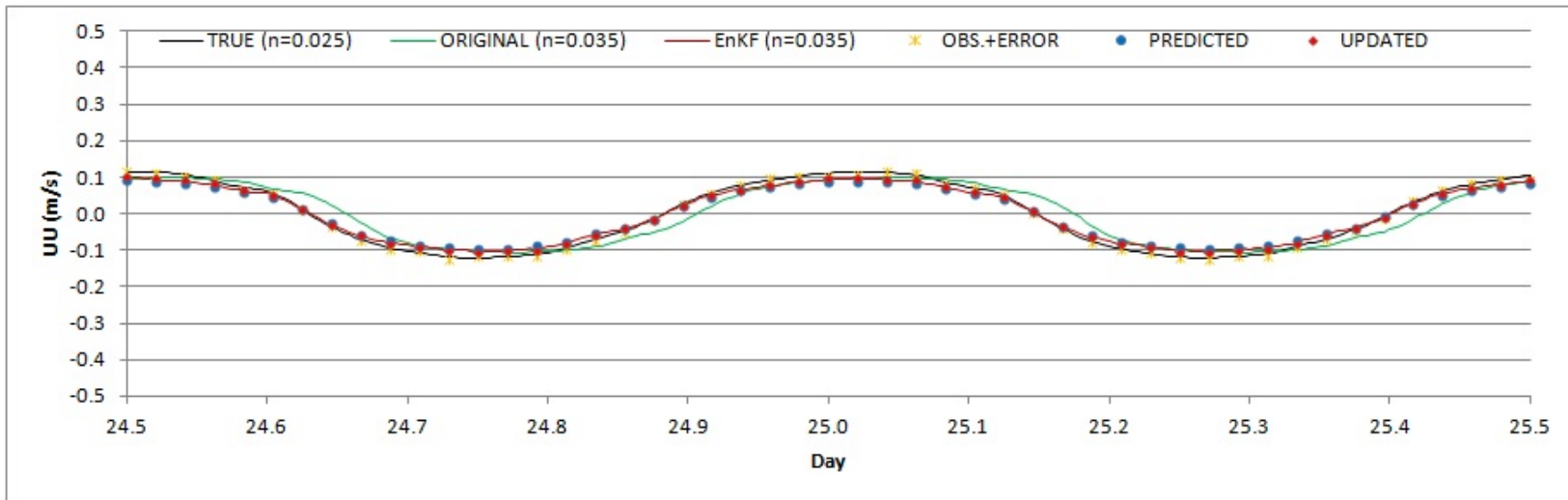
Figure 64   Time series of WSE at gauge b (upper) and gauge c (bottom) at the last day.
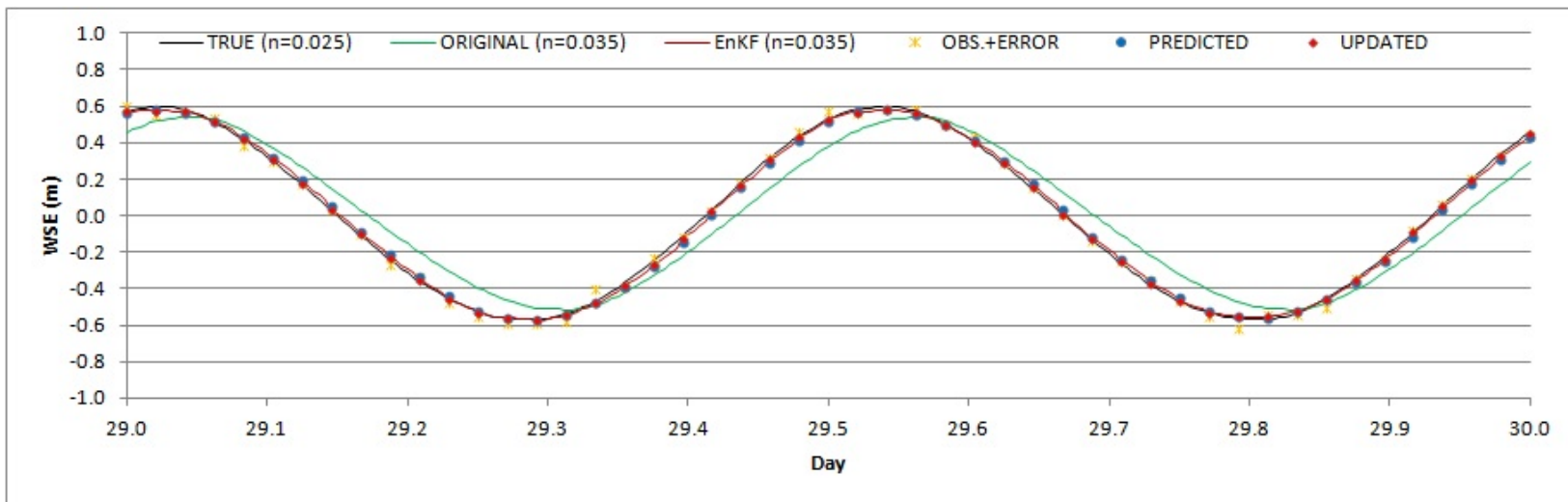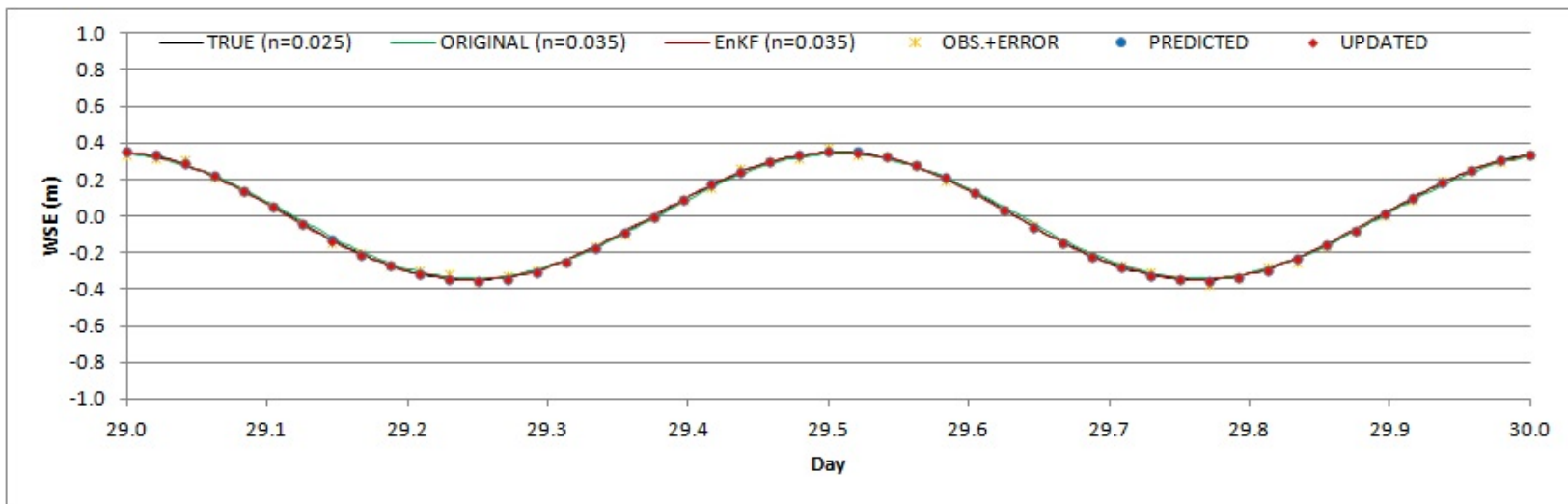
Figure 65   **Time series of WSE at gauge d (upper) and gauge e (bottom) at the last day.**

Table 22 **RMSE of WSE for the simulations at the gauging stations.**

Gauge No.	RMSE of WSE		
	Original (m)	EnKF (m)	$\dfrac{RMSE_{Original} - RMSE_{EnKF}}{RMSE_{Original}}(\%)$
b	1.118E-02	3.415E-03	69.5
c	1.134E-01	1.521E-02	86.6
d	9.161E-03	3.763E-03	58.9
e	1.126E-01	1.580E-02	86.6
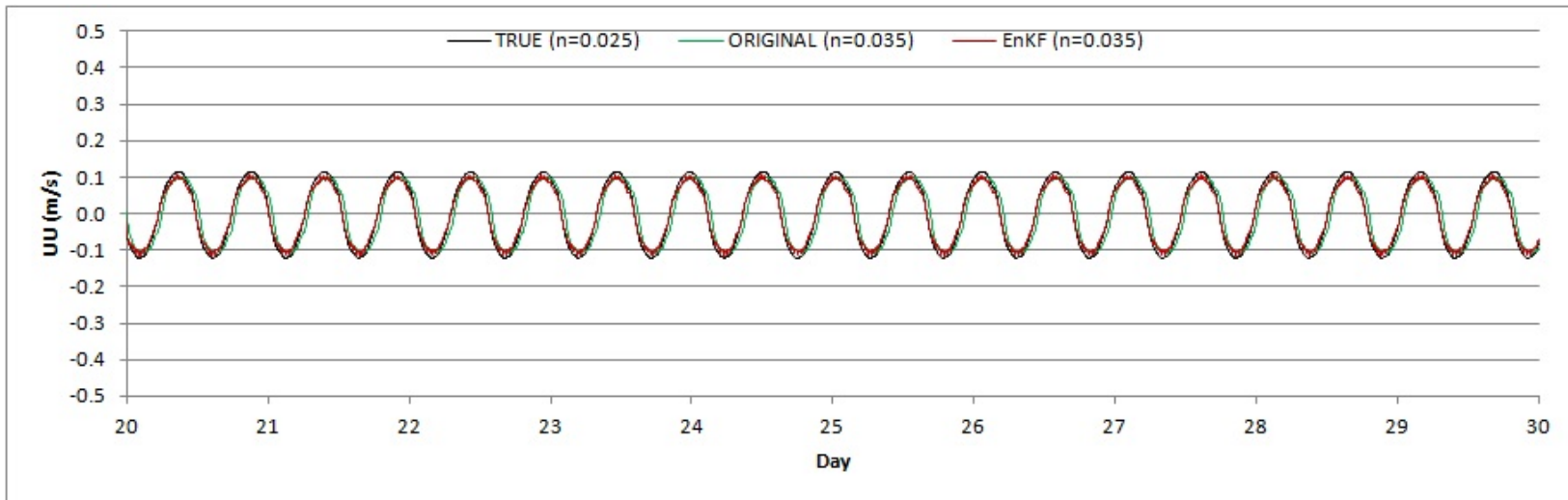
Figure 66   **Time series of UU at gauge b (upper) and gauge c (bottom) during last 10 days.**
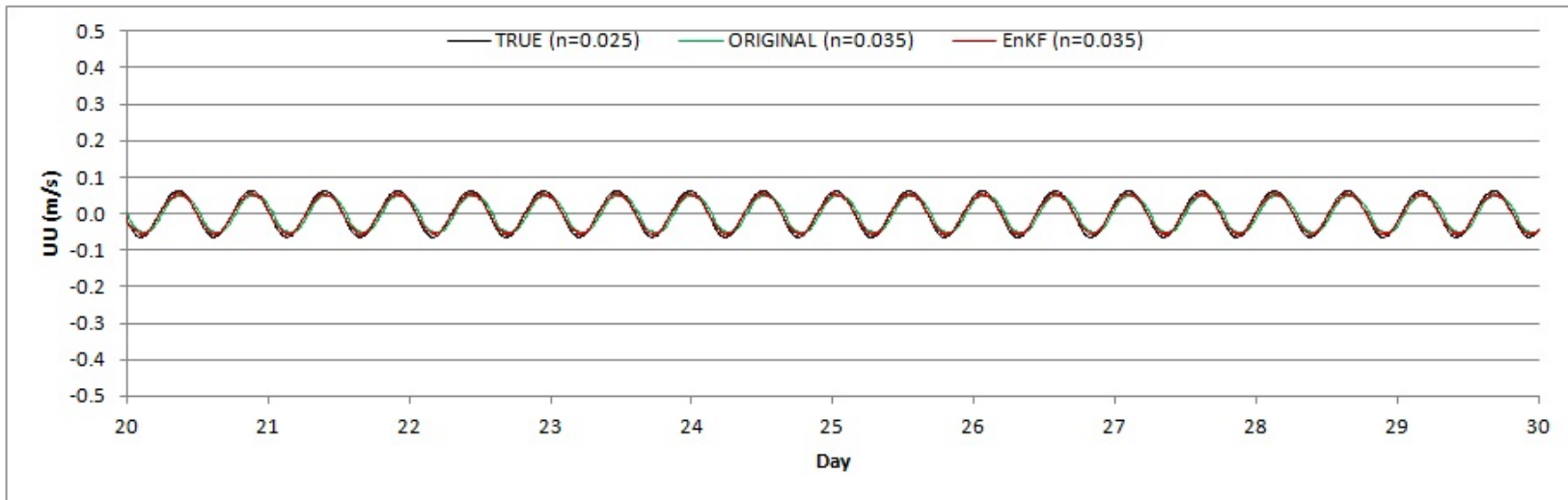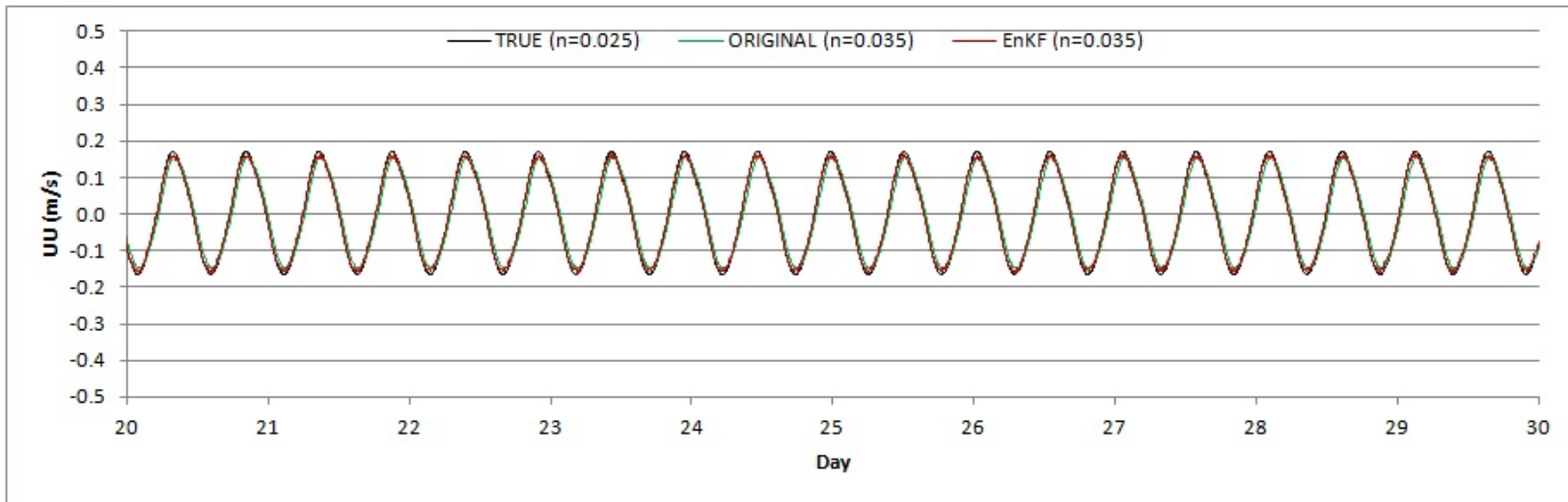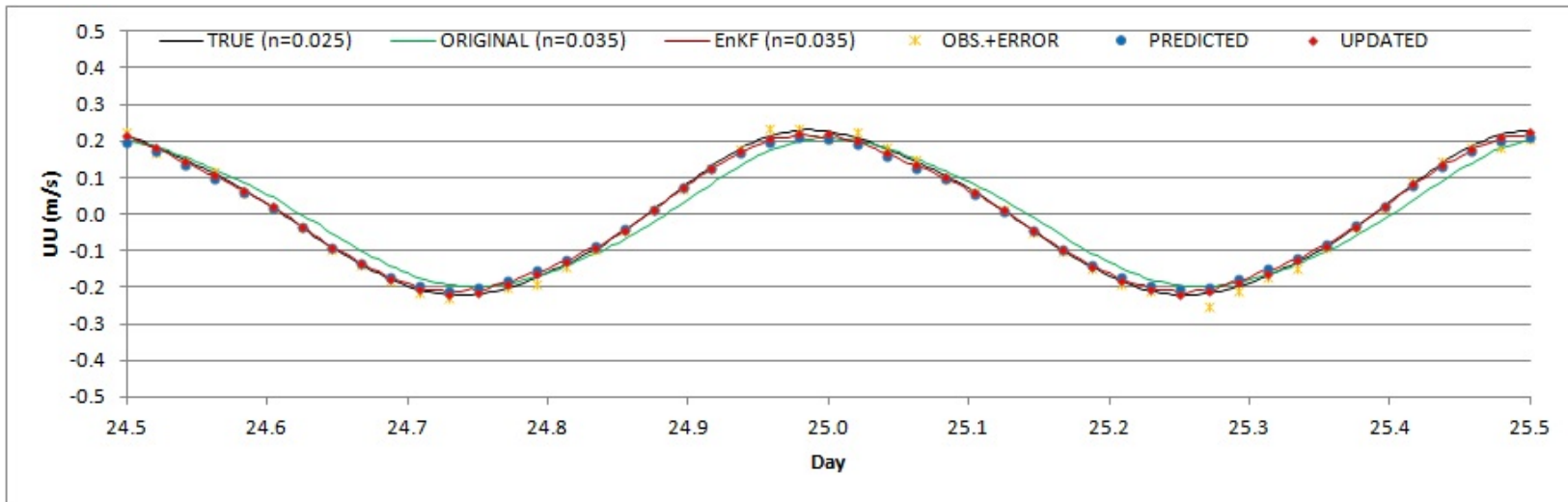
Figure 67   **Time series of UU at gauge d (upper) and gauge e (bottom) during last 10 days.**

131
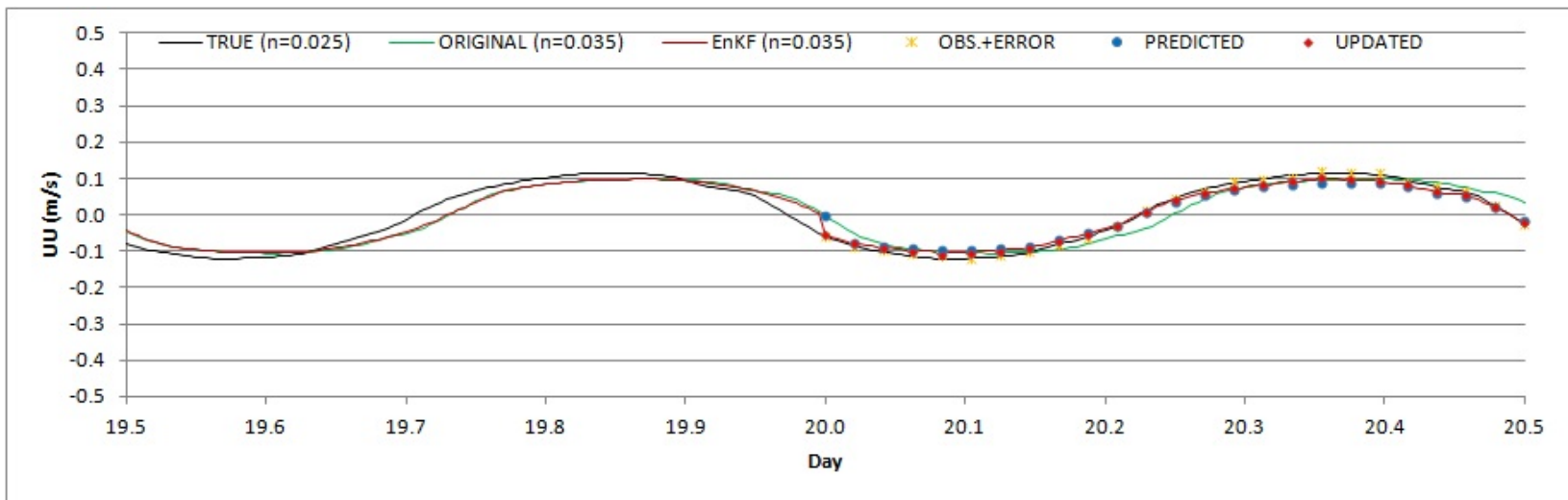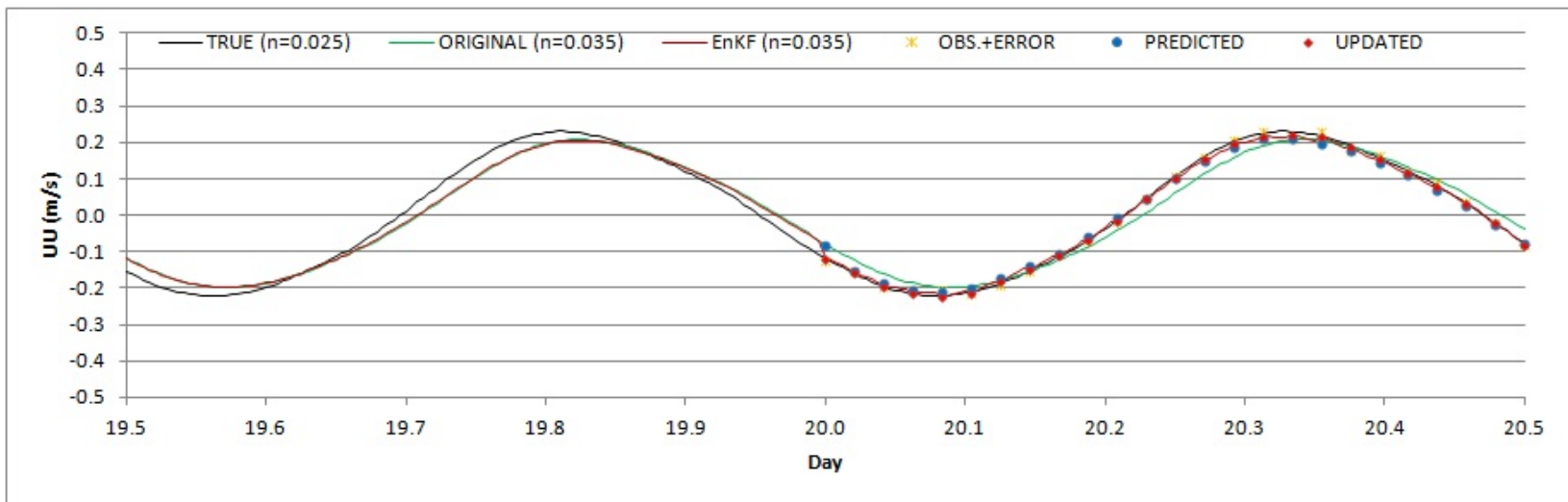
Figure 68 Time series of UU at gauge b (upper) and gauge c (bottom) at the first day.

Figure 69 Time series of UU at gauge d (upper) and gauge e (bottom) at the first day.

133

Figure 70   Time series of UU at gauge b (upper) and gauge c (bottom) at the middle day.
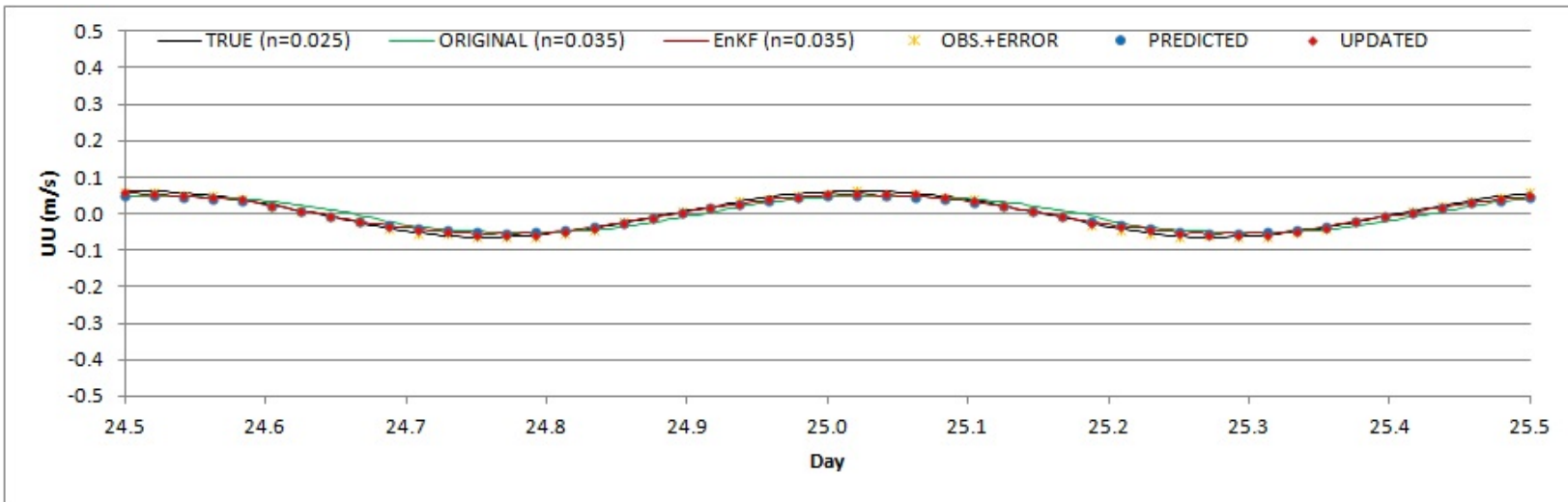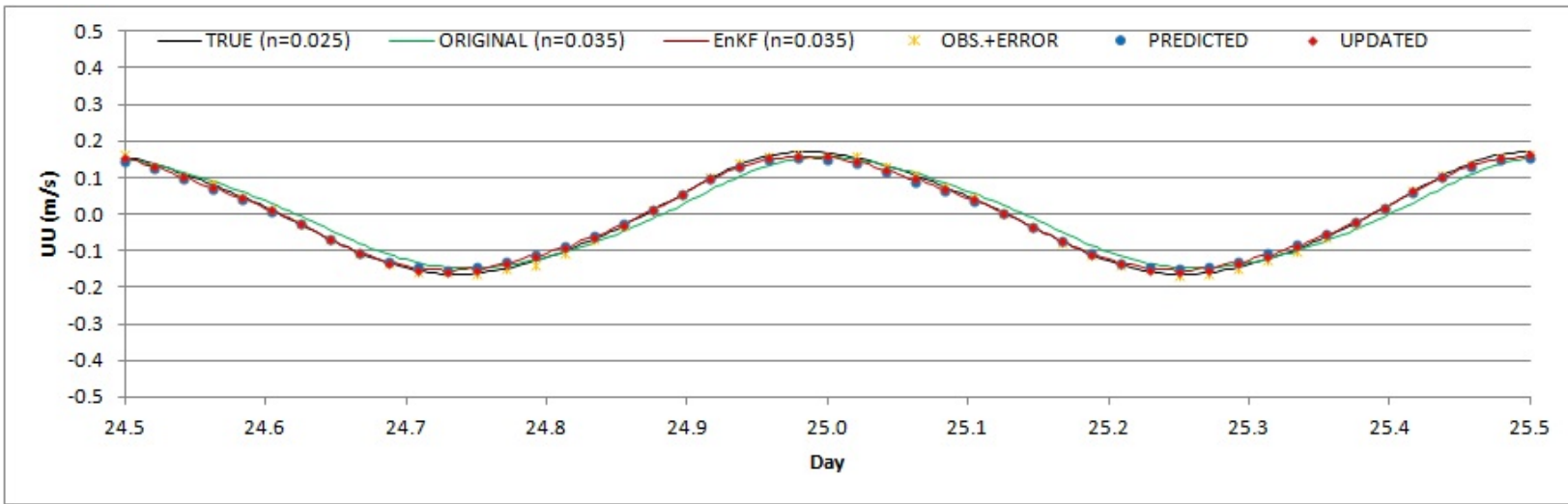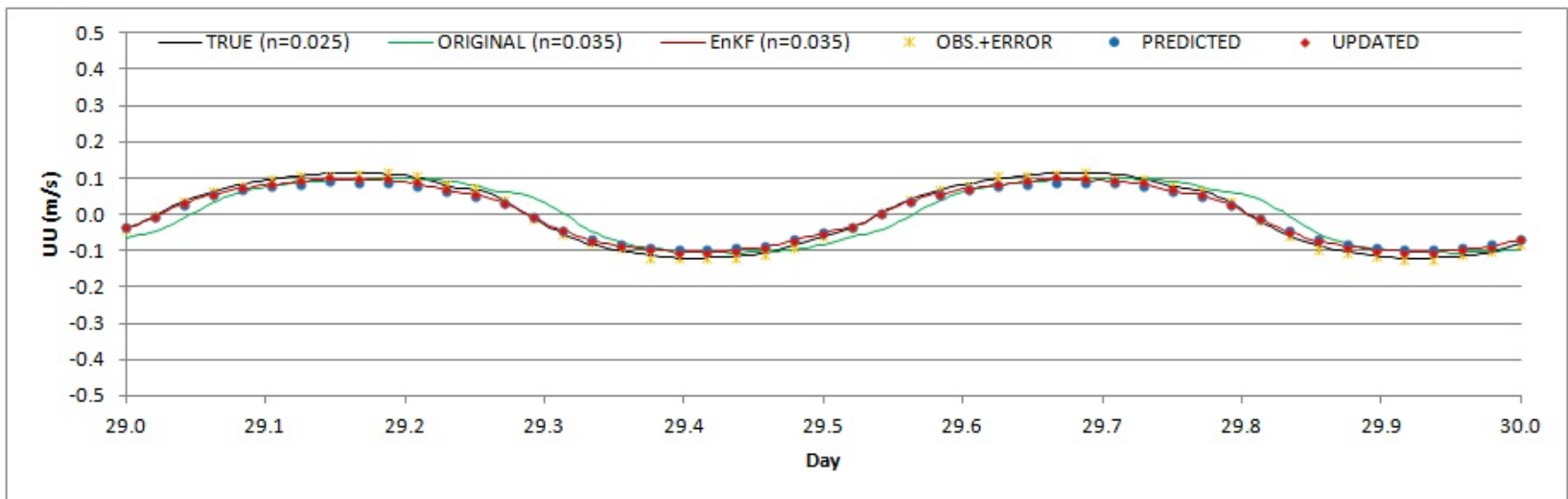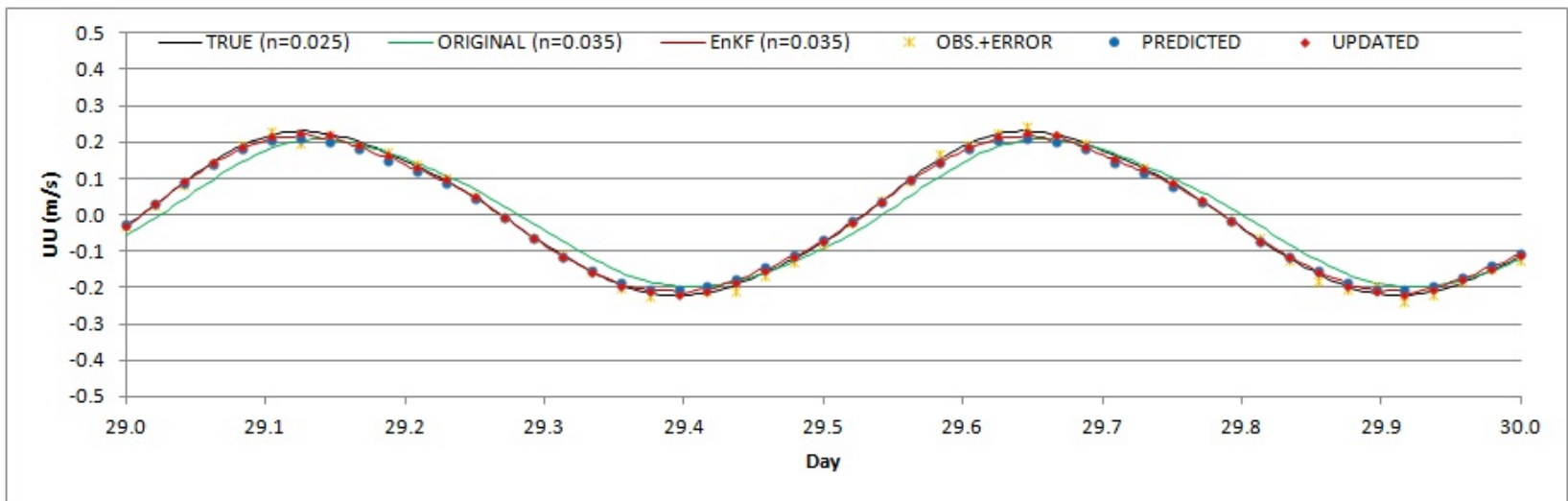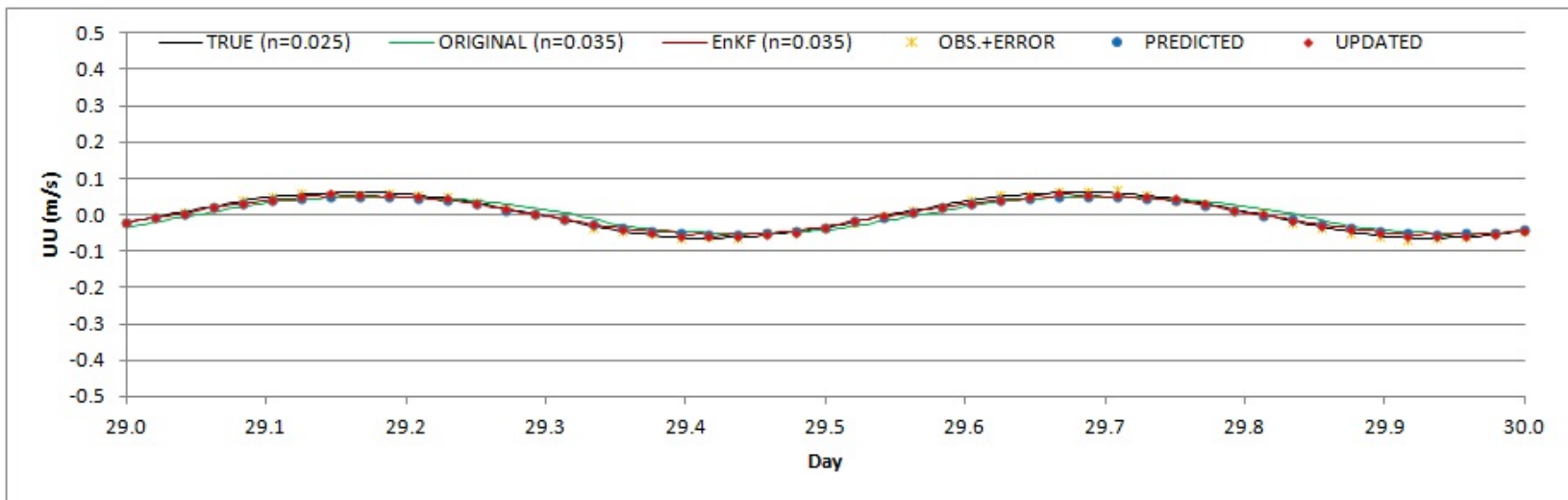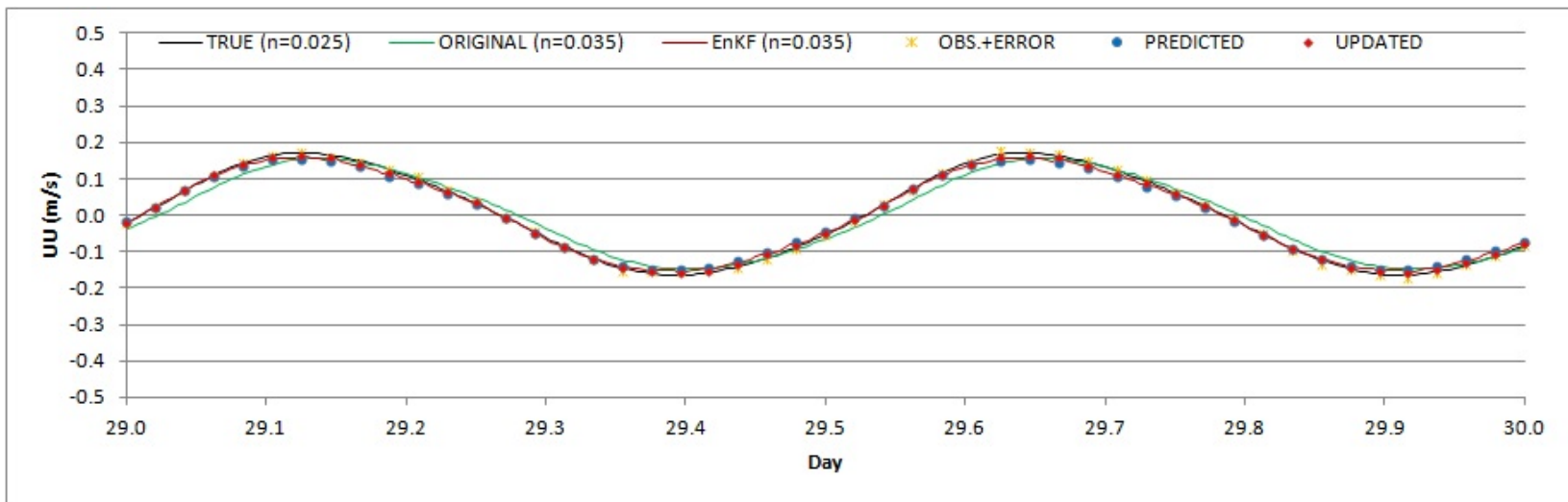
Figure 71 Time series of UU at gauge d (upper) and gauge e (bottom) at the middle day.

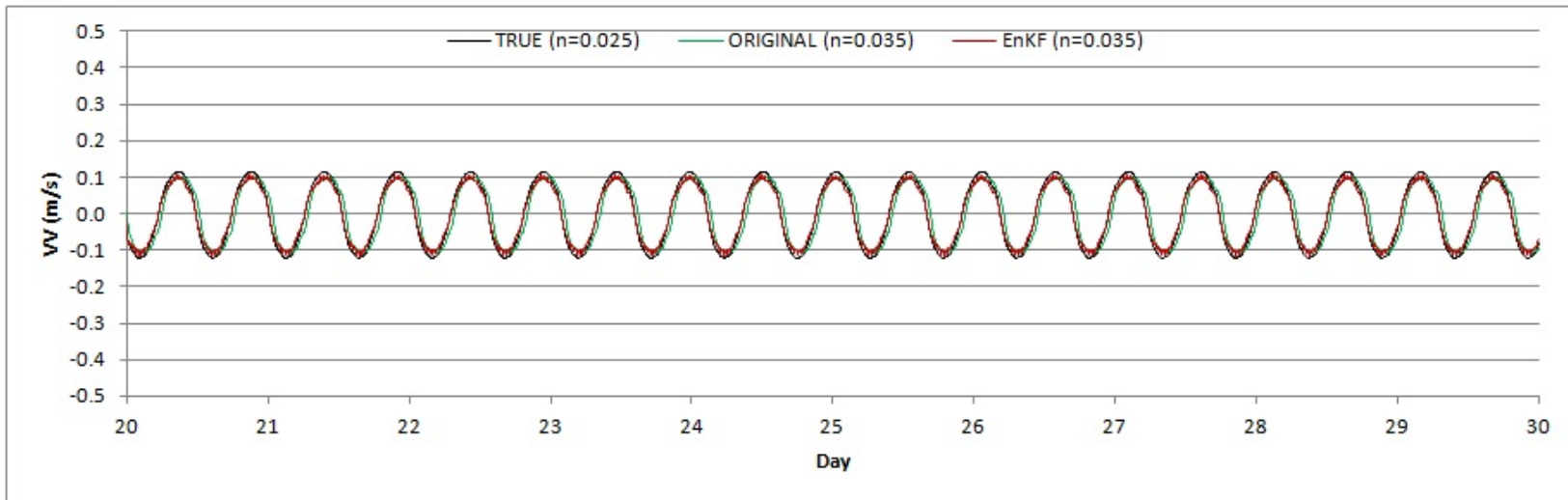**Figure 72**   Time series of UU at gauge b (upper) and gauge c (bottom) at the last day.
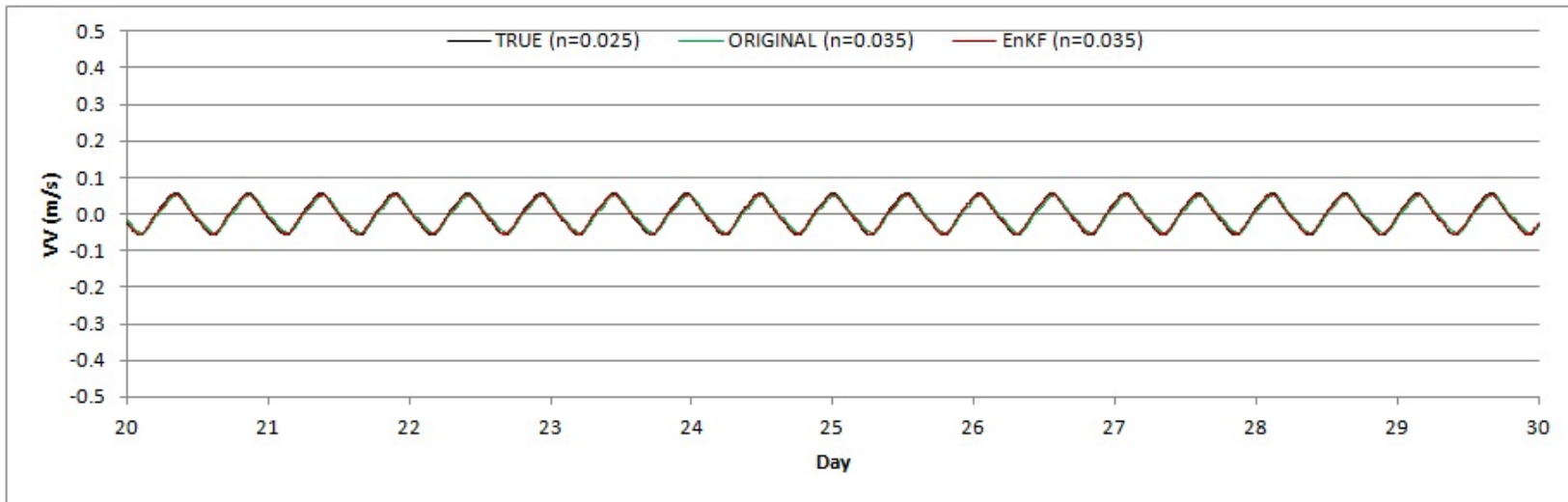
Figure 73   Time series of UU at gauge d (upper) and gauge e (bottom) at the last day.

Table 23   **RMSE of UU for the simulations at the gauging stations.**

Gauge No.	RMSE of UU		
	Original (m)	EnKF (m)	$\dfrac{RMSE_{Original} - RMSE_{EnKF}}{RMSE_{Original}}(\%)$
b	2.851E-02	8.043E-03	71.8
c	2.693E-02	1.289E-02	52.1
d	1.920E-02	8.208E-03	57.3
e	1.340E-02	6.367E-03	52.5

Figure 74   Time series of VV at gauge b (upper) and gauge c (bottom) during last 10 days.

Figure 75   **Time series of VV at gauge d (upper) and gauge e (bottom) during last 10 days.**
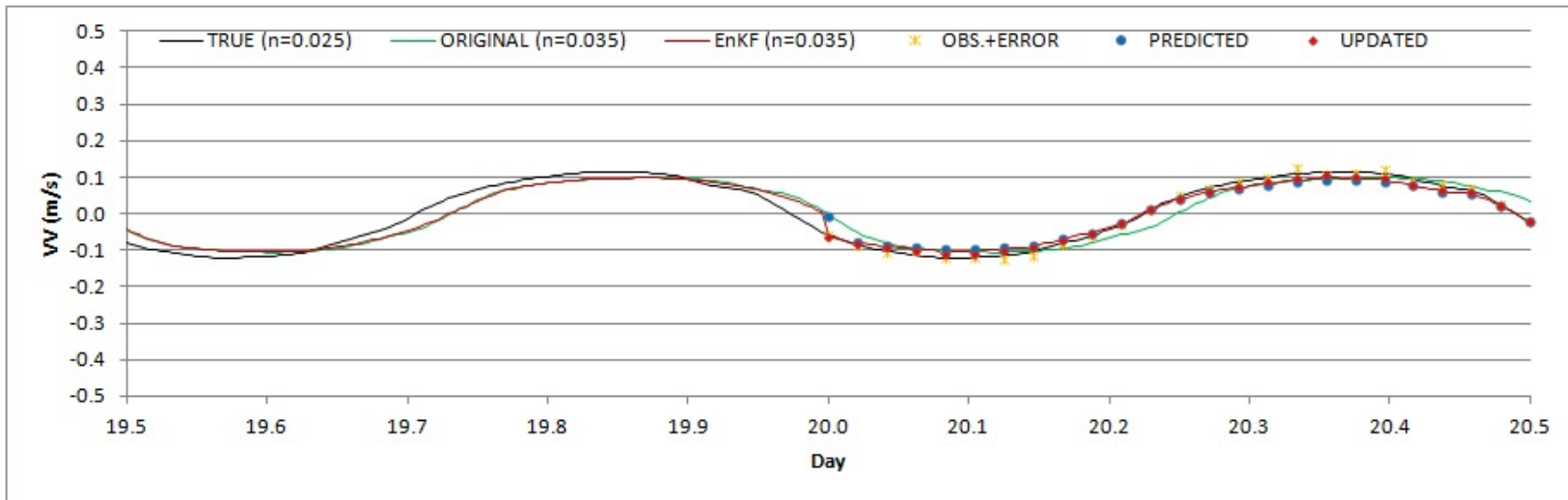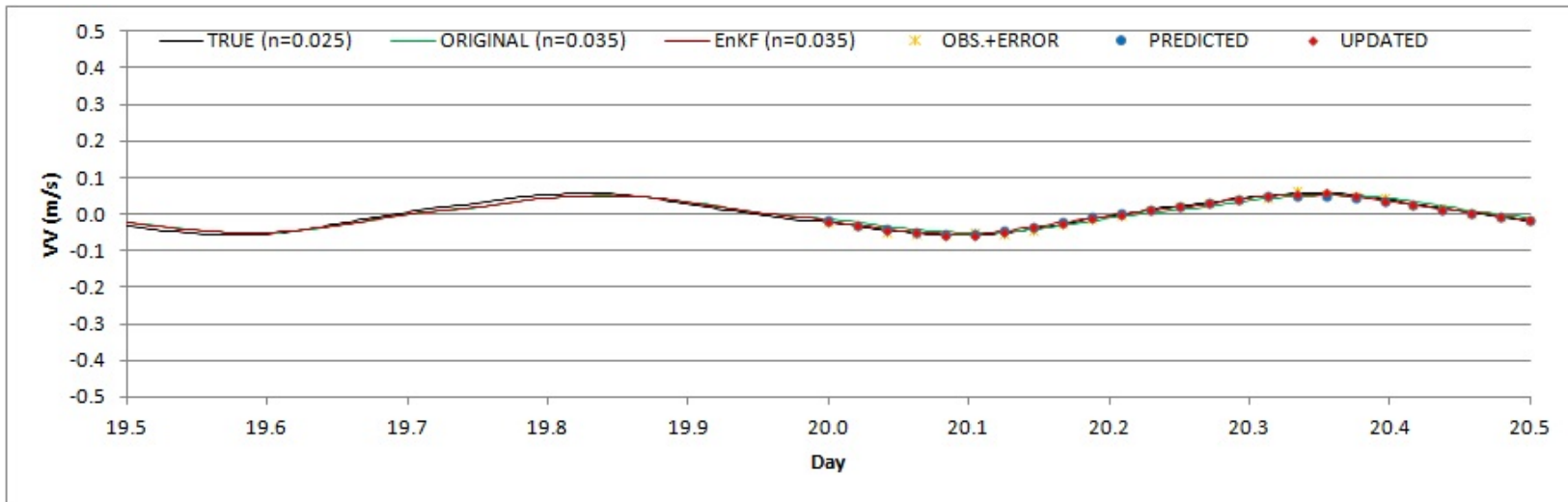
Figure 76 Time series of VV at gauge b (upper) and gauge c (bottom) at the first day.

141
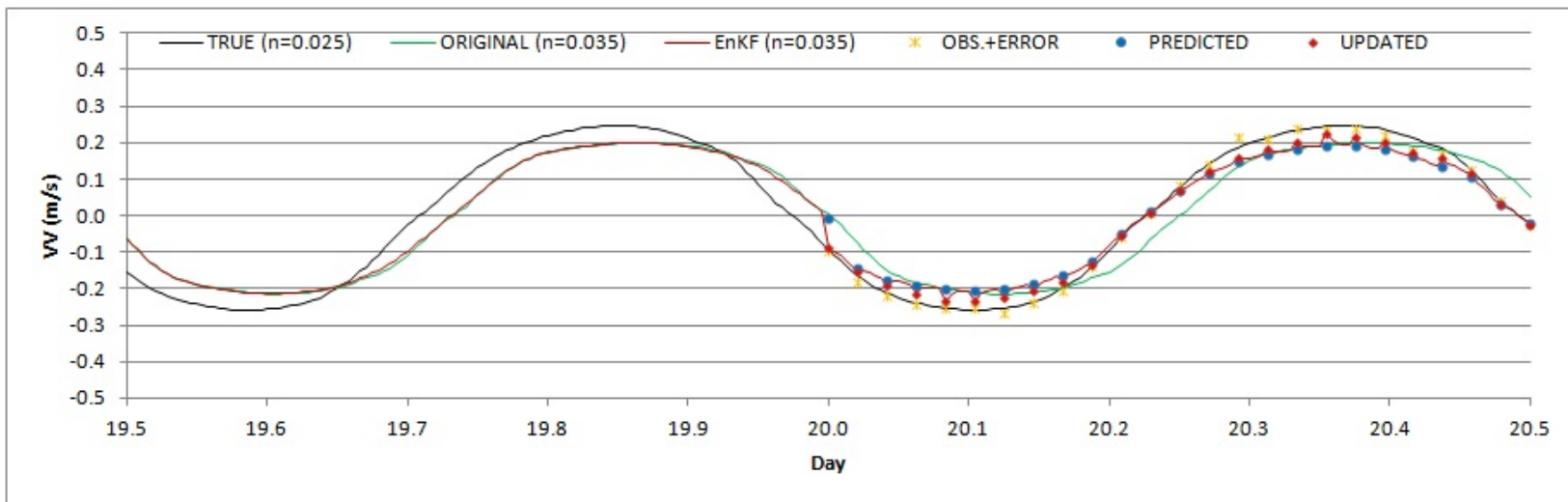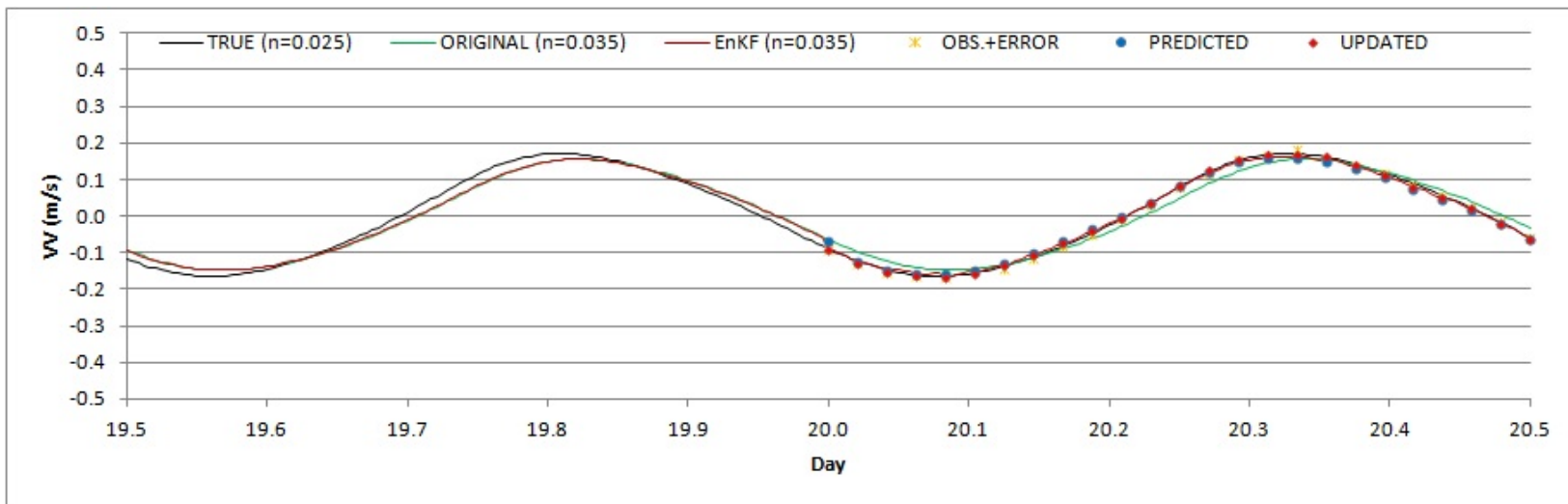
Figure 77   Time series of VV at gauge d (upper) and gauge e (bottom) at the first day.
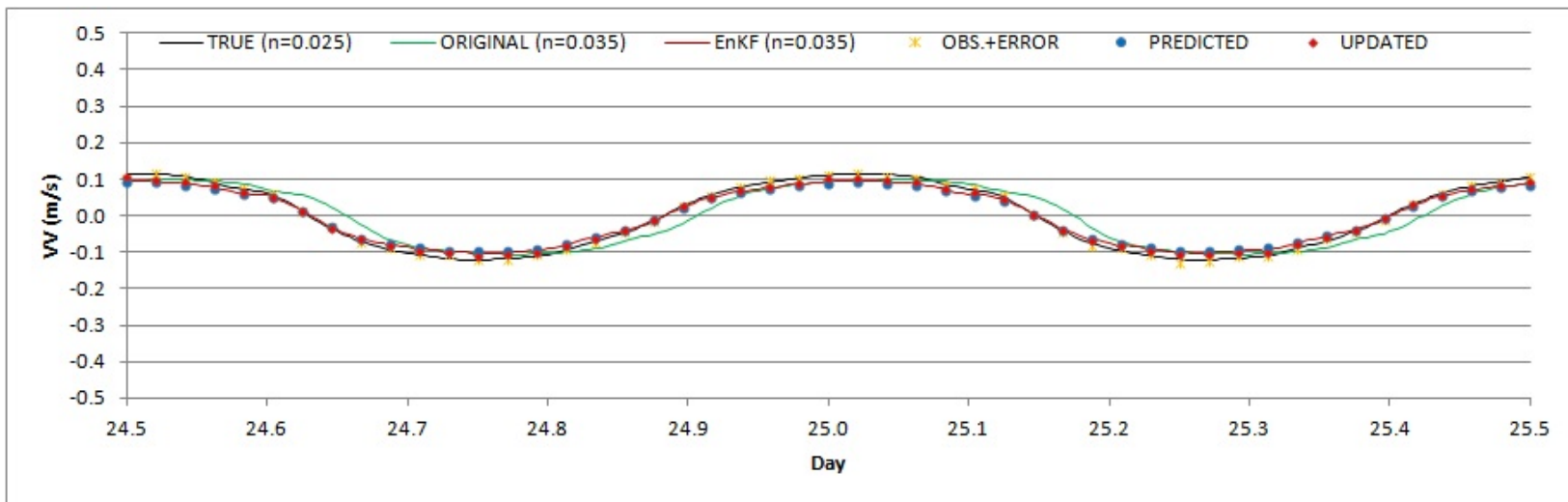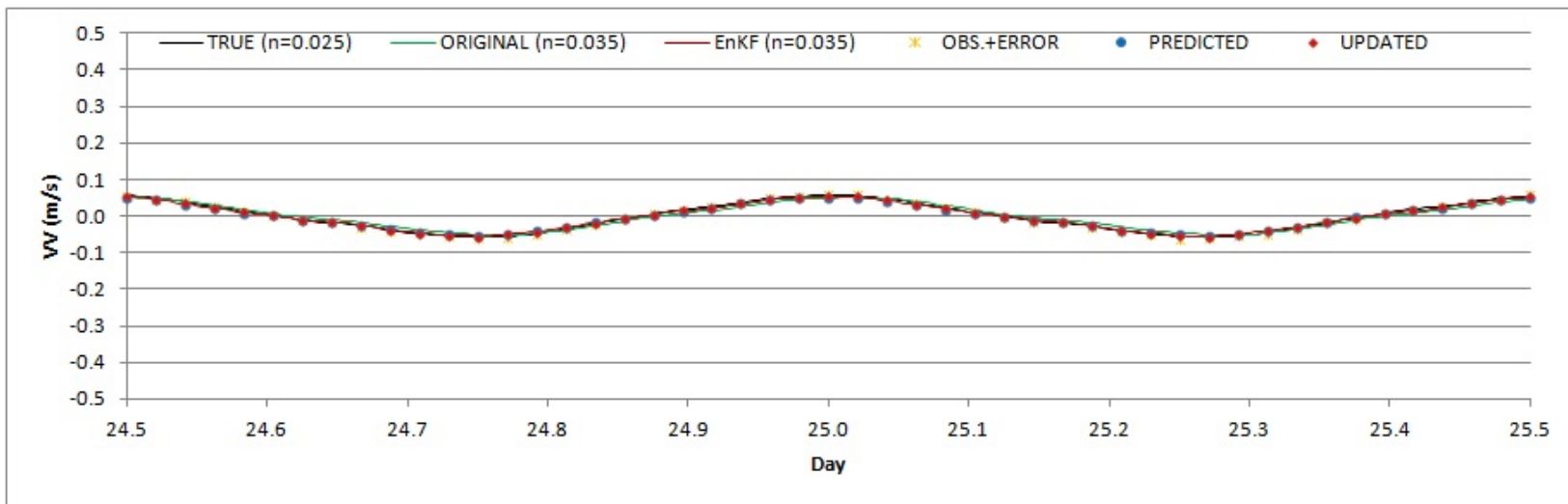
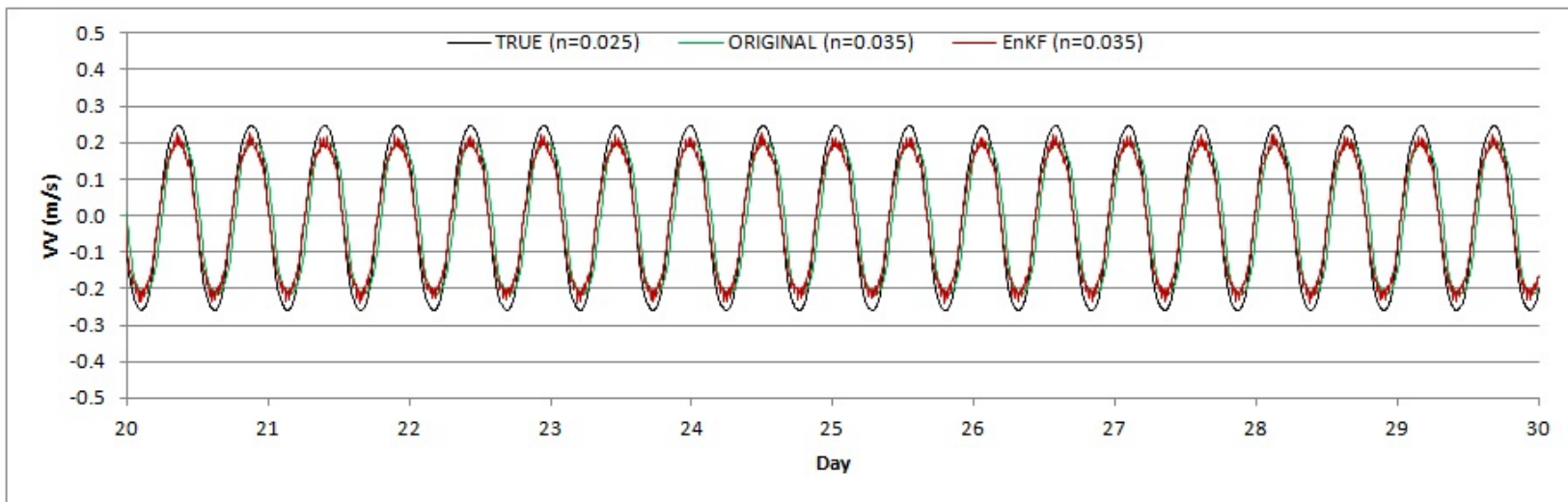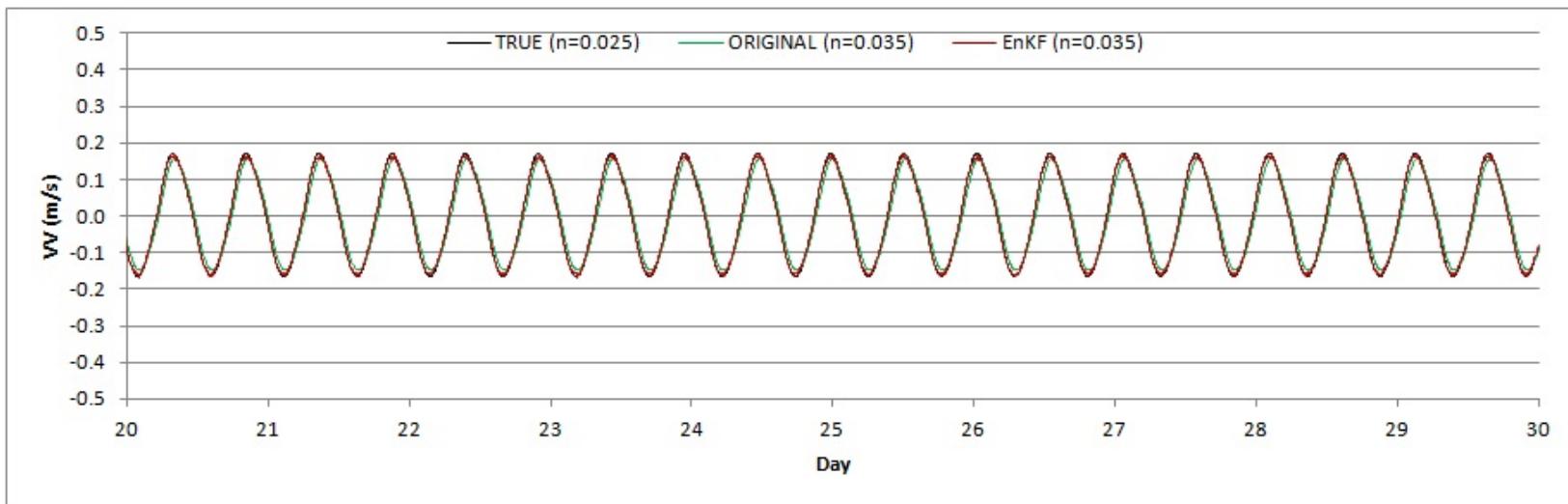**Figure 78**   Time series of VV at gauge b (upper) and gauge c (bottom) at the middle day.

143
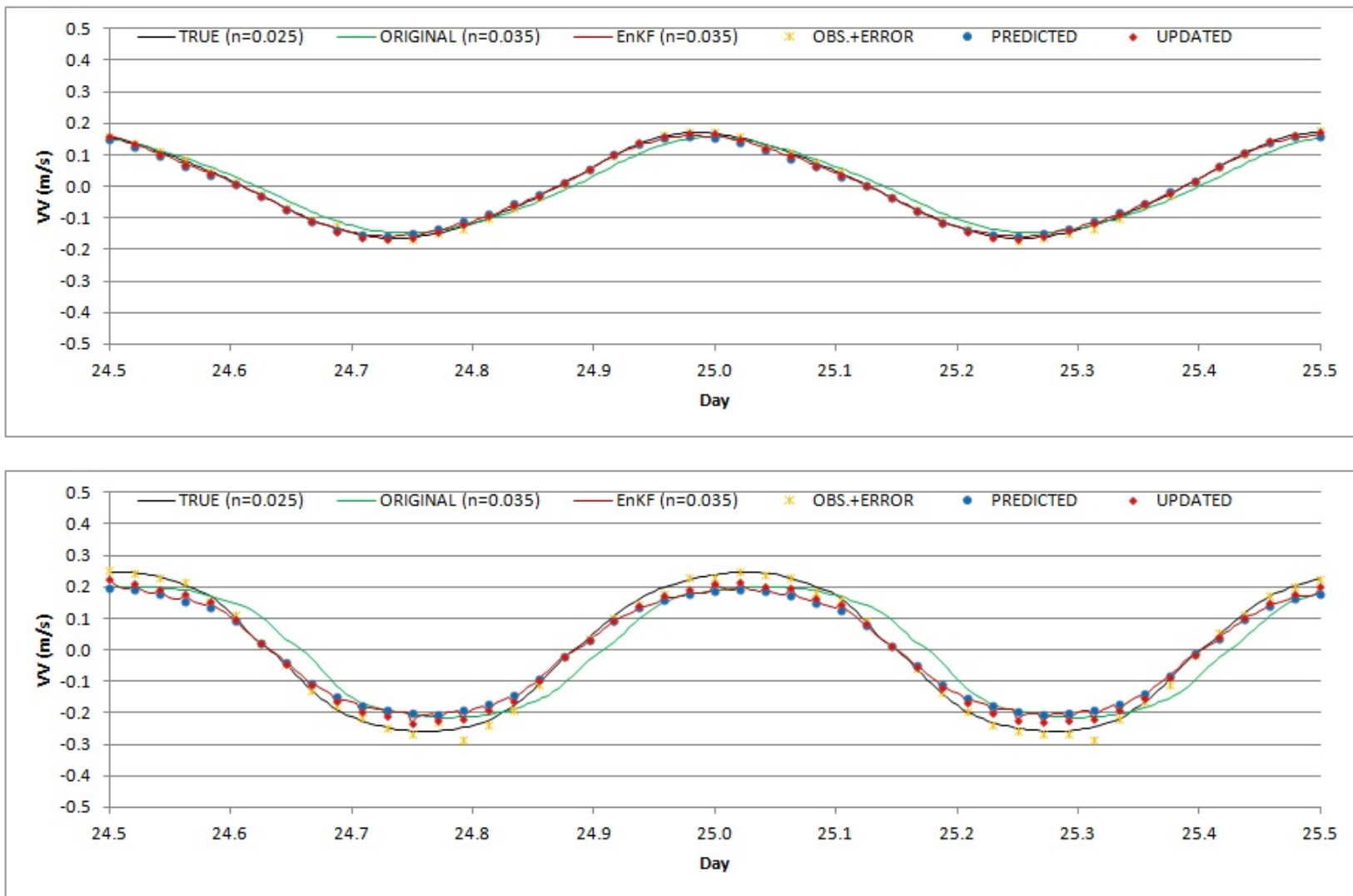
Figure 79 **Time series of VV at gauge d (upper) and gauge e (bottom) at the middle day.**

144
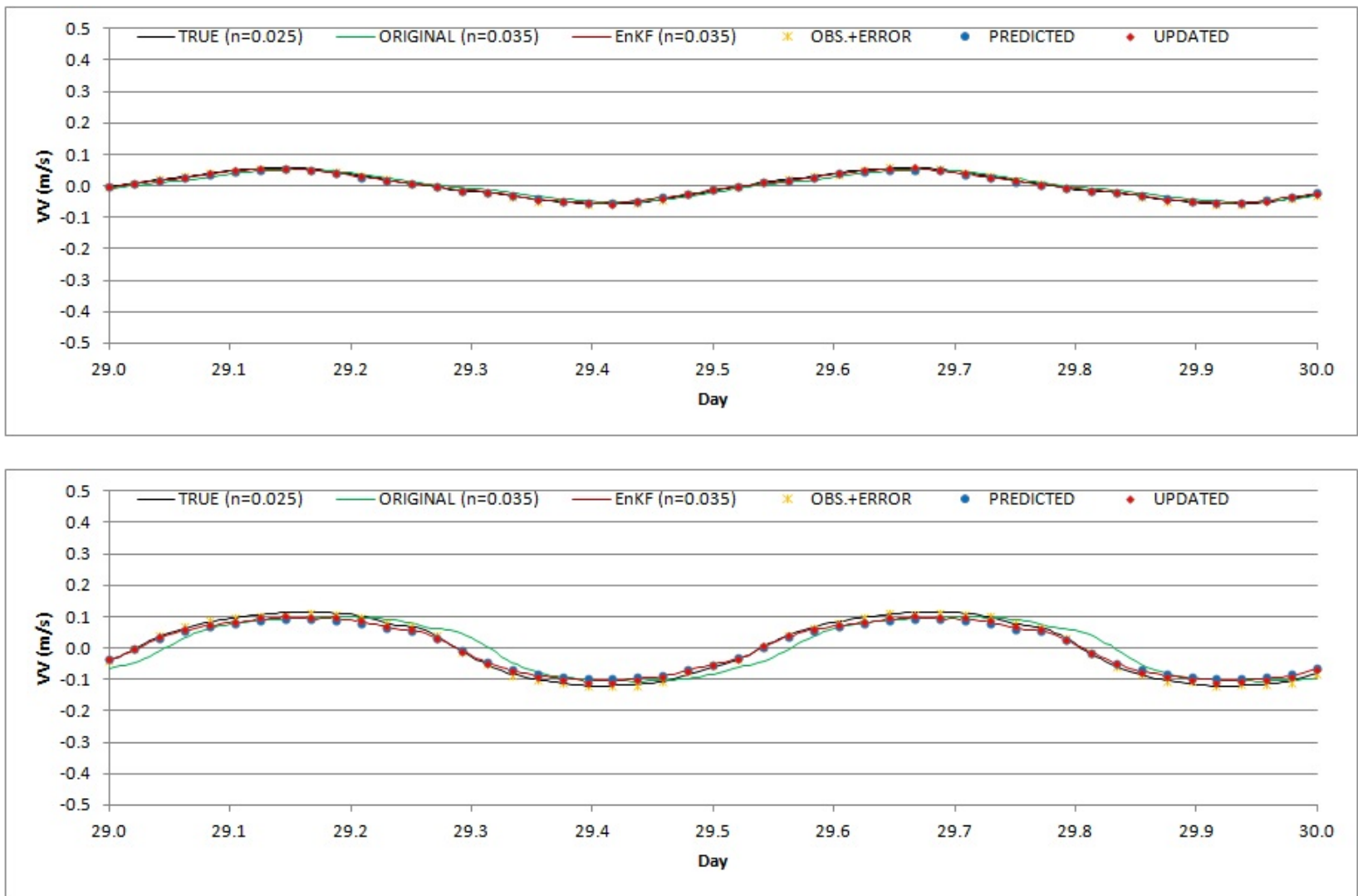
Figure 80 Time series of VV at gauge b (upper) and gauge c (bottom) at the last day.

145
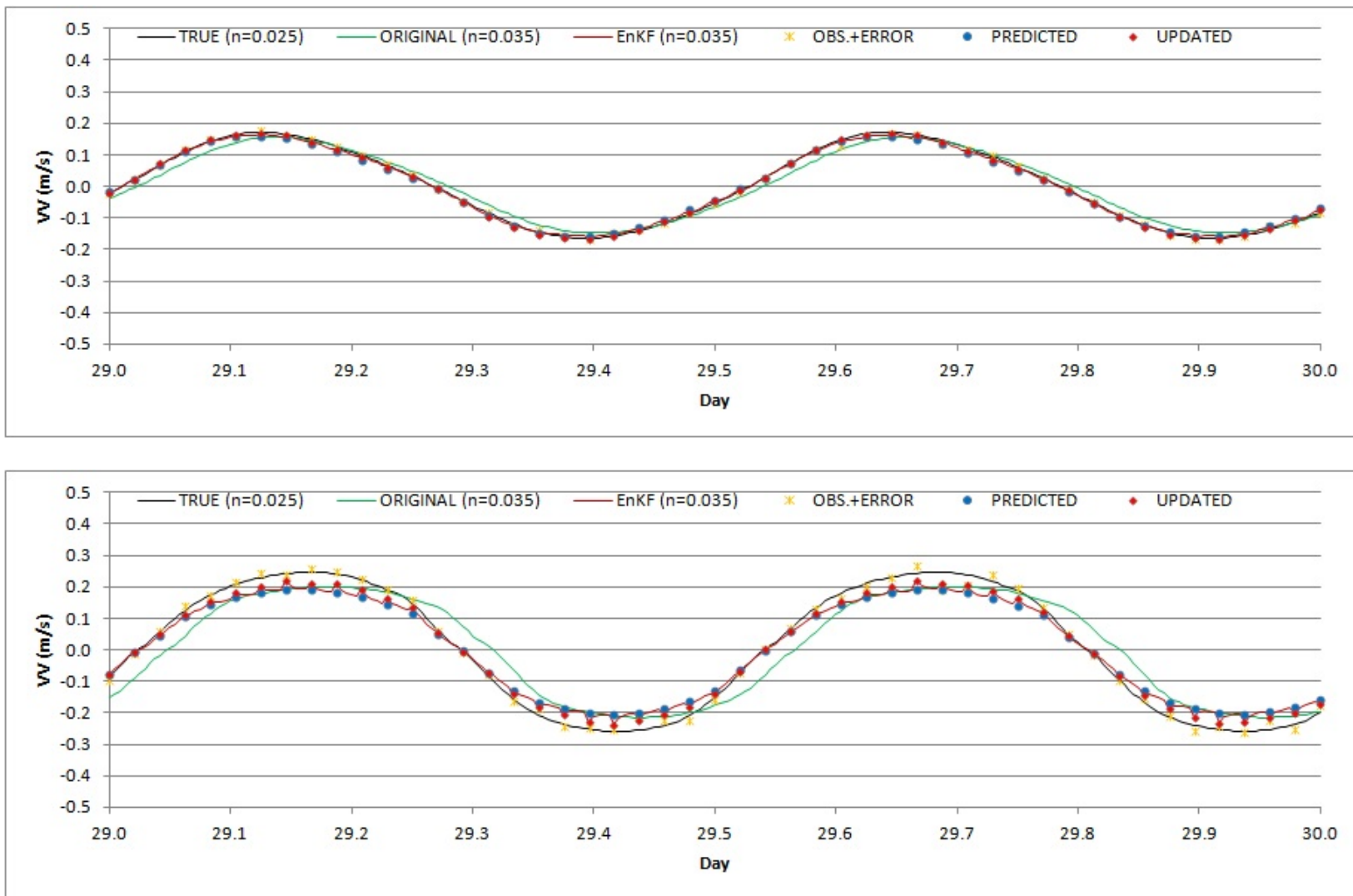
Figure 81   Time series of VV at gauge d (upper) and gauge e (bottom) at the last day.

146

Table 24   **RMSE of VV for the simulations on the gauging stations.**

Gauge No.	RMSE of VV		
	Original (m)	EnKF (m)	$\dfrac{RMSE_{Original} - RMSE_{EnKF}}{RMSE_{Original}}(\%)$
b	7.675E-03	3.144E-03	59.0
c	2.693E-02	1.307E-02	51.5
d	1.920E-02	5.337E-03	72.2
e	5.785E-02	3.673E-02	36.8

APPENDIX C: SIMULATION RESULTS REAL MODELS
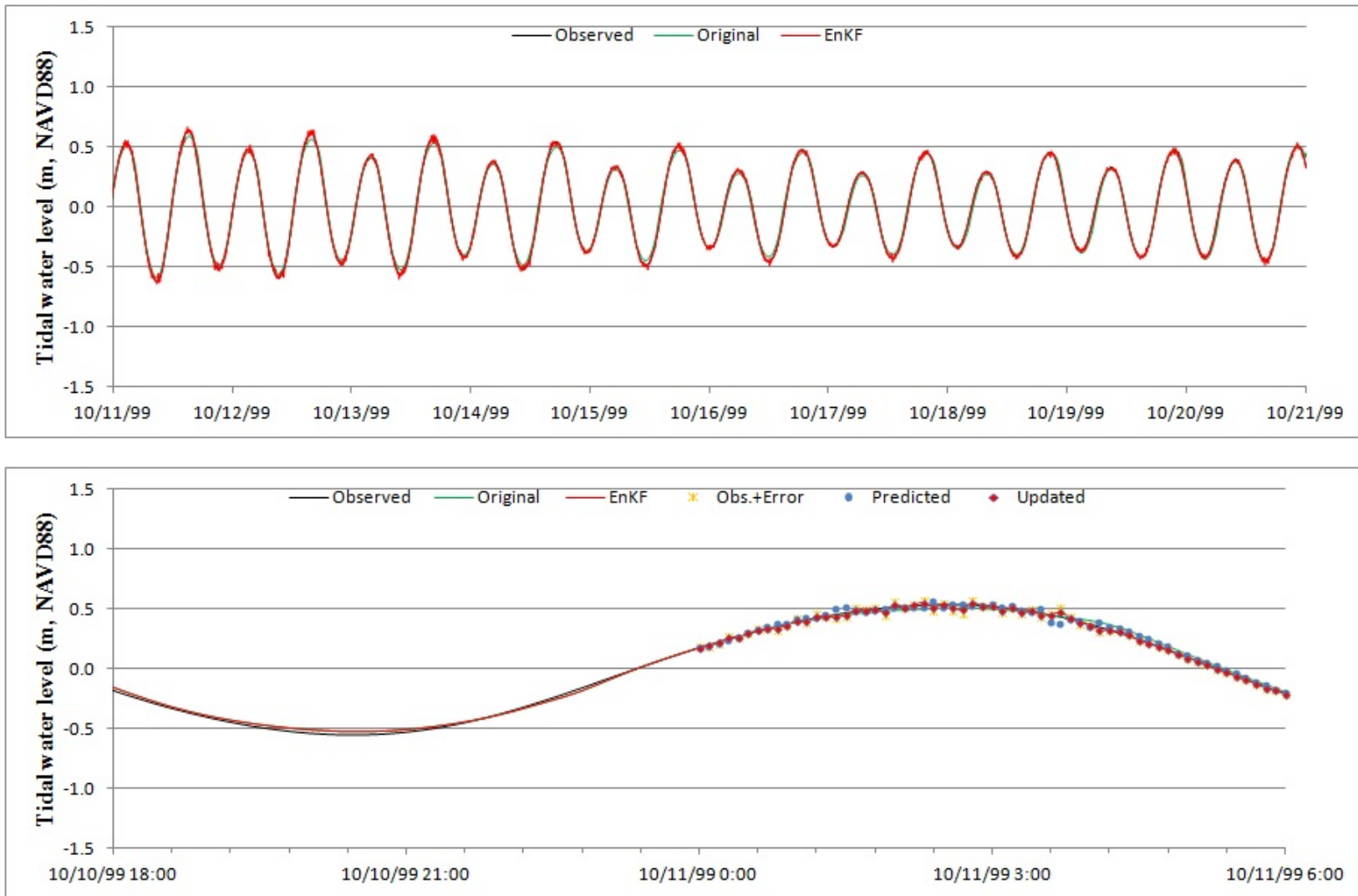
Figure 82 Time series of tidal water level during the last 10 days (upper) and at the first day (bottom) at Fulton from Simulation 1.

149
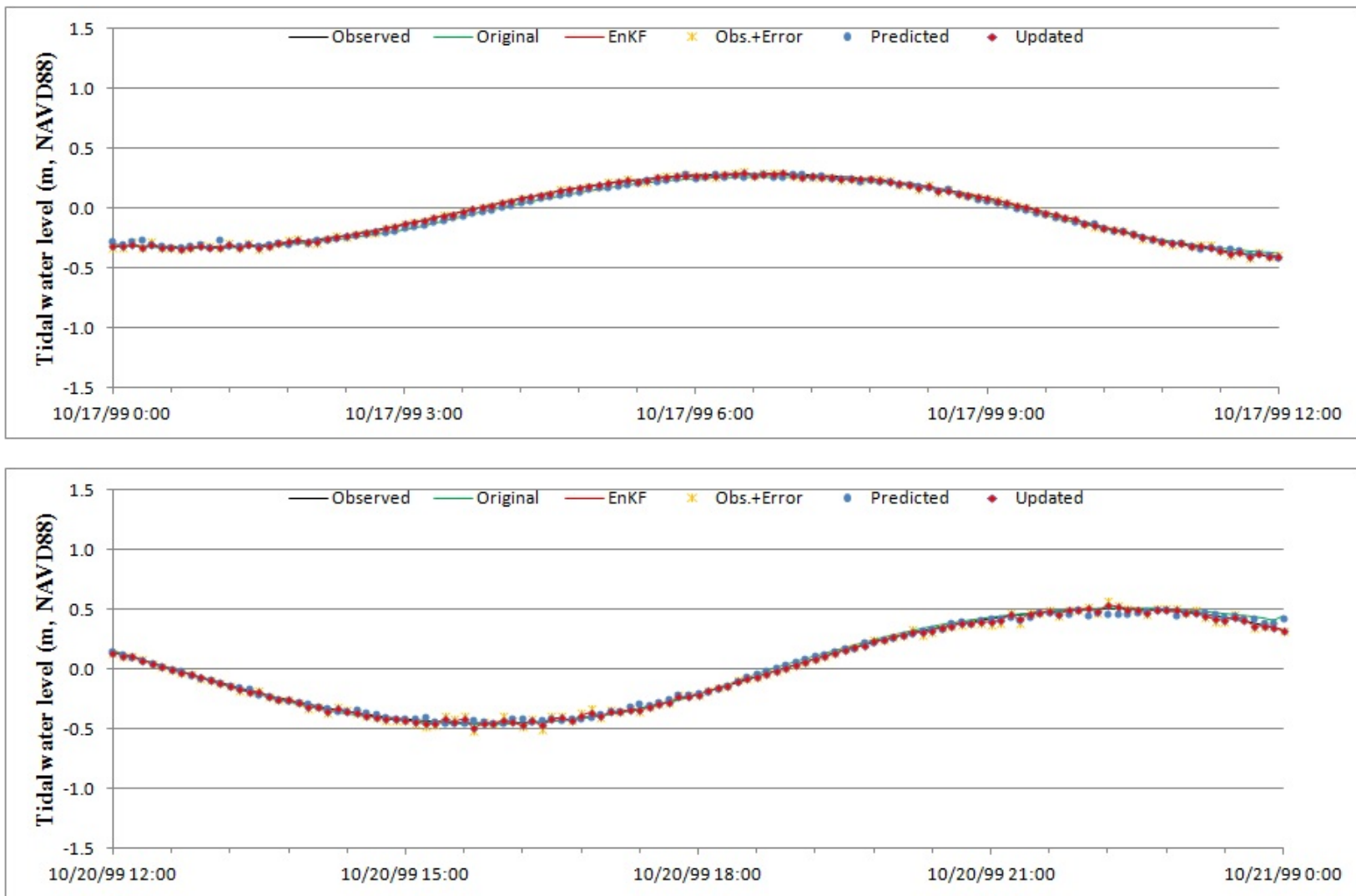
Figure 83   Time series of tidal water level at the middle day (upper) and the last day (bottom) at Fulton from Simulation 1.
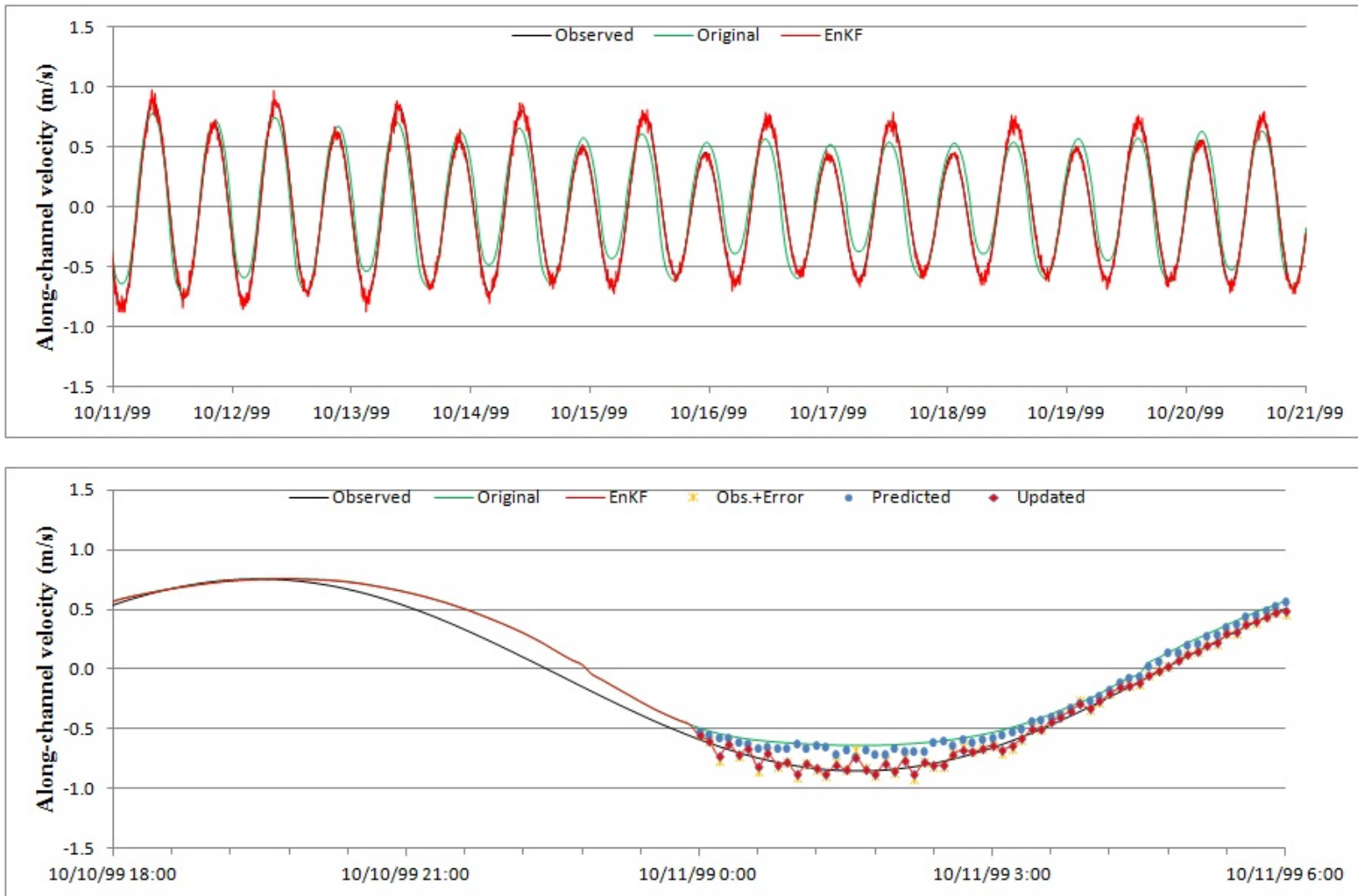
Figure 84 Time series of along-channel velocity during the last 10 days (upper) and the first day (bottom) at Fulton from Simulation 1.

Figure 85   Time series of along-channel velocity at the middle day (upper) and the last day (bottom) at Fulton from Simulation 1.

152

Figure 86   Time series of tidal water level during the last 10 days (upper) and at the first day (bottom) at Dames Point from Simulation 1.

Figure 87   Time series of tidal water level at the middle day (upper) and the last day (bottom) at Dames Point from Simulation 1.

Figure 88   Time series of along-channel velocity during the last 10 days (upper) and at the first day (bottom) at Dames Point from Simulation 1.

Figure 89   Time series of along-channel velocity at the middle day (upper) and the last day (bottom) at Dames Point from Simulation 1.
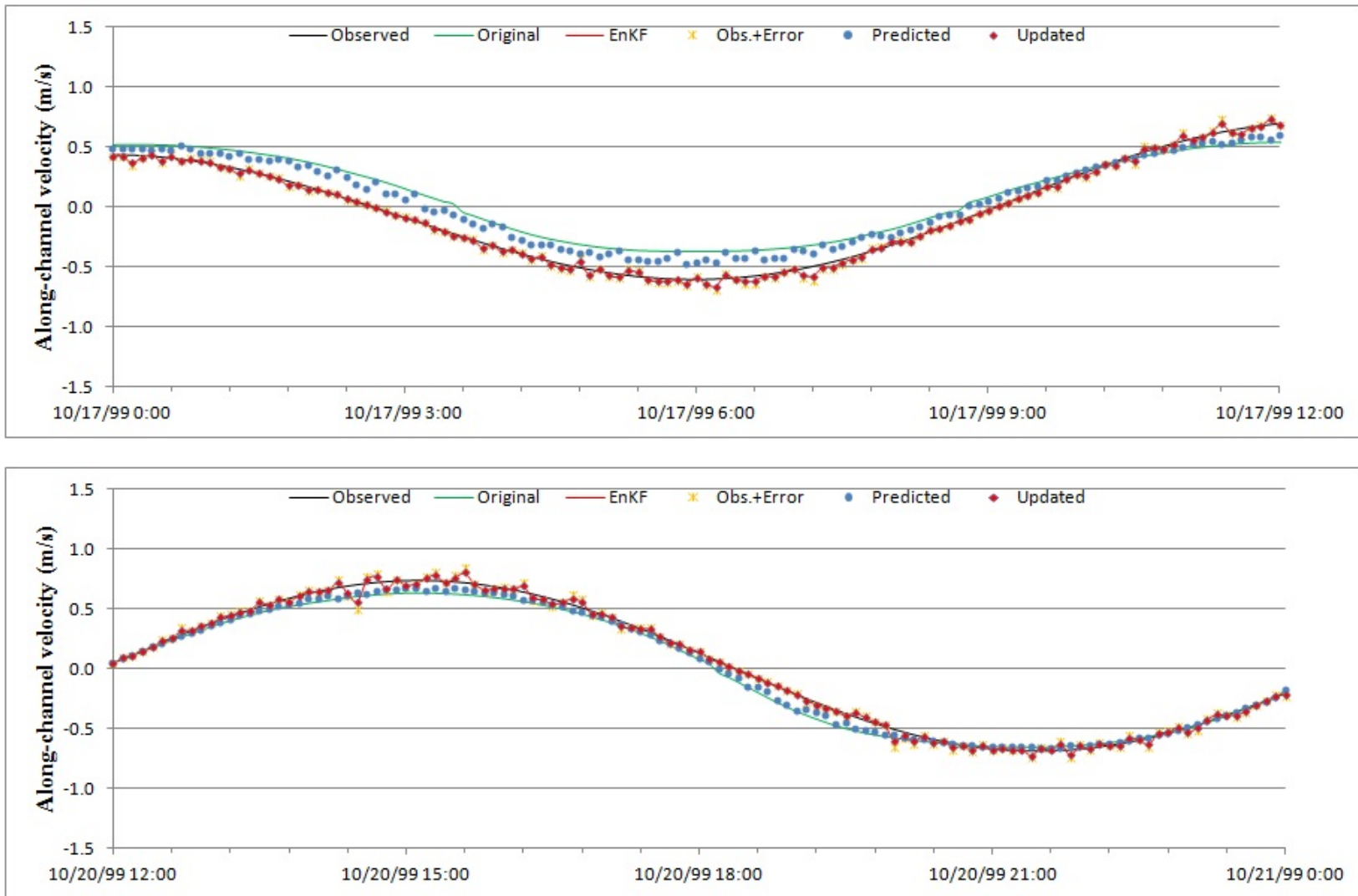
156

Figure 90   Time series of tidal water level during the last 10 days (upper) and at the first day (bottom) at Jacksonville from Simulation 1.

Figure 91   Time series of tidal water level at the middle day (upper) and the last day (bottom) at Jacksonville from Simulation 1.

Figure 92　　Time series of along-channel velocity during the last 10 days (upper) and at the first day (bottom) at Jacksonville from Simulation 1.
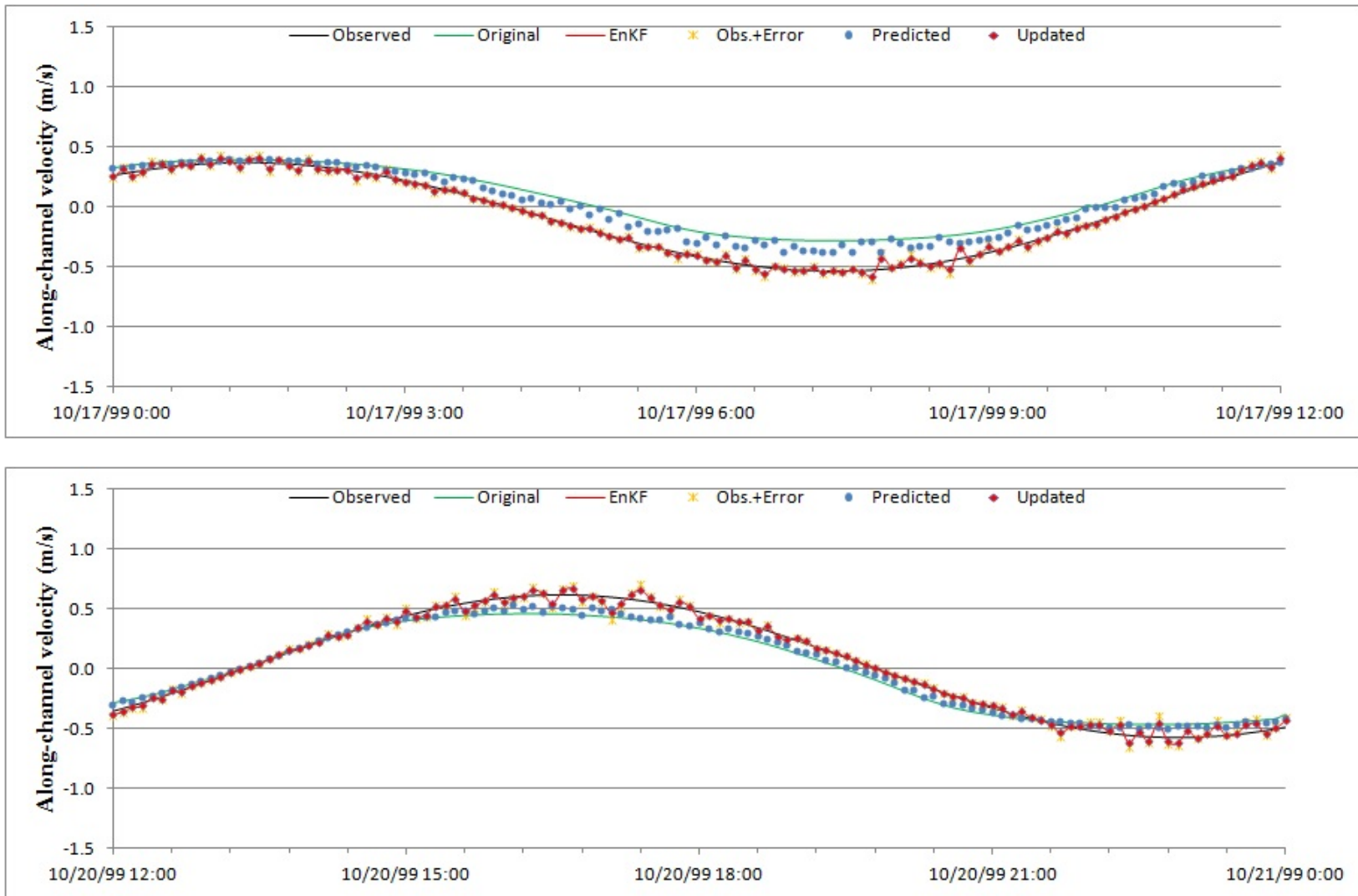
Figure 93   Time series of along-channel velocity at the middle day (upper) and the last day (bottom) at Jacksonville from Simulation 1.

Table 25   **RMSE of tidal water level at the gauging stations (Simulation 1).**

Gauge Name.	RMSE of tidal water level		
	Original (m)	EnKF (m)	$\dfrac{RMSE_{Original} - RMSE_{EnKF}}{RMSE_{Original}}(\%)$
Fulton	2.481E-02	2.028E-02	18.3
Dames Point	4.617E-02	1.967E-02	57.4
Jacksonville	4.695E-02	1.772E-02	62.3

Table 26   **RMSE of along-channel velocity at the gauging stations (Simulation 1).**

Gauge Name.	RMSE of along-channel velocity		
	Original (m/s)	EnKF (m/s)	$\dfrac{RMSE_{Original} - RMSE_{EnKF}}{RMSE_{Original}}(\%)$
Fulton	1.346E-01	3.710E-02	72.4
Dames Point	1.544E-01	3.501E-02	77.3
Jacksonville	1.343E-01	3.490E-02	74.0
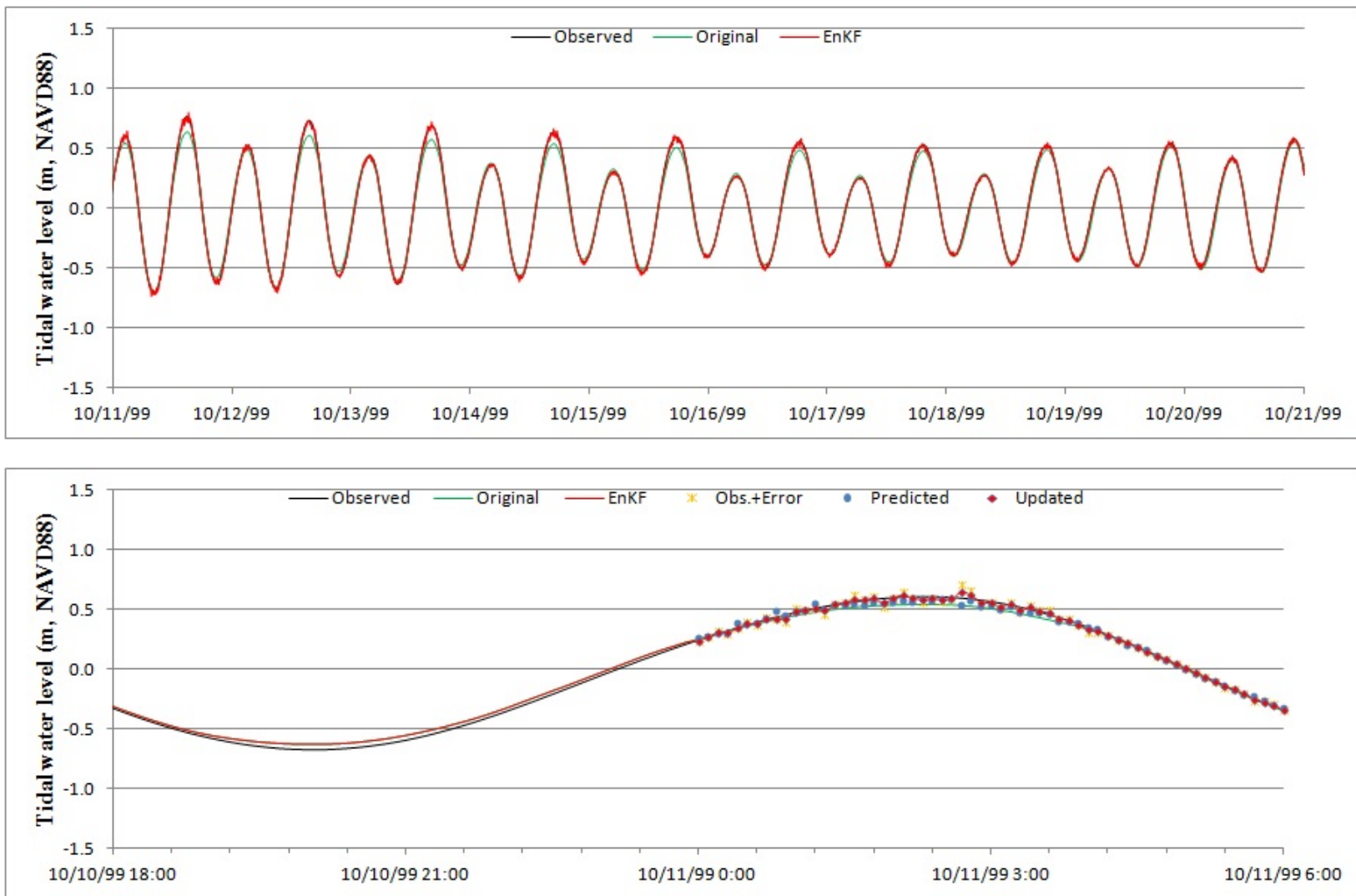
Figure 94   Time series of tidal water level during the last 10 days (upper) and at the first day (bottom) at Mayport from Simulation 2.

162
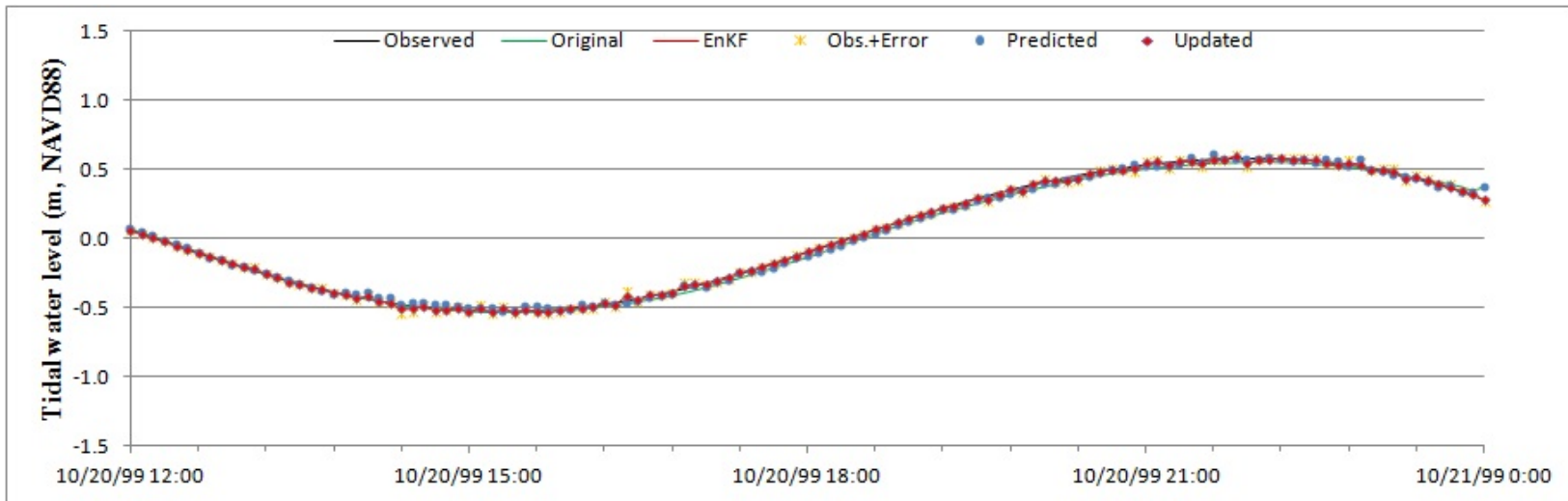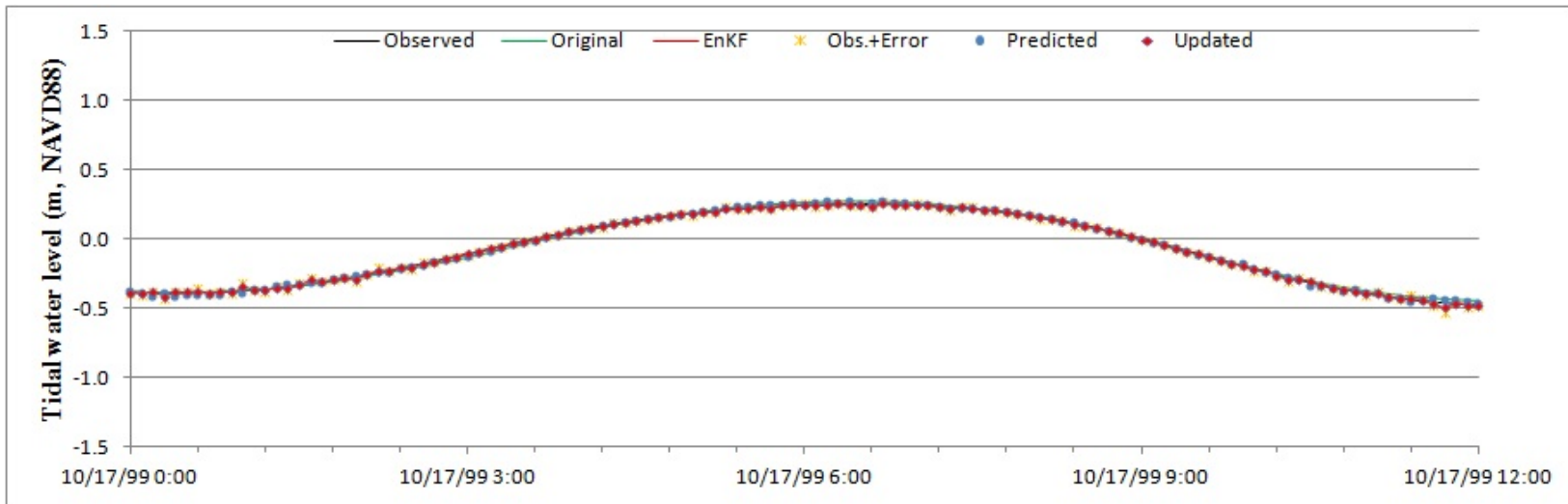
Figure 95   Time series of tidal water level at the middle day (upper) and the last day (bottom) at Mayport from Simulation 2.
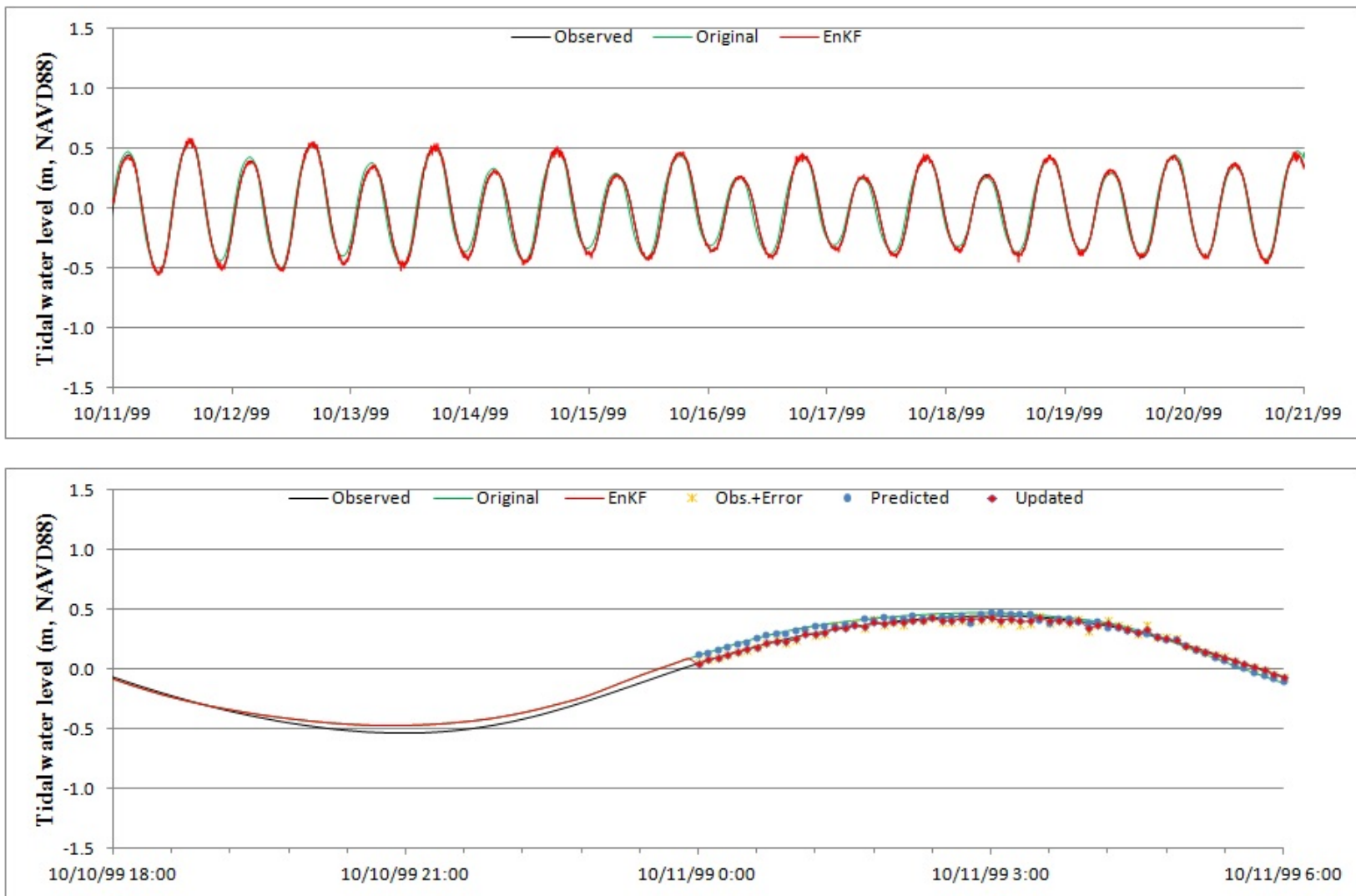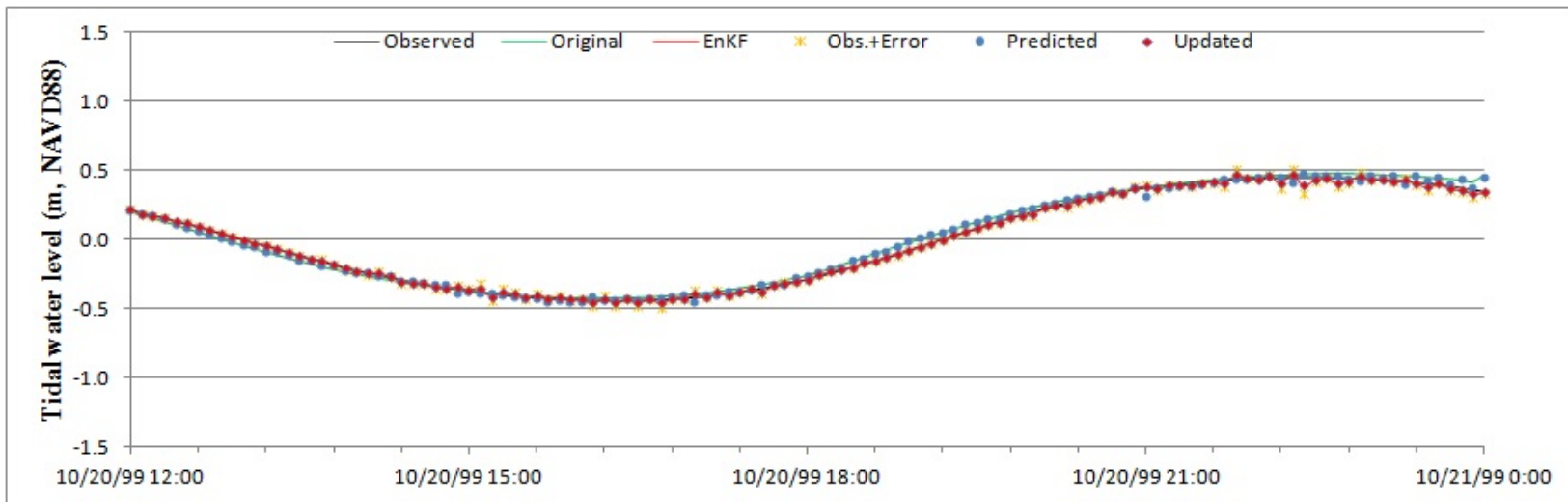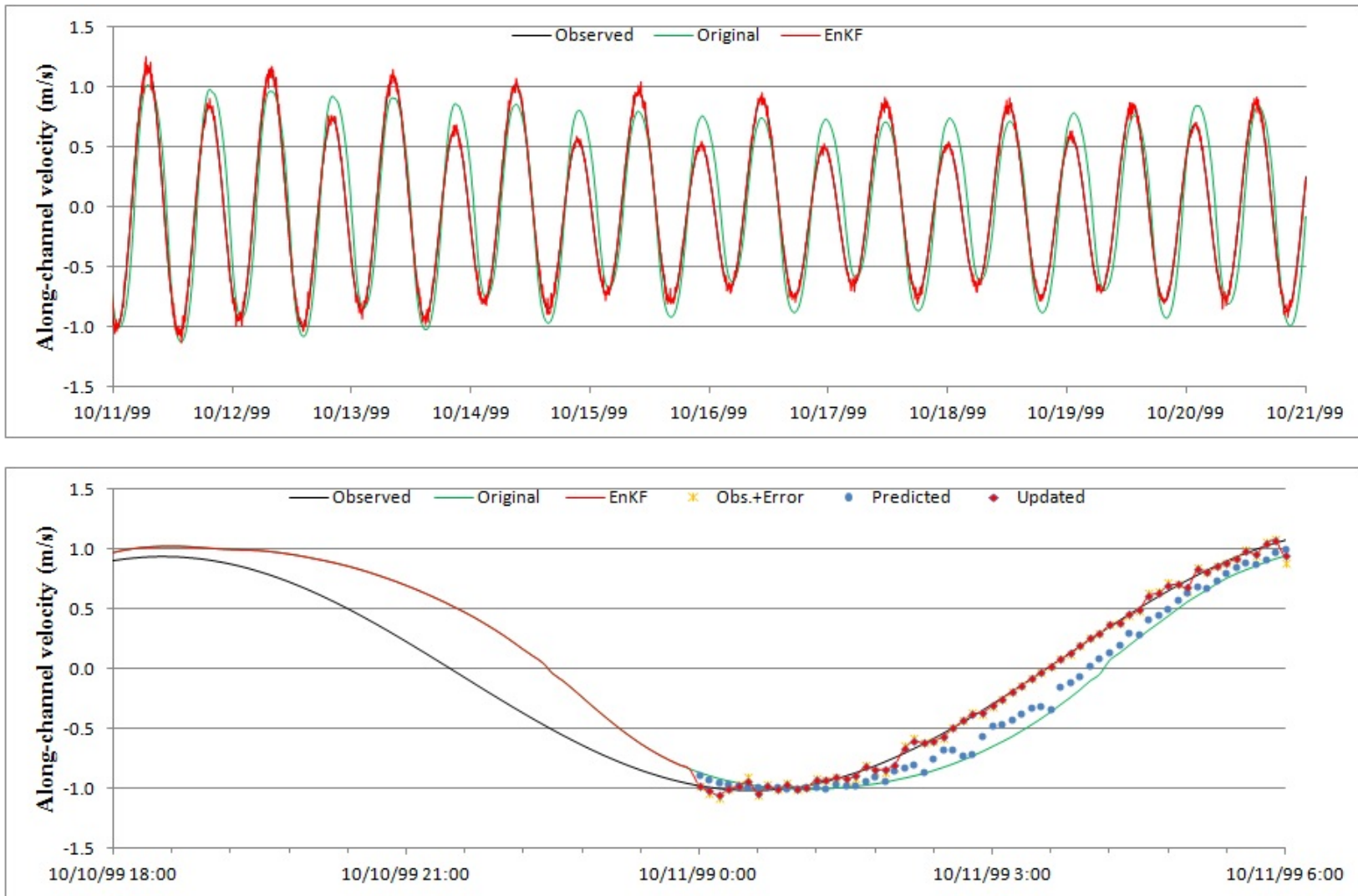
Figure 96 Time series of along-channel velocity during the last 10 days (upper) and at the first day (bottom) at Mayport from Simulation 2.
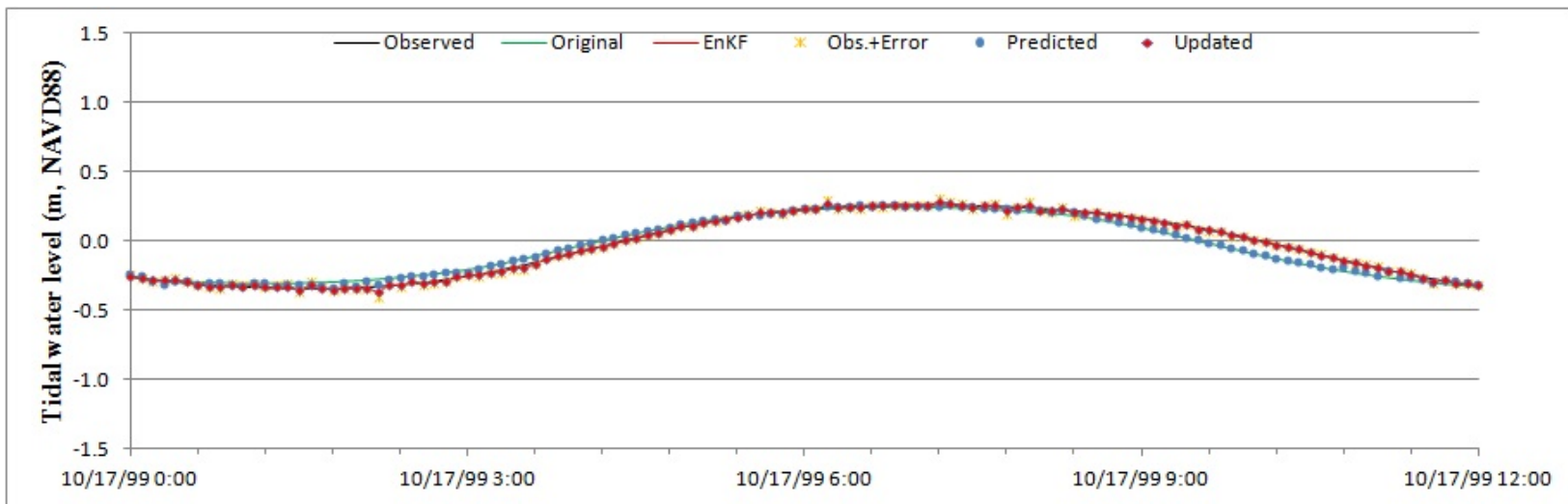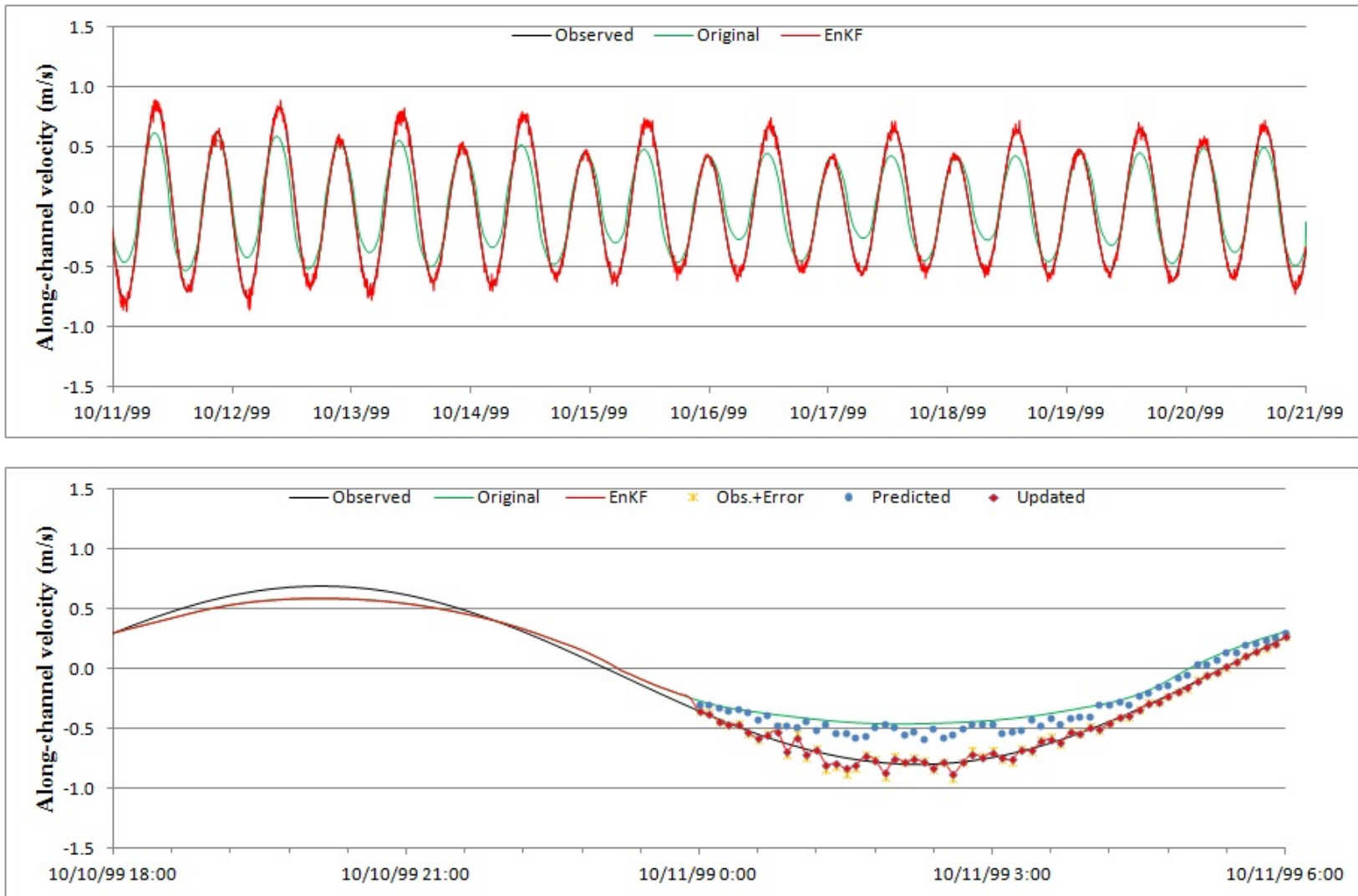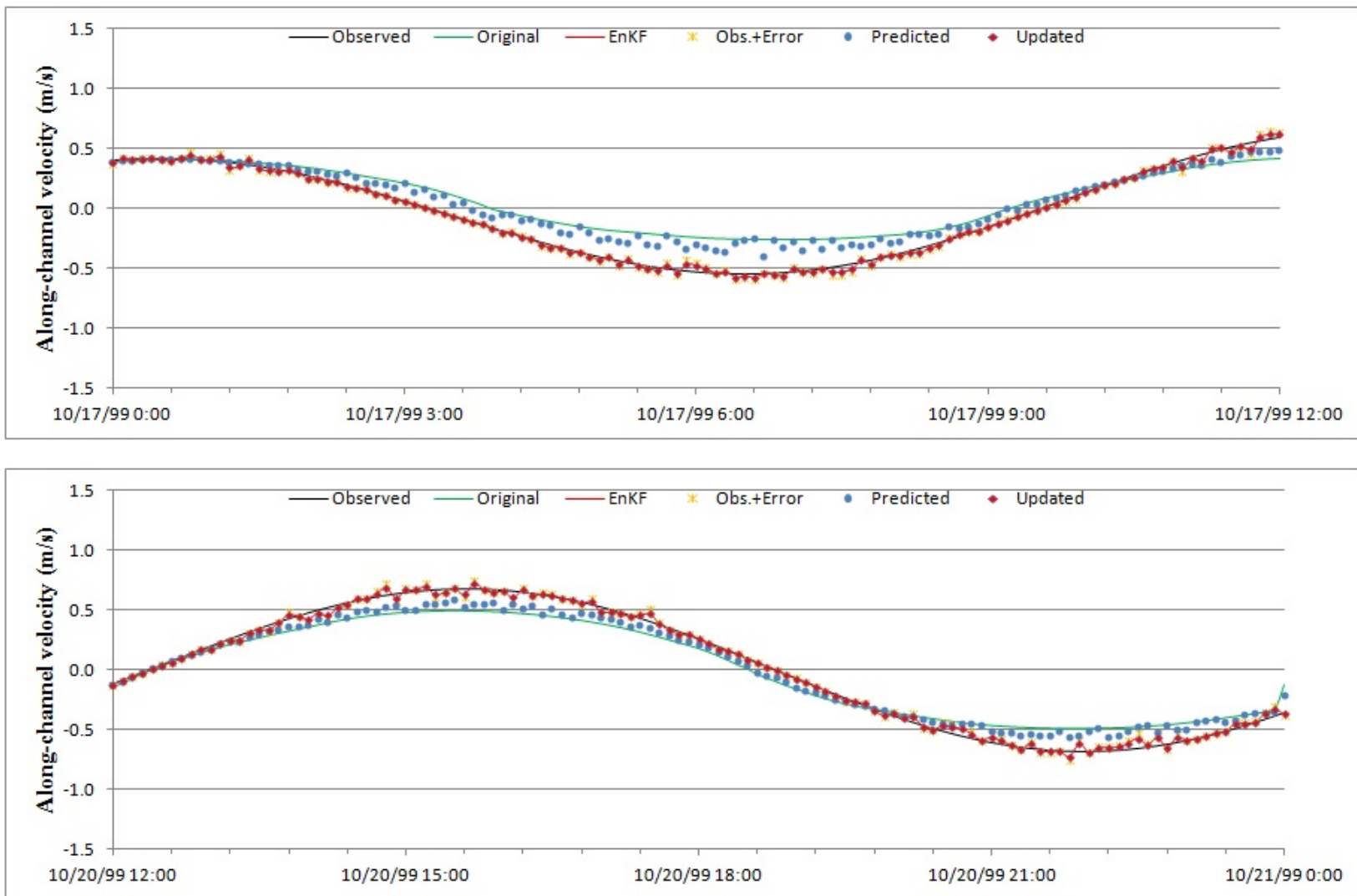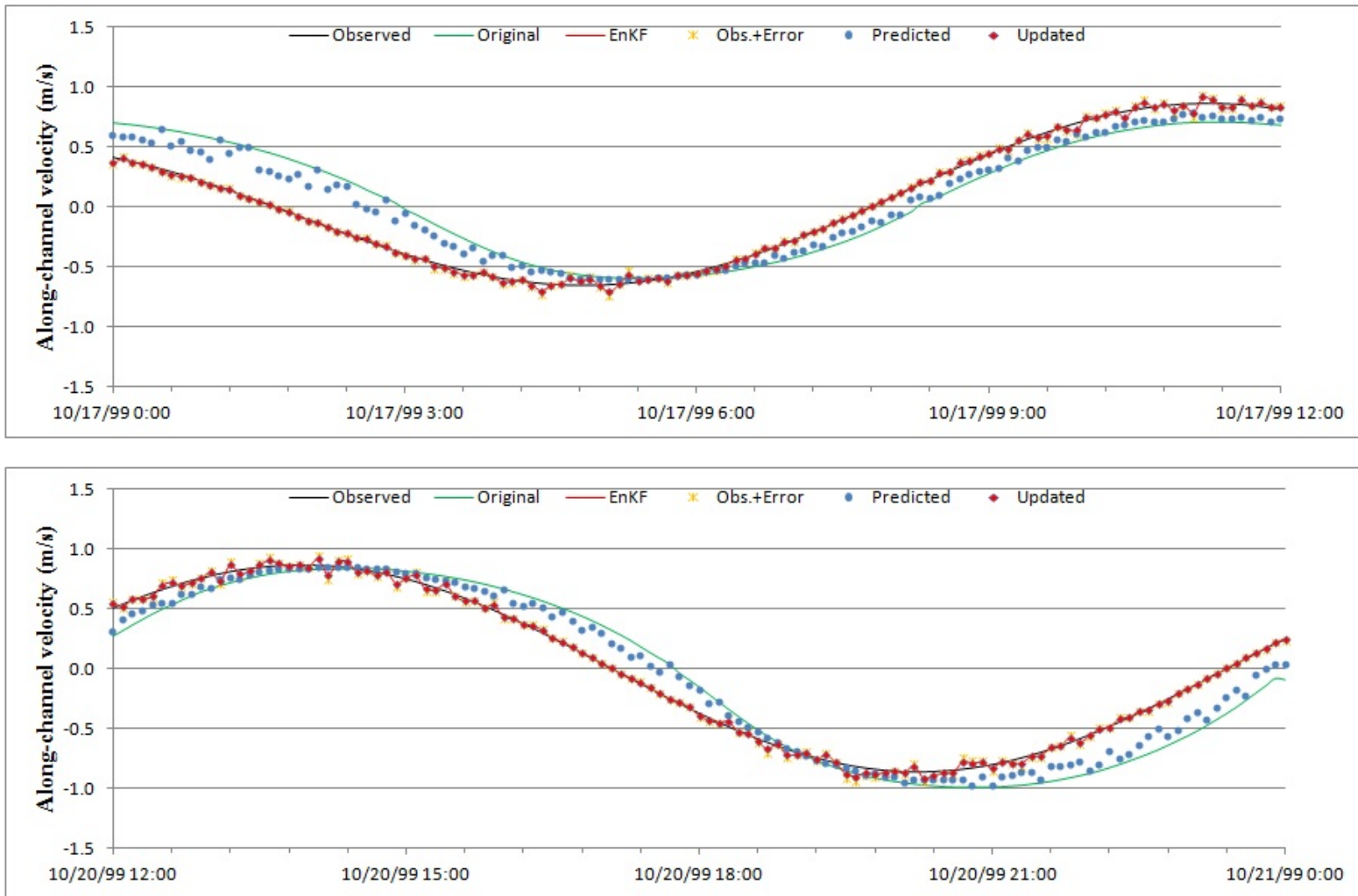
Figure 97   Time series of along-channel velocity at the middle day (upper) and the last day (bottom) at Mayport from Simulation 2.

165

Figure 98　　Time series of tidal water level during the last 10 days (upper) and at the first day (bottom) at Dames Point from Simulation 2.
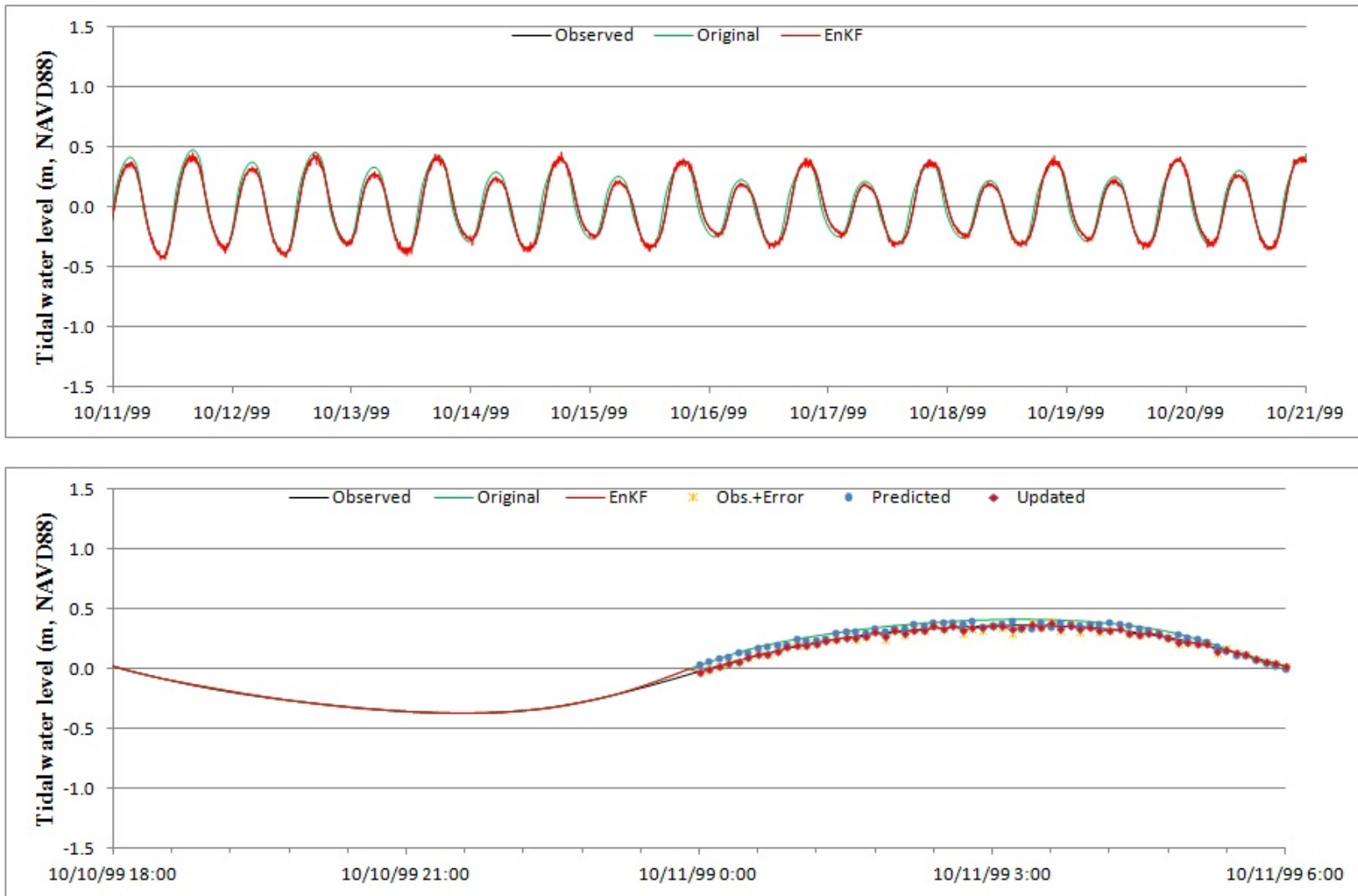
Figure 99   **Time series of tidal water level at the middle day (upper) and the last day (bottom) at Dames Point from Simulation 2.**
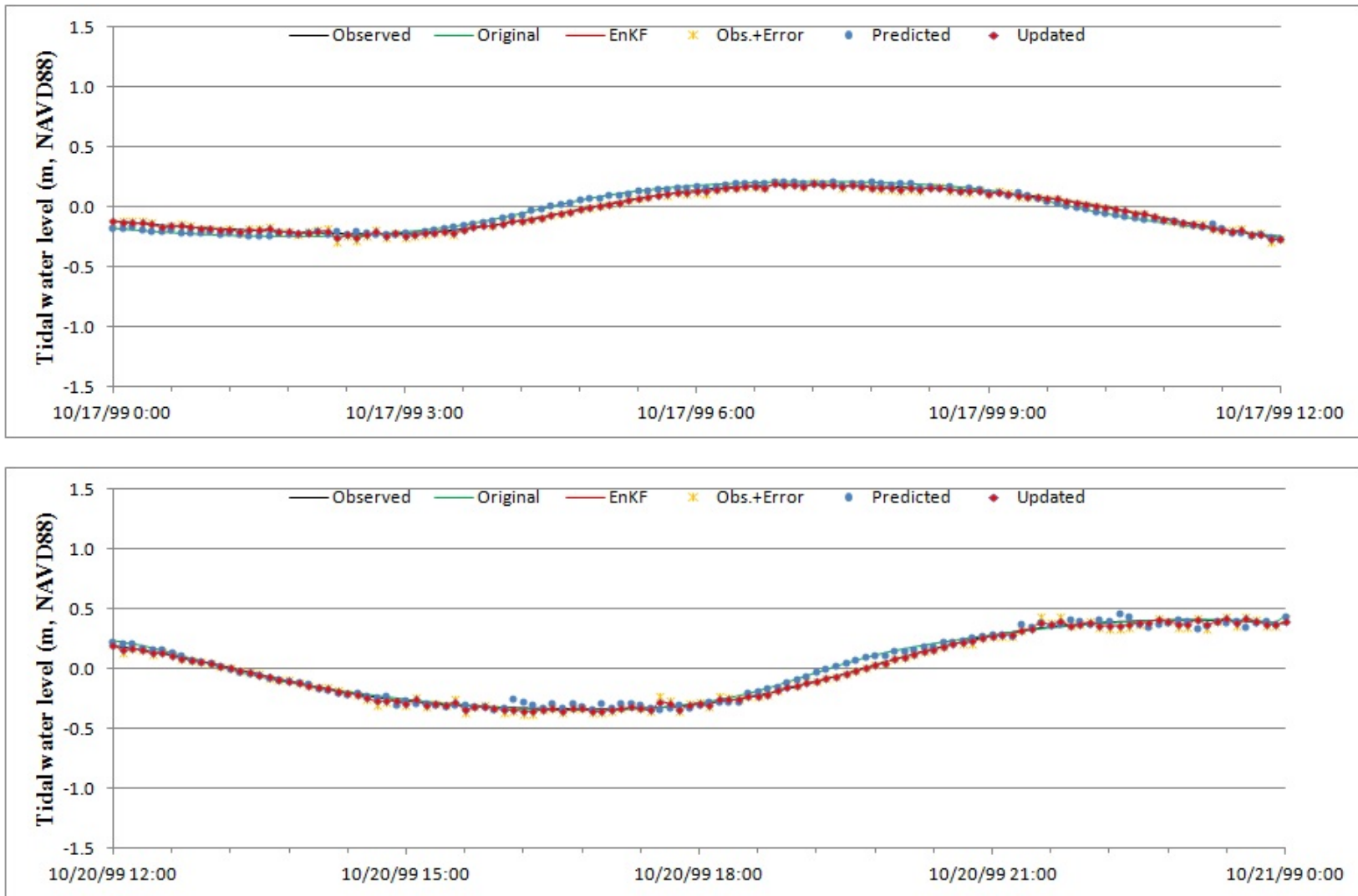
167

Figure 100 Time series of along-channel velocity during the last 10 days (upper) and at the first day (bottom) at Dames Point from Simulation 2.
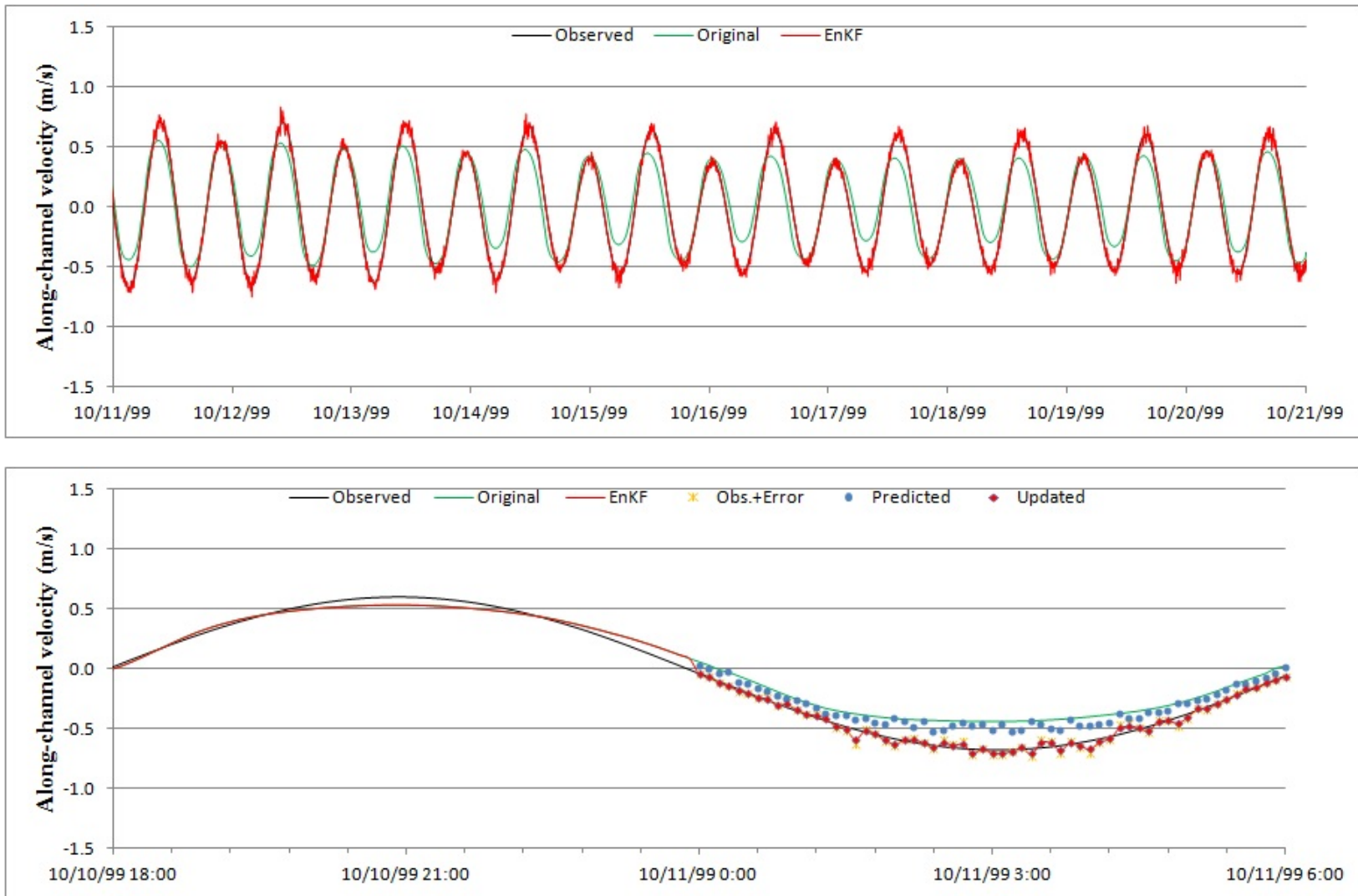
Figure 101   Time series of along-channel velocity at the middle day (upper) and the last day (bottom) at Dames Point from Simulation 2.

169

Figure 102   Time series of tidal water level during the last 10 days (upper) and at the first day (bottom) at Jacksonville from Simulation 2.

Figure 103   Time series of tidal water level at the middle day (upper) and the last day (bottom) at Jacksonville from Simulation 2.

Figure 104 Time series of along-channel velocity during the last 10 days (upper) and at the first day (bottom) at Jacksonville from Simulation 2.

172

Figure 105 Time series of along-channel velocity at the middle day (upper) and the last day (bottom) at Jacksonville from Simulation 2.

Table 27   **RMSE of tidal water level at the gauging stations (Simulation 2).**

Gauge Name.	RMSE of tidal water level		
	Original (m)	EnKF (m)	$\dfrac{RMSE_{Original} - RMSE_{EnKF}}{RMSE_{Original}}(\%)$
Mayport	3.2621E-02	2.216E-02	32.1
Dames Point	4.617E-02	1.931E-02	58.2
Jacksonville	4.695E-02	1.834E-02	60.9

Table 28   **RMSE of along-channel velocity at the gauging stations (Simulation 2).**

| Gauge Name.	RMSE of along-channel velocity		
	Original (m/s)	EnKF (m/s)	$\dfrac{RMSE_{Original} - RMSE_{EnKF}}{RMSE_{Original}}(\%)$
Mayport	2.354E-01	3.923E-02	83.3
Dames Point	1.544E-01	3.409E-02	77.9
Jacksonville	1.343E-01	3.564E-02	73.5
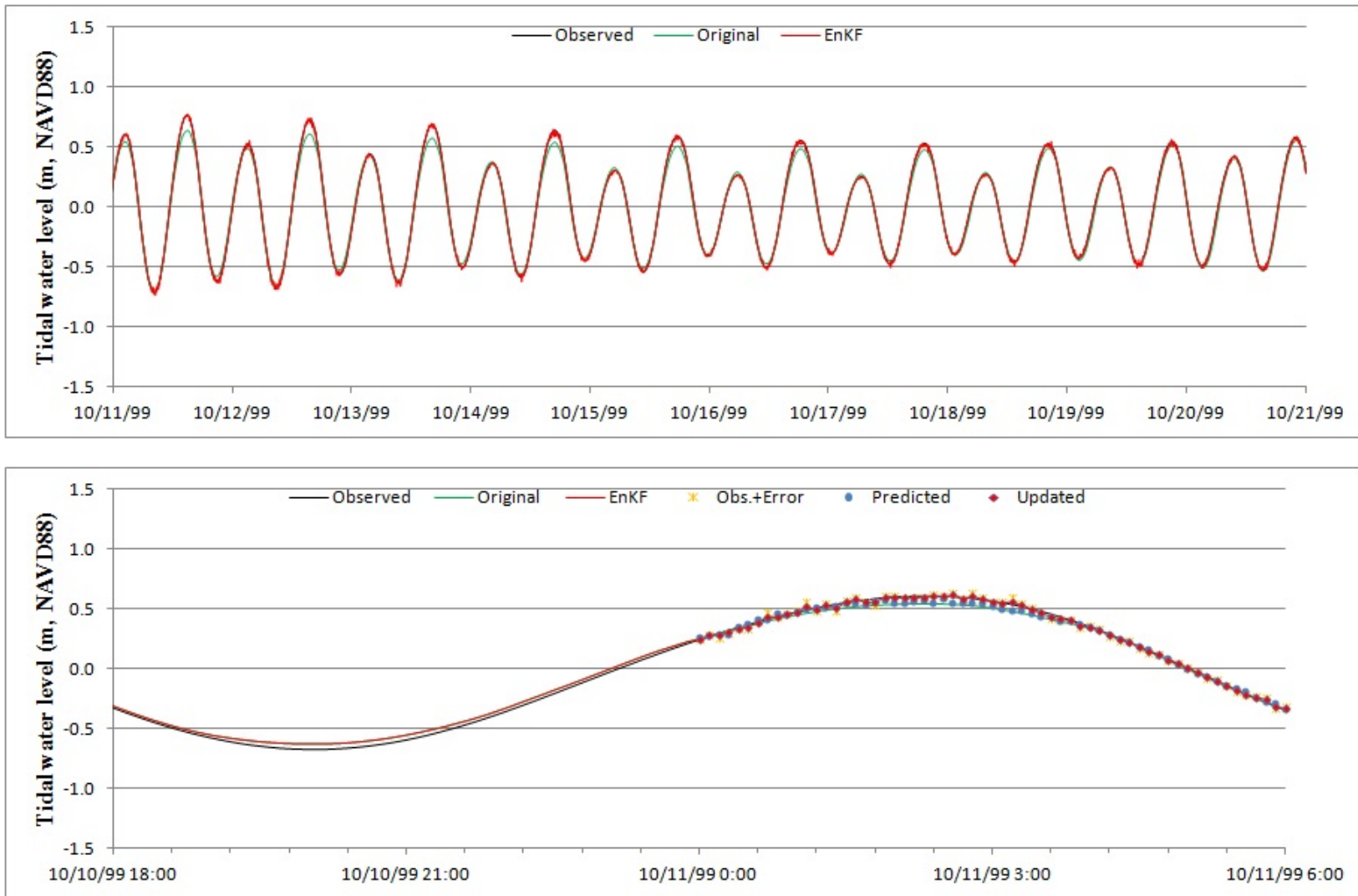
Figure 106   Time series of tidal water level during the last 10 days (upper) and at the first day (bottom) at Mayport from Simulation 3.
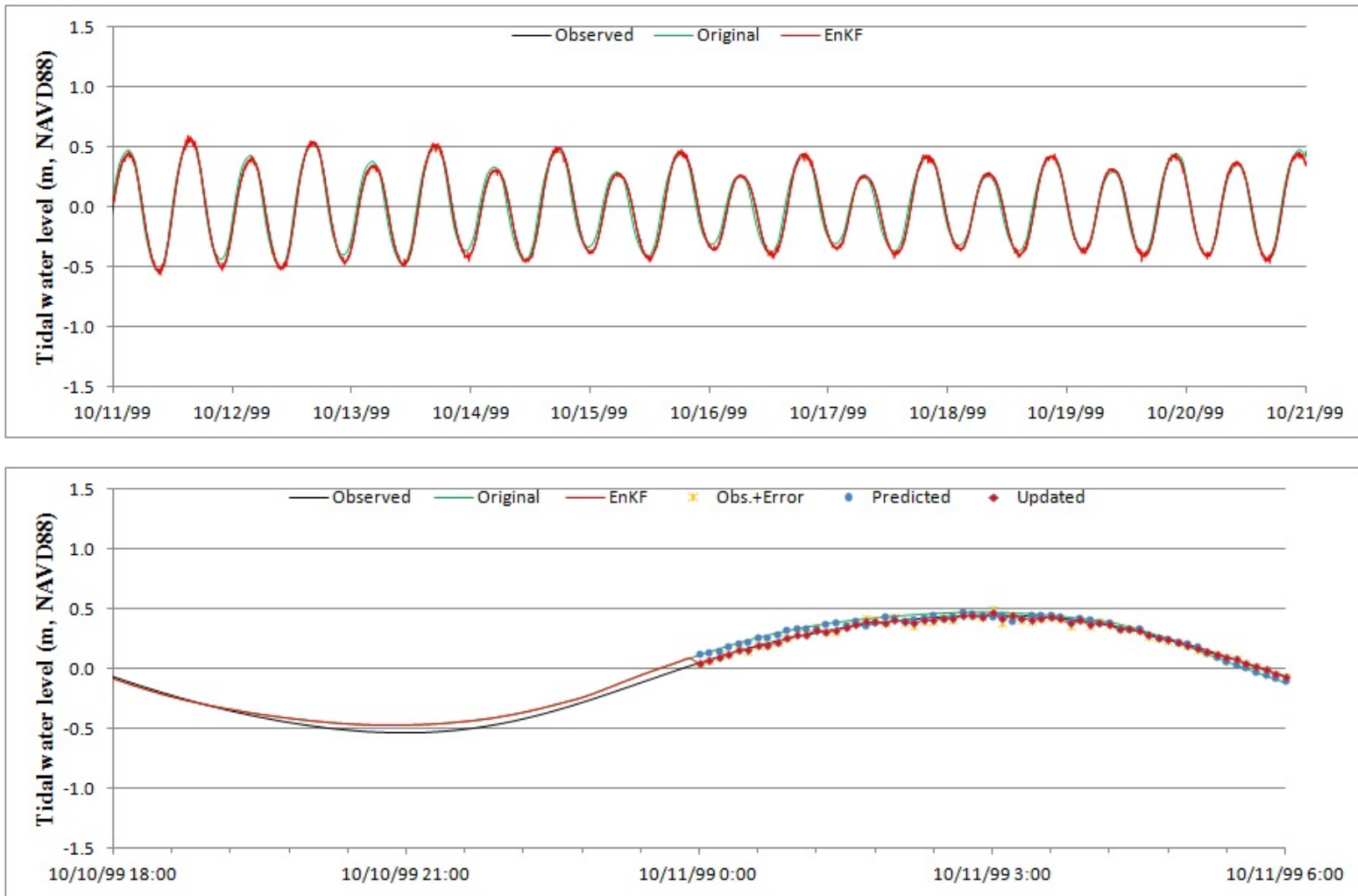
175
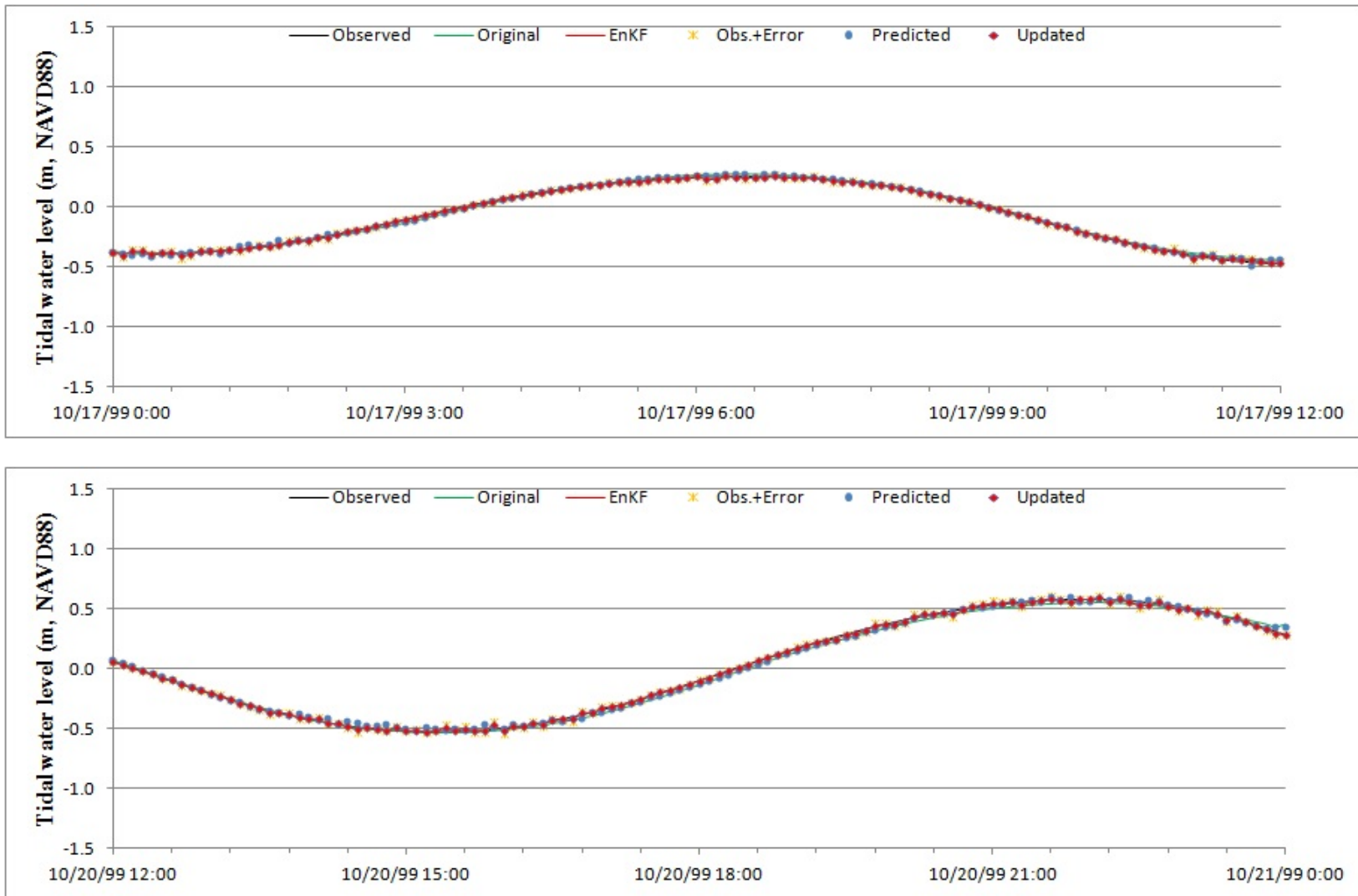
Figure 107 Time series of tidal water level at the middle day (upper) and the last day (bottom) at Mayport from Simulation 3.
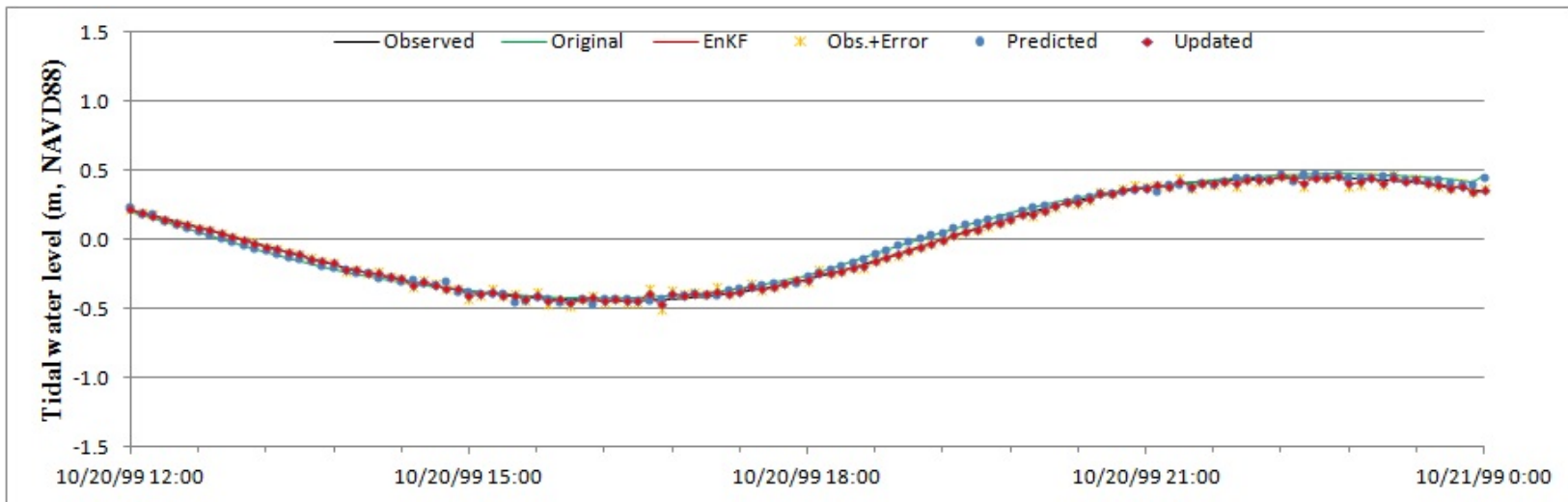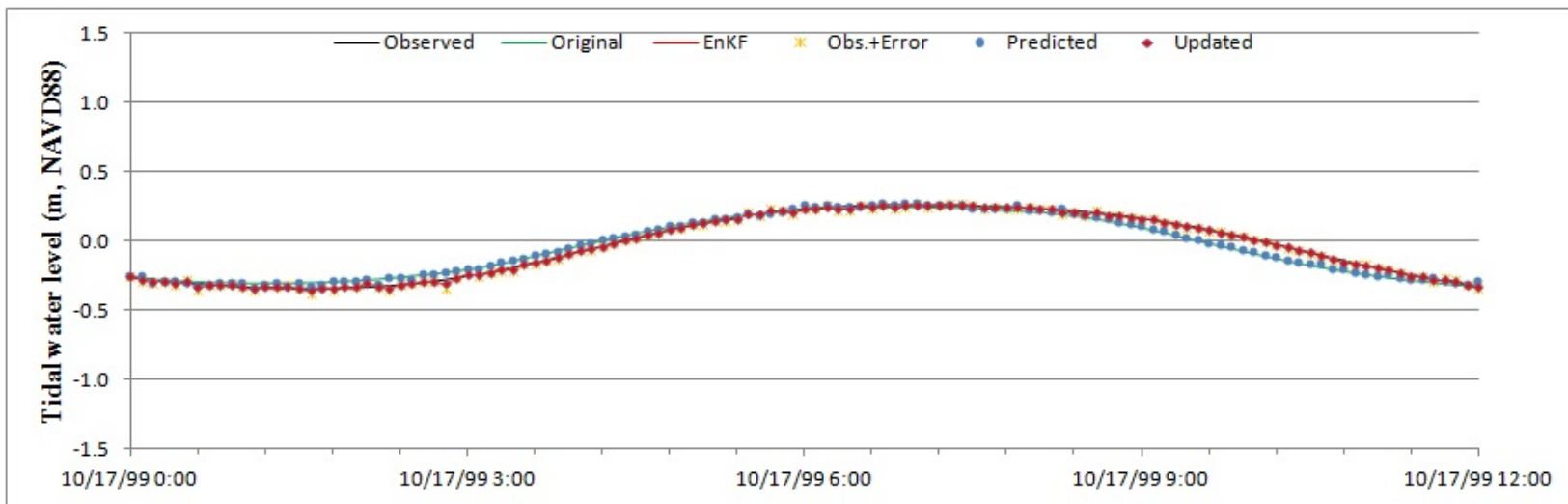
Figure 108   Time series of along-channel velocity during the last 10 days (upper) and at the first day (bottom) at Mayport from Simulation 3.
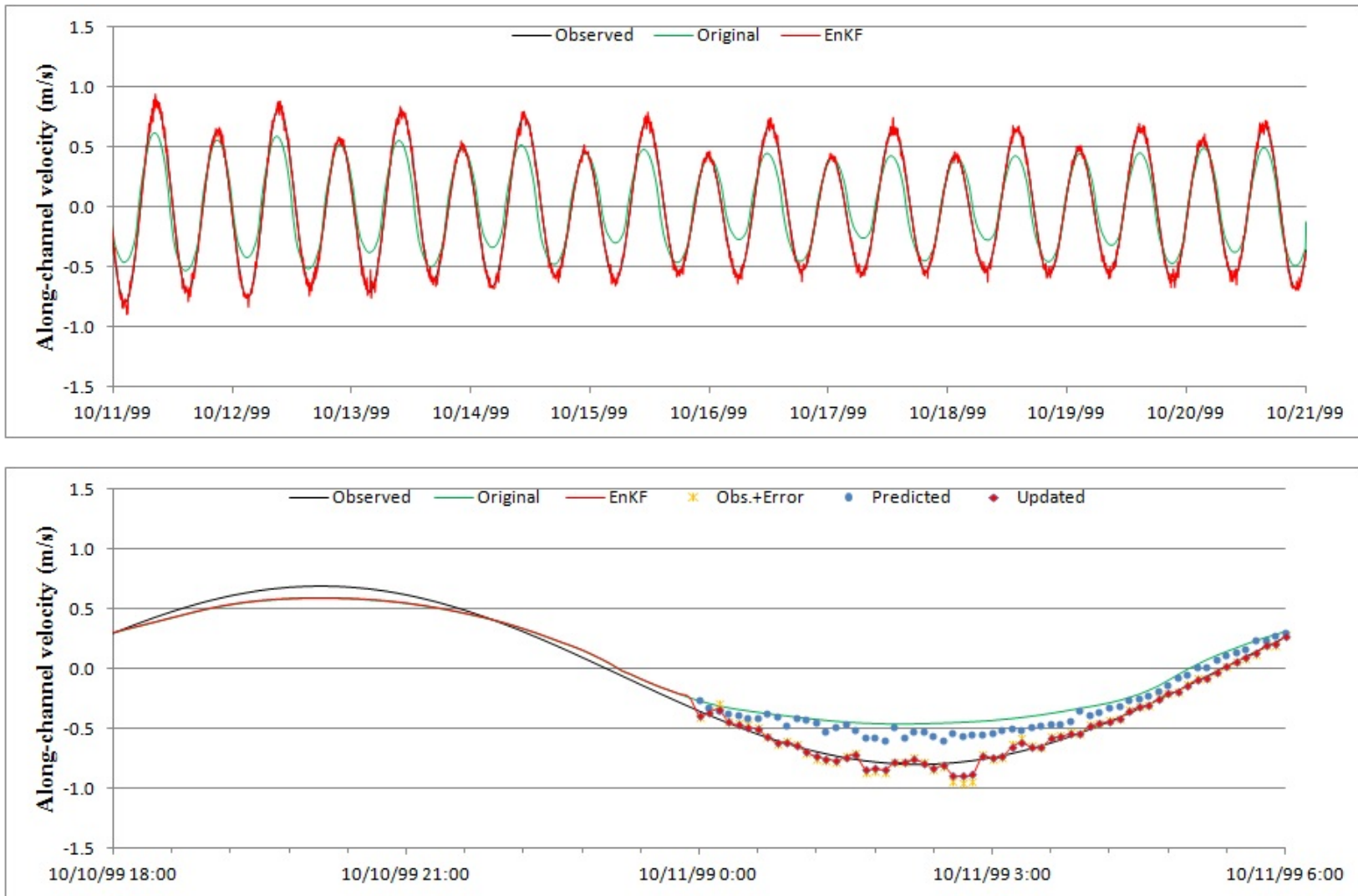
Figure 109   Time series of along-channel velocity at the middle day (upper) and the last day (bottom) at Mayport from Simulation 3.

178

Figure 110   Time series of tidal water level during the last 10 days (upper) and at the first day (bottom) at Fulton from Simulation 3.

Figure 111   Time series of tidal water level at the middle day (upper) and the last day (bottom) at Fulton from Simulation 3.

Figure 112 Time series of along-channel velocity during the last 10 days (upper) and at the first day (bottom) at Fulton from Simulation 3.
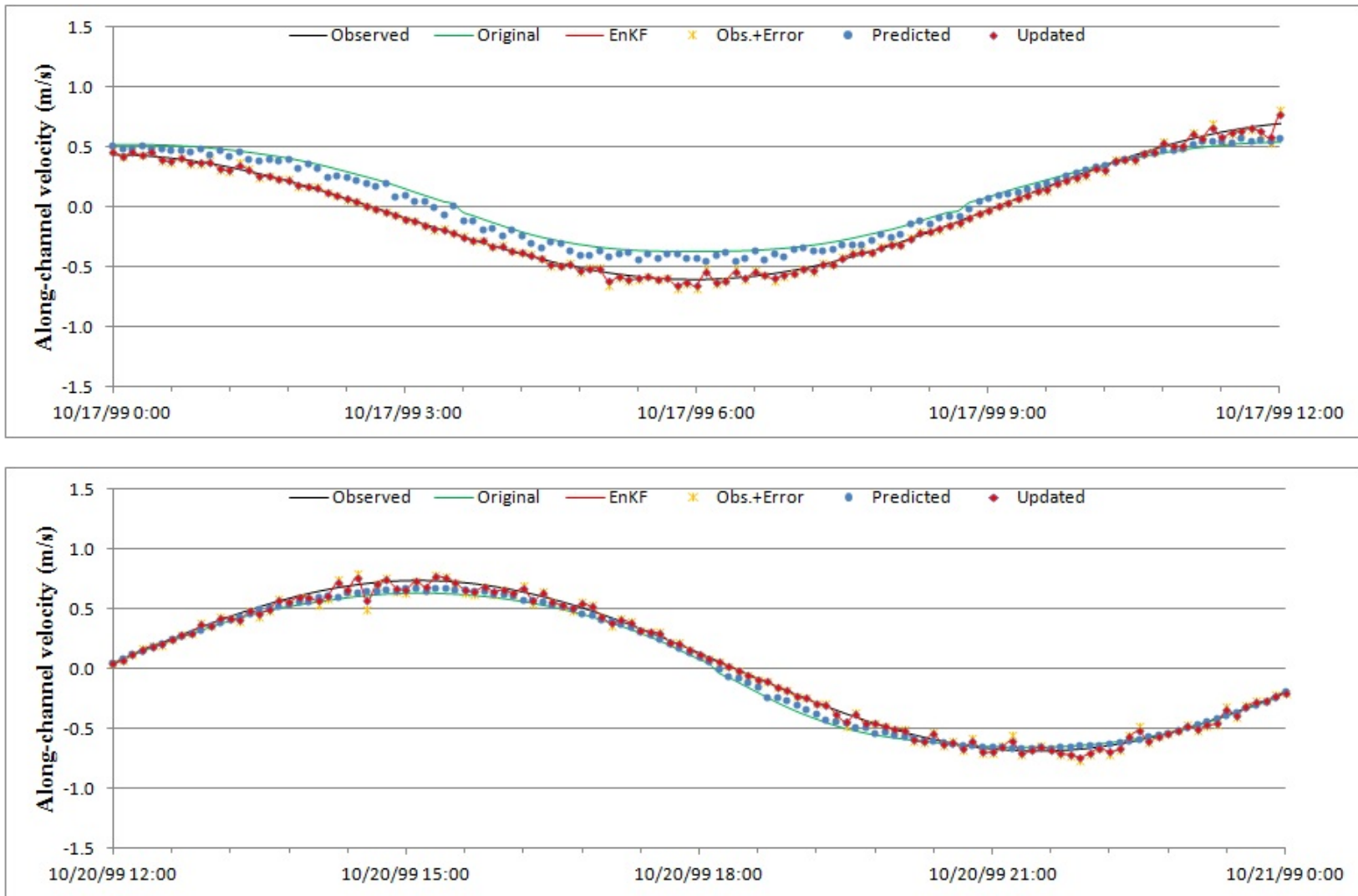
Figure 113 Time series of along-channel velocity at the middle day (upper) and the last day (bottom) at Fulton from Simulation 3.

Figure 114 Time series of tidal water level during the last 10 days (upper) and at the first day (bottom) at Jacksonville from Simulation 3.
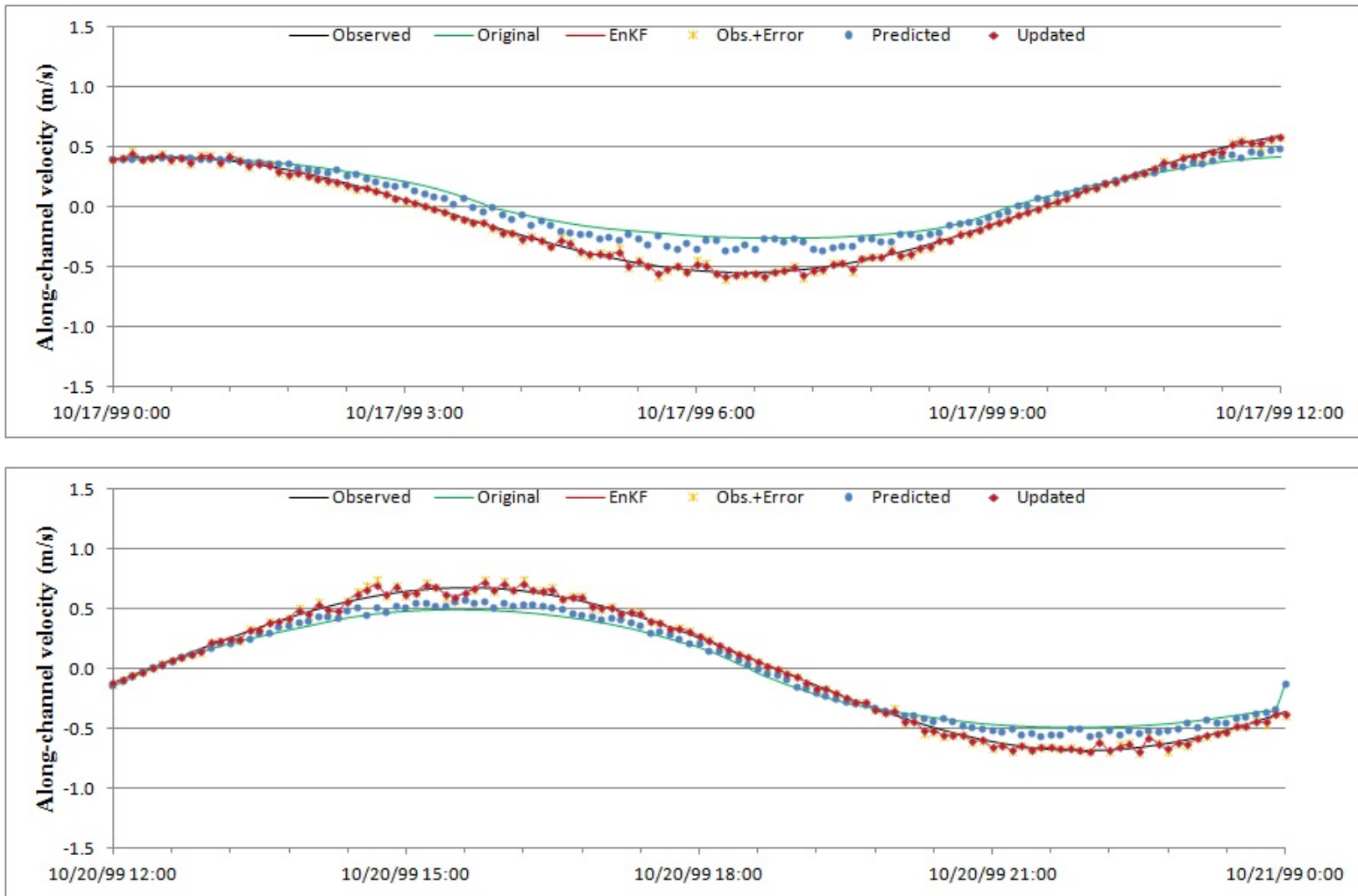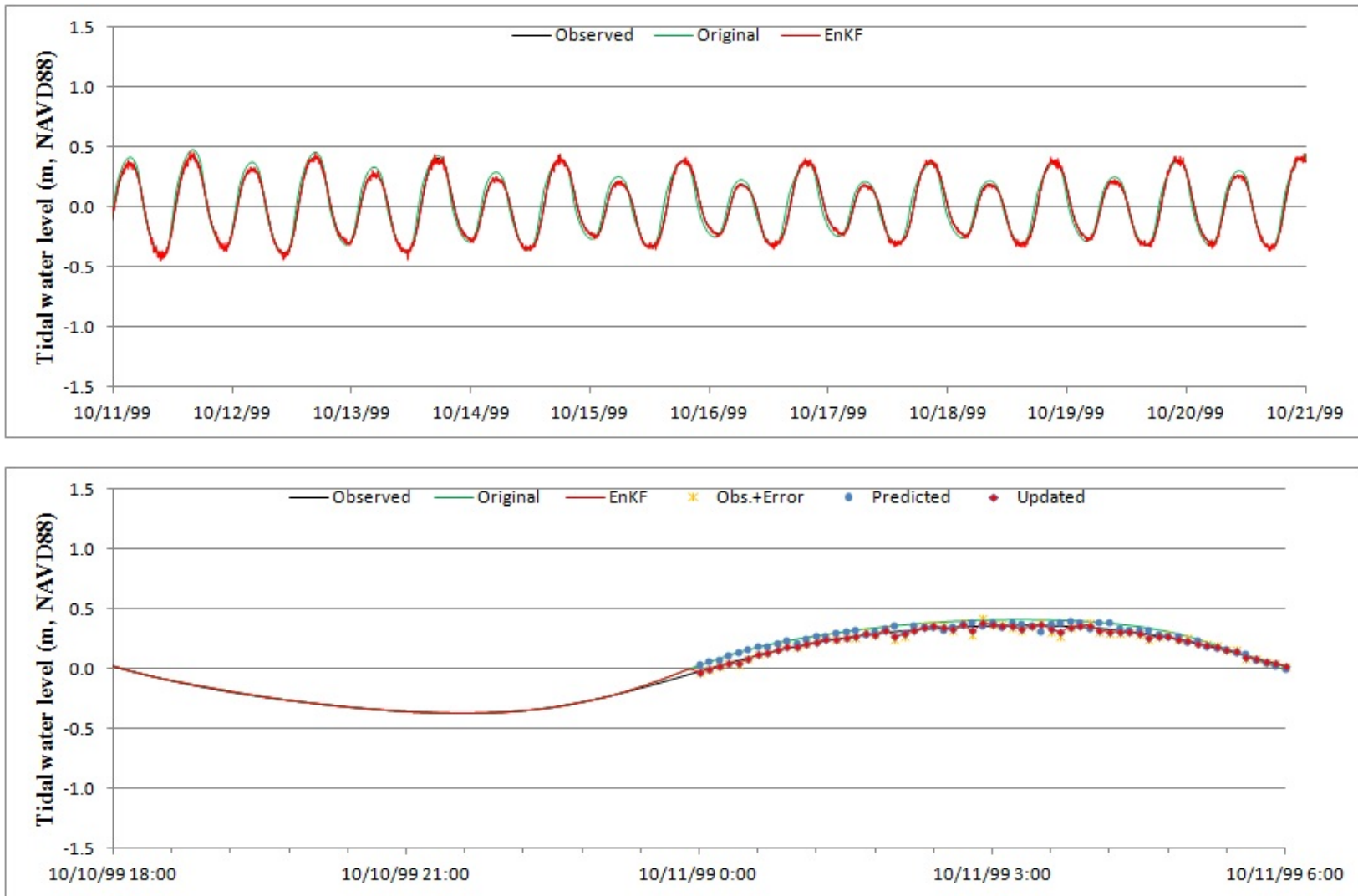
Figure 115   Time series of tidal water level at the middle day (upper) and the last day (bottom) at Jacksonville from Simulation 3.

Figure 116　Time series of along-channel velocity during the last 10 days (upper) and at the first day (bottom) at Jacksonville from Simulation 3.
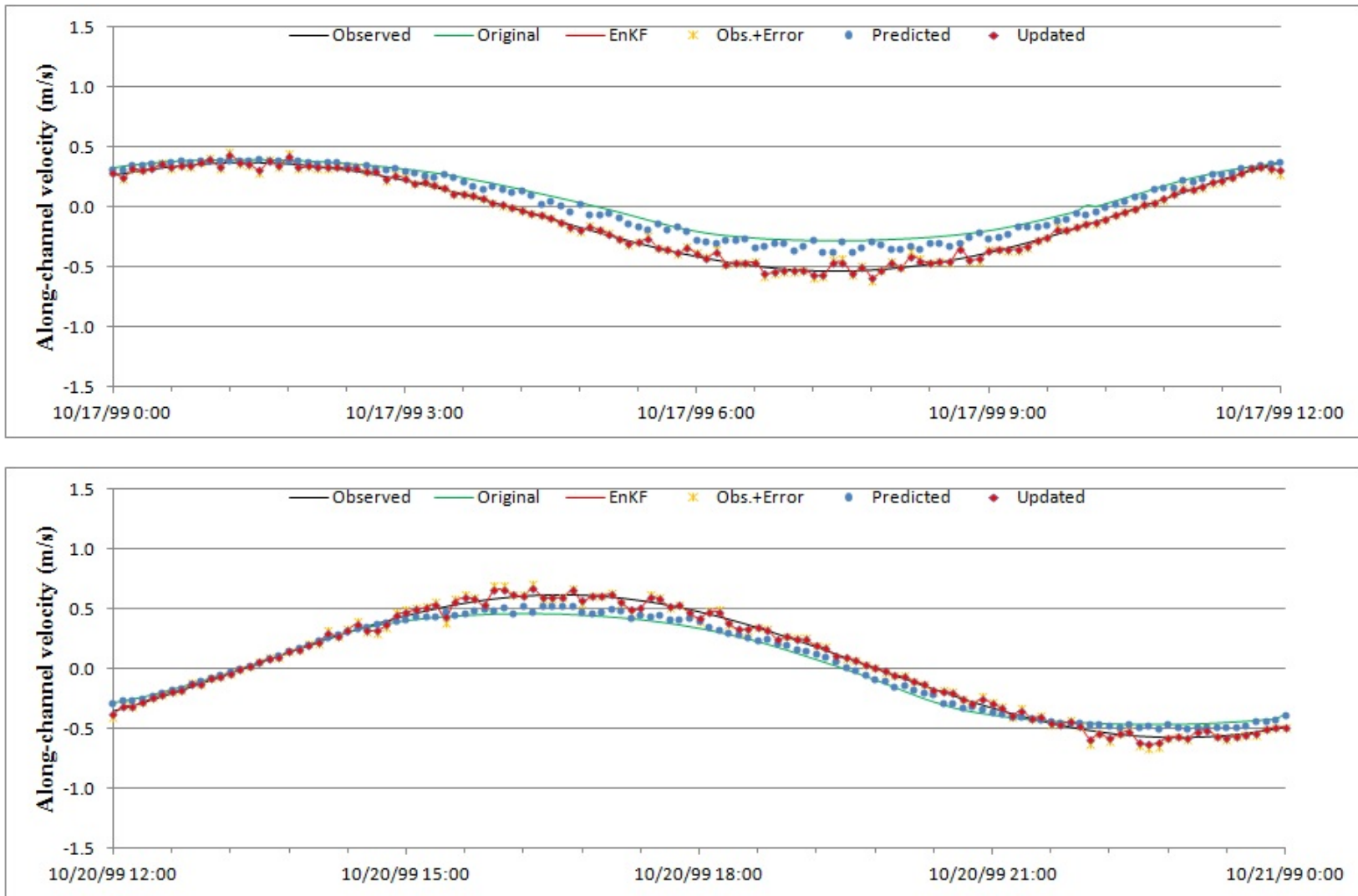
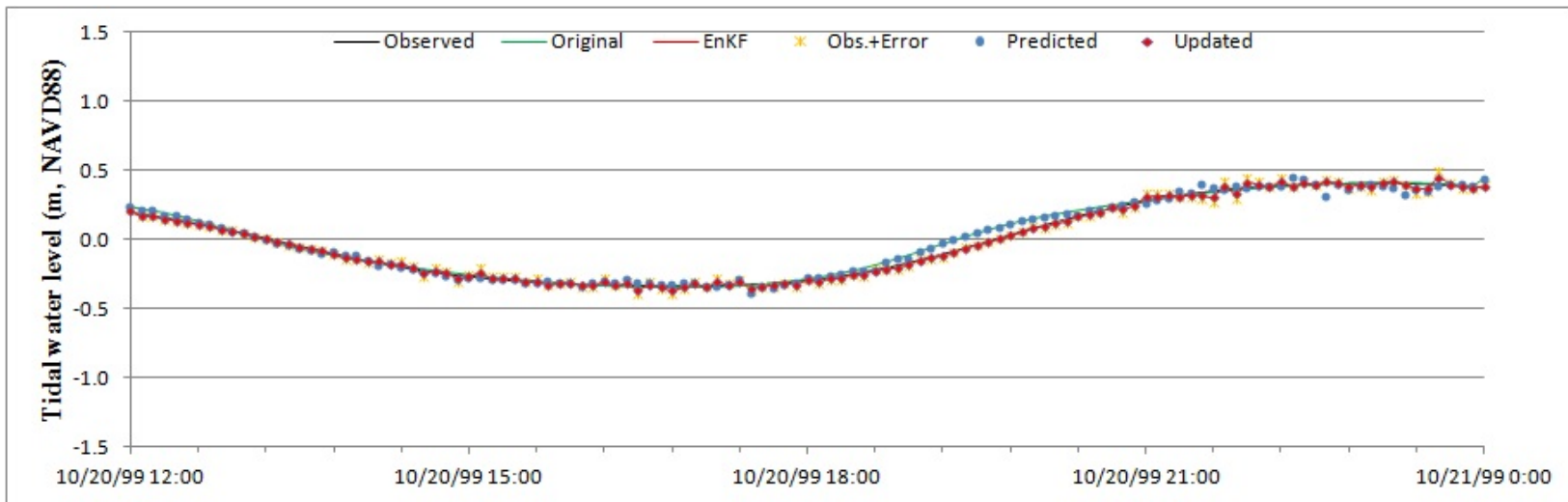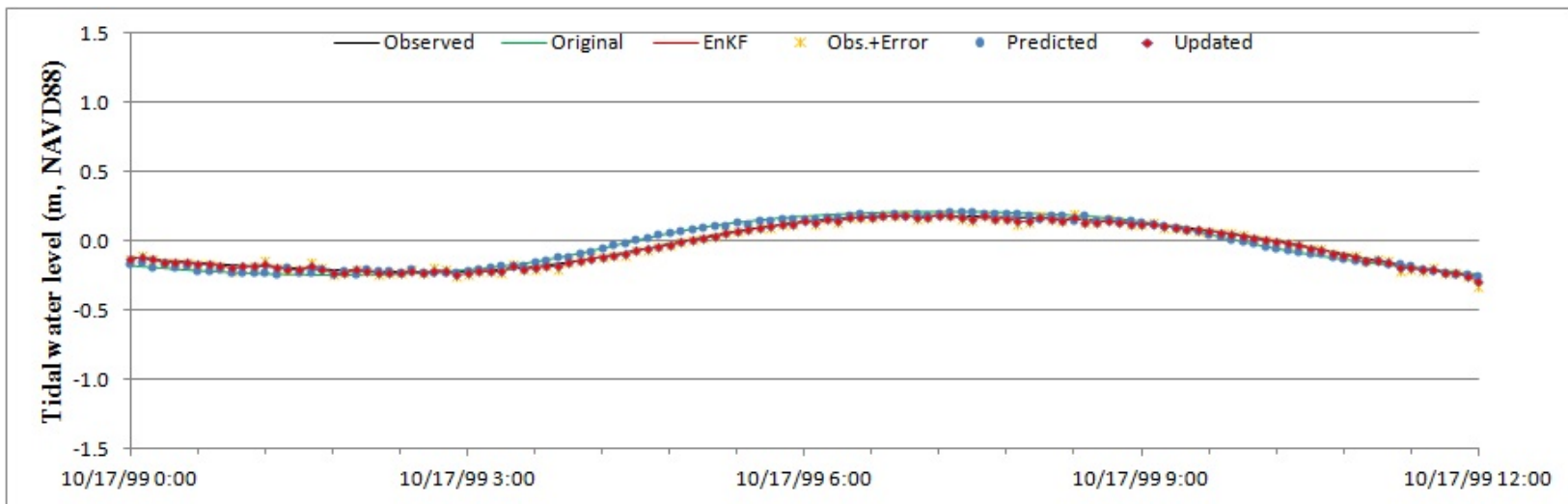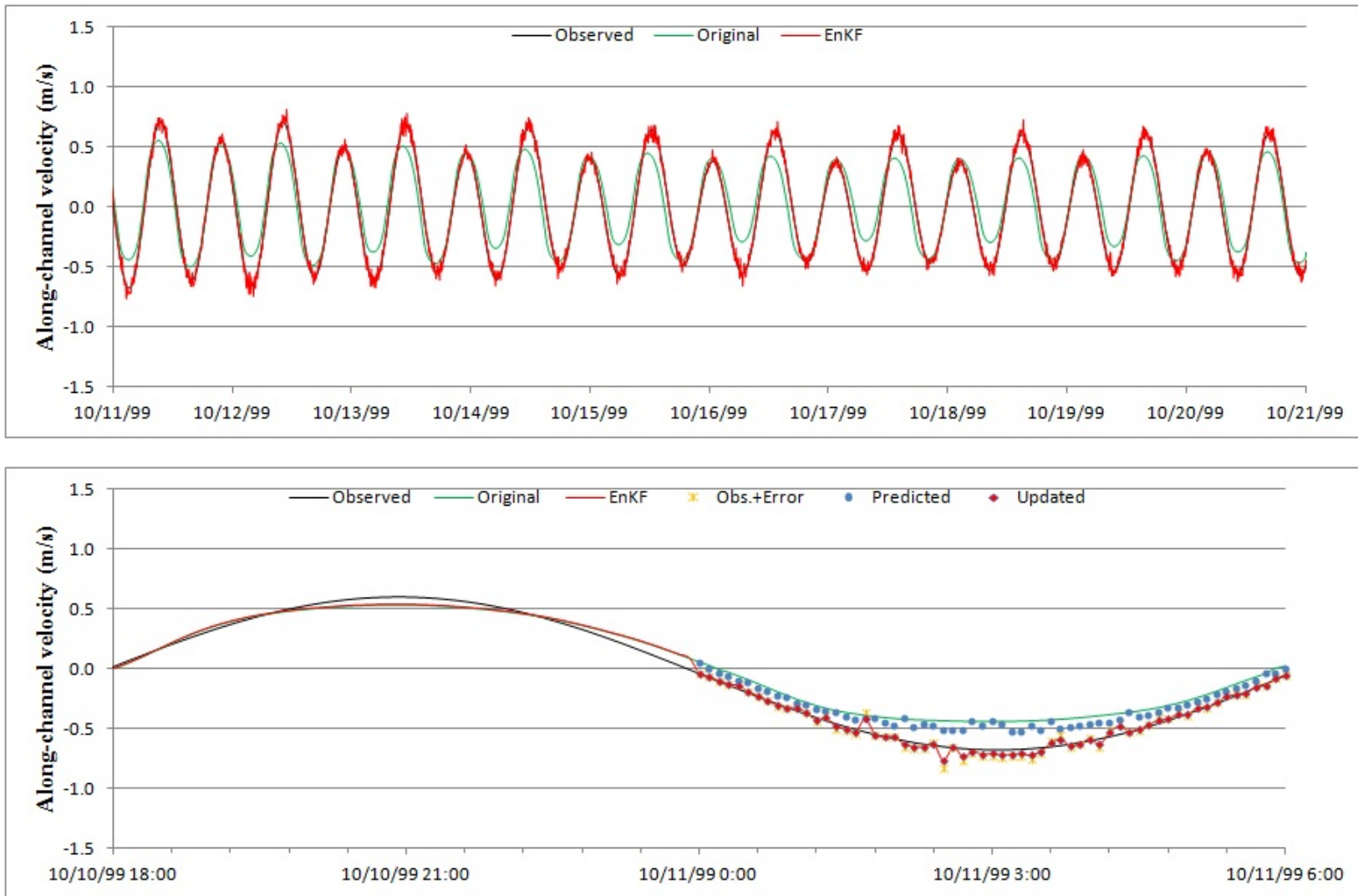**Figure 117**   Time series of along-channel velocity at the middle day (upper) and the last day (bottom) at Jacksonville from Simulation 3.
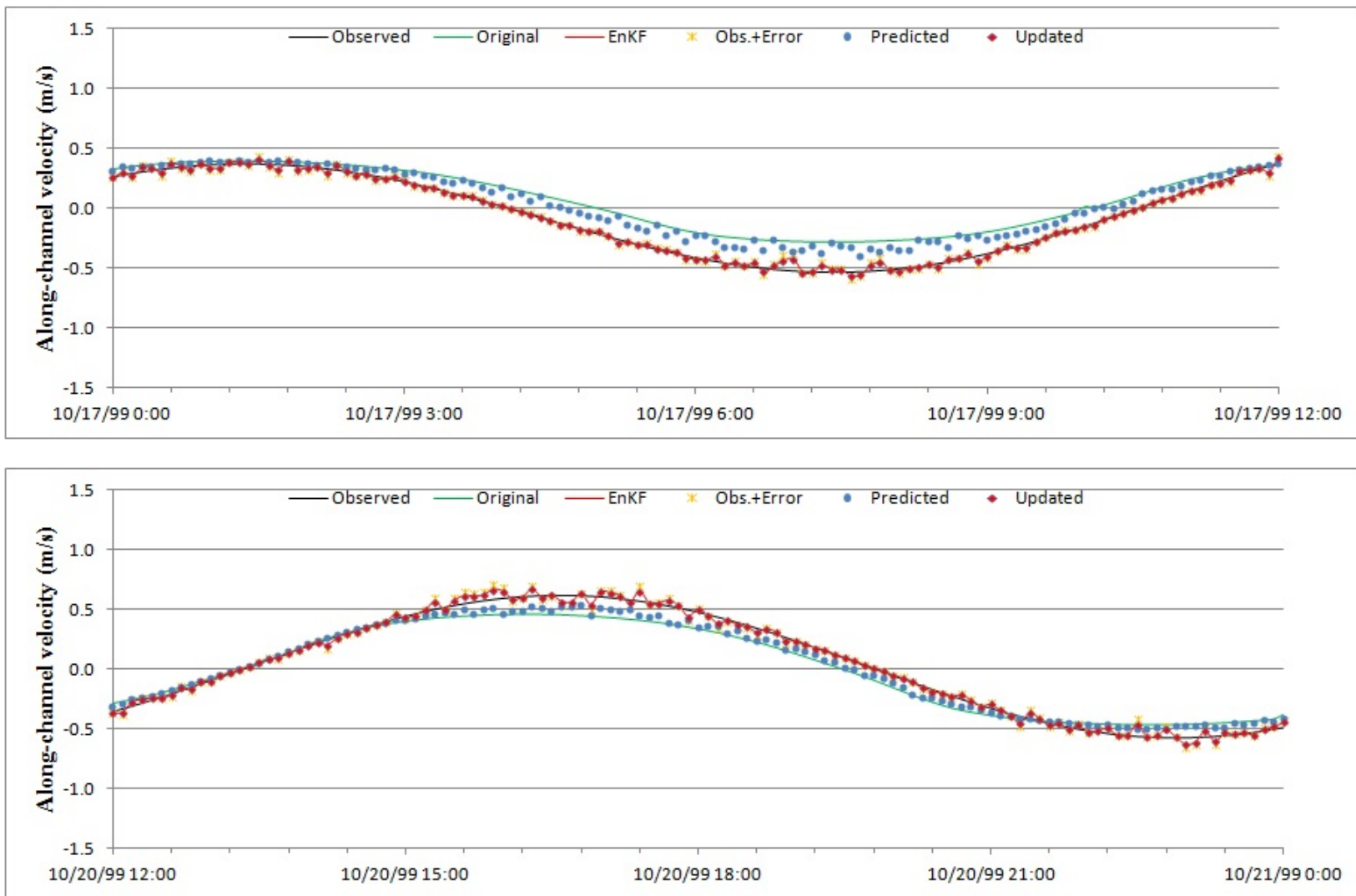
Table 29   **RMSE of tidal water level at the gauging stations (Simulation 3).**

Gauge Name.	RMSE of tidal water level		
	Original (m)	EnKF (m)	$\dfrac{RMSE_{Original} - RMSE_{EnKF}}{RMSE_{Original}}(\%)$
Mayport	3.2621E-02	2.146E-02	34.2
Fulton	2.481E-02	2.073E-02	16.5
Jacksonville	4.695E-02	1.788E-02	61.9

Table 30   **RMSE of along-channel velocity at the gauging stations (Simulation 3).**

Gauge Name.	RMSE of along-channel velocity		
	Original (m/s)	EnKF (m/s)	$\dfrac{RMSE_{Original} - RMSE_{EnKF}}{RMSE_{Original}}(\%)$
Mayport	2.354E-01	3.895E-02	83.5
Fulton	1.346E-01	3.810E-02	71.7
Jacksonville	1.343E-01	3.565E-02	73.5
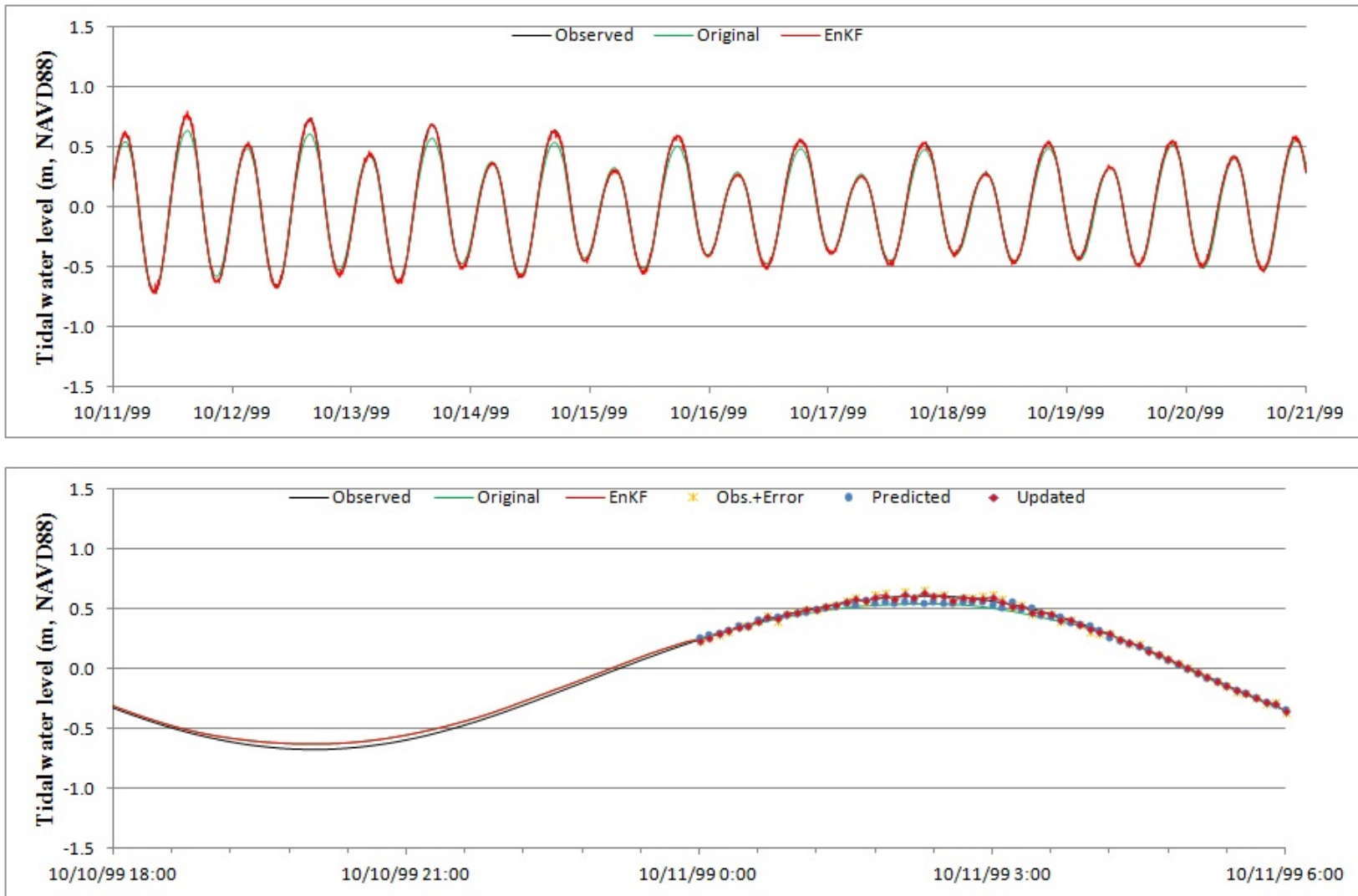
Figure 118 Time series of tidal water level during the last 10 days (upper) and at the first day (bottom) at Mayport from Simulation 4.
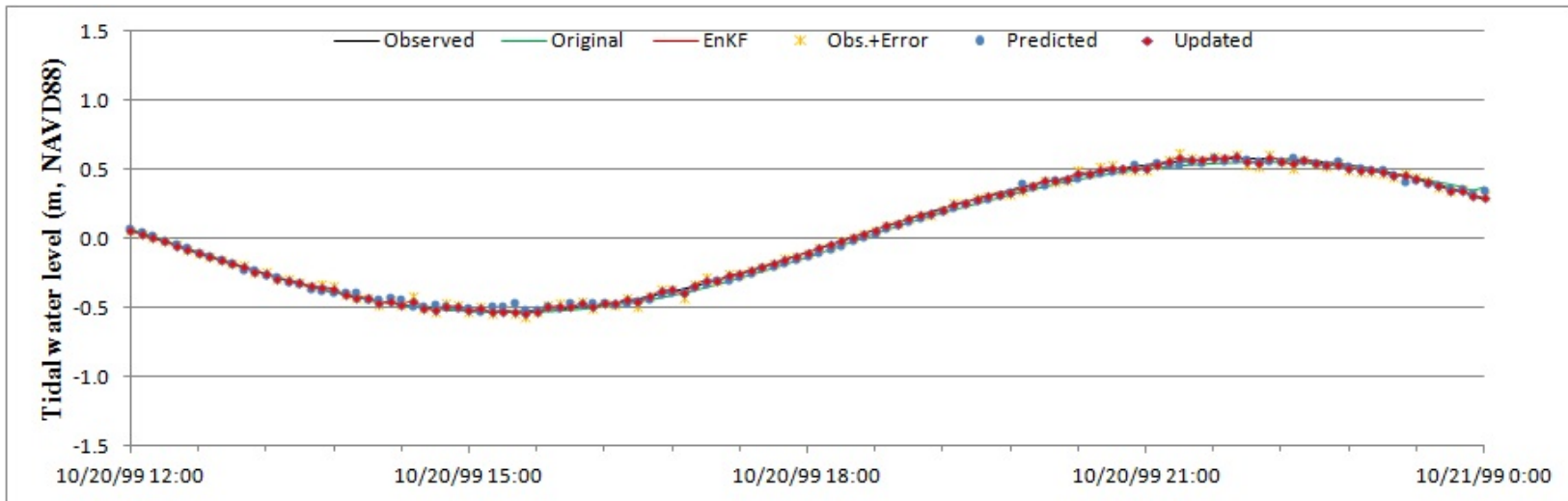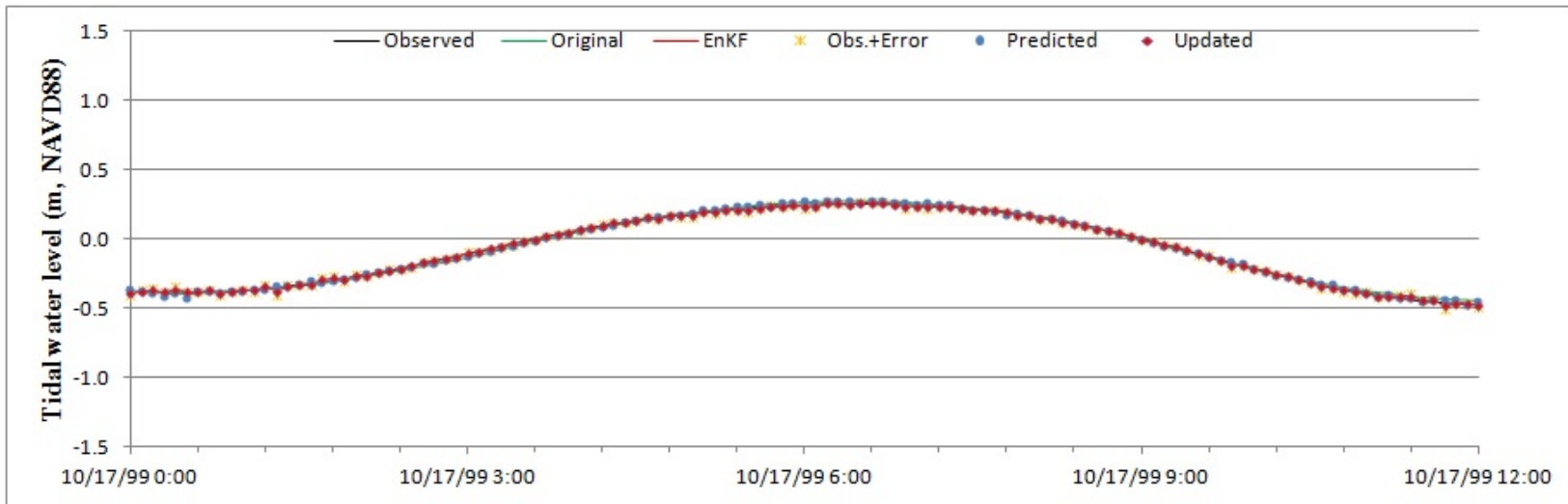
Figure 119 Time series of tidal water level at the middle day (upper) and the last day (bottom) at Mayport from Simulation 4.
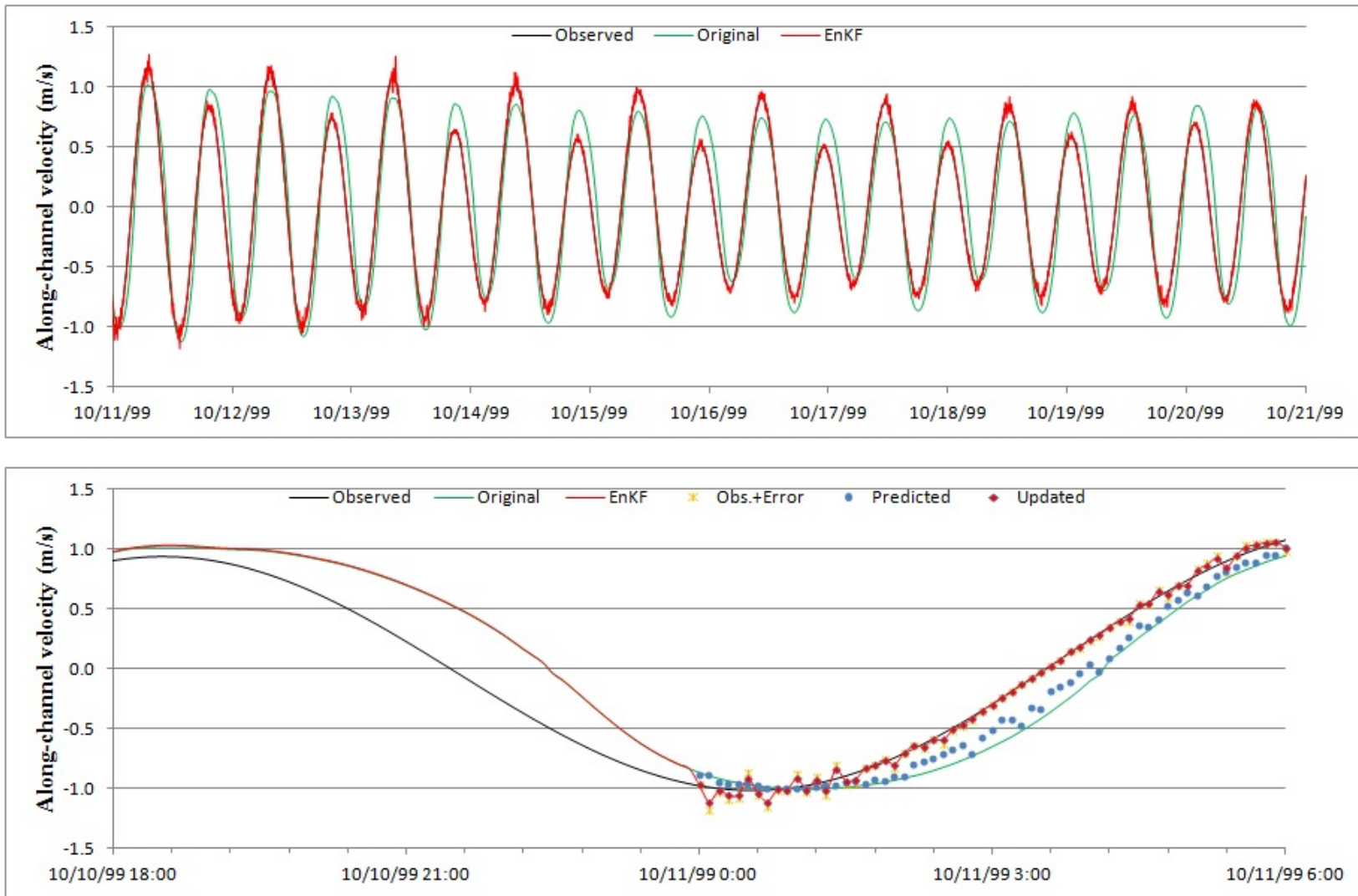
Figure 120 Time series of along-channel velocity during the last 10 days (upper) and at the first day (bottom) at Mayport from Simulation 4.

190
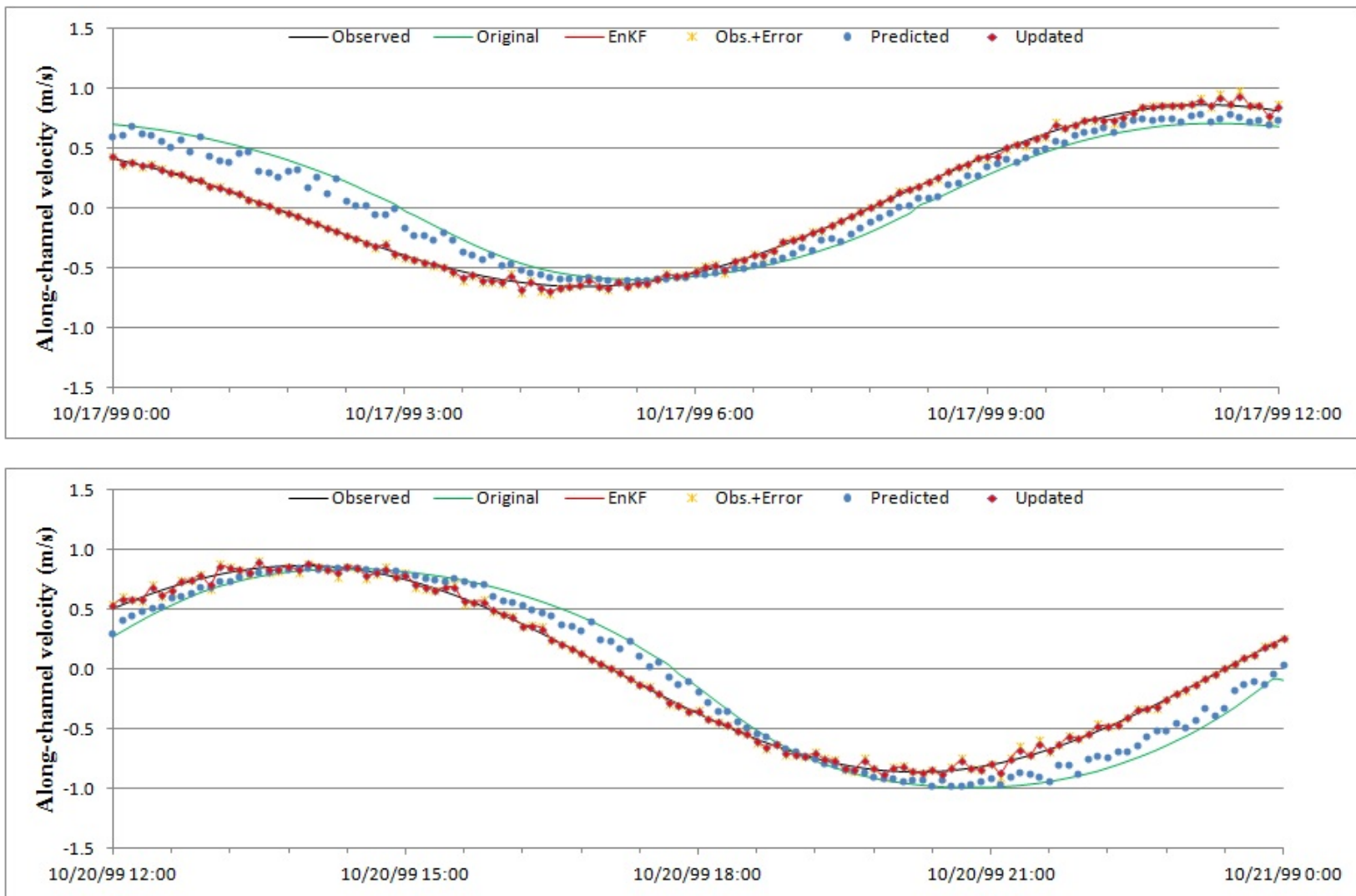
Figure 121   Time series of along-channel velocity at the middle day (upper) and the last day (bottom) at Mayport from Simulation 4.
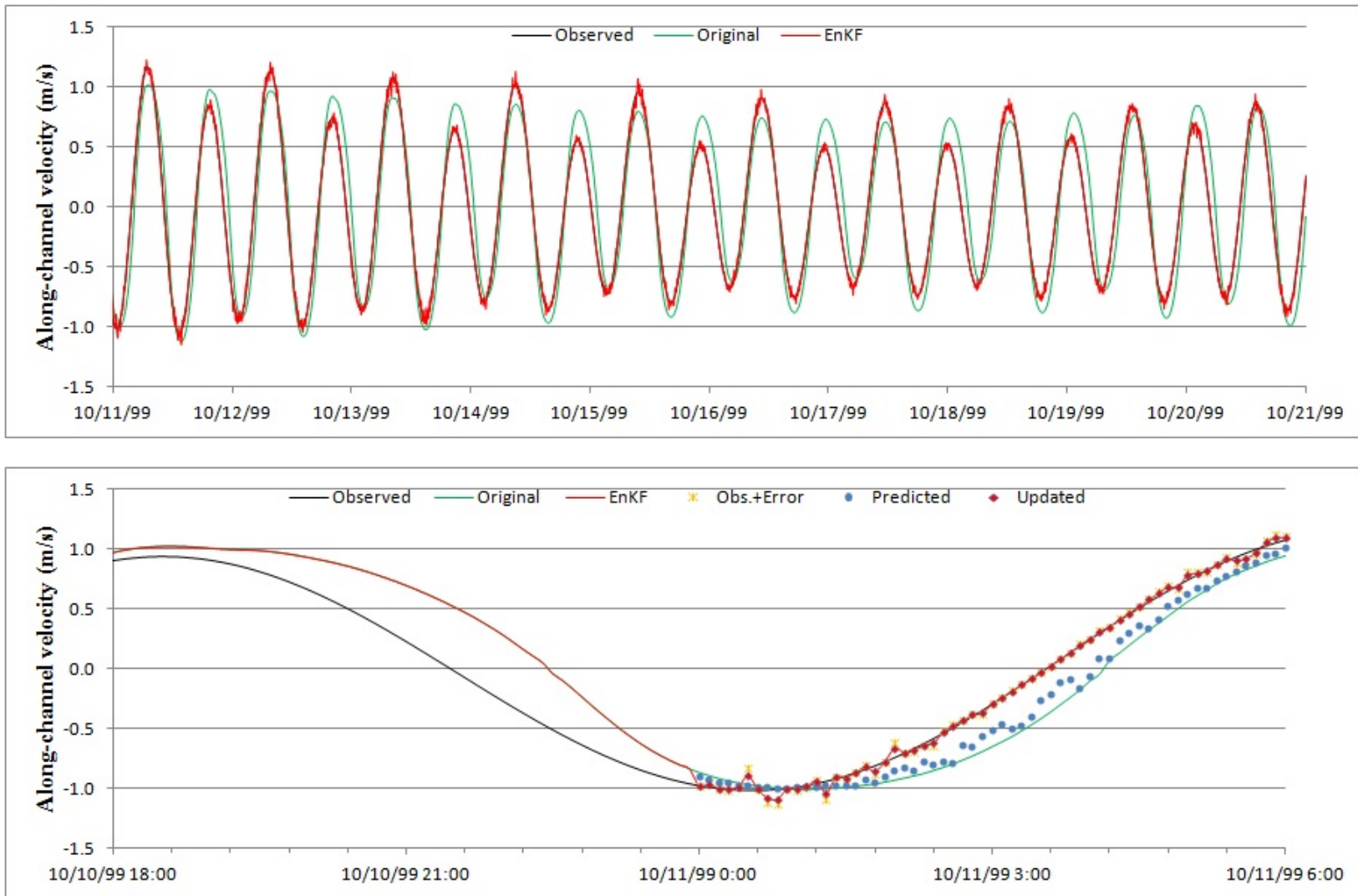
191
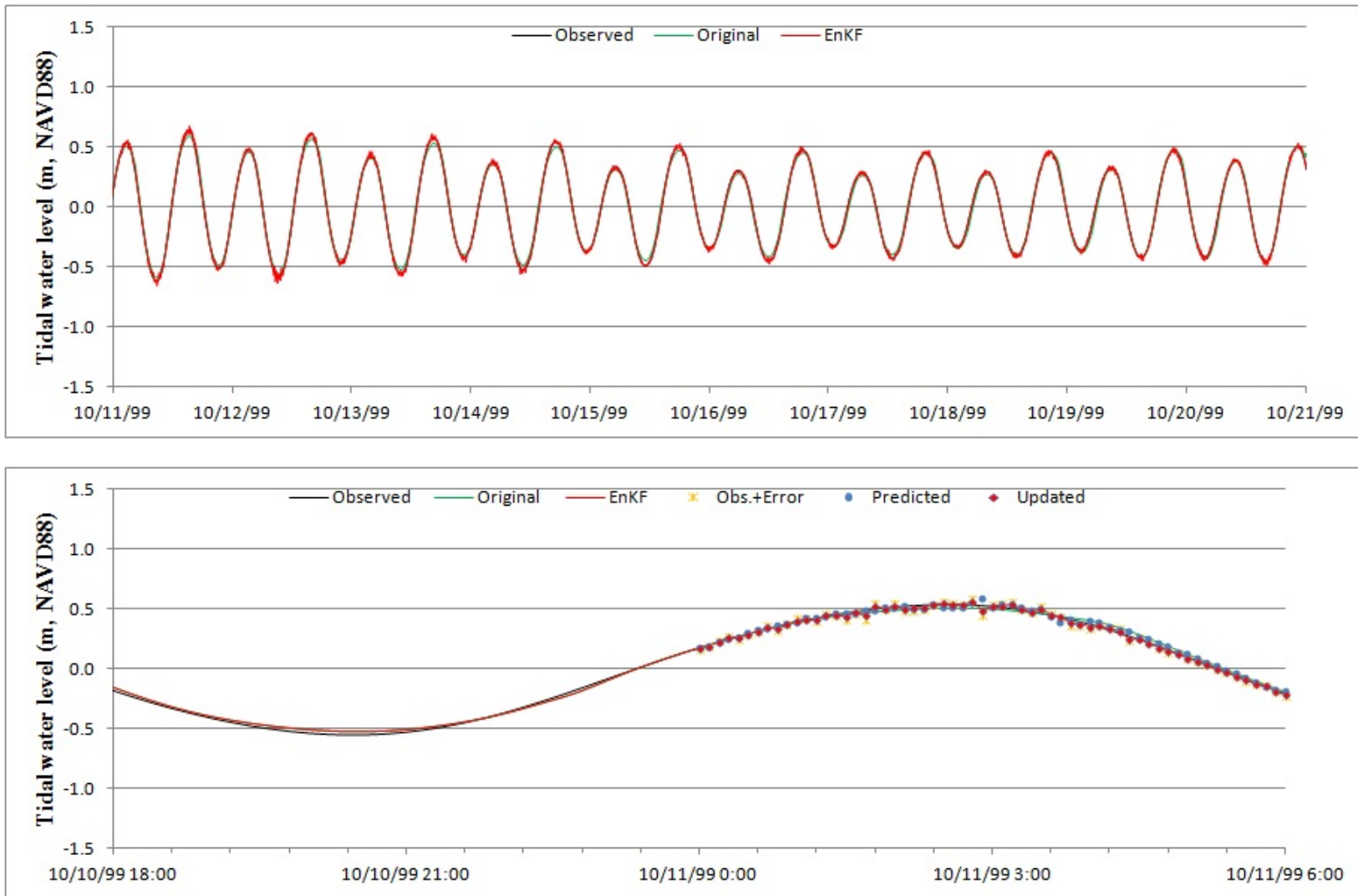
Figure 122 Time series of tidal water level during the last 10 days (upper) and at the first day (bottom) at Fulton from Simulation 4.
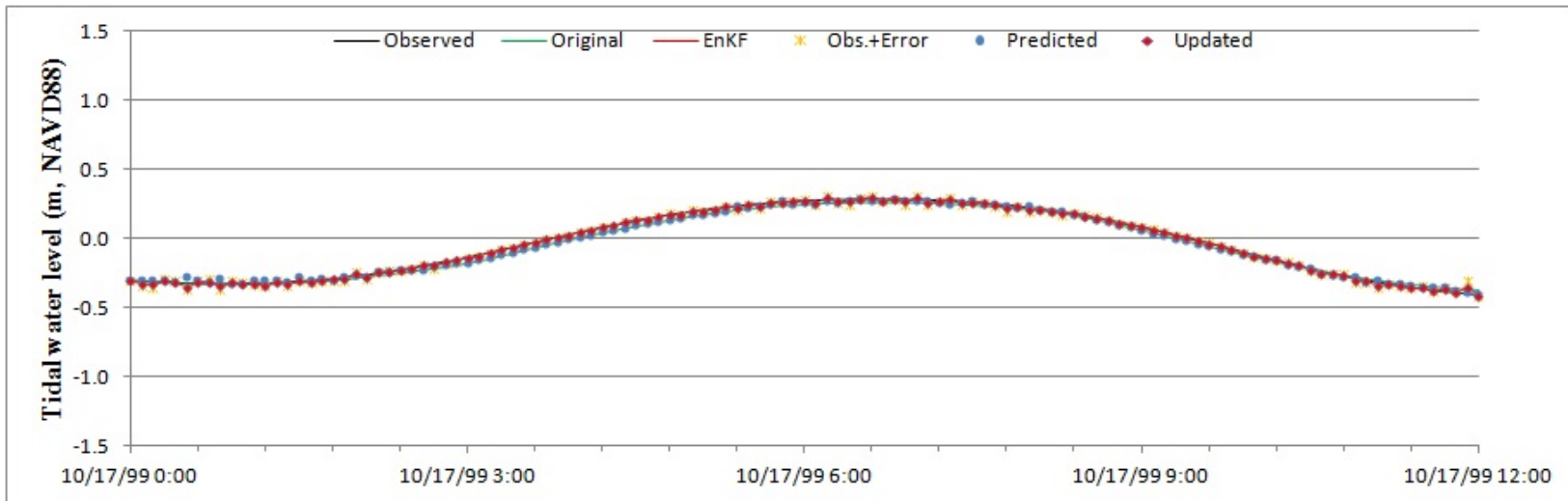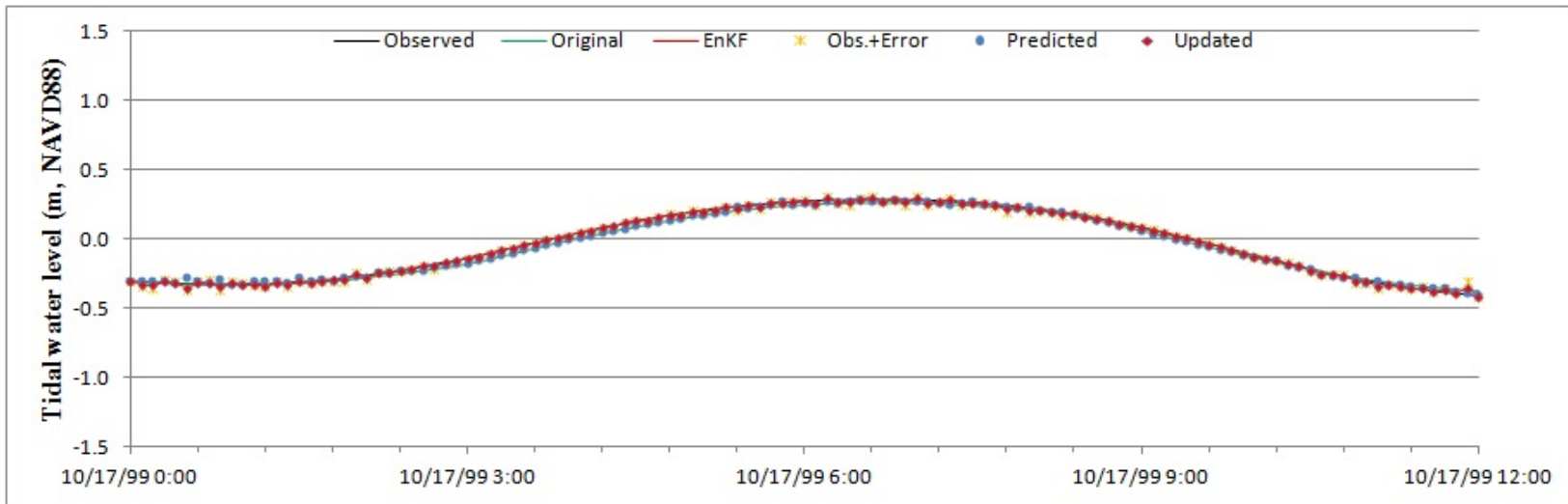
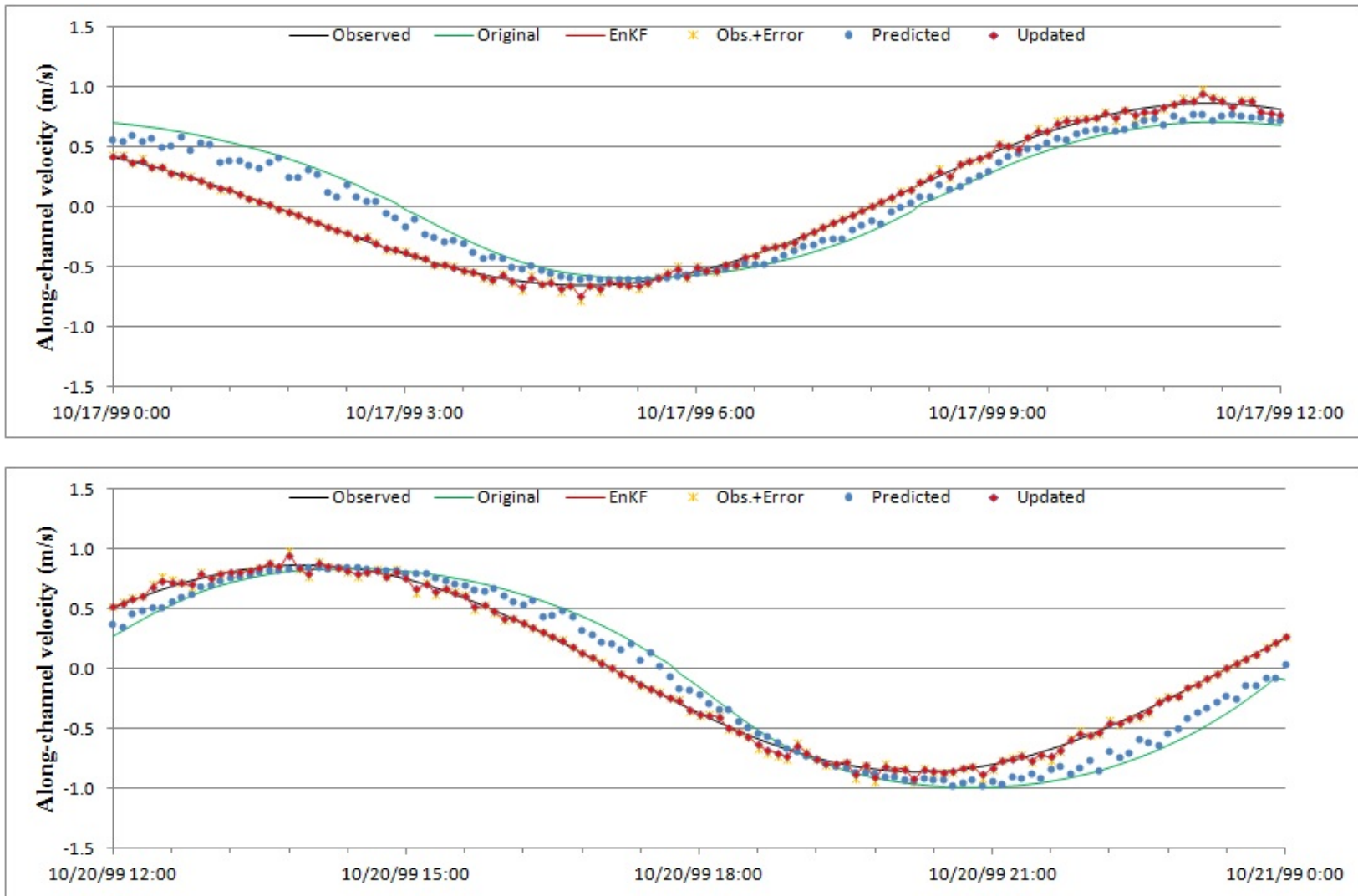**Figure 123   Time series of tidal water level at the middle day (upper) and the last day (bottom) at Fulton from Simulation 4.**
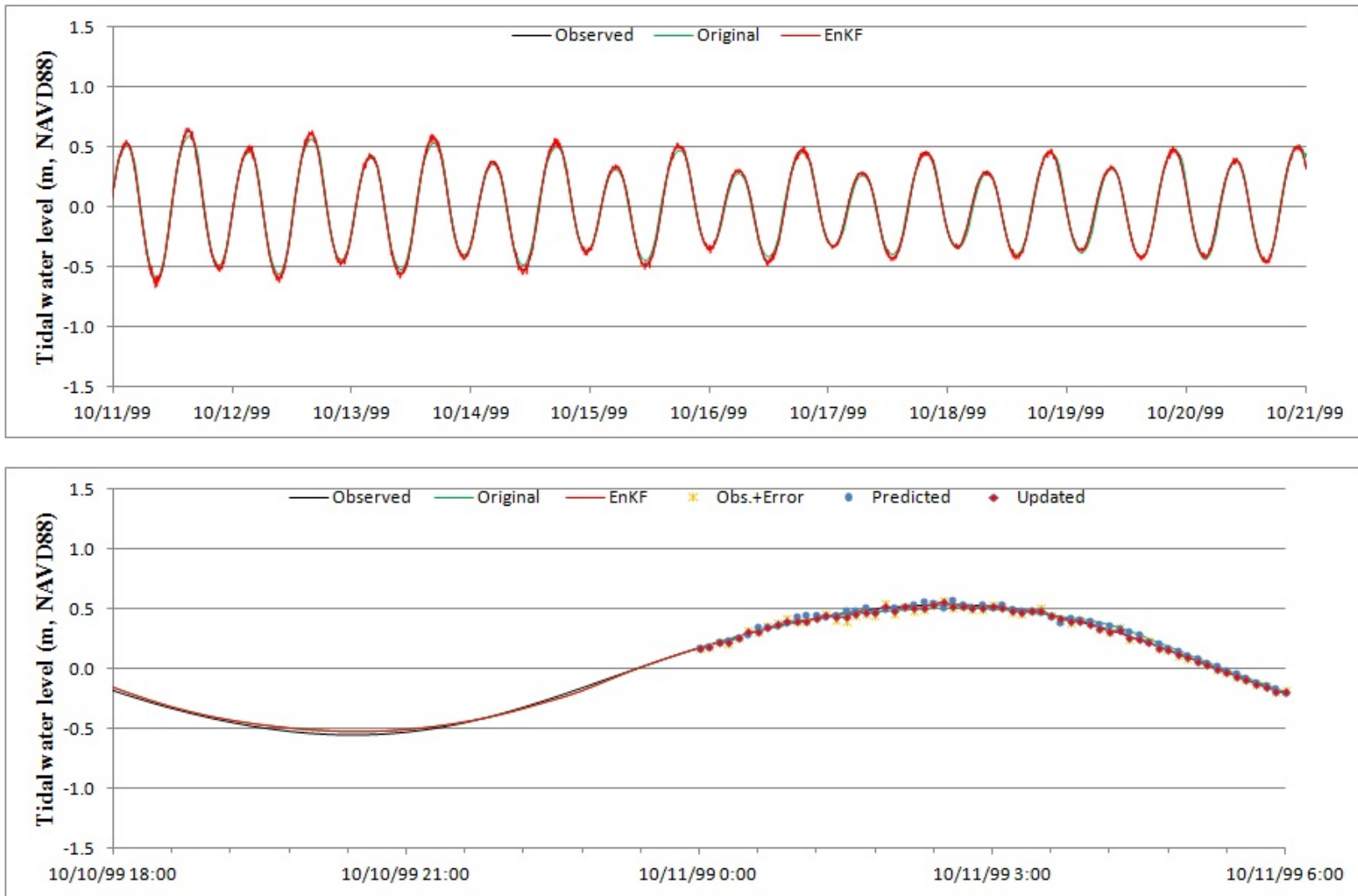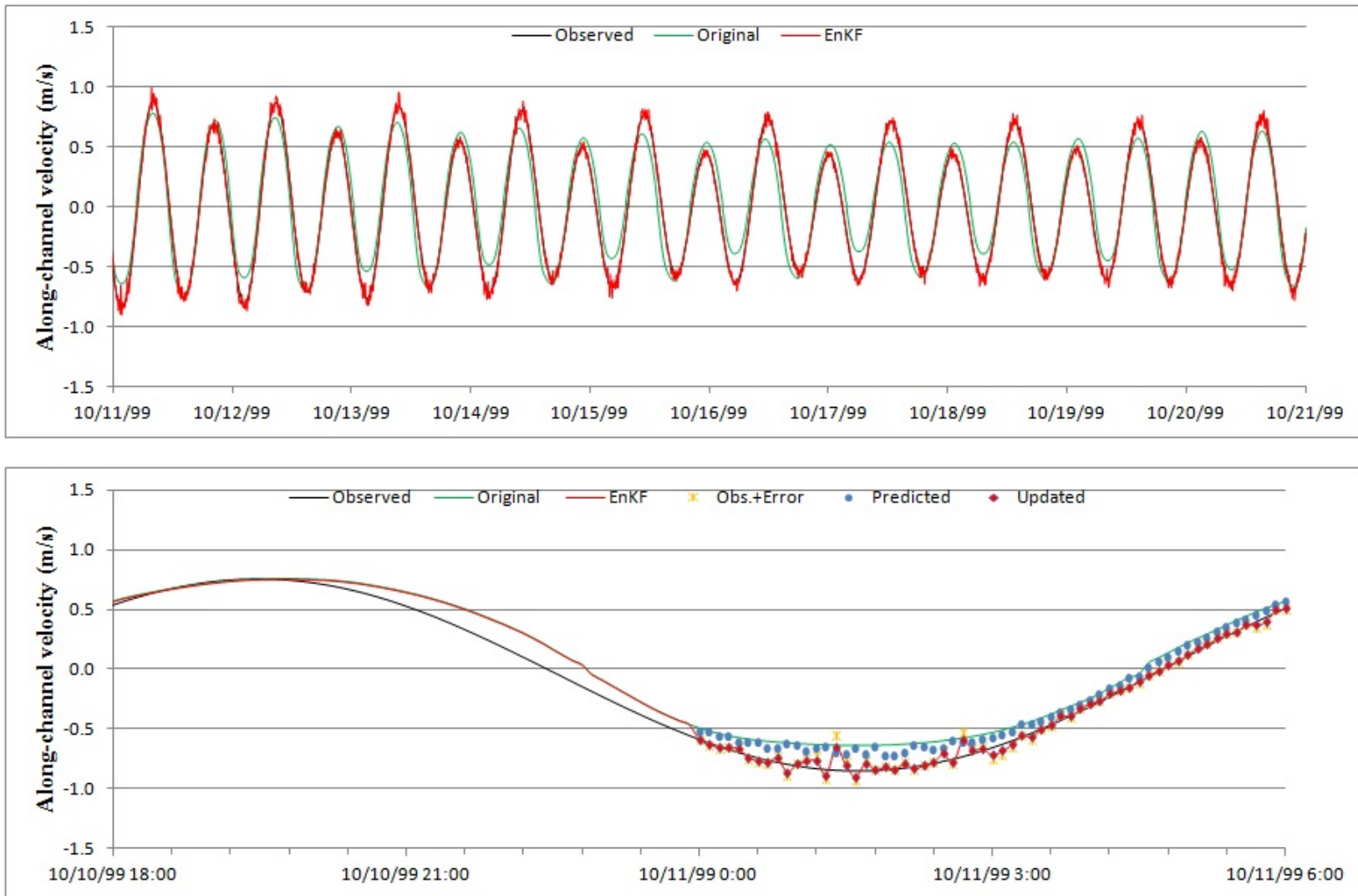
Figure 124 Time series of along-channel velocity during the last 10 days (upper) and at the first day (bottom) at Fulton from Simulation 4.

194
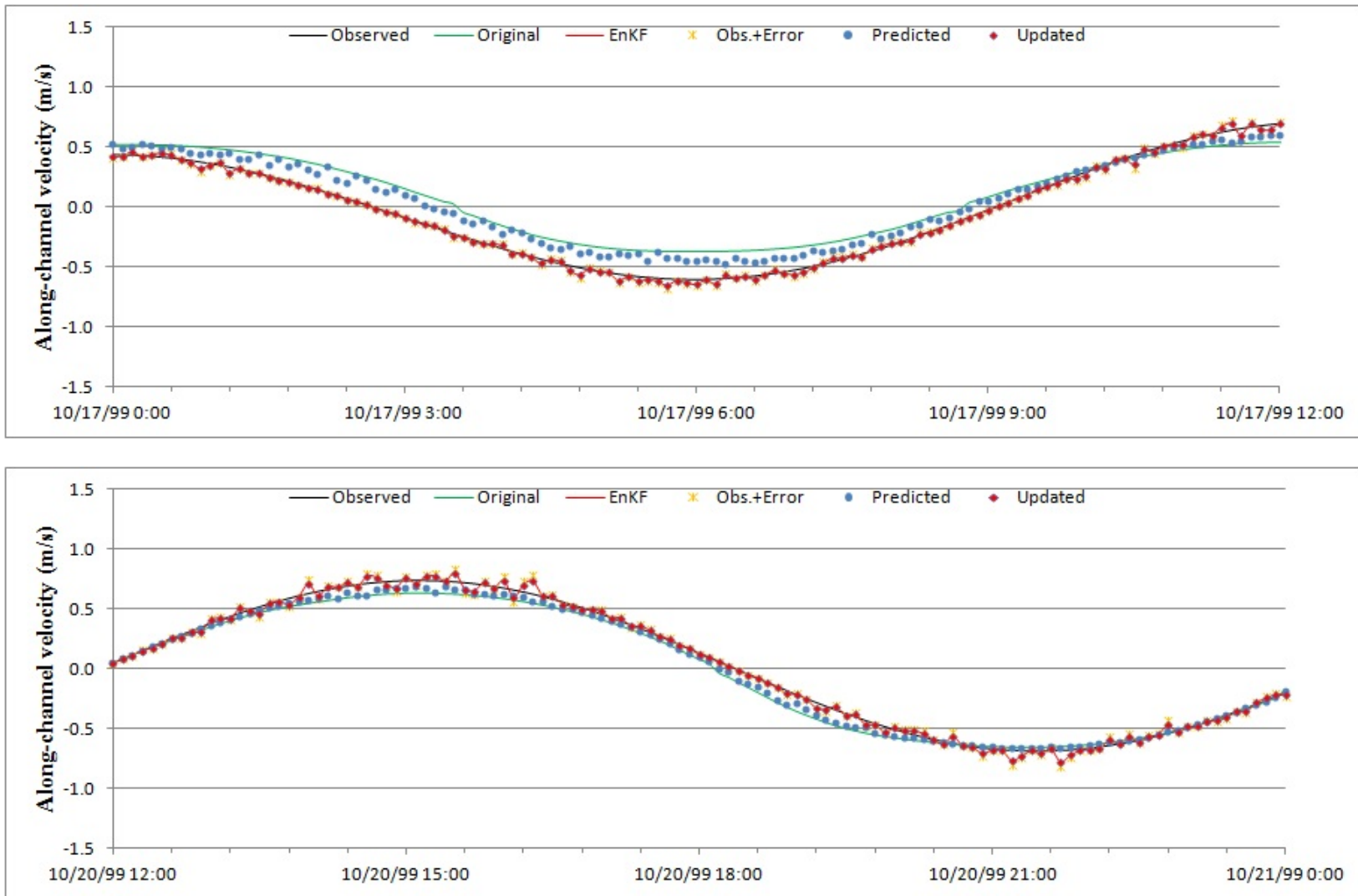
Figure 125   Time series of along-channel velocity at the middle day (upper) and the last day (bottom) at Fulton from Simulation 4.
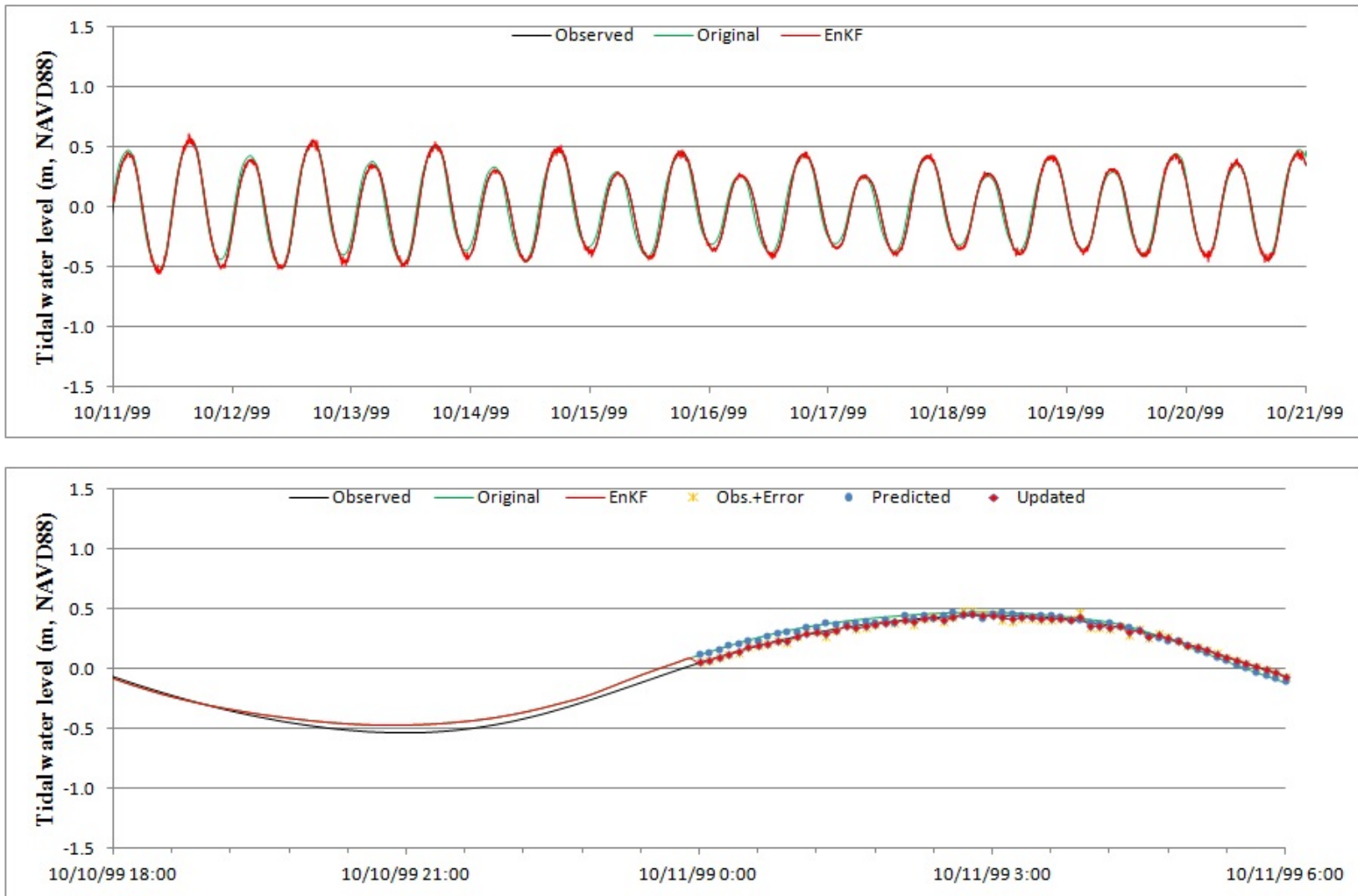
Figure 126 Time series of tidal water level during the last 10 days (upper) and at the first day (bottom) at Dames Point from Simulation 4.
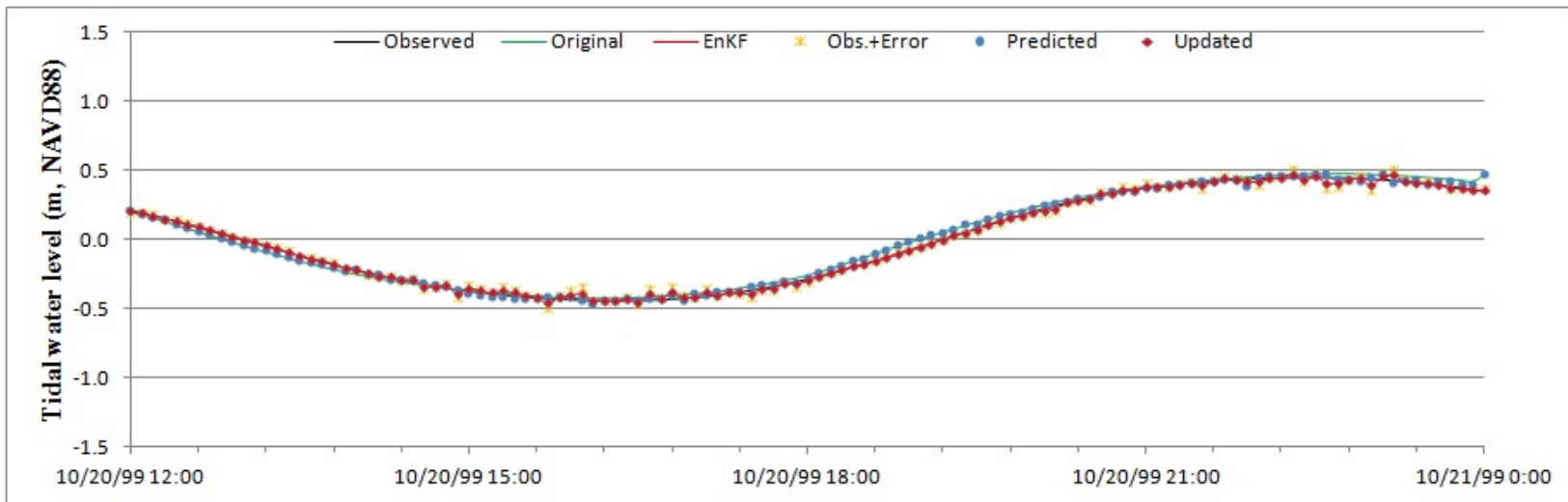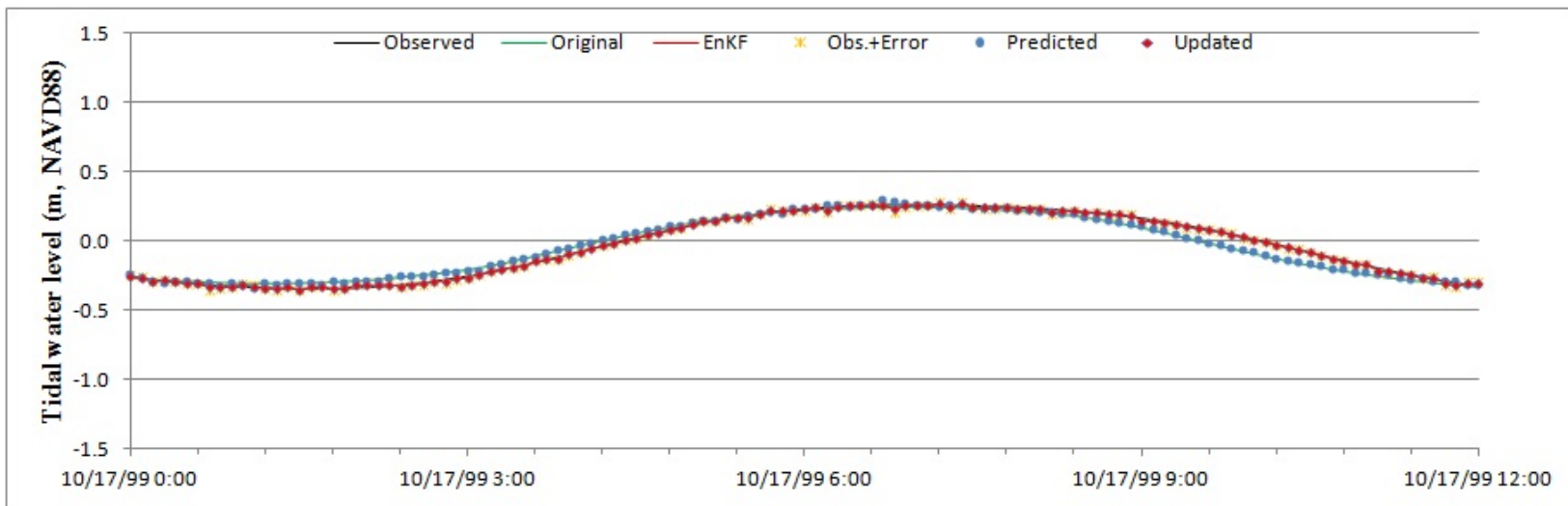
Figure 127   Time series of tidal water level at the middle day (upper) and the last day (bottom) at Dames Point from Simulation 4.
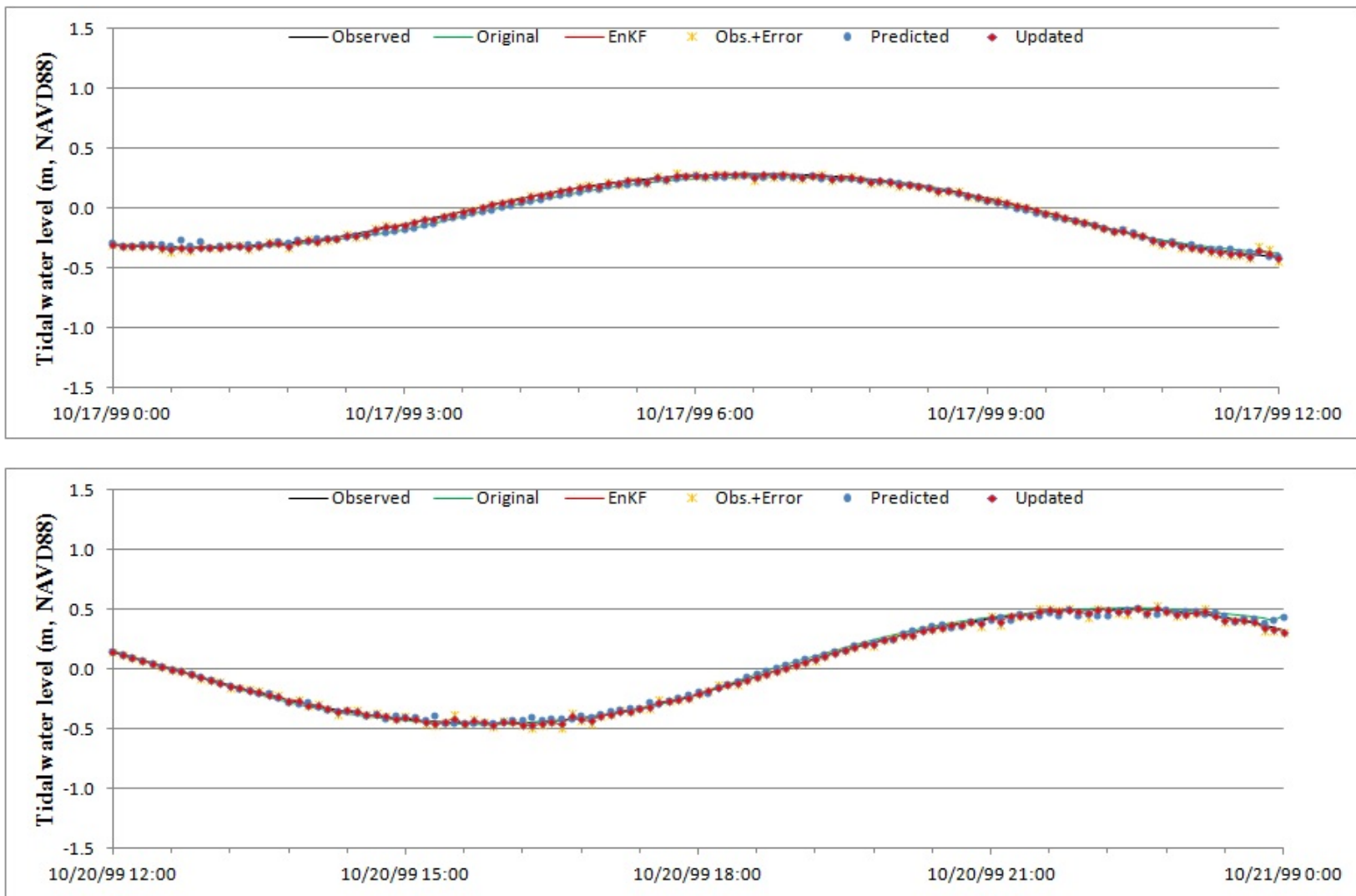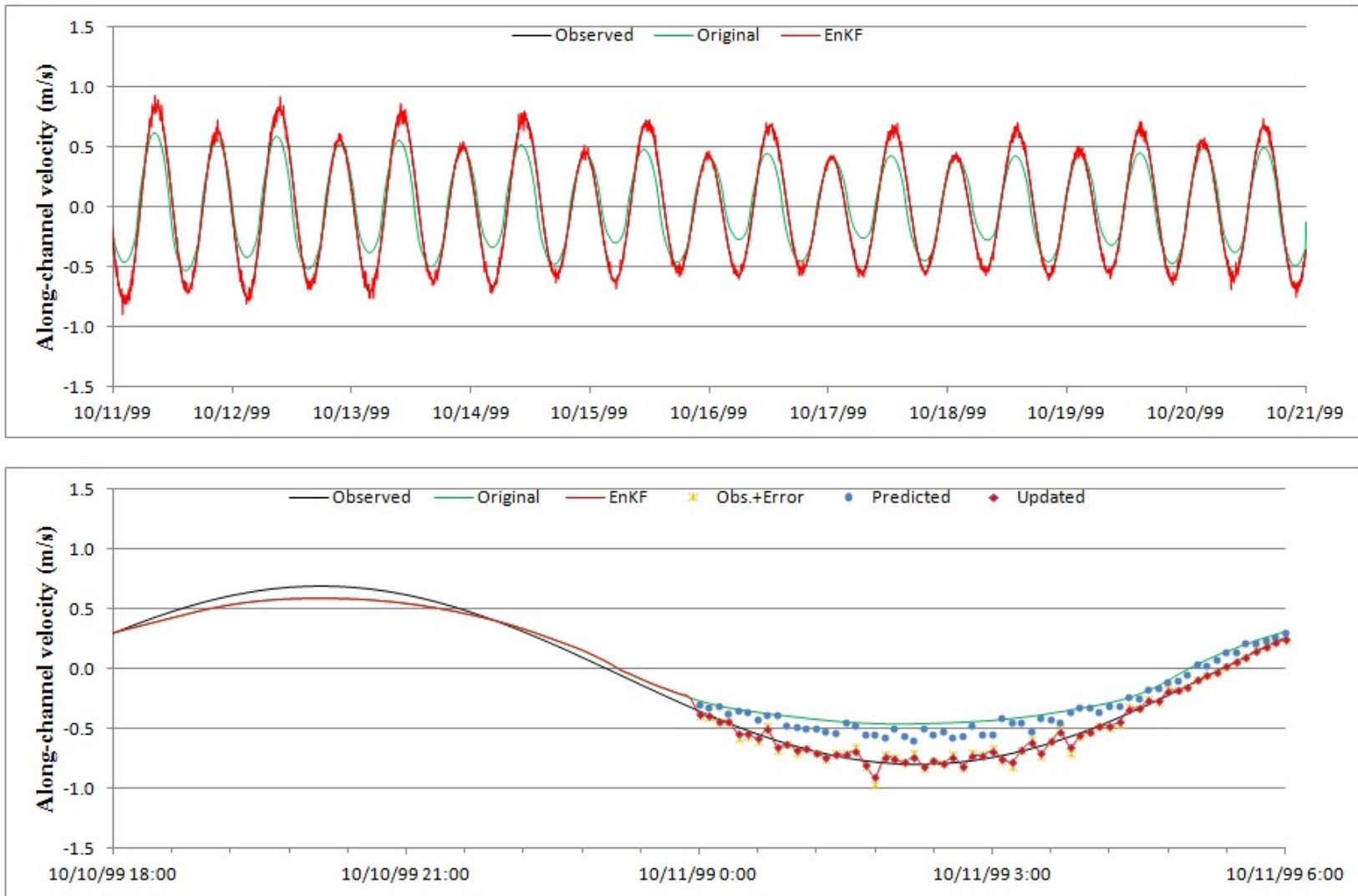
Figure 128 Time series of along-channel velocity during the last 10 days (upper) and at the first day (bottom) at Dames Point from Simulation 4.
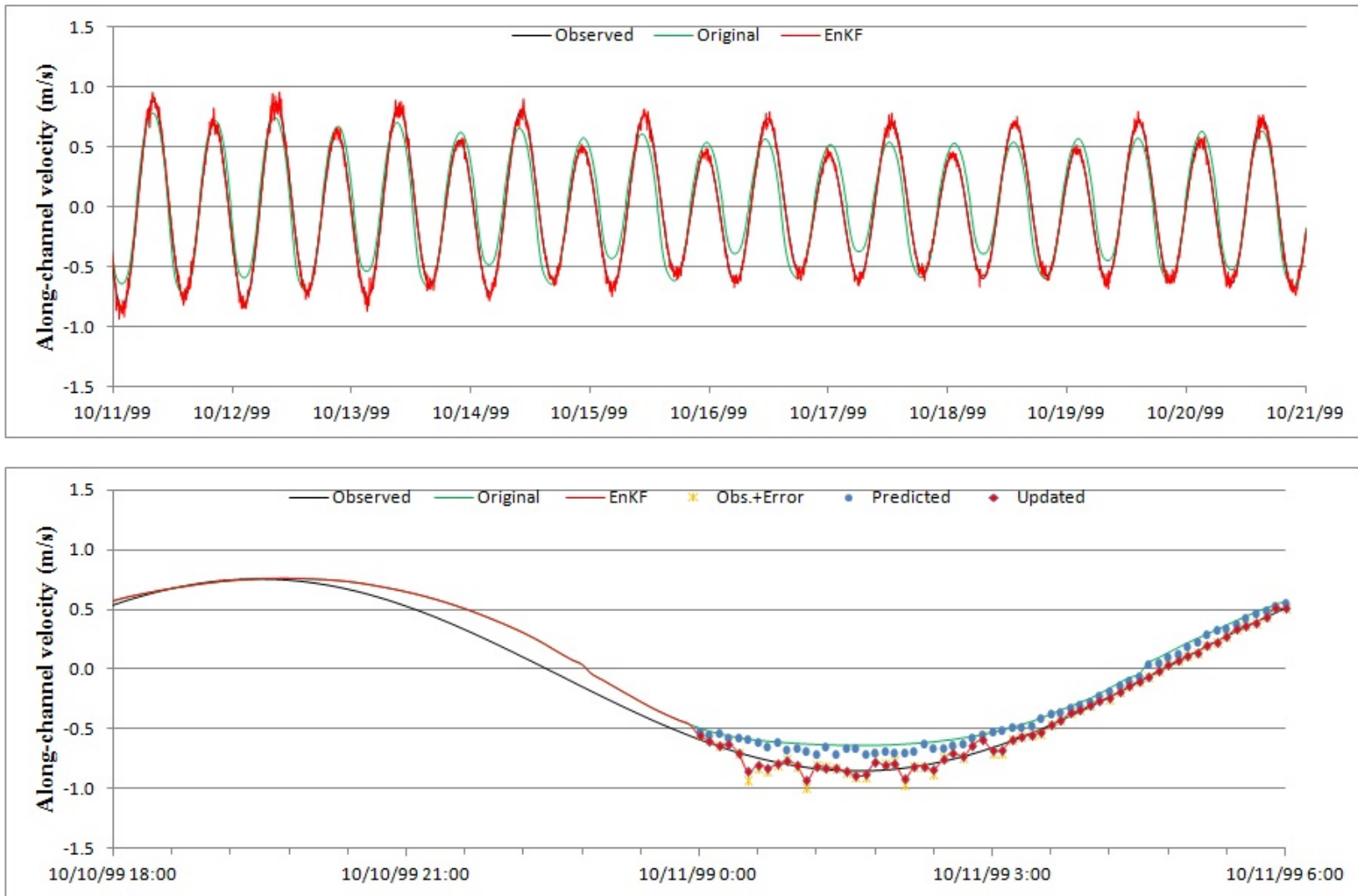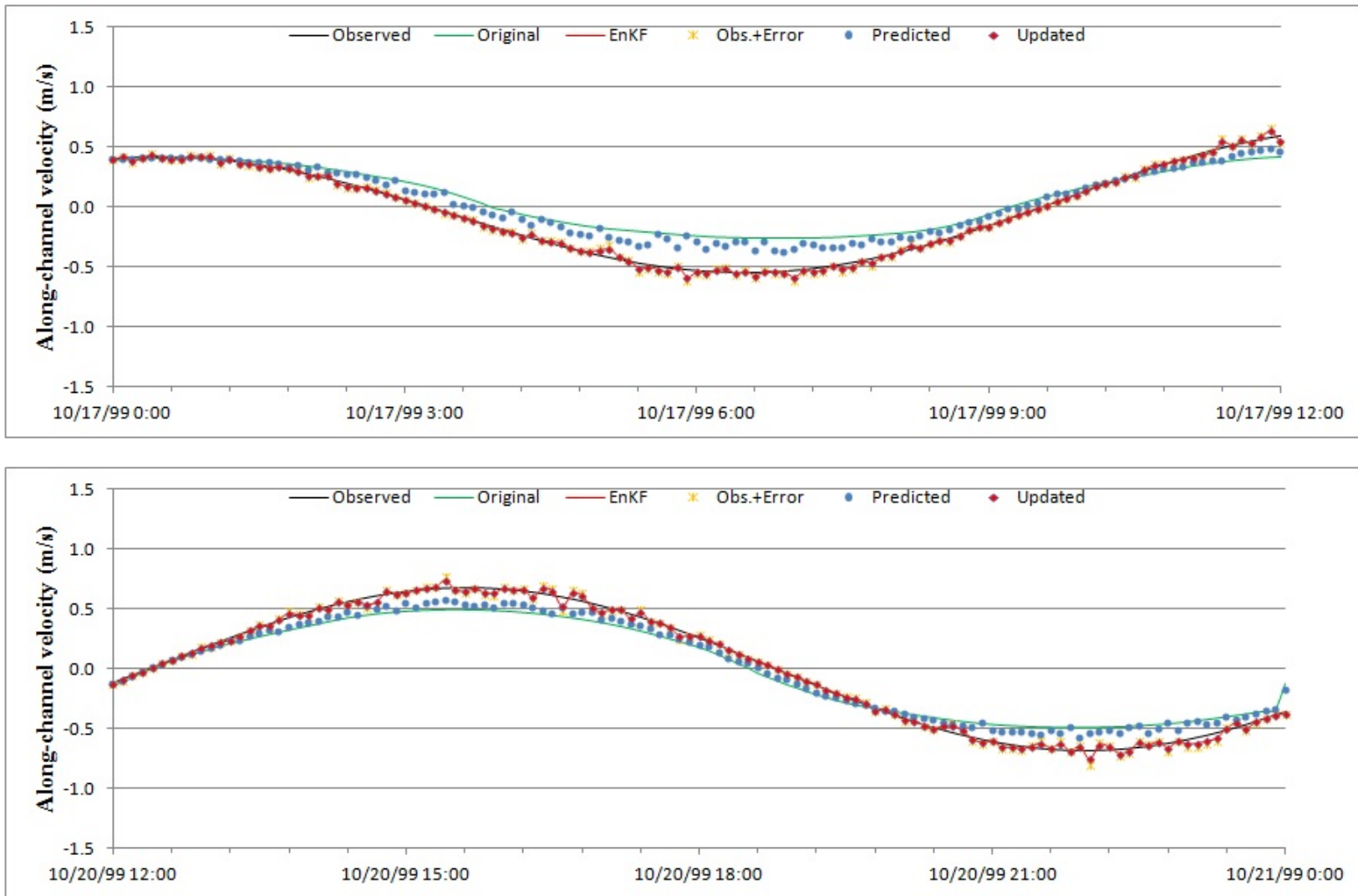
Figure 129   Time series of along-channel velocity at the middle day (upper) and the last day (bottom) at Dames Point from Simulation 4.
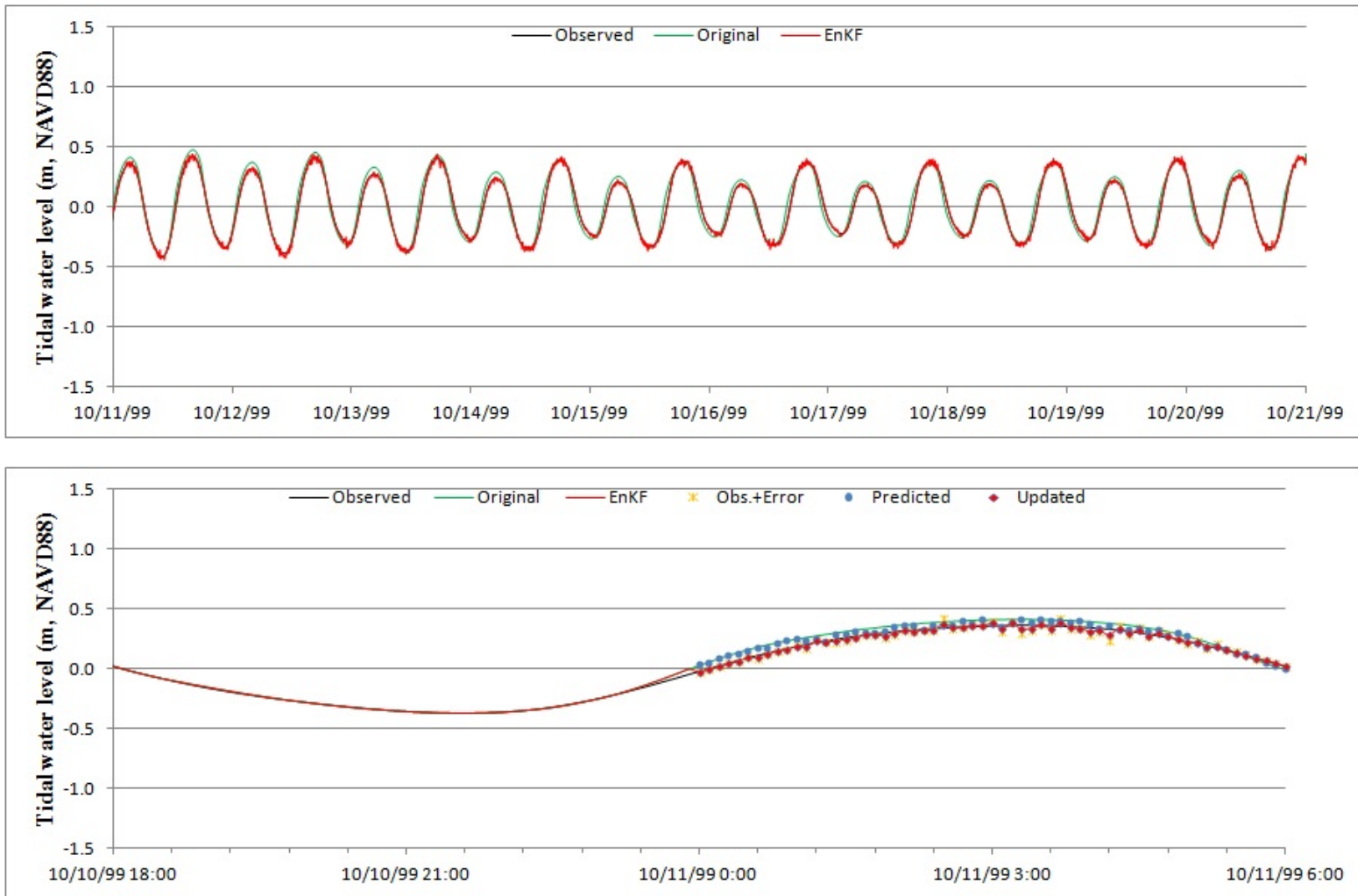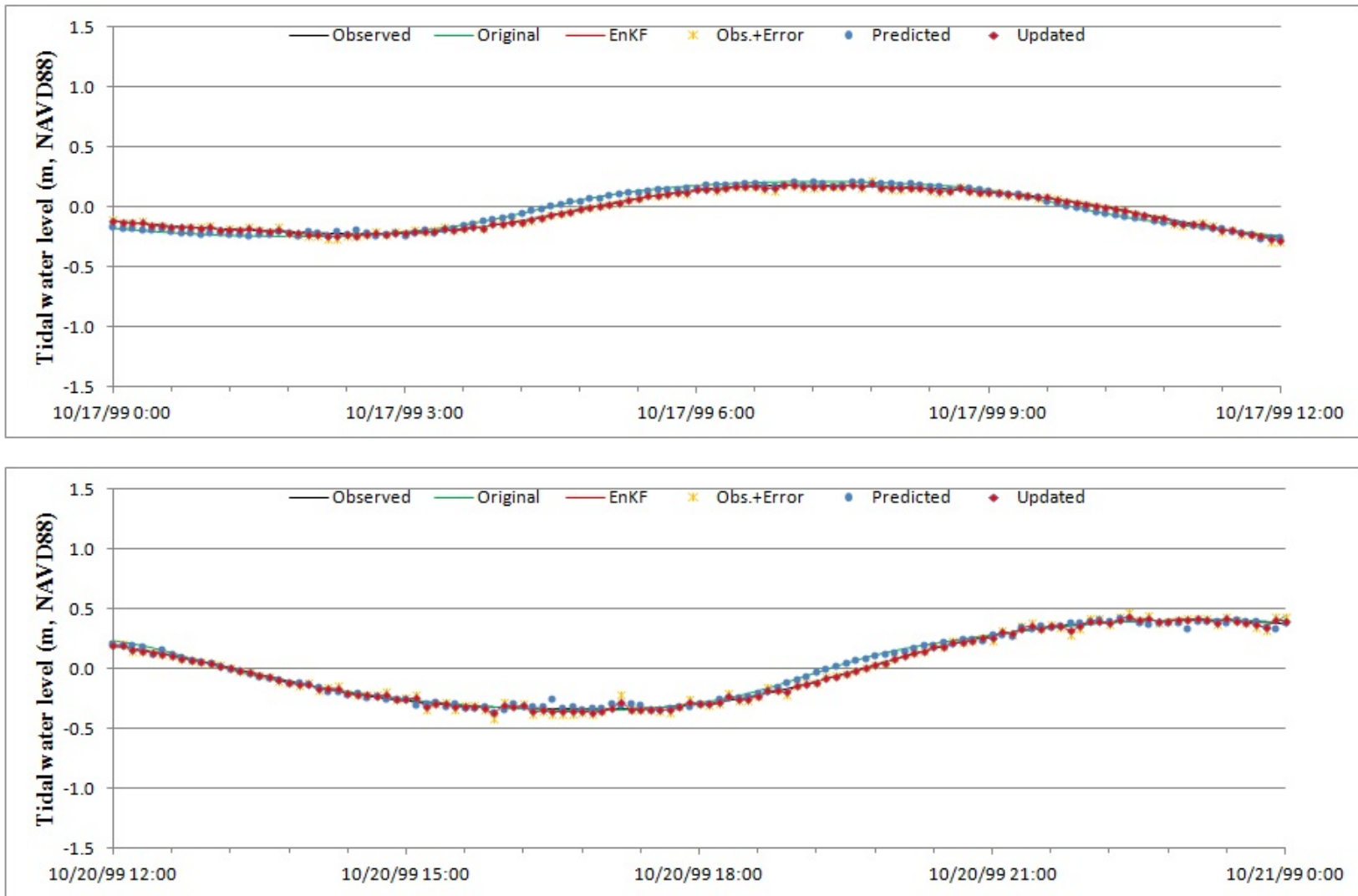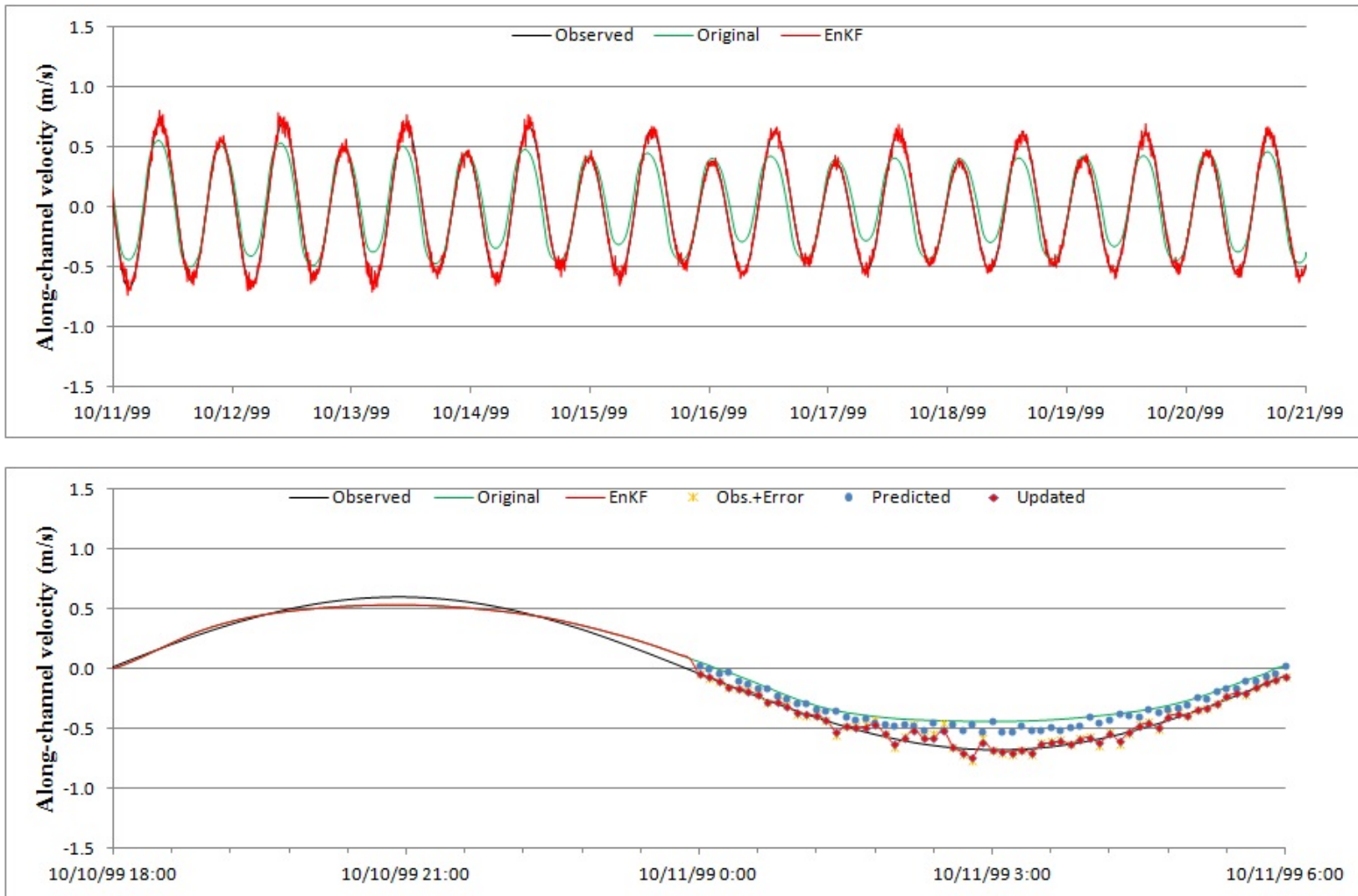
199

Table 31   **RMSE of tidal water level at the gauging stations (Simulation 4).**

Gauge Name.	RMSE of tidal water level		
	Original (m)	EnKF (m)	$\dfrac{RMSE_{Original} - RMSE_{EnKF}}{RMSE_{Original}}(\%)$
Mayport	3.2621E-02	2.179E-02	33.2
Fulton	2.481E-02	2.041E-02	17.7
Dames Point	4.617E-02	1.965E-02	57.4

Table 32   **RMSE of along-channel velocity at the gauging stations (Simulation 4).**

Gauge Name.	RMSE of along-channel velocity		
	Original (m/s)	EnKF (m/s)	$\dfrac{RMSE_{Original} - RMSE_{EnKF}}{RMSE_{Original}}(\%)$
Mayport	2.354E-01	4.007E-02	83.0
Fulton	1.346E-01	3.700E-02	72.5
Dames Point	1.544E-01	3.480E-02	77.5

LIST OF REFERENCES

Arcement, G. J., and Schneider, V. R. (1989). "Guide for selecting Manning's roughness coefficients for natural channels and floodplains." *Water Supply Paper 2339*, United States Geological Survey, Tallahassee, Florida.

Auroux, D., and Blum, J. (2008). "A nudging-based data assimilation method: the Back and Forth Nudging (BFN) algorithm." *Nonlinear Processes in Geophysics,* t15, 305-319.

Bacopoulos, P. (2009). "Estuarine influence on tidally driven circulation in the South Atlantic Bight." PhD thesis, University of Central Florida, Orlando, Florida.

Bacopoulos, P., Dally, W. R., Hagen, S. C., and Cox, A. T. (2011). "Observations and simulation of winds, surge, and currents on Florida's east coast during hurricane Jeanne (2004)." *Coastal Engineering*, 60, 84-94.

Bacopoulos, P., Hagen, S. C., Cox, A. T., Dally, W. R., and Braton, S. M. (2012) "Observation and simulation of winds and hydrodynamics in the St. Johns and Nassau Rivers." *Journal of Hydrology*, In press, doi: 10.1016/j.jhydrol.201112.032.

Barnes, H. H. (1967). "Roughness characteristics of natural channels." *Water Supply Paper 1849*, United States Geological Survey, Tallahassee, Florida.

Blumberg, A. F., and Mellor, G. L. (1987). "A description of a three-dimensional coastal ocean circulation model." *Three-Dimensional Coastal Ocean Models*, N. S. Heaps, ed., AGU Press, Washington, DC, 1–16.

Bourgerie, R. (1999). "Currents in the St. Johns River, Florida Spring and Summer of 1998." *NOAA Technical Report NOS CO-OPS 025*, National Oceanic and Atmospheric Administration, Silver Spring, Maryland.

Burgers, G., van Leeuwen, P. J., and Evensen, G. (1998). "Analysis scheme in the ensemble Kalman filter." *Monthly Weather Review*, 126(6), 1719–1724.

Chow, V. T. (1959). "Open-channel hydraulics." McGraw-Hill, New York, New York.

Chen, C., Malanotte-Rizzoli, P., Wei, J., Beardsley, R. C., Lai, Z. Xue, P. Lyu, S., Xu, Q., Qi, J., and Cowles, G. W. (2009). "Application and comparison of Kalman filter for coastal ocean problems: An experiment with FVCOM." *Journal of Geophysical Research*, 114, C05011, doi: 10.1029/2007JC004548.

Cowen, W. L. (1956). "Estimating hydraulic roughness coefficients." *Agricultural Engineering*, 37(7), 473–475.

Evensen, G. (1994). "Sequential data assimilation with a non-linear quasi-geostrophic model using Monte Carlo methods to forecast error statistics." *Journal of Geophysical Research*, 99(C5), 10143–10162.

Evensen, G. (2003). "The Ensemble Kalman Filter: theoretical formulation and practical implementation." *Ocean Dynamics*, 53, 343-367, doi: 10.1007/s10236-003-0036-9.

Evensen, G. (2009). "The Ensemble Kalman Filter for Combined State and Parameter Estimation." *IEEE Control System Magazine*, 29, 83-104.

Fathi-Moghadam, M., and Kouwen, N. (1997). "Nonrigid, nonsubmerged, vegetative roughness on floodplains." *Journal of Hydraulic Engineering*, 123(1), 51–57.

Fisher, M., Nocedal, J., Tremolet, Yannick., and Wright, S. J. (2009). "Data assimilation in weather forecasting: a case study in PDE-constrained optimization." *Optimal Engineering*, 10, 409-426, doi: 10.1007/s11081-008-9051-5.

Gelb, A. (1974). "Applied optimal estimation." MIT Press, Cambridge, Massachusetts.

Giardino, D. (2004). "Analysis of the physical forcing mechanisms influencing salinity transport for the Lower St. Johns River." M.S., University of Central Florida, Orlando, Florida.

Hagen, S. C., Zundel, A. K., and Kojima, S. (2006). "Automatic, unstructured mesh generation for tidal calculations in a large domain." *International Journal of Computational Fluid Dynamics*, 20, 593–608, 10.1080/10618560601046846.

Hill, B. R. (1994). "Effects of vegetation on hydraulic roughness and sedimentation in wetlands." *WRP Technical Note SD-CP-2.2*, U.S. Army Engineer Research and Development Center, Vicksburg, Mississippi.

Homer, C., Huang, C., Yang, L., Wylie, B., and Coan, M. (2004). "Development of a 2001

    national land-cover database for the United States." *Photogrammetric Engineering and*

    Remote Sensing, 70(7), 829–840.

Houtekamer, R. L., and Mitchell H. L. (1998). "Data Assimilation Using an Ensemble Kalman

    Filter Technique." *Monthly Weather Review*, 126 (March), 796–811.

Hsu, M. H., Kuo, A. Y., Kuo, J. T., and Liu, W. C. (1999). "Procedure to calibrate and verify

    numerical models of estuarine hydrodynamics." *Journal of Hydraulic Engineering*,

    125(2), 166–182.

Jarvela, J. (2002). "Flow resistance of flexible and stiff vegetation: A flume study with natural

    plants." *Journal of Hydrology*, 269(1/2), 44–54.

Kalman, R. E. (1960). "A new approach to linear filtering and prediction problems."

    Transactions of the American Society of Mechanical Engineers – Journal of Basic

    Engineering, 82(D), 35–45.

Kinnmark, I. (1985). "The shallow water wave equations: Formulation, analysis and

    application." *Lecture Notes in Engineering 15*, C.A. Brebbia and S.A. Orszag, eds., New

    York, New York, Springer, 1–187.

Kolar, R. L., and Gray, W. G. (1990). "Shallow water modeling in small water bodies." *Computational Methods in Surface Hydrology*, Gambolati et al., eds., WIT Press, Billerica, Massachusetts, 149–155.

Kolar, R. L., Gray, W. G., Westerink, J. J., and Luettich, R. A. Jr. (1994a). "Shallow water modeling in spherical coordinates: Equation formulation, numerical implementation, and application." *Journal of Hydraulic Research*, 32(1), 3–24.

Kolar, R. L., Westerink, J. J., Cantekin, M. E., and Blain, C. A. (1994b). "Aspects of nonlinear simulations using shallow-water models based on the wave continuity equation." *Computers and Fluids*, 23(3), 523–538.

Kubatko, E. J., Westerink, J. J., and Dawson, C. (2006a). "An unstructured grid morphodynamic model with a discontinuous Galerkin method for bed evolution." *Ocean Modelling*, 15, 71-89, doi: 10.1016/j.ocemod.2005.05.005.

Kubatko, E. J., Westerink, J. J., and Dawson, C. (2006b). "*hp* Discontinuous Galerkin methods for advection dominated problems in shallow water flow." *Computer methods in applied mechanics and engineering*, 196, 437-541, doi: 10.1016/j.cma.2006.05.002.

Kubatko, E. J., and Westerink, J. J. (2007a). "Exact Discontinuous Solutions of Exner's Bed Evolution Model: Simple Theory for Sediment Bores." *Journal of Hydraulic Engineering*, 133(3), 305-311, doi: 10.1061/(ASCE)0733-9429.

Kubatko, E. J., Westerink, J. J., and Dawson, C. (2007b). "Semi discrete discontinuous Galerkin methods and stage-exceeding-order, strong-stability-preserving Runge-Kutta time discretizations." *Journal of Computational Physics*, 222, 832-848, doi: 10.1016/j.jcp.2006.08.005.

Kubatko, E. J., Dawson, C., and Westerink, J. J. (2008). "Time step restrictions for Runge-Kutta discontinuous Galerkin methods on triangular grids." *Journal of Computational Physics*, 227, 9697-9710, doi: 10.1016/j.jcp.2008.07.026.

Kubatko, E. J., Bunya, S., Dawson, C., and Westerink, J. J. (2009a). "Dynamic p-adaptive Runge-Kutta discontinuous Galerkin methods for the shallow water equations." *Computer methods in applied mechanics and engineering*, 198, 1766-1774, doi: 10.1016/j.cma.2009.01.007.

Kubatko, E. J., Bunya, S., Dawson, C., Westerink, J. J., and Mirabito, C. (2009b). "A Performance Comparison of Continuous and Discontinuous Finite Element Shallow Water Models." *Journal of Scientific Computing*, 40, 315-339, dor: 10.1007/s10915-009-9268-2.

Loder, N. M., Cialone, M. A., Irish, J. L., and Wamsley, T. V. (2009). "Idealized marsh simulations: Sensitivity of hurricane surge elevation and wave height to bottom friction." *Technical Report ERDC/CHL-CHETN-I-79*, U.S. Army Engineer Research and Development Center, Coastal and Hydraulics Laboratory, Washington, DC.

Liu, J., and West, M. (2001). "Combined parameter and state estimation in simulation-based filtering." *Sequential Monte Carlo Methods in Practice*, A. Doucet, ed., Springer, New York, New York, 197–224.

Luettich, R. A. Jr., and Westerink, J. J. (2006a). "ADCIRC: A parallel advanced circulation model for oceanic, coastal and estuarine waters; users manual for version 45.08." [Available online at http://adcirc.org/document/ADCIRC_title_page.html.]

Luettich, R. A. Jr., and Westerink, J. J. (2006b). "Formulation and numerical implementation of the 2D/3D ADCIRC finite element model, version 44.XX." [Available online at http://adcirc.org/document/ADCIRC_title_page.html.]

Lynch, D. R., and Gray, W. G. (1979). "A wave equation model for finite element tidal computations." *Computers and Fluids*, 7, 207–228.

Madsen, H., and Canizares, R. (1999). "Comparison of Extended and Ensemble Kalman Filters for Data Assimilation in Coastal Area Modelling." *International Journal for Numerical Methods in Fluids*, 31, 961-981.

Mattocks, C., Forbes, C., and Ran, L. (2006). "Design and implementation of a real-time storm surge and flood forecasting capability for the state of North Carolina." *UNC-CEP Technical Report*, University of North Carolina, Chapel Hill, North Carolina.

Miyoshi, K. (2005). "Ensemble Kalman Filter –Data Assimilation and Ensemble Prediction–." *Technical Report*, 4011, Japan Meteorological Agency, Tokyo, Japan.

Moradkhani, H., Sorooshian, S., Gupta, H., and Houser, P. R. (2005). "Dual state-parameter estimation of hydrological models using ensemble Kalman filter." *Advances in Water Resources*, 28, 135–147.

Ojima, Y. (2009). "Estimation of River Current Using Reduced Kalman Filter Finite Element Method." M.S. thesis, Chuo University, Tokyo, Japan.

Ojima, Y., and Kawahara, M. (2009). "Estimation of river current using reduced Kalman filter finite element method." *Computer Methods in Applied Mechanics and Engineering*, 198(9–12), 904–911, doi: 10.1016/j.cma.2008.11.003.

Reid, R. O. (1990). "Tides and storm surges." *Handbook of Coastal and Ocean Engineering, Volume 1: Wave Phenomena and Coastal Structures*, J. B. Herbich, ed., Gulf Publishing Company, Houston, Texas, 533–590.

Robinson, A. R., and Lermusiaux, P. F. J. (2000). "Overview of Data Assimilation." Harvard Reports in Physical/Interdisciplinary, Ocean Science, 62, Harvard University, Cambridge, Massachusetts.

Sucsy, P. V., and Morris, F. W. (2002). "Calibration of a three-dimensional circulation and mixing model of the lower St. Johns River." *Technical Report*, St. Johns River Water Management District, Palatka, Florida

Suga, R., and Kawahara, M. (2006). "Estimation of tidal current using Kalman filter finite-element method." *Computers and Mathematics with Applications*, 52(8/9), 1289–1298, doi: 10.1016/j.camwa.2006.11.006.

Takagi, T., Inamoto, K., and Kawahara, M. (1998). "Estimation of wave propagation using Kalman filter." *International Journal of Computational Fluid Dynamics*, 9(1), 77–84.

Tippett, M. K., Bishop, C. H., Hamill, T. H., and Whitaker, J. (2003). "Ensemble Square Root Filters." *Monthly Weather Review*, 131, 1485-1490.

Toth, D. J.. (1993). "Volume 1 of the Lower St. Johns River Basin Reconnaissance: Hydrogeology." *Technical Report SJ93-7*, St. Johns River Water Management District, Palatka, Florida.

Tombette, M., Mallet, V., and Sportisse, B. (2009). "PM10 data assimilation over Europe with the optimal interpolation method." *Atmospheric Chemistry and Physics*, 9, 57-70, doi: 10.5194/acp-9-57-2009.

Vrugt, J. A., Diks, C. G. H., Gupta, H. V., Bouten, W., and Verstraten, J. M. (2005). "Improved treatment of uncertainty in hydrologic modeling: Combining the strengths of global

optimization and data assimilation." *Water Resources Research*, 41, W01017, doi: 10.1029/2004WR003059.

Vrugt, J. A., Gupta, H. V., Bouten, W., and Sorooshian, S. (2003). "A Shuffled Complex Evolution Metropolis algorithm for optimization and uncertainty assessment of hydrologic model parameters." *Water Resources Research*, 39(8), 1201, doi:10.1029/2002WR001642.

Wan, E. A., and Nelson, A. T. (1997). "Dual Kalman filtering methods for nonlinear prediction, smoothing, and estimation." *Advances in Neural Information Processing Systems*, 9, 793–799.

Wang, D., Chen, Y., and Cai, X. (2009). "State and parameter estimation of hydrologic models using the constrained ensemble Kalman filter." *Water Resources Research*, 45, W11416, 1–12, doi: 10.1029/2009WR007819.

Wei, J. and Malanotte-Rizzoli, P. (2009). "Validation and application of an ensemble Kalman filter in the Selat Pauh of Singapore." Massachusetts Institute of Technology, Cambridge, Massachusetts.

Welch, G. and Bishop, G. (2006). "An Introduction to the Kalman Filter." *TR 95-041*, University of North Carolina at Chapel Hill, Chapel Hill, North Carolina.

West, M. (1993). "Mixture models, Monte Carlo, Bayesian updating and dynamic models." *SIAM Journal on Scientific and Statistical Computing*, 24, 325–333.

Westerink, J. J., Luettich, R. A., Feyen, J. C., Atkinson, J. H., Dawson, C., Roberts, H. J., Powell, M. D., Dunion, J. P., Kubatko, E. J., and Pourtaheri, H. (2008). "A basin- to channel-scale unstructured grid hurricane storm surge model applied to Southern Louisiana." *Monthly Weather Review*, 136, 833–864.

Zang, X., and Malanotte_Rizzoli, P. (2003). "A comparison of assimilation results from the ensemble Kalman Filter and a reduced-rank extended Kalman Filter." *Nonlinear Processes in Geophysics*, 10, 477-491

Zwillinger, D. (2003). "Standard mathematical tables and formulae." Chapman & Hall/CRC, Boca Raton, Florida.